

The Structures and Extents of the Chromospheres of Late-type Stars

A dissertation submitted to the University of Dublin
for the degree of Doctor of Philosophy

Neal Ó Riain
Trinity College Dublin, September 2015

SCHOOL OF PHYSICS
UNIVERSITY OF DUBLIN
TRINITY COLLEGE



Declaration

I declare that this thesis has not been submitted as an exercise for a degree at this or any other university and it is entirely my own work.

I agree to deposit this thesis in the University's open access institutional repository or allow the library to do so on my behalf, subject to Irish Copyright Legislation and Trinity College Library conditions of use and acknowledgement.

Name: Neal Ó Riain

Signature: **Date:**

Summary

The chromosphere is the region of a star, above what is traditionally defined as the stellar surface, from which photons freely escape. As the definition implies, this region is characterised by complexity, non-equilibrium, and specifying its structure is a vastly non-linear, non-local problem. In this work we are concerned with the chromospheres of late-type stars, objects of spectral type K to M, the thermodynamic structure, extent, and heating mechanisms of whose chromospheres are not well understood. We use a number of observational and computational methods in order to gain a detailed quantitative understanding of these chromospheres.

We construct a model to compute the mm, thermal bremsstrahlung flux from the chromospheres of late-type objects, based on a number of simplifying assumptions concerning their thermodynamic structure. We compare this model with archival and recent observations, and find that the model is capable of reproducing the observed flux from objects of spectral type K to mid-M in the frequency range 100 GHz – 350 GHz. We suggest that, while this model is quite simple, it provides an accurate reflection the structure of the chromosphere of late-type stars.

We also make use of the unique insights into stellar structure provided by the eclipsing ζ Aurigae binaries. We present the “rediscovery” of periodic Si I emission in these objects. We hypothesise that this effect arises as a result of the UV radiation of the secondary object, which photo-ionizes Si I in the chromosphere of the primary. Since this UV radiation falls only on a portion of the visible hemisphere of the primary at a given phase, the line is periodic, and as a locally formed line in

disk-averaged spectrum this is a novel and powerful diagnostic. While we rule out this line being a result of simple reflection, we expect it to have the same phase variation as broadband reflection. We construct a geometric model of the system, and find that the computed reflection curve matches the observed line periodicity very well.

As the primary of ζ Aurigae undergoes an eclipse it is possible to effectively resolve its chromosphere, which allows us to place direct constraints on its structure. However, despite the unique insights afforded by the study of this system, no semi-empirical model has yet been constructed. Using archival observations of ζ Aurigae A we construct a full one-component, semi-empirical model of its chromosphere. As this binary system is detached its chromosphere is thought to be comparable to that of single stars — λ Velorum being a specific example — and we use the model constructed to comment on the structure of late-type chromospheres generally.

For my family

Acknowledgements

I'd like to acknowledge the scientific contribution of Dr. Graham Harper to the research of this thesis, I am very grateful for his input and direction at the early stages of this work. A sincere thanks to Dr. Peter Gallagher for all of his help and advice throughout my time at Trinity, and especially in the somewhat rocky final months of my PhD. The staff of the School of Physics, academic, administrative, and technical, have always been so welcoming and accommodating, and for that I am deeply appreciative.

A big thanks to all of the members of the Astrophysics Research Group, past and present, that I've had the misfortune and pleasure to work with. You're a great group of lads. The most important and lasting part of the past four years is my friendships with each of you. The science is a distant second.

Thanks also all my friends, you've put up with my complaints over the past few years; thanks for the patience and all the good times.

Most importantly thanks to my family, for everything. Without your support and encouragement I'd be nowhere.

List of Publications

1. **Ó Riain**, N., Harper, G. M.
“Non-LTE model of the Chromosphere of ζ Aurigae A”
in prep, 2015
2. Harper, G. M., **Ó Riain**, N., Griffin, R.E.M., Bennett, P.D.
“Periodic Photoexcited Si I Emission in Composite-Spectrum Binaries”
in prep, 2015
3. **Ó Riain**, N., Harper, G. M., Griffin, R.E.M., Bennett, P.D.
“ ζ Aurigae: Periodic Photoexcited Si I Emission”
Proceedings of the 18th Cambridge Workshop on Cool Stars, Stellar Systems,
and the Sun, 2014
4. Harper, G.M., **Ó Riain**, N., Ayres, T.R.
“Chromospheric thermal continuum millimetre emission from non-dusty K
and M red giants”
Monthly Notices of the Royal Astronomical Society, 2013

Contents

List of Publications	vii
List of Figures	xii
List of Tables	xx
1 Introduction	1
1.1 Motivation	2
1.2 Evolution of Late-type Stars	3
1.3 Structure of Late-Type Stars	6
1.4 Stellar Observation & Theory	11
1.5 Radiative Transfer	13
1.6 ζ Aurigae Binaries	16
1.7 Thesis Overview	18
2 Background & Theory	20
2.1 Absorption and Emission Mechanisms	21
2.1.1 Free-free absorption & emission	21
2.2 Bound-bound Absorption and Emission	24
2.2.1 Atomic Structure	25
2.2.2 Transitions	27
2.2.2.1 Line Profiles	30
2.2.3 Bound-Free Transitions	37
2.3 Rate Equations	38
2.3.1 Density Sensitive Transitions	40
2.4 Solving the Transfer Problem	43
2.5 Computation of Fluxes	50

2.5.1	Escape Probability	50
2.5.2	Feautrier Method	52
2.6	Modelling Binary Stars	56
2.6.1	System Geometry	56
2.6.2	Radiative Properties	62
3	Instrumentation	65
3.1	Spectrometers	66
3.1.1	Ground-based Observations	66
3.1.2	Hubble Space Telescope	69
3.2	Interferometry	73
3.2.1	Principles of an Interferometer	73
3.2.2	Interferometry with CHARA	77
3.3	Radio Observations	78
3.3.1	CARMA	78
3.3.2	APEX	79
4	Thermal Continuum Millimetre Emission from non-dusty K and M Giants	82
4.1	Introduction	83
4.2	Initial Model	84
4.2.1	Semi-Empirical Constraints on Stellar Chromospheres	84
4.2.2	Scale Height & Chromospheric Extent	86
4.2.3	Millimetre Optical Depth	87
4.2.4	Linear Source Function Method	88
4.2.5	α Tau Calibration	90
4.3	Extensions to the Model	92
4.3.1	Spherical Geometry	92
4.3.2	Exponential Layer	93
4.4	Calibration and Results	98
4.4.1	Solar Brightness Temperature	98
4.4.2	Stellar Fluxes	100
4.5	Predictions of the Model	104
4.5.1	Recent Observations	104

4.5.2	Spectral Indices	106
4.6	Summary and Conclusions	108
5	Geometric Modelling of the ζ Aurigae System	110
5.1	Introduction	111
5.1.1	Spectroscopic Observations	112
5.2	Geometric Model & Light Curve	118
5.2.1	Stellar Parameters & Orbital Elements	118
5.2.2	Synchronicity	121
5.2.3	Limb-Darkening & Gravity Darkening	124
5.2.4	Light Curve	125
5.3	Reflection Effect	125
5.3.1	Sobolev Reflection	128
5.3.2	PHOEBE Reflection Curve	131
5.3.3	Line Reflection	135
5.4	Conclusions	138
6	Chromospheric Model of ζ Aurigae A	140
6.1	Introduction	141
6.2	Construction of the Initial Model	142
6.2.1	MARCS Model Photosphere	142
6.2.2	Empirical Mass Column Densities	143
6.2.3	Empirical Temperatures and Turbulent Velocities	144
6.2.4	Electron Densities	146
6.3	Atomic Models	151
6.3.1	Hydrogen Model	152
6.3.2	Aluminium Model	154
6.3.3	Carbon Model	156
6.4	Spectral Observations	161
6.4.1	HST Data	161
6.4.2	Synthetic Spectra	171
6.4.3	Contribution Function	176
6.4.4	λ Velorum Ca K & H- α Profiles	177
6.5	Chromospheric Model	180

CONTENTS

6.5.1	Best-fit Chromospheric Model	180
6.5.2	Chromospheric Extent	183
6.6	Conclusions	186
7	Conclusions & Future Work	188
7.1	Radio Model	189
7.2	Periodic Si I Emission	193
7.3	Chromospheric Model of ζ Aurigae A	195
7.4	Concluding Remarks	198
A	Atomic Models	203
A.1	H atom	203
A.2	Al atom	204
A.3	C atom	209
B	Atmospheric Model	211
References		214

List of Figures

1.1	The Hertzsprung-Russell diagram with the stellar evolutionary tracks annotated for objects of various initial masses. This figure contains both the observational and theoretical HR diagrams. The observational diagram has axes of color and magnitude, which are directly observable, and the theoretical form has axes of effective temperature and luminosity, which require a model to determine. <i>Image Credit: Australia Telescope National Facility.</i>	4
1.2	The internal structure of red giant (left) and asymptotic giant branch stars (right), showing the different shells of internal burning. <i>Image Credit: Australia Telescope National Facility.</i>	5
1.3	The complexity of the solar atmosphere from the photosphere and above. <i>Image Credit: Wedemeyer-Böhm et al. (2009)</i>	8
1.4	A simple, 1-dimensional, time-independent model of the solar photosphere/chromosphere, annotated with the formation heights of various spectral lines. <i>Image Credit: Vernazza et al. (1976)</i>	9
1.5	Specific intensity passing through a volume of material, $dV = dSds$	14
2.1	Emission produced by the deflection of an electron by Coulomb interaction with a nucleus.	22
2.2	Voigt Profile	32
2.3	XRD Diagram	36
3.1	Diagram of a spectrograph with a reflecting diffraction grating.	67

LIST OF FIGURES

3.2	Diagram of the Hubble Space Telescope. This diagram is post-installation of the STIS instrument, which took the place of GHRS. <i>Image Credit: NASA.</i>	69
3.3	A schematic diagram of the GHRS. <i>Image Credit: Brandt et al. (1994).</i>	70
3.4	Diagram of Young’s double slit experiment. On the left-hand side of each image we see the source, and on the right-hand side we see the resultant interference pattern. Note that as the source size and slit separation is varied the interference pattern is modulated. <i>Image Credit: From Jackson (2008), adapted by E. O’Gorman.</i>	74
3.5	Diagram of a two element interferometer. Light enters the two telescopes, labelled 1 & 2, and is combined, resulting in the interference pattern shown. <i>Image Credit: National Radio Astronomy Observatory.</i>	75
4.1	Observed minus computed brightness temperatures at 250 GHz. The dotted lines represent $\pm 0.33T_{\text{eff}}$. Data from the catalogue of Altenhoff <i>et al.</i> (1994).	91
4.2	Rays in spherical geometry. Note the disk rays, which contain a photospheric component, and “grazing rays”, which do not.	93
4.3	Geometry of the atmosphere, featuring the photosphere, with radius R , a layer of exponentially increasing electron density, and the layer of constant electron density.	94
4.4	Ray passing through the exponential layer.	96
4.5	A best fit of the M2 model to the solar brightness temperatures of Loukitcheva <i>et al.</i> (2004). We see at low frequencies the model fails to reproduce the observations. Best fit values: $a_1 = 1.7$ and $a_2 = 4.55$, Initial parameters: $a_1 = 1$ and $a_2 = 4.4$)	99
4.6	<i>Top:</i> Brightness Temperature scatter for the M2 model. <i>Bottom:</i> Brightness Temperature scatter for the M3 model. The dotted lines in both plots represent $\pm 0.33T_{\text{eff}}$	101

LIST OF FIGURES

4.7	M2 model compared with high S/N CARMA and APEX observations. We see that the model again provides a good fit, with most objects falling within $\pm 30\%$ at all frequencies.	105
4.8	Spectral indices, computed at 225GHz and 100GHz, for a range of T_{eff} and $\log(g)$. We see that at high temperature and low gravity the spectral index index matches the optically thin limit, and as $\log(g)$ increases the optically thick case is recovered.	107
5.1	Si I in emission in composite-binary systems. The upper panel shows the spectra of three composite-spectrum binaries, with the CaII K line ($\lambda 3933.7\text{\AA}$) nearly central. Emission appears at $\lambda 3905\text{\AA}$ in the three systems observed at the phases indicated (see Table 5.1). The lower panel shows the emission line at $\lambda 4102\text{\AA}$. It can be seen redward of the core of H- δ , and due to this cannot be measured accurately. It is therefore less useful for quantitative measurements, but its presence is valuable in confirming the identity of the source of the emission. Figure from Harper <i>et al.</i> (2015) (REMG).	112
5.2	Line profiles of the Si I $\lambda 3905\text{\AA}$ obtained at several different phases, ϕ , where ϕ is the fractional orbit elapsed from periastron, which occurs shortly after second contact of the secondary's eclipse. They are offset vertically for clarity. The phase dependency of the line can be clearly seen.	114
5.3	The orbits of the ζ Aurigae system. We see the objects at periastron, $\phi = 0$. In the top down plot the inferior conjunction (secondary is eclipsed as viewed from Earth) and superior conjunction (primary is eclipsed as viewed from Earth) are marked. The objects are plotted to scale.	118
5.4	<i>Left:</i> Fractional change in the K-star equatorial radius, R_{eq} , and the polar radius, R_{pole} , as a function of phase over 1.5 periods. <i>Right:</i> $R_{\text{eq}}/R_{\text{pole}}$, demonstrating that even far from periastron the K-star is slightly oblate, with $R_{\text{eq}} = 1.008R_{\text{pole}}$. Note that in the figure on the left both curves are normalised to unity, and in the figure on the right the curve presented is $R_{\text{eq}}/R_{\text{pole}}$ at each phase.	120

LIST OF FIGURES

5.5	Radial velocity curve of the primary of ζ Aurigae. The data presented are those of Eaton <i>et al.</i> (2008).	122
5.6	<i>Upper panel:</i> The orbit of the ζ Aurigae system at various phases from periastron, ϕ , with the Johnson V-Band light curve superimposed. <i>Lower Panel:</i> V-Band light curve of the ζ Aurigae system. The PHOEBE synthetic light curve, in black, is in good agreement with the photometric data of Eaton <i>et al.</i> (2008).	126
5.7	Diagram of two stars, separated by a	127
5.8	Diagrams outlining the coordinate system in use.	129
5.9	Flux reflected from the K-star as a function of phase as predicted by Eqn. 5.25.	130
5.10	<i>Top:</i> Six images of the surface of the K-star and the reflected B-star flux. The images show (from top left to bottom right) 0, 0.16, 0.33, 0.5, 0.66 and 0.83 phase from periastron, respectively. <i>Bottom:</i> The reflected V-band flux as a function of phase, as calculated by PHOEBE. The black lines mark the phases shown in the above images.	132
5.11	PHOEBE model output (red), the Sobolev spherical approximation (black), and the observed Si I EEW (blue).	133
5.12	Contours of equal gravitational potential for the ζ Aurigae system, a slice through the plane of the orbit. The objects are plotted to scale.	134
5.13	Reflected line profiles at given phases for a rotational velocity of $v_{\text{rot}} = 6 \text{ km/s}$. The dotted line represents line centre.	136
5.14	<i>Left:</i> Reflected line profiles at given phases for a rotational velocity of $v_{\text{rot}} = 6 \text{ km/s}$ and a turbulent velocity of $v_{\text{turb}} = 10 \text{ km/s}$ overplotted with observation.	137
6.1	The run of temperature with mass column density for interpolated MARCS model photosphere, as compared with the models used to produce it.	142

LIST OF FIGURES

6.2	<i>Top Left:</i> Empirically measured temperatures as a function of height and column density through the atmosphere. We note the extent of the atmosphere. <i>Top Right:</i> Empirically determined turbulent velocities as a function of height. We note the large errors on these data. <i>Bottom:</i> The temperature and v_{turb} profiles for the model atmosphere, constructed from the empirical data, and the MARCS model.	145
6.3	Electron density as a function of height above the photosphere. We see the electron density computed using the the assumptions of CRD and PRD, compared with the empirically measured electron densities.	149
6.4	Grotian Diagram of the H model constructed. This model consists of 5 HI levels and one H II ionization level. The transition series (Lyman, Balmer, etc.) are colour coded.	152
6.5	Grotian Diagram of the AlI-III model constructed. The AlII] $\lambda 2669 \text{ \AA}$ line, for which we have HST spectra, is marked.	155
6.6	<i>Left:</i> Grotian diagram of the radiative transitions in the CII-III model constructed. The quintet transitions are marked in red. <i>Right:</i> A schematic Grotian diagram of the CII electron density sensitive quintet transitions.	157
6.7	Line ratios as a function of electron density for a fixed column density (10^{23} cm^{-2}) and temperature (6500 K). The ratios for the atomic data used in our model can be seen in red, and are contrasted with atomic parameters used in the analysis Judge & Carpenter (1998a).	159
6.8	Orbit of ζ Aurigae with the HST GHRS observation epochs annotated. Image adapted from Harper <i>et al.</i> (2005).	162
6.9	HST GHRS ζ Aurigae Epoch 8 spectra. <i>Top:</i> Spectrum covering the region of the CII] $\lambda 2325 \text{ \AA}$ quintet with the lines annotated. <i>Bottom:</i> Spectrum of the AlII] $\lambda 2669 \text{ \AA}$ region, again annotated. Note that both spectra have been converted to stellar surface flux using the angular diameter given, ϕ . Further note the very bright wind scattering features which dominate the spectra.	163

LIST OF FIGURES

6.10 HST GHRS ζ Aurigae Epoch 8 spectra with the spectra of λ Velorum over plotted. We can see how closely the surface fluxes of these objects match, and we also note the wind scattering features in the spectra of ζ Aurigae which are clearly absent in those of λ Velorum.	165
6.11 Scattered light spectra, as computed by Bennett (2015), for the regions of the CII] quintet and AlII] 2669Å.	166
6.12 Gaussian fits to five of the most prominent wind-scattered lines, and four of the lines of the CII] 2325Å quintet. The observed spectrum can be seen in black, the Gaussian fits to the contaminants in green, and the CII] lines in blue. The sum is plotted in red. The region of the 2328Å feature marked in red is removed from the fit. In the lower panel the percentage error in the spectrum is plotted. Note that the region excised from our fit is flagged with NaN values in the error array.	167
6.13 Gaussian fits to the lines of the CII] quintet in the spectrum of λ Velorum. The observed spectrum can be seen in black, and the Gaussian fits in red. The continuum is fitted, and offset from zero by 1×10^3 ergs/cm ² /s/Å. The lower panel shows the percentage error in the observed fluxes.	168
6.14 The density-sensitive CII] ratios, as computed from the Gaussian fits to the spectra, plotted on the line ratios as a function of electron density (for a fixed column density (10^{23} cm ⁻²) and temperature (6500 K)). The points with arrows denote upper limits. The line ratios are computed using the mean-escape probability method using the data of Tayal (2008), see Fig. 6.7	169
6.15 Asymmetry in the ζ Aurigae Al 2669Å line profile. Here we see the line plotted, on a velocity scale with the red-ward and blue-ward fluxes plotted (coloured accordingly). We see a clear excess on the blue side of the line (shorter wavelength, higher frequency, than line center). Both are fitted with Gaussians to quantify the asymmetry. The background and the FWHM of the Gaussians are annotated. . .	170
6.16 Flowchart describing the Markov Chain process by which the atmosphere is adapted to better fit the HST spectra.	172

LIST OF FIGURES

6.17	The optical depth due to interstellar dust as a function of wavelength. We can prominently see the well-known 2175Å feature (Stecher & Donn, 1965).	174
6.18	Synthetic spectra from the best fit ζ Aurigae atmosphere plotted with the HST GHRS ζ Aurigae Epoch 8 spectra and the HST spectra of λ Velorum.	175
6.19	<i>Top:</i> Contribution function of the C II] quintet. <i>Bottom:</i> Contribution function of the Al II] line. We note that both of these features appear to form at similar heights in the atmosphere.	177
6.20	<i>Left:</i> H- α and Ca II K profiles of λ Velorum taken from the atlas of Zarro & Rodgers (1983). The H- α is on top, and in the thinner line style, the Ca II below. <i>Right:</i> The computed H- α and Ca II K profiles, using the same line styles.	178
6.21	The run of temperature with height, and mass column density, for the best fit model atmosphere. The model is plotted in black, with the empirical data points plotted as annotated, and the empirical wind law – which was used as the initial temperature – is plotted in blue.	179
6.22	The run of turbulent velocity with height for the best fit model atmosphere. Note that it was necessary to reduce the turbulent velocity in the line-forming region ($h \sim 10 - 40 R_{\odot}$) to reproduce the observed line widths.	181
6.23	The best fit temperature grid, with the resultant electron densities, plotted against height. the empirically measured temperatures, black, and electron densities, red. The values plotted are the same as those used in preceding sections, where the plots are fully annotated.	182
6.24	Limb darkening curve for β Ceti, computed using MULTI, for the plane-parallel and the spherical case. Note that in the plane-parallel case we see increasing intensity as we move to the limb.	185

LIST OF FIGURES

7.1	<i>Top Panels:</i> The computed normalised brightness temperature distribution of α Tau (left) and α Boo (right) at 250 GHz. The photospheric radius is denoted by a dotted line. <i>Middle Panels:</i> Limb-darkening curves computed which were used to produce the images. <i>Lower Panels:</i> Visibility curves for both objects, showing the uniform disk visibility (black), and the visibility given the computed limb-darkening curve (red).	191
7.2	Spectra of ζ Aurigae, collected by O. Hashimoto using the Gunma Astronomical Observatory Echelle Spectrograph. Wavelengths are given in air.	194
7.3	Si I Grotrian diagram. The lines are colour-coded according to $\log(gf)$, thicker, darker lines have a higher value. The $\lambda 3905\text{\AA}$ and $\lambda 3905\text{\AA}$ transitions of interest are highlighted in blue.	196
7.4	Ratio of the emergent flux in the Si I $\lambda 3905\text{\AA}$ and $\lambda 3905\text{\AA}$ lines for an illuminated and un-illuminated boundary.	197

List of Tables

3.1	Bandpass and wavelength pixel correspondence for each of the optical elements of the GHRS.	73
3.2	Details of the CARMA observations collected for use in this work. .	79
3.3	Details of the APEX observations collected for use in this work. All observations were made at 345 GHz.	80
4.1	Adopted properties of α Tau.	90
4.2	The χ^2 and total scatter of the three models for the objects in Table 4.3.	100
4.3	Stellar parameters and 250 GHz flux densities of objects used to test M2 and M3. The flux densities are from Altenhoff <i>et al.</i> (1994), T_{eff} , Fe/H, & $\log(g)$ come from the PASTEL catalogue (bar the marked exceptions)(Soubiran <i>et al.</i> , 2010), parallaxes are from van Leeuwen (2007), ϕ from Mozurkewich <i>et al.</i> (2003) (bar the marked exceptions), and \mathcal{F} from Pérez Martínez <i>et al.</i> (2011)	103
4.4	<i>Top:</i> Stellar parameters of objects recently observed with CARMA, and APEX. The parameters are collected from various sources, as annotated. <i>Bottom:</i> The observed flux densities.	104
4.5	Spectral indices from the CARMA observations, and computed from M2.	106
5.1	Log of observations of the emission-line region near λ 3905Å in ζ Aur.117	
5.2	Orbital Elements and Stellar Parameters of ζ Aur.	119
5.3	Sensitivity of the phase variation of the reflection curve to various model parameters	131

LIST OF TABLES

6.1	Electron density as computed by Schroeder (1986); Schroeder <i>et al.</i> (1990) and recomputed using updated atomic data	150
6.2	Atomic data for the electron density sensitive C II quintet.	158
6.3	Analytic and computed (by the mean escape probability method) values for the flux ratios in the high and low density limits from the values of Tayal (2008)	161
6.4	The electron densities predicted from the measured HST GHRS line ratios. We note that this diagnostic predicts similar electron densities for both λ Velorum and ζ Aurigae.	169

1

Introduction

We begin by outlining the motivation behind the study of the atmospheres of cool stars. We then introduce the concepts at play in this study, taking time to discuss the physical properties of cool stars, focusing on the interiors of these objects and their evolution in time. We address the principal topic of study, discussing the atmospheres of these cool star in detail. We introduce the emission mechanisms and physical processes which will be the subject of the succeeding chapters, deriving the radiative transfer equation, and highlighting those topics which are the subject of debate in the literature. A brief overview of the field will be presented, outlining the history of observation and modelling. As much of this work is focused on the study of one unique class of object in particular (ζ Aurigae binaries) we will devote some time to discussing these objects, contextualising their study in this work. Finally we present an outline of the subsequent chapters of this thesis and the questions addressed therein.

1.1 Motivation

The core problem to be addressed in the study of stellar physics is the specification of the physical properties of a star — temperature, density, etc. — as a function of depth, given the star’s age, mass, and chemical composition. Despite the fact that the atmosphere of a star comprises $\sim 1/10^{10}$ of its total mass, the stellar atmosphere is key in understanding the structure of the stellar interior. This stems from the fact that only observational data upon which we can base our study of stellar physics is the emergent stellar spectrum, and this spectrum can only be understood through very close study of the stellar atmosphere.

All of the stellar radiation which we measure emerges from the stellar atmosphere, the stellar atmosphere is all that we can “see”, and as such all that we can measure directly. The interior of the star is opaque, effectively trapping photons, and as such is inaccessible to direct observation. The atmosphere itself represents the boundary between this dense stellar interior, and the tenuous stellar wind and near vacuum of the interstellar medium. The study of the stellar atmosphere is in effect the study of the interface between a material which is (almost) in perfect thermodynamic equilibrium and (almost) empty space. As radiation does begin to escape the interior it must pass through the atmosphere, transporting energy and interacting with the constituent material. As a result of this interaction the emergent radiation carries with it information regarding the physical properties of the material through which it has passed. The emergent radiation encodes this information, as it is integrated along the path of the radiation through the atmosphere. In this work we examine the inverse problem of determining a self-consistent set of physical properties, as a function of depth through the atmosphere, which, when path-integrated along each ray, reproduce the emergent spectrum.

The problem is vastly complicated by its non-linear, non-local nature. It is non-linear due to the fact that as the radiation field interacts with matter, the matter alters the state of the radiation field, coupling the state of the material and the state of the radiation. The non-locality arises due to the fact that the state of the matter at one point is dependent on the local radiation field, which in turn depends on the radiation field (and hence the state of the matter) at essentially

all other points in the atmosphere. This is because the mean free path of photons is typically much larger than the gradients of the physical properties.

By carefully untangling this complex problem it is possible to gain unique insight into the interior structure of stars. For example, high-dispersion spectroscopy provides diagnostic information on the structure of the atmosphere, but these observations can only be exploited if care is taken in treating the above problems. An accurate quantitative understanding of the atmosphere of the star provides us with the boundary conditions of the stellar interior and the chemical composition of the object — which taken synoptically informs our understanding of the abundances of the chemical elements in the Universe as a function of time and location. Despite comprising a small fraction of the star’s mass the atmosphere greatly shapes its evolution through the stellar wind, and in order to know the future evolution of an object we must study the structure of its atmosphere. Of great relevance to this work is the fact that, in the case of late-type objects (giants and supergiants), the radius is not well known due to their large, extended envelopes, and this fundamental parameter can only be determined through careful determination of the overall atmospheric structure.

1.2 Evolution of Late-type Stars

Stars of spectral classification K through mid-M are usually known as late-type stars, due to erroneous historical ideas about stellar evolution. This classification is based on the emission and absorption lines observed in the stellar spectrum, and arranged, by Annie Jump Cannon, in order of decreasing effective temperature (Hoffleit, 1943). Between O and M the effective temperature varies by a factor of ~ 15 . Around 1910 Hertzsprung and Russell independently produced diagrams plotting this classification of stars by colour (effective temperature) against magnitude (luminosity), producing what is known as the HR diagram. A HR diagram can be seen in Fig. 1.1 (Zeilik *et al.*, 1992). In this work we will concern ourselves primarily with post-main sequence objects, K- to mid-M type evolved stars, red giants and supergiants, and as such we focus in particular on their evolution.

The HR diagram neatly summarises the evolutionary life-cycle of a star. As a proto-stellar cloud condenses under the force of gravity the pressure at the core

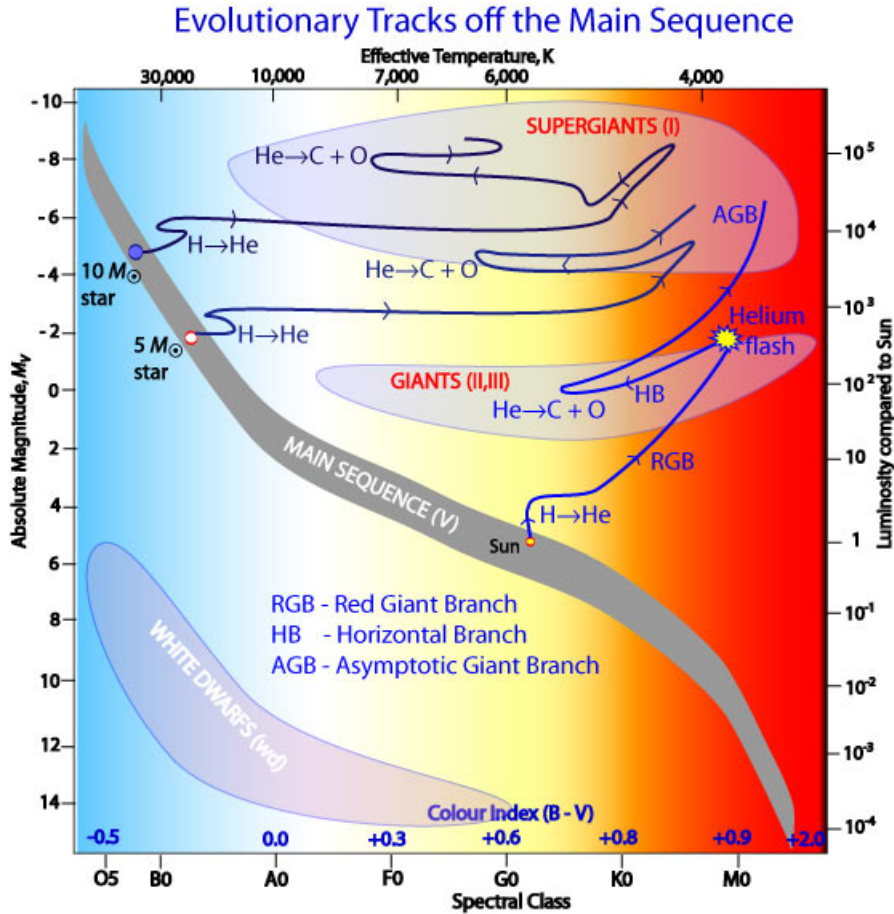


Figure 1.1: The Hertzsprung-Russell diagram with the stellar evolutionary tracks annotated for objects of various initial masses. This figure contains both the observational and theoretical HR diagrams. The observational diagram has axes of color and magnitude, which are directly observable, and the theoretical form has axes of effective temperature and luminosity, which require a model to determine. *Image Credit: Australia Telescope National Facility.*

begins the fusion of hydrogen to helium. Stars with masses below $\sim 1.5 M_\odot$ convert hydrogen to helium by what is known as the proton-proton (p-p I) chain, at higher masses the so-called CNO cycle is dominant in the core (Salaris & Cassisi, 2005). The energy released in this reaction balances gravity and arrests the star's contraction. For most of the star's lifetime the conversion of H to He is the dominant energy production process, and stars undergoing this process are known as main sequence stars. The time a star spends on the main sequence is governed

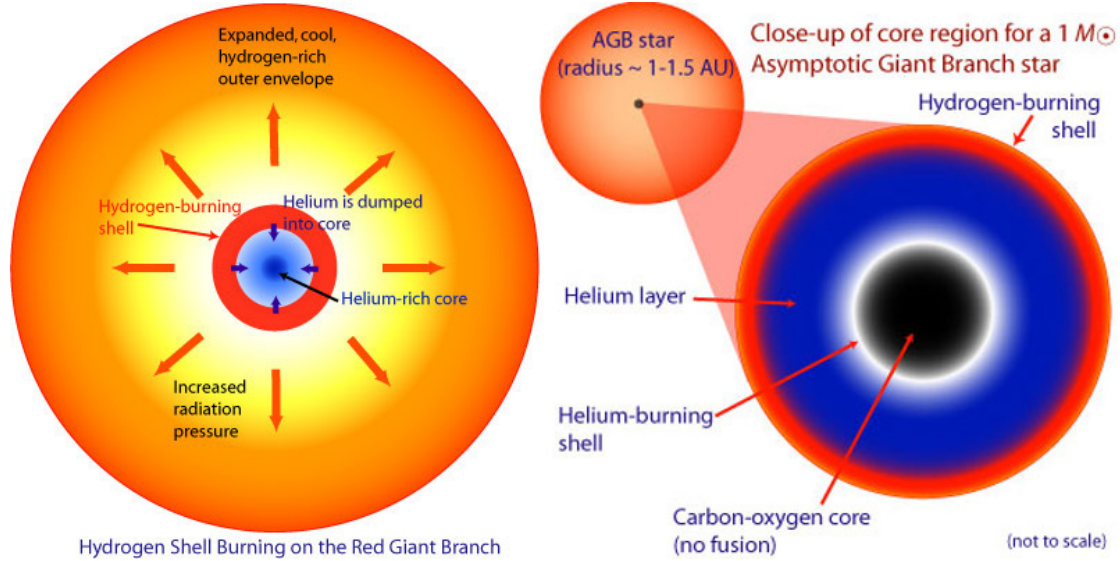


Figure 1.2: The internal structure of red giant (left) and asymptotic giant branch stars (right), showing the different shells of internal burning. *Image Credit: Australia Telescope National Facility.*

by its mass, heavier stars burning their fuel quickly and spending less time on the main sequence. Once a star has exhausted the supply of hydrogen at its core it begins its evolution off the Main Sequence (see annotated evolutionary tracks in Fig. 1.1).

When hydrogen burning has been extinguished in the core the star begins to contract.¹ This raises the temperature and ignites further hydrogen burning in the less processed shells surrounding the core. This is known as the Sub-Giant Branch, the period of time after H burning has halted, but before the He burning has yet begun. At this point the atmosphere expands, as it absorbs the excess energy from the heating of the core (Öpik, 1938). This increases the luminosity and decreases the surface temperature; moving the star off the main sequence, up and to the right on the HR diagram. This process occurs quickly, causing the so-called Hertzsprung Gap, and moving the star to the next phase of evolution.

The Red Giant Branch occurs next, the phase of the star's life during which the core continues to contract, increasing the luminosity and moving the star further

¹In practice it is very difficult to determine a H burning from a He burning star, though Bedding *et al.* (2011) presented such a result by astroseismological methods.

up the HR diagram. Convection begins to move the ash left from the H burning, and this process, known as the first dredge-up, mixes heavier elements into the star’s outer envelope. In stars of sufficient mass ($\gtrsim 0.5M_{\odot}$), at the tip of the Red Giant Branch, the core contracts and the pressure increases until helium burning becomes possible by the triple-alpha process (Iben, 1967). The core then begins to expand again, and the star ceases its rise up the Red Giant Branch, moving to the Red Giant Clump.

The Red Giant Clump is the phase of evolution wherein there is core He burning and shell H burning. This process will continue until there is no further He remaining in the core and, mirroring the previous phase of evolution, the core will contract causing shell He burning to begin. This leaves two shells, one burning hydrogen and one burning helium, around an inert carbon and oxygen core.

The next phase of the star’s life is the ascent of the Asymptotic Giant Branch, which runs almost parallel to the Red Giant Branch on the HR diagram. Stars of $M_* \gtrsim 8M_{\odot}$ will begin burning C and O in their cores. This leaves a core burning C-O inside shells of He and H burning. At this point a second dredge-up may occur. The internal structure of red giant and asymptotic giant branch stars can be seen in Fig. 1.2.

This process of shell burning of heavier and heavier elements will continue up to Fe for stars of sufficient mass. The outer atmosphere of the star will be shed, leaving the core behind. For objects of mass below the Chandrasekhar limit $M_* < 1.39M_{\odot}$ (Chandrasekhar, 1931; Mazzali *et al.*, 2007) the core will be supported against further gravitational contraction by electron degeneracy pressure as the outer atmosphere is shed. This is known as a white dwarf. For objects of $M_* > 1.39M_{\odot}$, electron degeneracy is unable to support the core, resulting in a supernova. The remnants of the supernova will form a neutron star, supported from further collapse by neutron degeneracy pressure, or a black hole if $M_* \gtrsim 3M_{\odot}$ (Chamel *et al.*, 2013).

1.3 Structure of Late-Type Stars

At their core objects undergoing p-p (I) chain interactions, due to the weak temperature dependence of the reaction (“only” T^7), have a shallow temperature gradient,

and as such radiation is the most efficient energy transport mechanism. This region is referred to as the radiative zone. Above this there is a region where hydrogen becomes ionised, increasing the opacity and reducing the efficiency of radiative transport, in this region convection is the dominant energy transport mechanism. In red giants the entire outer envelope is convective (Schrijver & Zwaan, 2000). This is not true of CNO objects ($M_* \gtrsim 1.5M_\odot$), where the temperature dependence of the reaction is much steeper (T^{20}), and hence convection dominates in the core and the outer envelope is in radiative equilibrium (Salaris & Cassisi, 2005).

In this interior region the material is in thermodynamic equilibrium (the amount of energy absorbed at a point is exactly balanced by the amount emitted) and all photons are trapped, undergoing a number of absorptions and re-emissions, being systematically lowered in energy as they travel outward. Due to their being repeatedly absorbed and re-emitted the photons are in their equilibrium distribution, the Planck distribution for a given frequency, resulting in the emitted black-body spectrum. The photosphere is defined as the region where the optical depth of the atmosphere, τ , drops below $2/3$,¹ which is to say where the material becomes transparent to photons and radiation can begin to escape. As a result of this loss of energy the material is no longer in thermodynamic equilibrium. Above this region lies the chromosphere.

In the solar case the chromosphere is a complex region of shocks, magnetic fields, and convection, as can be seen in Fig. 1.3. Despite this complexity, the solar chromosphere can be modelled quite successfully as a 1-dimensional, time-independent structure. The first such model was compiled by Vernazza *et al.* (1976), known as the VAL model, and this can be seen in Fig. 1.4. This model well reproduces the formation of the absorption and emission features of the solar spectrum. There are a number of important features to be noted in this model; first, the temperature minimum at the base of the chromosphere/top of the photosphere, followed the temperature gradient inversion in the chromosphere, and second, the extent of the chromosphere, $\sim 0.004R_\odot$.

These two features form the basis of all of the work undertaken in this thesis, giving rise to the questions; whether the chromosphere of a star a smoothly-

¹To an extent this value of $2/3$ is arbitrary, arising from the Eddington Approximation, however it does match well with observation.

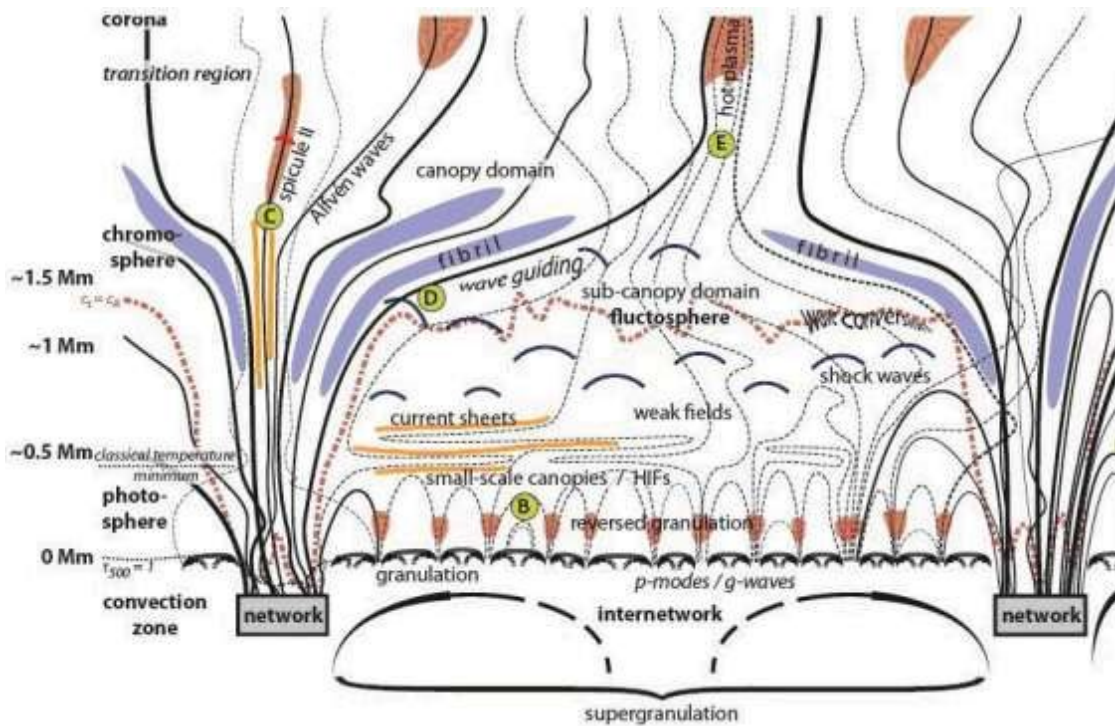


Figure 1.3: The complexity of the solar atmosphere from the photosphere and above. *Image Credit: Wedemeyer-Böhm et al. (2009)*

varying, homogeneous, time-independent structure with a temperature inversion, and if so what is its extent? In this thesis we will study many objects making use of a host of diagnostics as we attempt to address these questions in general for late-type stars.

On the question of the temperature inversion, it does appear that all stars possess a region heated above the prediction of radiative equilibrium (Linsky, 1980). This is thought to be due to the deposition of mechanical or magnetic energy into the plasma, however in chromospheres which are entirely in radiative equilibrium temperature inversions are still possible¹. We will address the question of the temperature structure in detail in all of the succeeding chapters of this work.

As to the question of atmospheric extent, in the photosphere and above the structure of the material is often simplified and modelled as being in hydrostatic

¹This is known as the Cayrel effect, however it is important to note that this effect is not possible in the solar atmosphere. (Cayrel, 1964; Jordan, 1969; Mihalas, 1978)

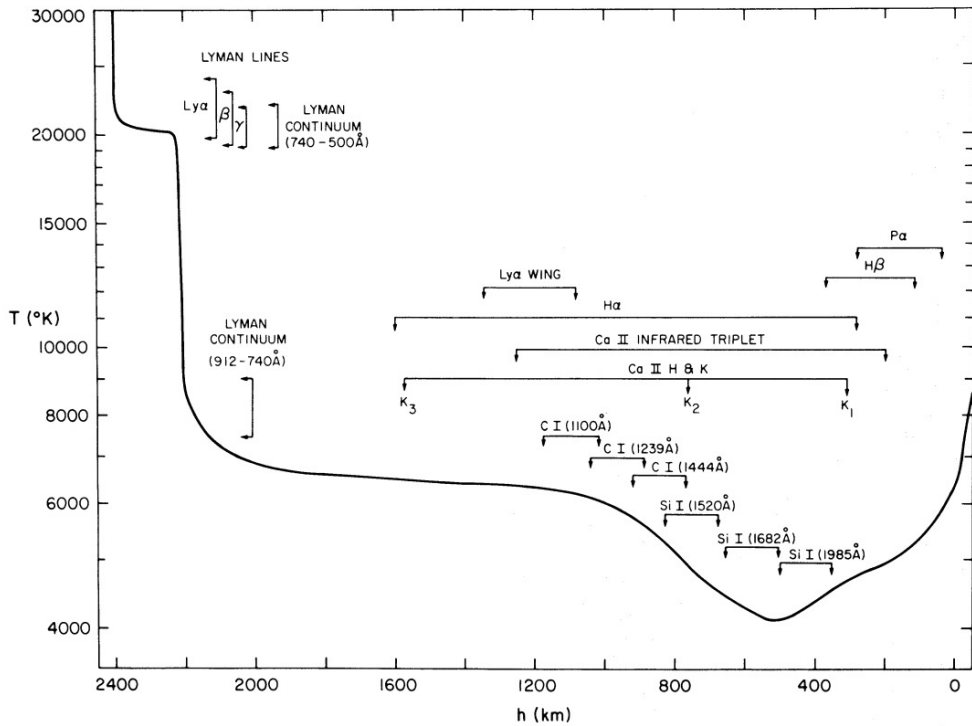


Figure 1.4: A simple, 1-dimensional, time-independent model of the solar photosphere/chromosphere, annotated with the formation heights of various spectral lines. *Image Credit: Vernazza et al. (1976)*

equilibrium, which is to say the gas pressure balances the gravitational force,

$$\nabla P = -\rho g_* \quad (1.1)$$

where P is the pressure, ρ is the mass density, and g_* is the surface gravity. Combining this equation with the ideal gas law, and assuming the material to be isothermal, we can derive the following relation,

$$\rho(r) = \rho_0 e^{-r/H} \quad (1.2)$$

where ρ_0 is the mass density at $r = 0$. H is the isothermal scale height,

$$H = \frac{k_B T}{\mu g_*} \quad (1.3)$$

where k_B is the Boltzmann constant, T is the temperature, μ is the mean molecular

mass, and g_* is the surface gravity,

$$g_* = \frac{GM}{R^2} \quad (1.4)$$

Taking a red giant and the Sun to be of comparable mass, but with $R_{rg} \approx 10R_\odot$

$$g_\odot = 100g_{RG} \quad (1.5)$$

$$\Rightarrow 100H_\odot = H_{RG} \quad (1.6)$$

Further, the scale height as a fraction of R linearly increases in R:

$$\frac{H}{R} = \frac{k_B T}{\mu GM} R \quad (1.7)$$

This simple derivation demonstrates that red giants have more extended chromospheres than the Sun, both in fractional and absolute terms. Due to the tenuous nature of their chromospheres it is not trivial to measure, or even to accurately define, the extents of these objects, and this will again be a matter much discussed in this work.

In general, late-type stars can be divided into two group: “solar”-type coronal stars, and non-coronal stars, separated by what is often called the Linsky-Haisch line (Linsky & Haisch, 1979). In the solar case there is, above the chromosphere, a transition region (Fig. 1.4) where the temperature rises sharply leading to a very tenuous region where $T \sim 10^6$ K, known as the corona. Stars later than approximately K2 do not appear to contain material at coronal temperatures, do not appear to be X-ray emitters (a sign of stellar magnetic activity), and appear to have slow winds not driven by the Parker-type mechanism which operates on the Sun. There are stars which show evidence of coronae and also the types of mass-loss rates associated with more massive winds, known as hybrid stars (Hartmann & MacGregor, 1980). The atmospheric properties of each class of object will be discussed in the course of this work.

1.4 Stellar Observation & Theory

We will now briefly outline the observational and theoretical history of modern, quantitative stellar astrophysics. The observational history discussed below will be expanded in Chapter 3 with detailed reference to the instruments specific to this work, and the mathematical/theoretical aspects will be rigorously discussed and derived in Chapter 2.

As mentioned above, the study of stellar atmospheres is reliant on careful observation of their spectra. One traditional method of observation has been optical spectroscopy using powerful ground-based telescopes. Over the history of the field — such as the work of spectral classification, the construction of the Henry Draper (HD) Catalogue, indeed some of the data contained in this thesis — observations were performed using large refracting telescopes (the 40" at Yerkes being the largest at the turn of the century), diffraction gratings, and photographic plates. These observations provided the radial velocities, proper motions, parallaxes, and effective temperatures of many objects. However, these early observations were limited by a number of factors such as the faintness of the objects which they could observe, the non-linear response of photographic film to incident radiation, and the limited spectral window which can pass through the Earth's atmosphere.

From the 1950's onward these limitations were overcome. Photomultipliers allowed very sensitive observations, and with the advent of CCDs, their high quantum efficiency and linear response enabling absolute calibration, high signal-to-noise observations, on a physical flux scale, of faint objects became possible. With this technology, and other advancements such as adaptive optics to account for seeing, ground-based optical spectroscopy has begun to approach the diffraction limit. Furthermore, satellite technology has allowed observers access to parts of the spectrum blocked by the atmosphere. The launch of the International Ultraviolet Observatory (IUE) in 1978 revolutionised the field of stellar astrophysics by enabling observation of the UV part of the spectrum. While not the first such satellite (the Orbiting Astronomical Observatory missions being the first in 1966/68) the technological capabilities of IUE, coupled with the unprecedented duration of the mission, led to a wealth of new science. The launch of the Hubble Space Telescope (HST) in 1990, with the capability to observe at very high resolution in

the near-infrared, visible, and ultraviolet regions of the spectrum, continued this advance and again provided a new vista in stellar astrophysics.

At radio wavelengths the detection of individual main-sequence/late-type stars has been possible for some decades using the “old” Karl G. Jansky Very Large Array (VLA) (White, 2000). For many objects detection would not be possible if their emission was solely black-body (thermal emission), and hence is evidence of magnetic (non-thermal) emission. However, very recently observations of thermal emission from solar-type stars have been made at radio wavelengths (Villadsen *et al.*, 2014). At these wavelengths the massive winds and molecule-rich circumstellar environments of nearby red giants have been detected, and these observations have proved powerful diagnostics for examining these winds (O’Gorman *et al.*, 2013). As we move to shorter wavelengths (from metre-wave to mm-wave) observations of thermal chromospheric emission from nearby red giants have become possible, and the power of this diagnostic is the subject of one chapter of this thesis.

Radio observations, and latterly infrared and visible observations, making use of very long baseline interferometry have made it possible to begin imaging distant objects. Using instruments at the Center for High Angular Resolution Astronomy (CHARA) and the Very Large Telescope Interferometer (VLTI), which can perform spectro-interferometric measurements (interferometric measurements made across spectral lines) astronomers can directly constrain the extent of the line-forming regions in red giants. This work has provided compelling insights into the question of chromospheric extent and will be given some attention in later chapters.

In order to make best use of these observations a detailed and rigorous theory of radiative transfer is required. This theory began with Schuster (1905), who devised the phenomenological transfer equation. This work, expanded by Chandrasekhar, Milne, Menzel, Sobolev, Eddington, and many others, put the theoretical underpinnings of radiative transfer on solid footing. Among the most interesting early results of their investigations were the determination of solar limb-darkening from the grey opacity (and hence radiative equilibrium), and the identification of hydrogen as the most abundant chemical element in the solar atmosphere.

The early advances in the field rested largely on two assumptions, that the atmosphere is in Local Thermodynamic Equilibrium (LTE), and that the opac-

ity is independent of frequency (the grey approximation), and these simplifications make many problems analytically solvable. However the work of Jefferies & Thomas (1959) on Non-Local Thermodynamic Equilibrium (NLTE) line-formation demonstrated the limitations of this approach. The advent of modern computing resources in the 1960’s revolutionised the study of stellar atmospheres by enabling detailed NLTE modelling. One particularly important advancement was the algorithm presented by Feautrier (1964) to compute fluxes, which has formed the basis of many algorithms since, and will be discussed in the succeeding chapters of this work. In the 1980’s a class of techniques known as the Lambda Iteration (LI — and latterly the Accelerated Lambda Iteration and the Multi-level Accelerated Lambda Iteration) were introduced. These are strongly convergent iterative methods which allow the efficient calculation of spectra with thousands of frequency points.

With these codes, and with the multi-wavelength observations and spectra, it became possible to determine the thermodynamic properties of a stellar atmosphere as a function of depth, and many of these models have been produced in the past few decades for main-sequence and late-type stars. From an initial chromospheric model, and using an appropriate atomic model, a synthetic spectrum can be computed. Comparing this synthetic spectrum with observation allows us to update our chromospheric model¹. By this procedure it is possible to arrive at a specification of the physical properties of the star’s atmosphere which can reproduce the observed spectrum. In this work we will construct such models, and discuss their physical validity and the insights they present.

1.5 Radiative Transfer

In the course of this work we will examine a number of emission processes, however the mathematics which underpins all radiation transport is based on the equation of radiative transfer. Hence we will begin by deriving this equation, introducing some of the basic notation and concepts which will be expanded in Chapter 2.

¹A number of complexities have been glossed over here: is the model atmosphere 1-D, 1.5-D, or 3-D? is it static or does it contain large-scale flows? These matters and others are discussed in detail in later chapters.

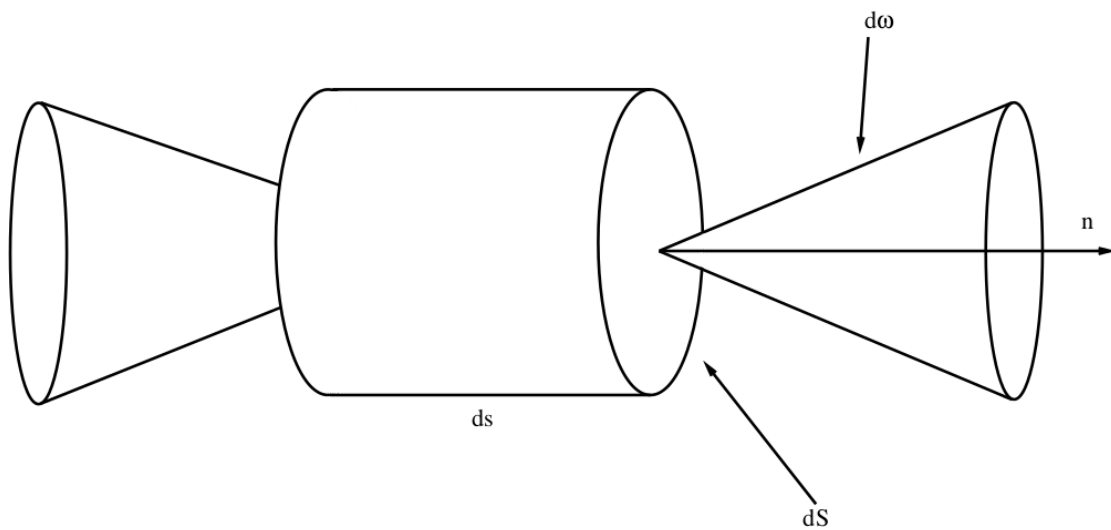


Figure 1.5: Specific intensity passing through a volume of material, $dV = dSds$

There are a number of ways in which the equation may be derived, we will look at the equation from the same phenomenological standpoint as Schuster (1905), however the equation could equally be derived by recasting the Boltzmann equation for photons.

To characterise the radiation transport we introduce the concept of *specific intensity*. Specific intensity provides a complete description of unpolarised radiation, it is the distribution function for photons. We define specific intensity as:

$$I = \frac{dE}{dS \cos \theta d\omega dt} \quad (1.8)$$

or energy passing through a normal surface, per solid angle, per unit time. In general we will look only at the specific intensity in a frequency increment, and denote this (and other monochromatic quantities) by a subscript ν , e.g. I_ν . From the specific intensity we can also define another quantity, the flux, which is the net flow of energy per unit time, per frequency, per unit area

$$F_\nu = \oint I_\nu \cos \theta d\omega \quad (1.9)$$

Note that we have integrated over solid angle. The flux is the total power incident on a unit surface area, whereas the intensity is the energy contribution

arriving from a unit solid angle

Because the specific intensity is defined per unit solid angle, and because photons do not decay, it is clear that intensity is a spatially invariant quantity; it is not radially diluted and only changes in the presence of sinks or sources. These sinks and sources are *extinction* and *emissivity*. Across an increment, ds , see Fig. 1.5, the change in intensity will be equal to the the energy emitted in that volume minus energy removed. The number of photons emitted in an increment, the emissivity, is denoted by η_ν , and the number of photons removed is χ_ν .¹

Hence we can write, where we will denote the incoming ray at the coordinates (q, t) and the outgoing ray with the coordinates $(q + \Delta q, t + \Delta t)$

$$[I_\nu(q + \Delta q, t + \Delta t) - I_\nu(q, t)]dS \cos \theta d\omega dt = [\eta_\nu - \chi_\nu I_\nu(q, t)]dS \cos \theta ds d\omega dt \quad (1.10)$$

This equation can be written in differential form as

$$\frac{\partial I_\nu}{\partial s} = \eta_\nu - \chi_\nu I_\nu \quad (1.11)$$

Traditionally this equation is written as a differential equation over *optical depth*. The optical depth is the extinction integrated over the path of the photon,

$$\tau_\nu = - \int_q^{q+\Delta q} \chi_\nu ds \quad (1.12)$$

Optical depth can be interpreted as the number of photon mean-free-paths between two points. By convention the observer is at 0, leading to the negative sign. Defining one further quantity the *source function*, S_ν , as the ratio of the emissivity to the extinction

$$S_\nu = \frac{\eta_\nu}{\chi_\nu} \quad (1.13)$$

¹These quantities are both somewhat more subtle than is mentioned here. The emissivity and extinction may not be isotropic, adding an angle term to the equation. Further the extinction is itself comprised of two terms, the number of photons absorbed, and the number scattered out of the direction of the observer. These complexities will be discussed at a later point, where relevant.

we can write the transfer equation as follows

$$\frac{\partial I_\nu}{\partial \tau_\nu} = I_\nu - S_\nu \quad (1.14)$$

This is the standard form of the equation of radiative transfer (though in this derivation we have made no reference to angle-dependence or the geometry of the medium, these matters will be tackled in due course), and it introduces a number of important concepts.

It is more physically intuitive to write the transfer equation as a differential equation over optical depth, as this is the quantity which photons actually encounter, to an object moving at the speed of light spatial distance is somewhat meaningless — in fact this distinction is one reason why chromospheric extents are so difficult to ascertain.

The introduction of the source function also serves to make the equation more physical than mathematical. While it would appear that η_ν and χ_ν provide a complete description of the radiation added to and taken from a beam this is not the case for line transitions, where the occupation numbers of the individual quantum levels determine these coefficients, and these occupation numbers are in turn determined by the radiation field, reflecting the non-linearity of the problem. The source function on the other hand, is proportional to the number of photons emitted per unit optical depth. Hence these two quantities make physical interpretation of the transfer equation more straightforward.

This derivation and these concepts will be returned to in the subsequent chapter, but with this historical and mathematical background we will now turn to discussion of the relevance of binary stars to this work.

1.6 ζ Aurigae Binaries

Of the 200,000 stars in the Henry Draper catalogue compiled at Harvard, one, ζ Aurigae, displayed a unique set of properties, and is of great importance to our study. In the 19th century the object was classified as a “composite-spectrum binary”, as it contained lines seen in the spectra of both hot and cool objects (Maury & Pickering, 1897). At Dominion Astrophysical Observatory (DAO) Harper (1924)

observed this object and, only measuring the spectrum of the cool star, determined that the hot star must be in eclipse. Later observations by Beer (1934) and Guthnick (1934) showed the variation of the spectrum during the orbit, most prominently the formation of narrow absorption features. This was interpreted by Menzel (1936)¹ as due to the hot star shining through thicker layers of the cool star atmosphere as it is eclipsed by the cool star — a *chromospheric eclipse*. This was likened by Menzel to “a planet setting in a smoky atmosphere, disappearing as it reaches the horizon” (Griffin & Ake, 2015).

Along with ζ Aurigae two other systems displaying this type of eclipse, now collectively referred to as ζ Aurigae binaries, were discovered, 31 & 32 Cyg (McLaughlin, 1950a,b). Other objects have been added to this list subsequently, such as VV Cep, τ Per, and 22 Vul. Despite their relative rarity, objects of this type have offered unique and compelling insights, unavailable through the study of other stars. As well the masses of the objects being available (due to their binarity), the chromospheric eclipse effectively allows us to resolve the chromospheres of the giants in these systems, and this provides the best available constraints on the physical parameters of stellar atmospheres.

In this respect the eponymous ζ Aurigae system is particularly useful. The object comprises a cool supergiant, ζ Aurgiae A (K4Ib), and a hot B-star, ζ Aurgiae A (B5V). These objects are coeval, however ζ Aurgiae A, being more massive, has evolved off the main sequence ahead of its counterpart. Schroder *et al.* (1997) attempted to model the evolution of the system and found ζ Aurgiae A may have debuted on the main-sequence as \sim B3 object, however some ambiguity arose due to the uncertainty in the mass ratio of the system.

The value of the system in providing insights into stellar atmospheres arises from it being long observed, and having systemic parameters which are well-suited to atmospheric study. In ζ Aurigae the B-star is comparable in size to the scale height in the K-star chromosphere ($H \sim 1R_{\odot}$, $R_B = 5R_{\odot}$), and at ingress and egress the B-star moves by approximately its own diameter each day, meaning that nightly observing gives almost continuous coverage of the atmosphere with good resolution.

¹It is interesting to note that Menzel concludes this paper with a brief mention of the Si emission line at $\lambda 3906 \text{ \AA}$, the re-discovery of which is the topic of one chapter of this thesis.

Beginning in the 1950’s with optical observations of Wilson & Abt (1954) and Wright (1959) the inner chromospheres of these objects were studied, measuring temperatures, turbulent velocities, and ionization balances as a function of height. These observations pointed to an atmosphere which is anisotropic, or “clumpy”, but (McKellar & Petrie, 1952) presented a lower-bound model which may underlie the inhomogeneity. With the advent of IUE, and hence access to the intrinsically stronger UV lines, the structure of the outer atmosphere could be also probed (see the series “A study of UV spectra of ζ Aur/VV Cep systems” (Hempe, 1982)).

These observations yield information which allows us to determine parameters with greatly superior accuracy than is the case for single stars, and the interest in these objects is premised on the fact that the constraints derived from their study are equally applicable to single stars. The ζ Aurigae binaries are detached objects, which is to say that they do not interact by mass transfer, hence the evolution of the primary should be unaffected by the secondary, a contention supported by Schroder *et al.* (1997). Furthermore the observed spectrum of ζ Aurigae A appears to be entirely analogous to the spectra of other objects of the same spectral type. Over the course of this work we aim to keep in mind this connection, and to discuss our results in the context of the atmospheres of single stars.

1.7 Thesis Overview

We have now introduced many of the basic concepts that will be discussed in this thesis. In Chapter 2 we will derive the relevant equations and provide a detailed description of the theory and underlying assumptions of the work undertaken. This chapter will focus on discussion of the mathematics and computational methods behind radiative transfer, while also discussing the physics of binary systems. Chapter 3 will contain a discussion of the instruments specific to this work, giving a detailed description of their capabilities. We will focus particularly on the Hubble Space Telescope, the Combined Array for Research in Millimetre-wave Astronomy, and the Center for High Angular Resolution Astronomy.

In Chapter 4 we will present a simple model to compute an object’s thermal, chromospheric mm-radio flux. This model is based on a number of simplifying assumptions relating to the thermal structure and the extent of the chromosphere.

This model is then compared with archival radio observations of stellar fluxes, as well as solar radio observations. Finally the model is compared with high signal-to-noise data collected by Eamon O’Gorman.¹ Predictions are made for future observations, and our model is confronted with the data as a test of the validity of our assumptions.

In Chapter 5 we present the “re-discovery” of the phenomenon of periodic Si emission in ζ Aurigae binaries. This emission is seen in a small number of lines of neutral Si, and varies during the orbit of the star. A qualitative explanation of the emission mechanism is provided. A detailed geometrical model of the ζ Aurigae system is then undertaken and used to predict the expected phase variation of reflection. This prediction is compared with the observed Si emission and found to be in very good agreement. The possible uses of this novel, and potentially powerful, diagnostic are discussed.

Chapter 6 builds on the work of the previous chapter, and we present a model constructed for the chromosphere of the primary of ζ Aurigae. Despite the unique insights afforded by the study of ζ Aurigae no full, semi-empirical chromospheric model has been attempted for this object, and in this chapter we will discuss the development of such a model. This model is developed with its relation to single stars in mind, and the findings of this chapter are discussed in this context. The model is also used to add somewhat more detail to our consideration of the line-formation at play in the emission discussed in the previous chapter.

Finally, Chapter 7 will summarise the work undertaken in this thesis, drawing together the various strands of the research to comment generally on the structures and extents of chromosphere. We will also discuss some future research and observations which could build upon and complement this work.

¹Onsala Space Observatory, Chalmers University of Technology

2

Background & Theory

In this chapter we provide the background equations and theory relevant to understanding the research presented in later sections. We discuss the emission and absorption mechanisms at play in stellar atmospheres. We begin with thermal and non-thermal free-free emission, and the resultant radio spectrum. We then discuss the formation of spectral lines in stellar atmospheres, with particular emphasis on line-profiles and spectral density diagnostics. We discuss the approximate and algorithmic solutions of the transfer equation and the equations of statistical equilibrium. We devote some time to describing the Featurier method in some detail, as we will return to it at a later stage, and we discuss the mathematics underlying the computational methods used to compute synthetic spectra. We discuss the algorithms used to obtain solutions for the orbits of binary systems and the calculation of synthetic light-curves.

2.1 Absorption and Emission Mechanisms

We will begin with a discussion of the radiation absorption and emission mechanisms at different wavelengths of the stellar spectrum. We can think of these processes as falling broadly into two categories: those involving continuous or discrete energy spectra. In the former category is what is known as free-free emission, and in the latter bound-bound and bound-free emission. We will discuss both in turn.

2.1.1 Free-free absorption & emission

Free-free emission arises from the acceleration of a charged particle, most commonly an electron, and hence is referred to as *bremsstrahlung*, braking radiation. This acceleration may be due to the electron's interaction with matter, or its deflection by an electric or magnetic field.

It is possible that coherent radiation may be produced by resonance with wave-modes in the plasma; mechanisms known as plasma oscillation, and electron-cyclotron emission. Plasma oscillations, also known as Langmuir waves, are caused by the displacement of electrons in a plasma, which are then subject to a restoring Coulomb force. From the equation of simple harmonic motion the frequency of the oscillation, and hence the emission, can be shown to be (in the “cold” case):

$$\nu_p = \sqrt{\frac{n_e e^2}{\pi m_e}} \approx 9000\sqrt{n_e} \quad [\text{Hz}] \quad (2.1)$$

where n_e is the electron density, e is the electron charge, and m_e is the electron mass. For a typical chromospheric electron density, $n_e \sim 10^9 \text{ cm}^{-3}$, we get $\nu_p = 280 \text{ MHz}$. Electron-cyclotron emission arises from electrons spiralling around magnetic field lines, and has a frequency, often known as the gyro-frequency, of

$$\nu_{gyro} = \frac{eB}{2\pi m_e} = 2.8B \quad [\text{MHz}] \quad (2.2)$$

where B is the magnetic field density measured in Gauss. For field strengths typical of cool stars (Sennhauser & Berdyugina, 2011), we would expect $\nu_{gyro} \sim 50 \text{ MHz}$.

2.1 Absorption and Emission Mechanisms

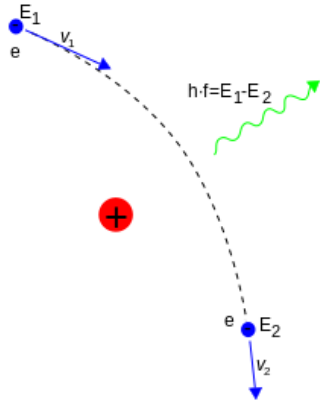


Figure 2.1: Emission produced by the deflection of an electron by Coulomb interaction with a nucleus.

Non-equilibrium electron distributions may produce similar emission by three-wave interaction bringing about plasma emission (Robinson, 1993).

Of greater relevance to this work is non-coherent, thermal free-free emission. This emission occurs as a result of the deflection of electrons by ions, as can be seen in Fig. 2.1. In the relatively rarefied environment of stellar atmospheres small-angle deflections, with high impact parameters, dominate the emission, and as a result can be computed without recourse to quantum mechanics. The emission, ϵ_{ff} ($dE dt d\nu$), is (see Rybicki & Lightman (1979) and Hubeny & Mihalas (2014)):

$$\epsilon_{ff} = \frac{32\pi^2 e^6}{3\sqrt{3}c^3 m_e^2} \sqrt{\frac{2m_e}{\pi k_B}} Z^2 n_e n_i T^{-1/2} e^{-h\nu/k_B T} g_{ff} \quad [\text{erg/cm}^3/\text{s}/\text{Hz}] \quad (2.3)$$

Where Z is the ion charge, and g_{ff} is the free-free Gaunt factor, a quantum mechanical correction factor. This is a function of temperature and frequency, and is tabulated in Karzas & Latter (1961). In the notation of the transfer equation derived in Chapter 1, the traditional notation for astrophysics, $\eta_{ff} = \epsilon_{ff}/4\pi$.

Since free-free absorption, χ_{ff} , and emission are collisional processes they occur at LTE rates, and hence are related by Kirchoff's law¹ to the LTE intensity,

¹The energy absorbed is balanced by that emitted *at all frequencies*

2.1 Absorption and Emission Mechanisms

Planck's Law, B_ν :

$$B_\nu = \frac{\eta_{ff}}{\chi_{ff}} = \frac{2h\nu^3}{c^2} \frac{1}{e^{h\nu/k_B T} - 1} \quad (2.4)$$

$$\chi_{ff} = \frac{\sqrt{32\pi}e^6}{3\sqrt{3}ch\sqrt{k_B m_e^3}} \frac{Z^2 n_e n_i g_{ff}}{\sqrt{T}\nu^3} (1 - e^{-h\nu/k_B T}) \quad (2.5)$$

With these values defined we can now use the equation of radiative transfer

$$\frac{\partial I_\nu}{\partial s} = \eta_\nu - \chi_\nu I_\nu \quad (2.6)$$

In thermodynamic equilibrium, which is a valid approximation for free-free emission in an optically thick slab, the intensity is constant, hence

$$I_\nu = \frac{\eta_{ff}}{\chi_{ff}} = S_\nu = B_\nu \quad (2.7)$$

Free-free emission falls-off exponentially at high frequencies, hence we are only interested in low frequency, radio wavelengths. As a result we can use the Rayleigh-Jeans law in place of Planck's Law

$$B_\nu = \frac{2\nu^2 k_B T}{c^2} \quad (2.8)$$

In radio astronomy the temperature which produces a given intensity is referred to as the brightness temperature, T_{Br} , and we will frequently use this as a direct proxy for intensity¹.

We can now solve the transfer equation in this relatively simple case.

$$\frac{\partial I_\nu}{\partial \tau_\nu} = I_\nu - S_\nu \quad (2.9)$$

This equation has the solution

$$I_\nu(0) = I_\nu(z)e^{-\tau_\nu} + \int_{\tau(z)}^0 S_\nu e^{-\tau_\nu} d\tau \quad (2.10)$$

¹There is no requirement that T_{Br} be reflective of the thermodynamic temperature of an object. In the case of non-thermal emission T_{Br} is still often used, despite there being no physically meaningful sense in which the brightness has a related temperature.

2.2 Bound-bound Absorption and Emission

which has the physical interpretation of the first term being radiation shining through the medium, and the second being the radiation produced in the medium (this is for a single ray, passing through a semi-infinite slab). In the thermal equilibrium case, where the η_{ff} and χ_{ff} are constant through the medium, and writing in terms of brightness temperature rather than intensity,

$$T_b = T_e(1 - e^{-\tau_\nu}) \quad (2.11)$$

where T_e is the electron temperature throughout the medium. In the case that the medium is optically thick $T_{Br} = T_e$, and in the case that the medium is optically thin $T_{Br} = \tau_\nu T_e$.

From this we can define a spectral index,

$$\alpha = \frac{d \log_{10}(F_\nu)}{d \log_{10}(\nu)} \quad (2.12)$$

which is the slope of the flux-frequency power-law. For instance, in the optically thick case the flux will clearly follow the frequency dependence of the Rayleigh-Jeans law, hence $\alpha = 2$. In the optically thin case, given no background illumination, the flux will follow the frequency dependence of the Gaunt factor, $\alpha \approx -0.1$. By measuring the flux at multiple frequencies it is possible to compute the spectral index, which has the power to differentiate between optically thin and thick emitting regions, and hence to help diagnose the properties of the medium.

In Chapter 3 of this work we will present a simple radio flux model, designed to predict the thermal, free-free emission from stellar chromospheres. In this chapter the concepts introduced here will be expanded upon and used practically in an attempt to determine the temperature structure of the chromosphere.

2.2 Bound-bound Absorption and Emission

In this section we will discuss bound-bound emission and absorption, and the formation and shape of spectral lines. As an introduction to this discussion we will begin with a description of the quantum structure of atoms.

2.2.1 Atomic Structure

Electrons form an organized structure when bound by the attractive potential of an atomic nucleus. The bound electron is described by 4 numbers, arising from the solutions of the Schrödinger wave equation (Pradhan & Nahar, 2011). These being quantum mechanical properties they can only hold discrete, quantised values, and the Pauli Exclusion Principle states that no two electrons can have the same quantum numbers. These four numbers are:

- Principal quantum number (n), describes the energy level, or shell (as increasing n corresponds to increasing distance from the nucleus), of the electron. A value n corresponds to the n^{th} eigenvalue of the Hamiltonian, i.e. the energy. In a hydrogenic system:

$$\Delta E = R_\infty Z^2 \left(\frac{1}{n_1^2} - \frac{1}{n_2^2} \right) \quad (2.13)$$

where ΔE is the energy difference between states n_1 and n_2 , and R_∞ is Rydberg's constant. The statistical weight for the level, degeneracy, n , is given by $2n^2$.

- Azimuthal quantum number (l), gives the quantised orbital angular momentum

$$L^2 = \hbar l(l + 1) \quad (2.14)$$

where L is the total angular momentum, and \hbar is the reduced Planck constant. l varies from 0 to $n - 1$. This number describes the shape of the atomic orbital, and they are labelled with the letters, s, p, d, f...

- Magnetic quantum number (m_l), is thought of as the orientation of the subshell's shape, the projection of the angular momentum in given direction. It varies from $-l$ to l in integer steps. Hence there are $2l + 1$ available orientations to a subshell. The magnetic quantum number determines the shift of an atomic orbital when in the presence of an external magnetic field.
- Spin quantum number (m_s), is the final quantum number, proposed by Pauli, and is related to the spin of the electron, an intrinsic property like mass or

2.2 Bound-bound Absorption and Emission

charge. m_s will vary from $-s$ to s , where s is the electron spin, $1/2$, hence $m_s = (-1/2, 1/2)$.

From these quantum numbers we define auxiliary values. The parity of a level

$$\pi = (-1)^{\sum_i l_i} = \begin{cases} \text{even} & \text{if } +1 \\ \text{odd} & \text{if } -1 \end{cases} \quad (2.15)$$

which describes the behaviour of the wavefunction under reflection. Typically odd parity is denoted with a superscript 'o', and even a superscript 'e'.

In atoms of $Z < 40$ (all atoms of astrophysical interest to this work), electron spins interact among themselves and combine to form a total spin S . We can also compute the total spin,

$$S = \left| \sum_i s_i \right| \quad (2.16)$$

$s = \pm 1/2$ for each electron, hence a closed shell has $S = 0$, and S will be an integer for an even number of electrons, or half integer for an odd number. The multiplicity here, $2S + 1$, gives rise to multiplets, e.g. singlets ($S = 0$), doublets ($S = 1/2$), etc.

Finally we compute the total angular momentum. The interaction between the quantum numbers L and S is called Russell-Saunders coupling or LS coupling, where L and S couple to give J

$$J = L + S \quad (2.17)$$

For electrons $s = 1/2$, and hence J , being a vector sum, will have value $J = l \pm 1/2$ for a single outer shell electron. This has the effect of splitting into spin-aligned and spin-antialigned states that would otherwise be degenerate, known as fine-structure levels. In addition to fine-structure, hyperfine-structure levels also emerge, as a result of the relative spin orientation of the nucleus and the electron, causing a magnetic interaction. In the 1s state of hydrogen, in the higher energy state, the proton and electron are spin-aligned, and hence their magnetic moments are antialigned. A spin flip transition may occur, where the spins spontaneously align, this emits a photon with a wavelength of 21.1 cm. This transition has a very

2.2 Bound-bound Absorption and Emission

low probability, but owing to the abundance of neutral hydrogen the line is easily observed in the interstellar medium (Ewen & Purcell, 1951).

From these atomic numbers we can construct the electronic configuration, as written in spectroscopic notation. For instance carbon, consisting of 6 electrons, has a ground state configuration of $1s^2 2s^2 2p^2$ denoting 2 electrons in 1s shell, and two electrons in each of the two subshells of the second shell.

In general the outer most electron is the one with which we will be concerned, and so we look at the term notation which is used to describe it. This term notation is of the form,

$$n^{2S+1}L_J^\pi \quad (2.18)$$

Taking an outer electron configuration in CII, which we will encounter later, as an example: $2s^2 2p^2 P_{1/2}^o$. This corresponds to two electrons in the $n = 2$; $l = 0$ orbital, with one in the $n = 2$; $l = 1$ orbital. This orbital has a total spin of $S = 1/2$ (as there is one electron), a total orbital angular momentum of $L = 1$, an odd parity, and a total angular momentum of $J = 1/2$ (the electron spin is $s = -1/2$). This is hence a doublet ($S = 1/2$), as it is also possible for the electron to have spin $s = 1/2$, and the term be $2s^2 2p^2 P_{3/2}^o$.

Now that we have introduced the notation used to designate the bound states of an atom/electron system, we will now discuss transitions between these states.

2.2.2 Transitions

As electrons transition from higher to lower energy bound states they emit photons, carrying away the energy excess. This process gives rise to emission at discrete frequencies corresponding to the energy separation of the bound states, the spectral line emission spectrum unique to each atomic system. There are a set of selection rules which determine the probability of a transition occurring, these rules arising from the overlap of the wavefunctions of the initial and final states. The transition moment integral is zero, the transition is forbidden, if the transition moment function is odd, and this can be determined from examining the quantum numbers of the states. The rules for LS coupling are (Kramida *et al.*, 2015);

1. Change in parity.

2.2 Bound-bound Absorption and Emission

2. $\Delta J = 0, \pm 1$; except $0 \leftrightarrow 0$
3. $\Delta \sum |l \pm s| = 0, \pm 1$; except $0 \leftrightarrow 0 \wedge \Delta J = 0$
4. $\Delta l = \pm 1$.
5. $\Delta S = 0$
6. $\Delta L = 0, \pm 1$

Transition which satisfy these conditions are said to be allowed, and those which do not are “forbidden”. These selection rules apply for electric dipole transitions, but may be violated for electric quadrupole and magnetic dipole transitions (confusingly referred to as both intersystem and intercombination lines depending on the author), in which case the transition will occur, but with far lower ($\sim 10^{-5}$) probability than an allowed transition. Semi-forbidden transitions are electric dipole transitions for which the selection rule that the spin does not change is violated (rule 5 above). In this work forbidden transitions are denoted by double square brackets (i.e. [O III]), and semi-forbidden by a single square bracket (i.e. O II]).

In two papers Einstein (1916a,b) (Hubeny & Mihalas, 2014) demonstrated that three different transition processes occur in bound atomic systems, and provided a probability coefficient for each — now known as the Einstein coefficients.

Consider two bound states, i and j , with $E_i < E_j$, and statistical weights g_i and g_j (this is the number of energetically degenerate states, for hydrogen $g = 2J + 1$). There are three possible radiative processes which these states can undergo; spontaneous decay from the higher energy level to the lower, photo-excitation from the lower to the higher, and stimulated decay from the higher to the lower.

Taking these in turn, the spontaneous decay rate is

$$\frac{dn_j}{dt} = -n_j A_{ji} \quad (2.19)$$

where A_{ji} is the probability of decay (s^{-1}) and n_j is the population of the level.

The rate of photo-excitation is given by

$$\frac{dn_i}{dt} = n_i B_{ij} I_\nu \quad (2.20)$$

2.2 Bound-bound Absorption and Emission

where B_{ij} is the rate of photon absorption ($\text{erg}^{-1}/\text{cm}^{-3}/\text{s}^2$) which is the probability of absorption per unit time per unit spectral energy density of the radiation field (here $\nu = (E_j - E_i)/h$).

Finally, the rate of stimulated emission (negative absorption), can be written as

$$\frac{dn_j}{dt} = n_j B_{ji} I_\nu \quad (2.21)$$

where B_{ij} is the induced emission probability ($\text{erg}^{-1}/\text{cm}^{-3}/\text{s}^2$). A photon with the same energy as the transition can affect the quantum mechanical state of the electron in the upper state, causing the emission of an identical photon (since photons are integer spin bosons and not bound by the Pauli Exclusion Principle.)

The Principle of Detailed Balance demands that these three rates balance one another,

$$n_i B_{ij} I_\nu = n_j (A_{ji} + B_{ji} I_\nu) \quad (2.22)$$

$$I_\nu = \frac{A_{ji}/B_{ji}}{(n_i B_{ij}/n_j B_{ji}) - 1} \quad (2.23)$$

Setting I_ν to its equilibrium value, the Planck function, and using Maxwell-Boltzmann statistics for the level populations, we get

$$B_{ij} = \frac{g_j}{g_i} B_{ji} \quad (2.24)$$

$$A_{ji} = \frac{2h\nu^3}{c^2} B_{ji} \quad (2.25)$$

Though we have derived these ratios based on arguments stemming from statistical mechanics of a photon gas in thermodynamic equilibrium, it can be shown (and in Hubeny & Mihalas (2014) a rigorous derivation is provided), that the Einstein coefficients rely solely on the quantum mechanical properties of the initial and final states, and hence these ratios hold in all cases.

If we were to model this emission as being due to a classical oscillator (assuming an electron bound by a potential, driven by an oscillating electric field) there would be a single cross-section for all transitions, $\sigma_{classical} = \pi e^2/mc$. In reality, as we have seen, the absorption probability, B_{ij} , is related to the quantum mechanical properties of the bound state. It is convenient to write the cross-section in terms

2.2 Bound-bound Absorption and Emission

of a classical oscillator strength, called the f-value

$$\sigma_{ij} = \frac{\pi e^2}{mc} f_{ij} = \frac{h\nu_{ij}}{4\pi} B_{ij} \quad (2.26)$$

The oscillator strength is a useful quantity as it will be approximately unity for strong (allowed) transitions, and far smaller for weaker ones.¹

We must also compute the rate of transitions due to collisions with electrons. To compute the collisional excitation rates, a commonly used method is that of van Regemorter (1962), which expresses the collisional cross-section (integrated over a Maxwellian velocity distribution) for a dipole-permitted transition in terms of the oscillator strength,

$$q_{ij}(T) = C_0 T^{1/2} 14.5 f_{ij} \left(\frac{E_H}{E_{ij}} \right)^2 u_0 e^{-u_0} \Gamma(u_0) \quad (2.27)$$

where

$$\Gamma(u_0) = \max[\bar{g}, 0.276 e^{u_0} E_1(u_0)] \quad (2.28)$$

Where $C_0 = \pi a_0^2 (8k_b/m\pi)^{1/2}$, E_H is the ionization energy of hydrogen, E_{ij} is the energy of the level, $u_0 = E_{ij}/k_b T$, \bar{g} is the effective Gaunt coefficient, and E_1 is the first exponential integral.

From this we can compute the collisional excitation, and hence the de-excitation rates from detailed balance:²

$$C_{ij} = n_e q_{ij}(T) \quad (2.29)$$

$$C_{ji} = \left(\frac{n_i}{n_j} \right)^{\text{LTE}} n_e q_{ij}(T) \quad (2.30)$$

2.2.2.1 Line Profiles

In our discussion to this point we have glossed over the fact that atomic line transitions are not infinitely sharp δ -functions, but are in fact spread out in energy (wavelength). By studying shape of spectral lines, the line profile, we can determine the properties of the medium in which the lines formed.

¹An emission oscillator strength, f_{ji} , can be written as $f_{ji} = f_{ij}(g_i/g_j)$

²This amounts to saying that the collision strengths are symmetric.

2.2 Bound-bound Absorption and Emission

The shape of a line profile is determined by two factors: the atomic parameters of the transition and the macroscopic conditions under which the line was formed. Spontaneous de-excitation limits the lifetime of an excited state and therefore causes an uncertainty in the energy of a photon emitted from a transition, according to the Heisenberg Uncertainty Principle, $\Delta E \Delta t \geq \hbar/2$. This is called *natural broadening*. A single atom's profile is also broadened by collisions. For a high density plasma, radiative timescales can be much greater than the interval between atomic collisions, and hence perturbations may initiate a transition. The decreased lifetime of the state causes an increased uncertainty in photon energy, broadening the emission line. These effects lead to a Lorentzian profile.

$$\phi_{\text{lorentz}}(\nu) = \frac{A_{ji}/2\pi}{(\nu - \nu_0)^2 + (A_{ji}/2)^2} \quad (2.31)$$

Here ν is the independent variable and ν_0 is the centre of the profile. This formulation contains a number of assumptions. It is only accurate in the case that the only transition from j is to i , when stimulated emission is ignored, and when the i level has an infinite lifetime. The first assumption can be addressed by replacing A_{ji} with the sum of all A 's out of the level, the second by adding the stimulated emission term to the A 's (though stimulated emission will be negligible in our work, for the most part). The final assumption, of an infinite lifetime for level i , will be addressed later in this section.

Next consider the profile from an ensemble of atoms. These atoms will have a range of velocities given by the Maxwell-Boltzmann Distribution, and this distribution of velocities will broaden the line due to the Doppler effect. This will lead to a Gaussian profile, as the probability that an atom has a velocity in the range $(v, v + dv)$ is

$$W(v)dv = \frac{e^{-(v/v_0)^2}}{\sqrt{\pi}} \frac{dv}{v_0} \quad (2.32)$$

where $v_0 = (2k_B T/m)^{1/2}$. Hence the observed line profile will be the Lorentzian profile intrinsic to each atom, convolved with the Doppler shifted profile of all of the atoms:

$$\phi(\nu) = \int_0^{\infty} \phi_L[\nu(1 - v/c)]W(v)dv \quad (2.33)$$

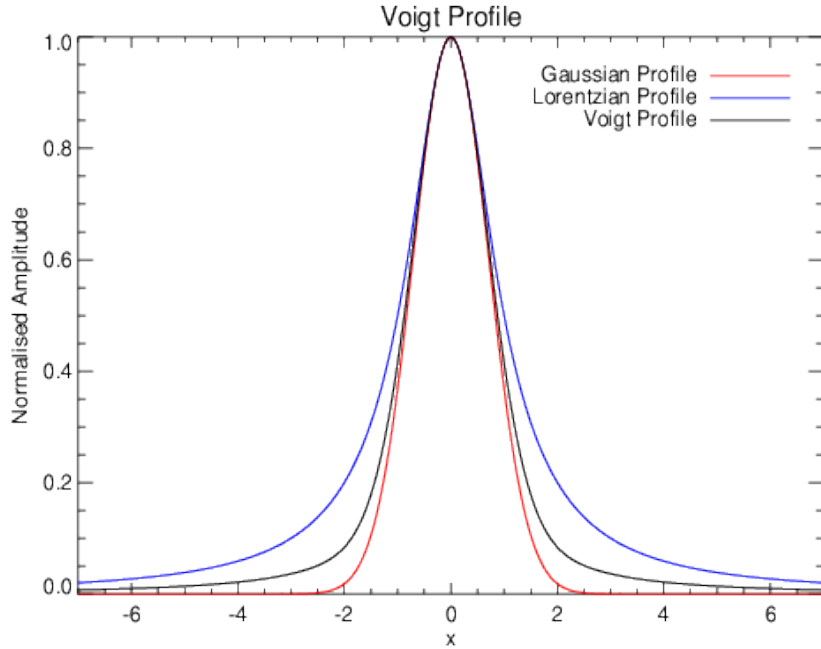


Figure 2.2: The convolution of a Gaussian and a Lorentzian, giving the Voigt profile. We can see that the core is primarily Gaussian, with the extended wings due to the Lorentzian *Image Credit: (Schreier, 2009)*.

From this we can determine the profile to be

$$\phi(\nu) = \frac{\sqrt{\pi}e^2}{mcv_D} f_{ij} H(a, x) \quad (2.34)$$

$$H(a, x) = \frac{a}{\pi} \int_{-\infty}^{\infty} \frac{e^{-y^2}}{(x-y)^2 + a^2} dy \quad (2.35)$$

Here we have defined a number of new variables, $v_D = v_0\nu_0/c$ (the Doppler velocity), $a = A_{ji}/4\pi v_D$, $x = (\nu - \nu_0)/v_D$, $y = v/v_D$. $H(a, x)$ is the convolution of a Gaussian and a Lorentzian profile, known as a Voigt profile (Fig. 2.2.)

To this point we have made the assumption that when a photon excites a transition from one state to another, and when another photon is emitted by the de-excitation, this photon is redistributed randomly across the line profile; that is to say the scattering is completely incoherent, there is no correlation between the incoming photon and the outgoing photon. This is known as Complete Redistribution (CRD), and is a valid assumption for the majority of spectral lines.

2.2 Bound-bound Absorption and Emission

This assumption is invalid, however, for strong resonance transitions in low density plasma, where there is no requirement that the emission and absorption line profiles have the same shape.

Following Hummer (1962), there are four standard atom-frame redistribution functions¹, and I will discuss them in turn.

In this discussion we will make use of the frequency redistribution function, $p(\nu, \nu')$, which gives the probability that a photon absorbed in the frequency increment $(\nu, \nu + \Delta\nu)$ is scattered into the range $(\nu', \nu' + \Delta\nu')$. We will also use the angle scattering function $g(n, n')$, which gives the probability that a photon coming from the solid angle $d\omega$ around the direction n is scattered into the solid angle $d\omega'$ around the direction n' ($g(n, n') = 1$ for isotropic emission). Hence the probability that a photon (ν, n) is absorbed and redistributed to (ν', n') is $\phi(\nu)p(\nu, \nu')g(n, n')d\nu d\nu'(d\omega/4\pi)(d\omega'/4\pi)$.

Qualitatively, the four² redistribution functions are

- Case I: Perfectly sharp upper and lower levels, where $\phi(\nu)$ and $p(\nu, \nu')$ are both δ -functions. In this case there can be no redistribution in the atom frame, and so the only redistribution seen will be from the Doppler effect.
- Case II: Describes a perfectly sharp lower state and an upper state broadened by the uncertainty relation (a Lorentzian profile), but without redistribution; the scattered photon is emitted at the same frequency at which it is absorbed, $p(\nu, \nu') = \delta(\nu - \nu')$. This function applies in the case of low density plasma, such as the hydrogen of the interstellar medium.
- Case III: Describes the case of a sharp lower level and a broadened upper state, in a medium where collisions are frequent enough that photons are redistributed completely, with no correlation to their absorption frequency. In this case $p(\nu, \nu') = \phi(\nu')d\nu'$, which is to say that the probability has the

¹These redistribution functions must be convolved with a Maxwell-Boltzmann distribution to take account of Doppler shifting, yielding the lab-frame redistribution function.

²Owing to an inconsistency in the fourth redistribution function an incorrect form was adopted in the literature, and after some confusion, a corrected form was introduced and called Case V. Since we will not be particularly concerned with Case IV/V in this work we will not discuss this any further than to draw attention to it.

2.2 Bound-bound Absorption and Emission

same shape as the emission line profile and is independent of the incoming photon frequency. From this we can recover the well-known result, that the probability of absorbing a photon at ν and emitting it at ν' is simply the product of the emission and absorption line profiles; $\phi(\nu)\phi(\nu')$.

- Case IV: In this case both the upper and lower level are broadened, and this leads to the most complex redistribution function (Heitler, 1954; Weisskopf, 1933). In simple terms this redistribution function provides two peaks; one due to absorptions at line-centre to some part of the upper level followed by de-excitation back to the centre of the lower level (hence $\nu = \nu'$), the other due peak being at line-centre, due to the high probability of de-excitation to line-centre.

Cases II and III are the cases which are of greatest astrophysical interest, as it was shown by Zanstra (1941) and Omont *et al.* (1972), that from these (physically, if not mathematically) uncomplicated components it is possible to construct the redistribution function as it applies to a line under Partial Redistribution (PRD).

PRD allows that, for broad transitions, different mechanisms dominate the emission profile at different frequencies. In other words, the probability distribution of photon emission is a function of absorption frequency. In the core of a spectral line formed in a stellar atmosphere Doppler redistribution is dominant, as it is in CRD. In the inner wings we observe essentially coherent scattering, as this part of the line emerges from high in the atmosphere where low densities ensure that the radiative damping factor exceeds collisional damping. In the outer line wings, formed deep in the atmosphere, collisional redistribution dominates. In the solar case, the Ly- α , Mg II h & k, and Ca II H & K lines all display PRD effects (Hubený, 1981, 1985). For instance, the assumption of PRD is required to explain the observed centre-to-limb variation of the Ca II K line (Shine *et al.*, 1975).

For the most part we will be interested in lines whose upper levels have been broadened by both natural broadening and collisions, as described by Cases II & III,¹ with damping widths (probability of leaving the state radiatively or collision-

¹You will note that this does assume a sharp lower level. Most lines requiring PRD treatment are resonance transitions to the ground state, which having an effectively infinite lifetime, will be sharp, so our assumption is apt.

2.2 Bound-bound Absorption and Emission

ally) A_{ji} and C_{ji} . We would expect a fraction, γ , of the atoms to decay radiatively, and hence emit coherently in the atom frame, and hence $1 - \gamma$ to suffer collisions and be redistributed, where

$$\gamma = \frac{A_{ji} + C_{ji}}{A_{ji} + C_{ji} + Q_E} \quad (2.36)$$

where Q_E is the rate of elastic collisions, i.e. transitions to another sub-level of the upper level.

Hence the redistribution function will be

$$R(\nu, \nu') = \gamma R_{II}(\nu, \nu') + (1 - \gamma)R_{III}(\nu, \nu') \quad (2.37)$$

$$R(\nu, \nu') \approx \gamma R_{II}(\nu, \nu') + (1 - \gamma)\phi(\nu)\phi(\nu') \quad (2.38)$$

where the second formulation assumes that CRD in the atom frame causes CRD in the observer's frame.

In the frame of the observer the explicit redistribution functions are

$$R_{II}(x, n; x', n') = \frac{g(n, n')}{\pi \sin \theta} e^{-\frac{1}{4}(x'-x)^2 \csc^2(\theta/2)} H(a \sec(\theta/2), 1/2(x' + x) \sec(\theta/2)) \quad (2.39)$$

$$R_{III}(x, n; x', n') = \frac{g(n, n')}{\pi} a \csc \theta \int_{-\infty}^{\infty} \frac{e^{-u^2} H(a \csc \theta, x' \csc \theta - u \cot \theta)}{(x - u)^2 + a^2} du \quad (2.40)$$

where $a = \gamma/v_D$, $\cos \theta = n \cdot n'$, and $u = (m/2k_B T)^{1/2}v$. R_{III} , despite representing coherent scattering in the atom frame, can not be decomposed into simple functions in the lab frame, and hence must be computed by numerical integration.

Finally we will examine the process of Cross Redistribution (known as XRD). Take for instance a three-level atom with a metastable state between the ground-state and the upper level. In this configuration there is a probability that an electron will be excited from the ground-state to the broadened upper level, before de-exciting to the metastable level. A schematic of one possible form of XRD can be seen in Fig. 2.3. This is also known as resonance Raman scattering, and it creates a correlation between the absorbed photon and the photon emitted in the

2.2 Bound-bound Absorption and Emission

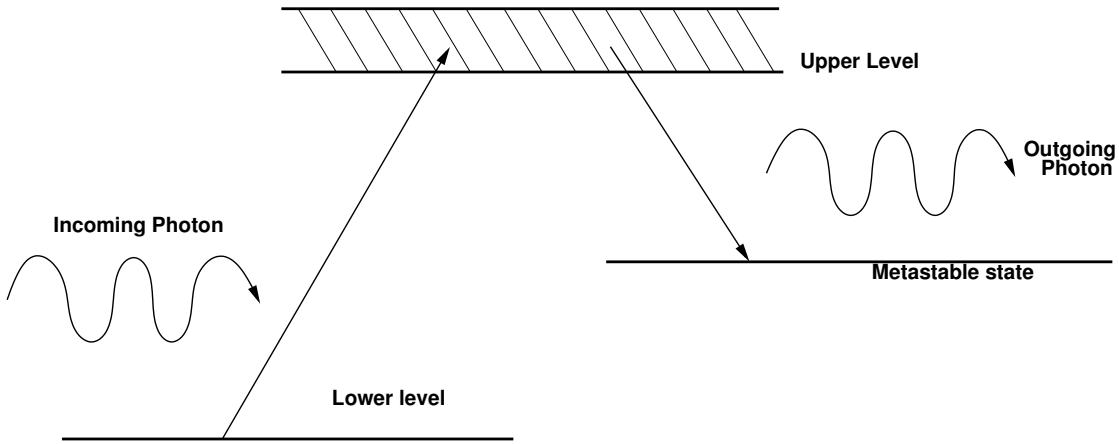


Figure 2.3: The energy level schematic of a type of XRD interaction, showing excitation to a broadened upper level followed by de-excitation to a metastable level.

subordinate line. The associated redistribution function was provided by Milkey *et al.* (1975).

$$R(\nu, \nu') = \gamma R^X(\nu, \nu') + (1 - \gamma) R_{III}(\nu, \nu') \quad (2.41)$$

where, as distinct to the previous case, ν and ν' belong to different lines.

$$R^X(\nu, \nu') = \frac{\pi^{-3/2}}{v_D v'_D} \int_{u_{min}}^{\infty} e^{u^2} \left(\tan^{-1} \left(\frac{y_{max}}{\beta} \right) - \tan^{-1} \left(\frac{y_{min}}{\beta} \right) \right) du \quad (2.42)$$

where

$$y_{min} = \max(\nu - v_D u, \nu - v'_D u) \quad (2.43)$$

$$y_{max} = \min(\nu + v_D u, \nu + v'_D u) \quad (2.44)$$

$$u_{min} = \frac{|\nu - \nu'|}{v_D + v'_D} \quad (2.45)$$

The variables marked with a prime are associated with the outgoing photon, and hence the subordinate level.

As a result of energy conservation, the wavelength of the emitted photon will

be related to that of the incident photon by the relationship:

$$\frac{\Delta\lambda_i}{\lambda_i} = \frac{\lambda_i}{\lambda_o} \frac{\Delta\lambda_o}{\lambda_o} \quad (2.46)$$

where $\Delta\lambda_i$ is the variation in the incident radiation corresponding to a variation in the outgoing radiation of $\Delta\lambda_o$ (Lee *et al.*, 2003).

2.2.3 Bound-Free Transitions

Finally, we discuss transitions where the electron receives sufficient energy to lift it from the potential well of the atom to the continuum of free states. This can happen by the absorption of a photon of sufficient energy, or by collision with a free electron.

The cross-section for photon absorption was computed by extension of the discrete principal quantum number system to continuous, imaginary quantum numbers which accounted for the free states. Menzel & Pekeris (1935) provided an expression for the bound-free cross-section

$$\sigma_{bf}(n, \nu) = \frac{64\pi^2 Z^4 e^{10} m_e}{3\sqrt{3} c h^6} \frac{g_{bf}(n, \nu)}{n^5 \nu^3} \quad (2.47)$$

where $g_{bf}(n, \nu)$ is the bound-free Gaunt factor, as tabulated in Karzas & Latter (1961). The inverse process is electron-ion recombination, wherein a free electron is captured by an ion, emitting a photon. As before we can relate the cross-sections of these inverse processes by the principle of detailed balance

$$\sigma_{bf} \frac{g_j}{p_e^2} = \sigma_{rc} \frac{g_s}{p_{h\nu}^2} \quad (2.48)$$

where g_j is the statistical weight of the state being photoionised, and g_s is the statistical weight of the recombined state, $p_{h\nu}$ is the photon momentum ($p_{h\nu} = (I + \epsilon)/c$ where I is the ionization energy, and ϵ is the excess), and $p_e = mv = \sqrt{2m\epsilon}$ is the electron momentum. Hence

$$\sigma_{rc} = \sigma_{bf} \frac{g_j}{g_s} \frac{(I + \epsilon)^2}{2mc^2\epsilon} \quad (2.49)$$

This is known as the Milne relation.¹ From these cross-sections the total bound-free rates can be determined, however, this involves integrating over all atomic states, in practice this is instead done by the R-matrix method. Seaton (1959) provided an analytic method for performing this calculation for hydrogenic atoms, and his result will be discussed in the closing sections of this thesis.

For collisions it is possible to compute the rate of ionizing collisions by another expression provided by Seaton (Bates, 1962; Hubeny & Mihalas, 2014)

$$q_{ik} = 1.55 \times 10^{13} T^{-1/2} \bar{g}_i \sigma_{ik}(\nu_0) \left(\frac{e^{-u_0}}{u_0} \right) \quad (2.50)$$

where $\sigma_{bf}(\nu_0)$ is the threshold photoionization cross-section, and \bar{g}_i is the Gaunt factor for an ion of given charge which of order 0.1 for $Z = 1$, and 0.2 for $Z = 2$.

2.3 Rate Equations

Now that we have defined the transitions into and out of bound atomic states we can construct a set of rate equations which govern these transitions. The total probability of a transition from one level to another is given by,

$$P_{ij} = R_{ij} + C_{ij} \quad (2.51)$$

where R_{ij} is the total rate due to radiative processes, and C_{ij} the total rate due to collisional processes. R_{ij} can be written as follows

$$R_{ij} = B_{ij} \int_0^\infty \phi(\nu) J_\nu d\nu \quad E_i < E_j \quad (2.52)$$

$$R_{ji} = A_{ji} + B_{ji} \int_0^\infty \phi(\nu) J_\nu d\nu \quad E_j < E_i \quad (2.53)$$

$$R_{ik} = \frac{4\pi}{h\nu} \int_{\nu_0}^\infty \sigma_{bf} J_\nu d\nu \quad i \rightarrow k \text{ (continuum)} \quad (2.54)$$

where J_ν is the mean intensity

$$J_\nu = \frac{1}{4\pi} \oint I_\nu d\omega \quad (2.55)$$

¹Interestingly Milne's results on bound-free transitions are quantum mechanically correct, despite being developed before quantum theory.

In general

$$\frac{\partial n_i}{\partial t} + \nabla \cdot (n_i \mathbf{v}) = \sum_{j \neq i} n_j P_{ji} - n_i \sum_{j \neq i} P_{ij} \quad (2.56)$$

which states that the time-variance of the population (Term 1, RHS) plus the spatial gradient due to velocity (Term 2, RHS), must be balanced by the rate out of each level (Term 1, LHS) minus the rate into each level (Term 2, LHS). For the problems tackled in this work, which are time-independent and static, the equation simplifies to

$$\sum_{j \neq i} n_j P_{ji} - n_i \sum_{j \neq i} P_{ij} = 0 \quad (2.57)$$

which is the equation of detailed balance, stating that the rates into and out of the levels must balance in aggregate. For N possible transitions we will have $N - 1$ linearly independent equations, as the information in the last equation will have been accounted for in the equations for previous levels. Hence we replace one of the equations with the expression for the total number density of the atom

$$n_{\text{tot}} = \sum_{j=1}^N n_j \quad (2.58)$$

These equations can be, and usually are, written in matrix form

$$\mathbf{A} \cdot \mathbf{n} = \mathbf{b} \quad (2.59)$$

where \mathbf{A} is the rate matrix, \mathbf{n} is the vector of the level populations, and \mathbf{b} is the vector solution. Explicitly

$$\begin{pmatrix} -\sum_j P_{0j} & P_{10} & P_{20} & \dots & P_{N0} \\ P_{01} & -\sum_j P_{1j} & P_{21} & \dots & P_{N1} \\ \vdots & \vdots & \vdots & \vdots & \vdots \\ 1 & 1 & 1 & \dots & 1 \end{pmatrix} \begin{pmatrix} n_0 \\ n_1 \\ \vdots \\ n_N \end{pmatrix} = \begin{pmatrix} 0 \\ 0 \\ \vdots \\ n_{\text{tot}} \end{pmatrix}$$

Using this rate equation notation we will examine one case in detail, that of a density sensitive diagnostic.

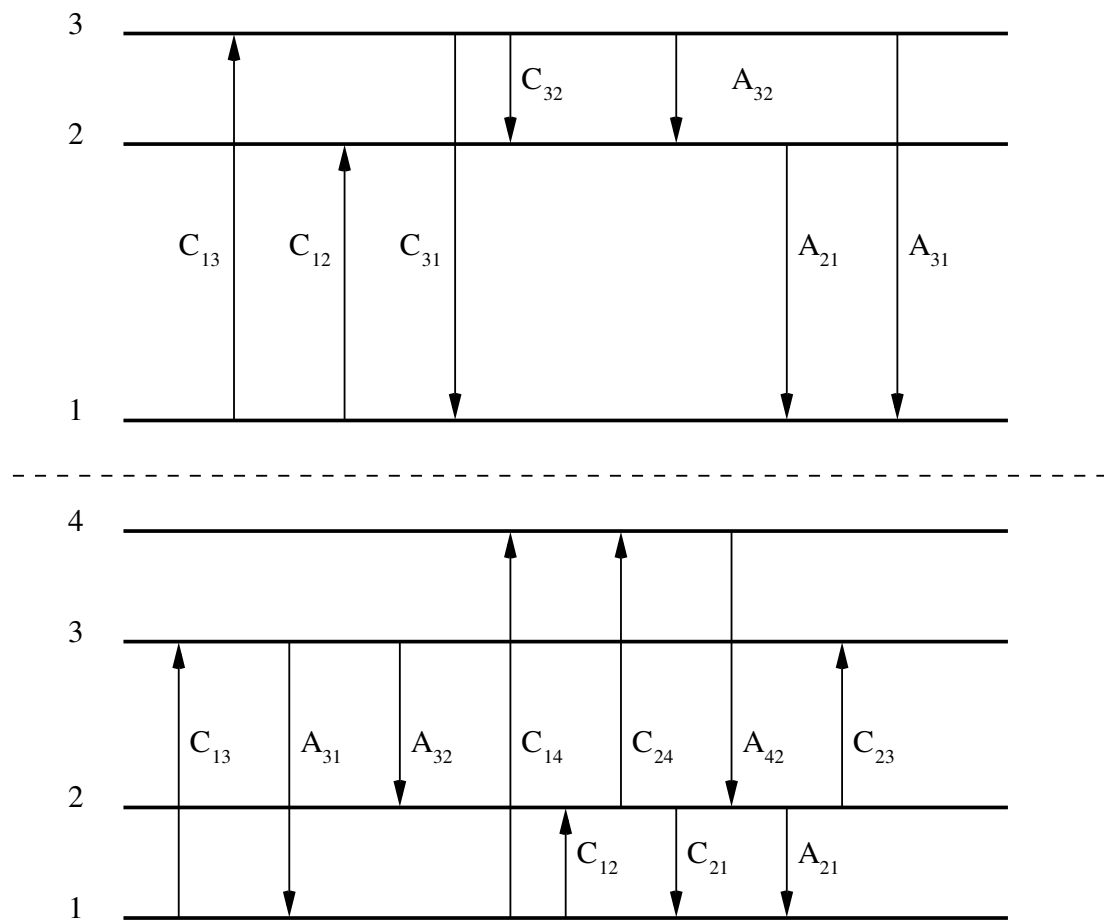


Figure 2.4: Transitions in a three and four level atomic systems. Image adapted from Mariska (1992)

2.3.1 Density Sensitive Transitions

Of great importance to this work is the use of density-sensitive transitions. These transitions provide powerful insights, as they allow us to directly diagnose the properties of the line-forming region by careful attention to the ratios of lines formed from common upper and lower levels. Furthermore these diagnostics do not require any assumptions regarding the properties of the atmosphere, being solely dependent on the measured flux and the atomic structure of the system.

These density-sensitive lines arise in three (and more) level systems, wherein there are both allowed, and intercombination or forbidden transitions (electric dipole, and electric quadrupole or magnetic dipole transitions). In these systems,

2.3 Rate Equations

the levels are populated collisionally, with the allowed transition depopulating one level by radiative decay (the coronal approximation), and the other being depopulated by radiative transition (with far lower probability, due to being forbidden) and collisions. Hence the ratio of these lines will be dependent on the density, through the collisional rates.

In the simplest three level case, we can construct the following rate equations for levels 2 and 3:

$$n_2 A_{21} = n_1 n_e C_{12} + n_3 (A_{32} + n_e C_{32}) \quad (2.60)$$

$$n_3 (A_{31} + A_{32} + n_e C_{31} + n_e C_{32}) = n_1 n_e C_{13} \quad (2.61)$$

where this assumes that level 2 is collisionally populated by level 1 (as well as being populated from level 3), and radiatively decays to level 1. Level 3 depopulates to all levels, but is only populated by collisions from the level 1. The ratio of these populations is

$$\frac{n_3}{n_2} = \frac{C_{13} A_{21}}{C_{12} (A_{31} + n_e C_{31})} \quad (2.62)$$

The flux from these (optically thin) lines will be $F_\nu \propto h\nu_j n_j A_{ji}$, and hence the line ratios from the two spontaneous transitions will be

$$R_{31/21} = \frac{n_3 A_{31}}{n_2 A_{21}} \quad (2.63)$$

$$\rightarrow R_{31/21} = \frac{C_{13} A_{31}}{C_{12} (A_{31} + n_e C_{31})} \quad (2.64)$$

If $n_e C_{31} \ll A_{31}$ the ratio reduces to C_{13}/C_{12} , however this ratio is inversely proportional n_e for sufficiently large densities.

In the slightly more complex four level case we can construct similar statistical equilibrium equations, however for compactness of notation we will use the rate matrix to express this:

$$\begin{pmatrix} -n_e \Sigma_j C_{1j} & A_{21} + n_e C_{21} & A_{31} & A_{41} \\ -n_e C_{13} & -n_e C_{23} & A_{32} + A_{31} & 0 \\ -n_e C_{14} & n_e C_{24} & 0 & A_{42} + A_{41} \\ 1 & 1 & 1 & 1 \end{pmatrix} \begin{pmatrix} n_0 \\ n_1 \\ n_3 \\ n_4 \end{pmatrix} = \begin{pmatrix} 0 \\ 0 \\ 0 \\ n_{\text{tot}} \end{pmatrix}$$

The benefit of this notation is that the coupling of the levels can be seen clearly, simply by examining the structure of the matrix. Levels 3 and 4 are collisionally populated by, and radiatively depopulated to, levels 1 and 2 (a simple extension of the previous case). As we can see from the zeros, these levels are not coupled to one another.

The line ratio of the two radiative transitions to the lower doublet is

$$R_{42/31} = \frac{n_4 A_{42}}{n_3 A_{31}} \quad (2.65)$$

Which, by the same analysis as above, becomes

$$R_{42/31} = \frac{\frac{A_{42}}{A_{4tot}} (C_{14} + (n_2/n_1)C_{24})}{\frac{A_{31}}{A_{3tot}} (C_{13} + (n_2/n_1)C_{23})} \quad (2.66)$$

$$\frac{n_2}{n_1} = \frac{\Sigma_j C_{1j} - \frac{A_{31}}{A_{3tot}} C_{13} - \frac{A_{42}}{A_{4tot}} C_{14}}{A_{21}/n_e + C_{21} + C_{23} \frac{A_{31}}{A_{3tot}} + \frac{A_{41}}{A_{4tot}} C_{24}} \quad (2.67)$$

where A_{jtot} is the total radiative rate out of level j . Again, this ratio is density sensitive

In this work we will primarily be concerned with the density sensitivity of lines in the (Boron I-like) multiplet $2s^2 2p^2 {}^2P - 2s^2 2p^2 {}^4P$, which has been frequently used as a diagnostic of the solar atmosphere (N III and O IV (Feldman & Doschek, 1979; Flower & Nussbaumer, 1975)). Specifically, we will make use of the C II] 2325Å quintet lines (Stencel *et al.*, 1981). Despite being comprised of 5 levels, the density-sensitive ratios which emerge can be written using the expressions we have derived here. Owing to the forbidden transition in the system, one of the ratios (R_3) effectively emerges from a four level sub-system, and hence is described by the equation above. The others (R_1 and R_2) can be written using a very similar

2.4 Solving the Transfer Problem

expression, requiring one extra term, derived by exactly the same method as above,

$$R_1 = \frac{n_5 A_{52}}{n_3 A_{31}} \quad (2.68)$$

$$\frac{n_5}{n_3} = \frac{C_{15} + C_{25} \frac{n_2}{n_1}}{A_{52}} \frac{A_{3tot}}{C_{13} + C_{23} \frac{n_2}{n_1}} \quad (2.69)$$

$$\frac{n_2}{n_1} = \frac{A_{12}/n_e + C_{12} + C_{13} \frac{A_{32}}{A_{3tot}} + \frac{A_{42}}{A_{4tot}} C_{14}}{\sum_j C_{2j} - \frac{A_{32}}{A_{3tot}} C_{23} - \frac{A_{43}}{A_{4tot}} C_{24}} \quad (2.70)$$

In Chapter 6 we will discuss this system in detail, and make use of this diagnostic to determine the thermodynamic properties of the chromosphere of ζ Aurigae A.

2.4 Solving the Transfer Problem

Now that we have discussed bound states and the equations of statistical equilibrium we will return to the transfer equation and describe how a self-consistent solution to this combined system of equations can be found. Beginning with the transfer equation as derived, we proceed to split the emissivity and the absorptivity into two components each

$$\chi_\nu = \chi_\nu^{\text{abs}} + \chi_\nu^{\text{scat}} \quad (2.71)$$

$$\eta_\nu = \eta_\nu^{\text{emis}} + \chi_\nu^{\text{scat}} \quad (2.72)$$

The absorptivity has two components, absorption and scattering, the emissivity is split into two terms, the emission and the scattering. Using these expressions for the source function

$$S_\nu = \frac{\eta_\nu^{\text{emis}} + \chi_\nu^{\text{scat}}}{\chi_\nu^{\text{abs}} + \chi_\nu^{\text{scat}}} \quad (2.73)$$

Here we will define a new concept, the photon destruction probability

$$\epsilon_\nu = \frac{\chi_\nu^{\text{abs}}}{\chi_\nu^{\text{abs}} + \chi_\nu^{\text{scat}}} \quad (2.74)$$

This is the probability that a photon which is absorbed not be re-emitted, and so

2.4 Solving the Transfer Problem

is converted to thermal energy. From this we get

$$S_\nu = \epsilon_\nu \frac{\eta_\nu^{\text{emis}}}{\chi_\nu^{\text{abs}}} + (1 - \epsilon_\nu) \frac{\eta_\nu^{\text{scat}}}{\chi_\nu^{\text{scat}}} \quad (2.75)$$

For isotropic scattering $\eta_\nu^{\text{scat}}/\chi_\nu^{\text{scat}} = J_\nu$. If the emission is thermal then $\eta_\nu^{\text{emis}}/\chi_\nu^{\text{abs}} = B_\nu(T)$. Hence we can write the transfer equation as

$$\frac{\partial I_\nu}{\partial \tau_\nu} = \epsilon_\nu B_\nu(T) + (1 - \epsilon) J_\nu - I_\nu \quad (2.76)$$

Now we introduce the Lambda Operator¹ (Cannon, 1973)

$$J_\nu = \Lambda[S_\nu] \quad (2.77)$$

$$\Lambda[S_\nu] = \frac{1}{2} \int_0^\infty S_\nu E_1 |t - \tau| dt \quad (2.78)$$

where E_1 is the first exponential integral. From this operator we construct the Lambda Iteration,

$$S_\nu^{n+1} = \epsilon_\nu B_\nu(T) + (1 - \epsilon_\nu) \Lambda[S_\nu^n] \quad (2.79)$$

This is the simplest form of the Lambda Iteration, where we successively apply the operation until we reach convergence of the source function. This iterative process of back-substitution of the previous iterate is referred to as a first-order, relaxation method, and this method will converge extremely slowly. Each iteration corresponds to the photons moving by one mean free path in the medium, and, in a medium of high optical depth and low photon destruction probability (high thermalization length) many iterations are required. This method can be vastly improved upon by what is known as the Accelerated Lambda Iteration (ALI). In order to see how this method can be employed we will recast the Lambda Iteration as a matrix operation, dropping the subscripts for notational convenience,

$$\mathbf{S}^{n+1} = \epsilon \mathbf{B} + (1 - \epsilon) \mathbf{\Lambda} \mathbf{S}^n \quad (2.80)$$

where $\mathbf{\Lambda}$ is a matrix whose elements determine the coupling between each point (i.e. a function of optical depth). This equation is identical to the previous integral

¹This is the angle-integrated Lambda Operator

2.4 Solving the Transfer Problem

formalism, and again will converge very slowly in the (standard) case that $\epsilon \ll 1$, where a photon may undergo a long chain of consecutive scatterings and a correspondingly large number of iterations are required. We can solve directly for \mathbf{S}

$$\mathbf{S} = [1 - (1 - \epsilon)\Lambda]^{-1}\epsilon\mathbf{B} \quad (2.81)$$

however performing this operation requires inverting the Λ matrix, which is impractical.

At this point we introduce a method known as operator splitting. This method has a long mathematical history and was introduced into the field of radiative transfer in a very important paper by Olson *et al.* (1986), often referred to as OAB.

$$\Lambda = (\Lambda - \Lambda^*) + \Lambda^* \quad (2.82)$$

where Λ^* is an approximate Lambda operator with an easily computable inverse. Hence we arrive at

$$\mathbf{S}^{n+1} = [1 - (1 - \epsilon)\Lambda^*]^{-1}[\epsilon\mathbf{B} + (1 - \epsilon)(\Lambda - \Lambda^*)\mathbf{S}^n] \quad (2.83)$$

where, as we can see, the only inverse to be computed is the (computationally inexpensive) inverse of the approximate operator.

We can cast this equation in a somewhat different form by the introduction of a new source function, obtained from the old source function (known as the Formal Solution source function)

$$\mathbf{S}^{\text{FS}} = \epsilon\mathbf{B} + (1 - \epsilon)\Lambda\mathbf{S}^n \quad (2.84)$$

This definition provides a new way to write the iteration scheme, and hence a new insight into its structure,

$$\delta\mathbf{S}^n = \mathbf{S}^{n+1} - \mathbf{S}^n = [1 - (1 - \epsilon)\Lambda^*]^{-1}[\mathbf{S}^{\text{FS}} - \mathbf{S}^n] \quad (2.85)$$

We can see from this equation that the factor which determines the iterative change is the difference between the old source function and the source function determined from the formal solution, and the iteration is accelerated by the $[1 - (1 - \epsilon)\Lambda^*]^{-1}$ factor. We note at this point that there is nothing significant about

2.4 Solving the Transfer Problem

applying this operation to the source function, a similar scheme could be applied to the mean intensity.

Despite the fact that we are using an approximate operator it is clear from Eqn. 2.83 that a converged solution will be exact. If we set $\Lambda^* = 0$ then we will recover the original Lambda Iteration, and $\Lambda^* = \Lambda$ will provide the exact solution, at the expense of the costly matrix inversion.

The selection of an approximate operator, Λ^* , is a difficult matter. Our requirements are that the operator have an easily computed inverse, and be an approximation of the full operator. There are a number of possible choices for the approximate operator, however OAB, in their foundational analysis, presented a set of strict mathematical criteria which determine the suitability of an approximation (based on the convergence speed-up attained, rather than the physics of the problem). The most common choice of approximate operator is

$$\Lambda^* = \text{diag}(\Lambda) \quad (2.86)$$

This is often referred to as the local operator, as its application will provide the radiation field at a point as a result of the source function at that point, ignoring the contribution of the rest of the medium. Using this approximate operator we remove the self-coupling term from the iteration (we are only “iterating” photons on a scale appropriate to the medium). This makes the equations local and hence makes the solution far easier to determine (the equations remain non-linear, this is a fact of the physics of the problem). The diagonal operator can often be evaluated analytically, for instance using the two-stream approximation in a 1-D slab, in the case that $\Delta\tau \gg 1$,

$$\text{diag}(\Lambda) \approx 1 - \frac{2}{\Delta\tau^2} \quad (2.87)$$

$$\mathbf{S}^{n+1} = \left(\epsilon + \frac{2}{\Delta\tau^2} \right)^{-1} [\epsilon \mathbf{B} + (1 - \epsilon)(\Lambda - \Lambda^*) \mathbf{S}^n] \quad (2.88)$$

which equates to a speed-up in convergence of $1/(\epsilon+2/\Delta\tau^2)$ (Hamann, 1985). More complex approximate operators may be employed with a tridiagonal matrix being commonly used (Olson & Kunasz, 1987a). This operator introduces a degree of “non-localness” into the equations, by coupling each point to its neighbours. This

operator is useful for radiative equilibrium cases, as it natively supports radiation diffusion.

The iterative scheme outlined above is known as the Jacobi Method, and the generalised algorithmic process has the following form (Hamann, 1985),

- For a general linear system we begin with:

$$Ax = b \quad (2.89)$$

- We break our matrix into three components, the diagonal D , the upper triangle $-U$, and the lower $-L$ (note the sign convention)

$$A = -L + D - U \quad (2.90)$$

- From this we obtain the iteration scheme (here D is known as the preconditioner)

$$Dx^{n+1} = b + (L + U)x^n \quad (2.91)$$

which can be rewritten as

$$\delta x^{n+1} = D^{-1}(b + (L + U)x^n) - x^n \quad (2.92)$$

- This process is repeated until $\delta x^{n+1}/x^n$ is below some threshold value.

This method is very efficient as it requires no matrix inversions.

In order to improve the convergence of this method it is altered to employ a convergent Newton-Raphson scheme. The technique of Complete Linearisation, introduced by Auer & Mihalas (1969), is effectively a multi-dimensional Newton-Raphson scheme. This method has been superseded by the ALI, however this Newton-Raphson (or the Quasi-Newton) formalism remains important to these implementations, as is the idea of approximating (linearising) the equations in order to quickly generate an inaccurate solution, followed by successive iteration to reduce the error.

In Complete Linearisation, the Newton-Raphson method enters the iteration through the rate equations (Peraiah, 2001). The iteration proceeds as follows: the

Lambda Operator provides the mean radiation field from the source function, and from the mean radiation field, through the rate equations, we can compute the populations. From these populations a new set of populations can be determined. Hence, very loosely, we have

$$J^k = \Lambda[S^k] \quad (2.93)$$

$$n^k = P_{ij}(J^k)^{-1}b \quad (2.94)$$

$$n^{k+1} = n^k - \frac{P_{ij}(J^k)}{\partial P_{ij}(J^k)/\partial n^k} \quad (2.95)$$

The application of the Newton-Raphson method provides the the subsequent iterate of the populations from which we can construct a new source function. This loop is repeated until the populations converge. However in multi-level ALI implementations the repeated inversion of the Jacobian required to perform this calculation may be costly, as well as being difficult to implement, and there are a number of techniques which avoid this.

Another important development is the careful preconditioning of the rate equations to ensure numerical accuracy and linearity. Photons in the wings of a spectral line will encounter a lower optical depth, and will travel a greater distance between extinctions than line core photons. As such these wing photons play a greater role in the non-locality of the transfer problem, and removing the core photons improves the numerical stability of the solution schemes at little cost. Hence we precondition the rate equations, employing the “core-saturation” method outlined in Rybicki (1972); Rybicki & Hummer (1991), which, as well as ensuring linearity, removes the effect of passive scatterings from the high optical depth line-core. This process of preconditioning is essentially equivalent to linearisation. This was demonstrated by Socas-Navarro & Trujillo Bueno (1997), who showed that preconditioning effectively takes into account the linear response of the radiation field to perturbations in the source function (Hubeny & Lanz, 2003).

In this thesis we will make use of two implementations, MULTI (Scharmer & Carlsson, 1985), and RH (Uitenbroek, 2001), both of which are based on the ideas we have discussed to this point. In the case of MULTI the iterations begin with an estimate for the populations, n^k and the radiation field J^k which determines

P_{ij} ,

$$\sum_{j \neq i} n_j^k P_{ji}^k - n_i^k \sum_{j \neq i} P_{ij}^k = -E^k \quad (2.96)$$

where E^k is the error at this iteration. We require a new set populations and rates, of the form

$$n^{k+1} = n^k + \delta n^k \quad (2.97)$$

$$P_{ij}^{k+1} = P_{ij}^k + \delta P_{ij}^k \quad (2.98)$$

such that the error term goes to zero. Substituting this equation into the statistical equilibrium equation (linearising the equation by neglecting all cross-term perturbations) we get

$$\sum_{j \neq i} n_j^k \delta P_{ji}^k + \delta n_i^k \sum_{j \neq i} P_{ij}^k - \sum_{j \neq i} \delta n_i^k P_{ij}^k - \sum_{j \neq i} n_i^k \delta P_{ij}^k = -E^k \quad (2.99)$$

In order to determine the appropriate change to the populations we must determine δP_{ij}^k in terms of δn_i^k . Since $\delta C_{ij} = 0$ (the rate equations only couple to the radiation through the radiative rates) we determine the perturbation in the rate equation from the perturbation in the mean radiation field

$$\delta P_{ij}^k = B_{ij} \delta J^k \quad (2.100)$$

To complete this set of equations δJ^k can be determined from the populations. In MULTI this calculation is carried out by the Scharmer Operator, which is a form of the Lambda Operator which returns the outgoing intensity,

$$I_\nu^+ = \Lambda_\nu^\dagger [S_\nu] = e^{\tau_\nu} \int_{\tau_\nu}^\infty S_\nu(t_\nu) e^{-t_\nu} dt_\nu \quad (2.101)$$

This equation is then solved using single point quadrature (Scharmer, 1981).

Since these equations will not result exactly in E^n going to zero, due to the linearisation, iteration is required.

In the case of RH, based on the method outlined in Rybicki & Hummer (1991), the equations are preconditioned, resulting in a linear expression for the populations. RH also makes use of a different operator, the Ψ operator, which is defined

as follows

$$J_\nu = \Psi_\nu[\eta_\nu] \quad (2.102)$$

which is to say the Ψ operator differs from the Λ operator by a factor of $1/\chi$. This operator has the benefit of being linear in the populations, where the Λ operator is not. Notwithstanding these differences in the operator and the preconditioning, the RH implementation (Uitenbroek, 2001) reaches a solution by effectively the same method as was outlined in the case of MULTI.

2.5 Computation of Fluxes

Now that we have discussed some of the methods by which the coupled transfer and statistical equilibrium problem may be solved we will discuss how flux may be computed. We will discuss two methods in particular which are employed later this work: the escape probability method, and the Feautrier method.

2.5.1 Escape Probability

Escape probability is a method of computing the emergent flux from a medium, based on the probability that emitted photon will escape the medium in a single flight (Hubeny, 2001). The escape probability of a photon is given by

$$p_\nu = e^{-\tau_\nu} \quad (2.103)$$

where τ_ν is the monochromatic optical depth from the point of emission to the boundary of the medium. If we consider a plane-parallel, semi-infinite slab, the optical depth of a ray may be specified by its direction cosine, μ (see Fig. 2.5). In this geometry the escape probability of an outgoing ray is

$$p_\nu = e^{-\tau_\nu(z)/\mu} \quad (2.104)$$

where $\tau_\nu(z)$ is the monochromatic optical depth along the central axis to depth z (a detailed review can be found in Rybicki (1984)). Averaging over all angles,

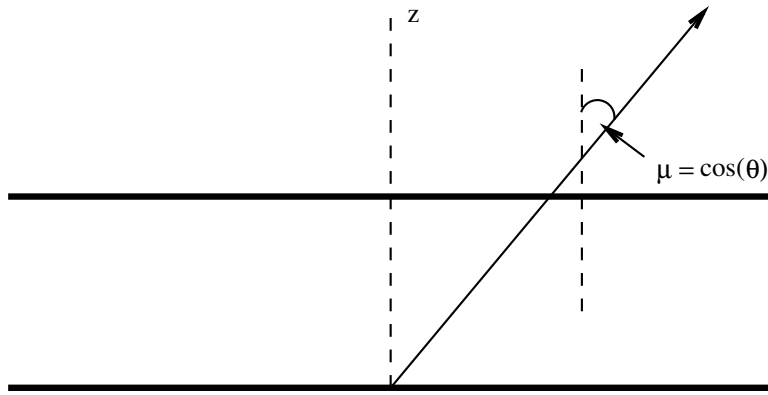


Figure 2.5: The ray geometry in the semi-infinite, 1-D slab.

and presuming that “escape” is only possible in the outward direction,

$$p_\nu(z) = \frac{1}{2} \int_0^1 e^{-\tau_\nu(z)/\mu} d\mu \quad (2.105)$$

This integral can be rewritten as

$$p_\nu(z) = \frac{1}{2} \int_1^\infty \frac{e^{-\tau_\nu(z)x}}{x^2} dx \quad (2.106)$$

where $x = 1/\mu$. This is the second exponential integral,

$$p_\nu = \frac{1}{2} E_2(\tau_\nu(z)) \quad (2.107)$$

This is often referred to as the one-sided escape probability, as it only takes account of photons which escape through one side of the medium. Consider emission from a spectral line with emission and absorption profile $\phi(\nu)$ (CRD). The monochromatic optical depth is given by $\tau\phi(\nu)$, and, as such, we can write the total escape probability for the line as:

$$p_\nu = \frac{1}{2} \int_0^\infty E_2(\tau\phi(\nu))\phi(\nu)d\nu \quad (2.108)$$

This integral arises often in radiative transfer calculations. It is known as the kernel function (K_2), after Avrett & Hummer (1965), and Hummer (1981) provides an algorithm for its evaluation.

The escape probability method has many uses in astrophysics. It is used in

the photoionization code CLOUDY (van Hoof *et al.*, 2000), and it is often used in conjunction with the net radiative bracket to simplify the solution of the transfer problem (Irons, 1978). In this thesis we make use of this method to compute line fluxes. This is achieved by constructing the rate matrix and using it to determine the populations, and from these populations computing the emergent flux using

$$F_\nu \propto n_j A_{ji} p_\nu \quad (2.109)$$

This approximation of the full transfer problem will provide a good estimate of the flux in the case that we are dealing with optically thin lines.

2.5.2 Feautrier Method

In discussing the Lambda Iteration method we described the method used to compute the source function, now we will discuss the calculation of the emergent intensity, given that the source function has been specified. This can be achieved by the Feautrier Method (Feautrier, 1964). The Feautrier Method has many uses in radiative transfer problems, and a number of modified algorithms have been presented (Rybicki, 1971; Rybicki & Hummer, 1991). These algorithms enable Feautrier-type schemes to be used to (very efficiently) compute the diagonal of the inverse Lambda Operator, or in the construction of large model atmospheres (see the temperature correction discussion in Mihalas (1978)). In this thesis we will use the Feautrier Method to compute a formal solution to the transfer equation; to determine the monochromatic intensity given a known source function (computed by the methods outlined in the previous sections).

We begin with the transfer equation in plane-parallel geometry,

$$\mu \frac{\partial I_\nu}{\partial \tau_\nu} = I_\nu - S_\nu \quad (2.110)$$

This equation can be rewritten as two equations, one taking account of intensity travelling in the “positive”, outward direction, the other in the “negative”, inward

direction.

$$\mu \frac{\partial I_\nu^+}{\partial \tau_\nu} = I_\nu^+ - S_\nu \quad (2.111)$$

$$-\mu \frac{\partial I_\nu^-}{\partial \tau_\nu} = I_\nu^- - S_\nu \quad (2.112)$$

This is known as the Schuster two-stream approximation (Schuster, 1905). Introducing two new variables we can rewrite the differential equations (where the dash represents the derivative with respect to τ_ν),

$$u = \frac{1}{2}(I_\nu^+ + I_\nu^-), \quad v = \frac{1}{2}(I_\nu^+ - I_\nu^-) \quad (2.113)$$

$$\mu v' = u - S \quad (2.114)$$

$$\mu u' = v \quad (2.115)$$

From these we can write a single second-order differential equation for u

$$\mu^2 u'' = u - S \quad (2.116)$$

Given that the source function is specified, we can solve this equation for a given optical depth grid (all quantities being monochromatic) τ_i , $i = 1, \dots, n$.

We can express this discretised differential as

$$u_i'' = -\frac{2}{\Delta \tau_{i-1}(\Delta \tau_{i-1} + \Delta \tau_i)} u_{i-1} + \frac{2}{\Delta \tau_i \Delta \tau_{i-1}} u_i - \frac{2}{\Delta \tau_i (\Delta \tau_{i-1} + \Delta \tau_i)} u_{i+1} \quad (2.117)$$

for $1 < i < n - 1$, where $\Delta \tau_i = \tau_{i+1} - \tau_i$. We can equally discretise the angles, usually choosing angles based on Gauss-Legendre quadrature, however for notational convenience we will remove the angle terms here; this does not alter the resultant equations, it simply requires that we solve the same set of equations for each angle.

As this is a second-order differential equation we require two boundary condi-

tions

$$I_1^- = r_1 I_1^+ + f_1 \quad (2.118)$$

$$I_n^+ = r_n I_n^- + f_n \quad (2.119)$$

where the first equation specifies the upper boundary condition as the incident intensity on the upper boundary (f_1) plus the fraction of outward travelling intensity which is reflected (r_1), and the second equation is analogous for the lower boundary.

We can express these boundary conditions in terms of u as

$$u'_1 = \frac{(1 - r_1)u_1 - f_1}{1 + r_1} \quad (2.120)$$

$$u'_n = \frac{(1 - r_n)u_n - f_n}{1 + r_n} \quad (2.121)$$

In order to implement the boundary conditions, following Auer (1967), we will Taylor expand at both boundaries, beginning with the upper boundary

$$u_2 = u_1 + u'_1 \Delta\tau_1 + \frac{1}{2}u''_1 \Delta\tau_1^2 \quad (2.122)$$

Substituting in for u'_1 and u''_1

$$u_2 = u_1 \left(1 + \frac{\Delta\tau_1(1 - r_1)}{1 + r_1} + \frac{1}{2}\Delta\tau_1^2 \right) - \Delta\tau_1 \frac{f_1}{1 + r_1} - \frac{1}{2}S_1 \Delta\tau_1^2 \quad (2.123)$$

Equally

$$u_{n-1} = u_n + u'_n \Delta\tau_{n-1} + \frac{1}{2}u''_{n-1} \Delta\tau_{n-1}^2 \quad (2.124)$$

$$u_{n-1} = u_n \left(1 - \frac{\Delta\tau_{n-1}(1 - r_n)}{1 + r_n} + \frac{1}{2}\Delta\tau_{n-1}^2 \right) - \Delta\tau_{n-1} \frac{f_n}{1 + r_n} - \frac{1}{2}S_n \Delta\tau_{n-1}^2 \quad (2.125)$$

From this we can see that we have a set of n equations, which is usually written in the following form

$$-A_i u_{i-1} + B_i u_i - C_i u_{i+1} = Y_i \quad (2.126)$$

where the boundary values are

$$A_1 = 0 \quad A_n = \frac{2}{\Delta\tau_{n-1}} \quad (2.127)$$

$$B_1 = 1 + \frac{2(1 - r_1)}{\Delta\tau_1(1 + r_1)} + \frac{2}{\Delta\tau_1^2} \quad B_n = 1 + \frac{2(1 - r_n)}{\Delta\tau_{n-1}(1 + r_n)} + \frac{2}{\Delta\tau_{n-1}^2} \quad (2.128)$$

$$C_1 = \frac{2}{\Delta\tau_1^2} \quad C_n = 0 \quad (2.129)$$

$$Y_1 = S_1 + \frac{2f_1}{\Delta\tau_1(1 + r_1)} \quad Y_n = S_n + \frac{2f_n}{\Delta\tau_{n-1}(1 + r_n)} \quad (2.130)$$

and for $1 < i < n - 1$

$$A_i = \frac{2}{\Delta\tau_{i-1}(\Delta\tau_{i-1} + \Delta\tau_i)} \quad (2.131)$$

$$B_i = \frac{2}{\Delta\tau_i\Delta\tau_{i-1}} \quad (2.132)$$

$$C_i = \frac{2}{\Delta\tau_i(\Delta\tau_{i-1} + \Delta\tau_i)} \quad (2.133)$$

$$Y_i = S_i \quad (2.134)$$

This can be re-arranged to form a tridiagonal matrix,

$$\mathbf{T} \cdot \mathbf{u} = \mathbf{Y} \quad (2.135)$$

whose elements are A_i , B_i , and C_i , where \mathbf{u} is the vector of the intensities, and \mathbf{Y} is the solution vector. The parallels between this operation and the Lambda Iteration are clear, as \mathbf{u} is effectively J , $\mathbf{Y} = S$ at all points other than the boundaries, and \mathbf{T}^{-1} is related to the Lambda Operator. This similarity is used by Rybicki & Hummer (1991) as a core part of their iteration, it is used to compute the formal solution while simultaneously delivering the diagonal elements of the approximate Lambda Operator. To determine \mathbf{u} we invert \mathbf{T}

$$\mathbf{u} = \mathbf{T}^{-1}\mathbf{Y} \quad (2.136)$$

again turning to Rybicki & Hummer (1991) who provide a highly efficient algorithm for computing this inverse ($O(mn)$, where m is the band width, compared with

$O(n^2)$ (Press *et al.*, 1992))

In our case, exploiting the 1-d nature of the problem, the computation could be carried out by a forward elimination–backward substitution scheme. Beginning with the outer boundary condition we can express u_1 in terms u_2 , allowing us to express u_2 in terms of u_3 . Proceeding in this manner we finally reach the lower boundary condition, which delivers u_n . Back substitutions then produces $u_n \rightarrow u_{n-1} \rightarrow \dots u_2 \rightarrow u_1$. Finally we obtain the emergent intensity

$$I^+ = u_1 + \frac{(1 - r_1)u_1 - f_1}{1 + r_1} \quad (2.137)$$

2.6 Modelling Binary Stars

In this thesis we will be concerned with the modelling of the ζ Aurigae binary system. The modelling of this system requires two elements, the modelling of the system orbit, and the computation of a synthetic light curve. In order to make these calculations it is necessary that we have information on the system geometry, and the radiative properties of the component stars. In making these models we will make use of the Physics Of Eclipsing Binaries (PHOEBE) suite of code (Degeroote *et al.*, 2013; Prša & Zwitter, 2005), which is an updated implementation of the older (and commonly used standard) Wilson-Devinney (WD) code (Wilson & Devinney, 1971). We will begin by discussing the modelling of the binary orbit based on observational constraints, and then discuss the modelling of the individual components.

2.6.1 System Geometry

One of the most accurate, and most commonly used, models for binary stars is the Roche model (Kallrath & Milone, 2009). This model is based on a number of simple assumptions, namely that both the stars behave as point masses surrounded by massless envelopes, there is no differential rotation, and the stars do not have appreciable radial pulsations (this is to ensure that the shape of star is, at any time, defined solely by the instantaneous gravitational force). The Roche model attempts to explain the morphology and interaction of the stars from this tidal

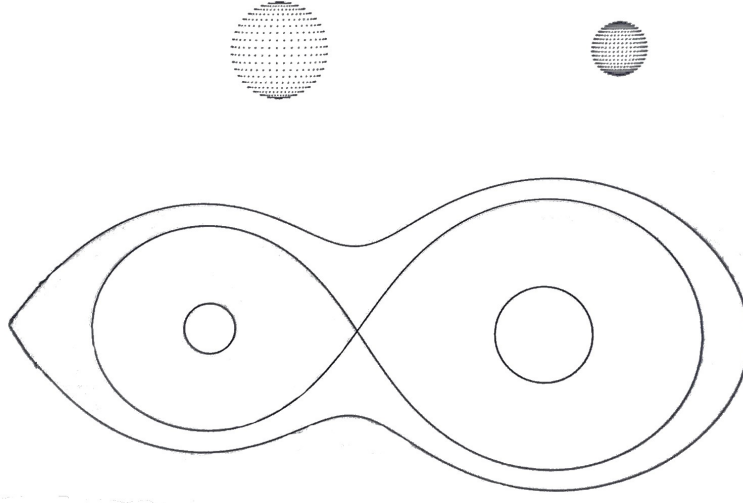


Figure 2.6: Roche potential lobes and morphology of a detached binary system. From a set of examples provided by Bradstreet (1993), from Kallrath & Milone (2009)

force. An expression for this potential was initially derived by Kopal (1959), and generalised by Wilson (1979) to apply to elliptic orbits.

We obtain an expression for the potential which can be solved iteratively for all points, with the equipotential surfaces determining the morphology of the star. This is most commonly computed by calculating the potential at the stellar pole, and using this as the value on equipotential surface.

Both objects will have a tear-drop shape with the apex pointing towards the other star, an equipotential shape known as the Roche Lobe. The filling of this Roche Lobe determines the morphological classification the system. In the case that the Roche Lobe reaches the first Lagrange point, L_1 mass transfer will occur (symbiotic binaries). In the case of ζ Aurigae both stars are bound within separate equipotential surfaces, and their evolution is more-or-less independent from one another, a configuration known as a detached binary system, see Fig 2.6.

This distortion of the stellar surface gives rise to a orbital modulation of the flux, as we see a larger surface cross-section at quarter-phases. This effect is known as ellipsoidal variation, and has the effect of introducing a fluctuation in the light curve from the binary system, even in non-eclipsing systems (though clearly systems viewed pole-on would not display this effect).

With the Roche model determining the shape of the objects in the system, the dynamical orbit of the system is the classic Kepler two-body problem. In the case of doubly-lined spectroscopic binaries (i.e. ζ Aurigae) our most important observable is the radial velocity curves of the two objects, which is the velocity component along the line-of-sight for both objects obtained from measurements of line Doppler shifts. From this radial velocity curve we define the semi-amplitude of the radial velocity for each object,

$$K_i = \frac{2\pi}{T} \frac{a_i \sin i}{\sqrt{1 - e^2}} \quad (2.138)$$

where T is the period, e is the eccentricity, i is the inclination of the orbit, and a_i is the semi-major axis of the orbit of i . The semi-amplitude of the radial velocity is half of the amplitude of the measured radial velocity curve for a given object. Since the distance of the objects from the barycentre will, at each instant, be in direct ratio to their masses, we can determine the mass ratio as

$$\frac{M_1}{M_2} = \frac{a_2}{a_1} = \frac{K_2}{K_1} \quad (2.139)$$

Using Kepler's third law we can determine the sum of the masses,

$$T^2 = \frac{4\pi^2}{G(M_1 + M_2)} a^3 \quad (2.140)$$

where $a = a_1 + a_2$. Substituting in the expression for the semi-major axis, in terms of the semi-amplitude of the radial velocity we obtain

$$M_1 + M_2 = \frac{T(1 - e^2)^{3/2}}{2\pi G \sin^3 i} (K_1 + K_2)^3 \quad (2.141)$$

Now that we have determined the sum and the ratio of the masses we can compute the individual masses of the components. This approach is only possible if the inclination is known, and this is difficult to ascertain, however for eclipsing object close attention to the light-curve can determine the inclination. Of course if the objects are eclipsing the inclination must be almost $\pi/2$ with respect to the plane-of-sky. The best determined stellar masses come from this type of binary analysis, as this method is not dependent on the (often not well known) distance

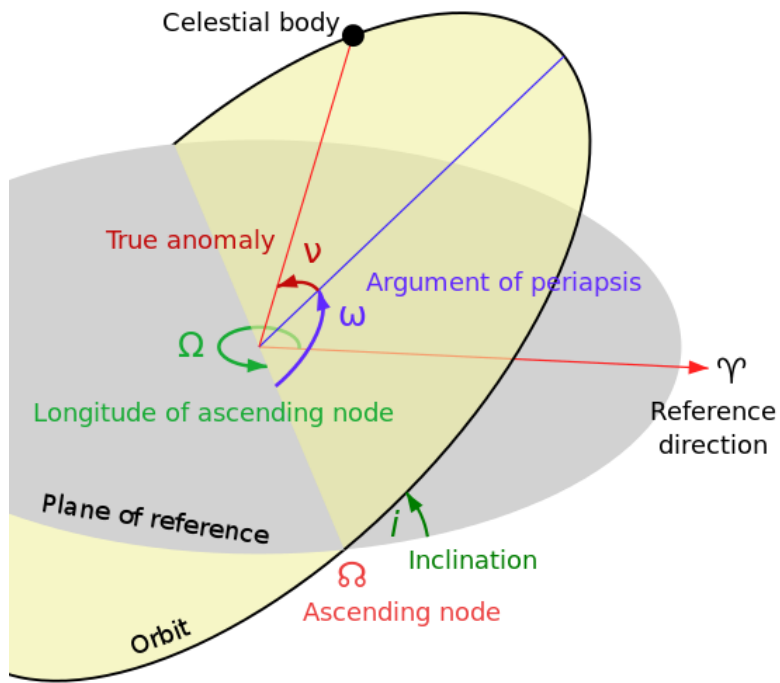


Figure 2.7: In this diagram the orbital plane is coloured yellow, and intersects a reference plane which is grey, with the orbital elements annotated. *Image Credit: Wikimedia*

to the system.

In order to study the orbits in detail we must define a number of important parameters, the six Keplerian orbital elements in the reduced mass frame. These can be seen graphically in Fig. 2.7.

The two which determine the shape of the orbit, and which were important in calculating the masses, are

- The semi-major axis a , the length of the longest diameter of the ellipse divided by two ($a = a_1 + a_2$).
- The eccentricity is defined as $e = 1 - (r_p/a)$ where r_p is the minimum distance between the objects, the point of periastron.

The two which determine the orientation of the orbit (with respect to the observer) are

- Inclination, i , the offset of the orbit from the reference plane.
- The longitude of the ascending node, Ω , is the angle between where the orbit passes upward through the reference plane and a reference direction. In general the reference plane is the plane-of-sky and so, as can be seen in our diagram, rotations about the axis connecting the barycentre and the reference direction do not have any physical significance, hence Ω can be arbitrarily fixed.

The final elements are

- The argument of periapsis, ω , is the angle measured from the ascending node to the point of periastron.¹
- The true anomaly, ν , which introduces a time varying property (ignoring apsidal motion), is the angle between the point of periastron, the focus of the orbit, and the position of the orbiting object at any given time (see Fig. 2.8).

In order to compute ν we must define two auxiliary anomalies, the mean anomaly, M , and the eccentric anomaly, E . The mean anomaly is not in fact an angle, it simply varies linearly over the orbit from 0 to 2π

$$M(t) = 2\pi((t - t_0) \bmod T) \quad (2.142)$$

where t_0 is some reference time, usually periastron or mid-eclipse.

The eccentric anomaly is the angle between the major axis and a line connecting the centre of the orbit, to the point where a line perpendicular to the major axis, passing through the object, intersects a circle inscribing the orbit (Fig. 2.8). The eccentric anomaly is related to the mean anomaly by

$$M = E - e \sin E \quad (2.143)$$

¹This value may change, a phenomenon known as apsidal motion, as a result of tidal interaction, perturbations, the stellar quadrupole, or general relativistic effects (famously so in the case of Mercury)

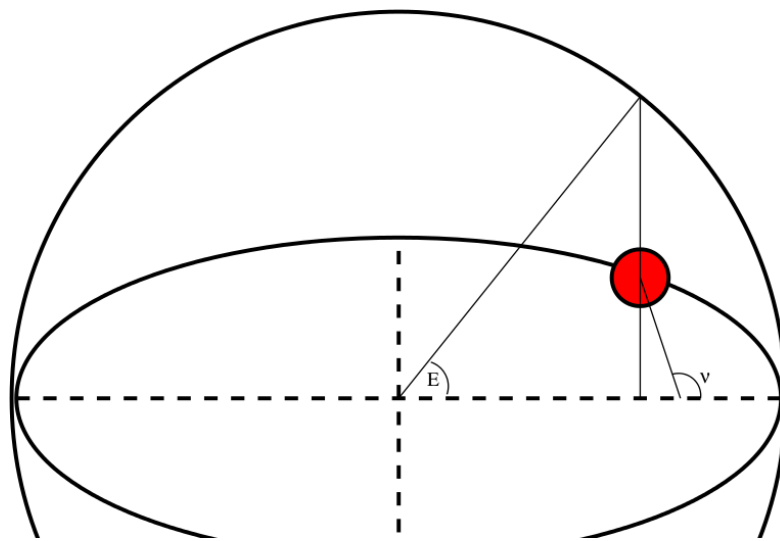


Figure 2.8: The eccentric anomaly, E , is the angle between major axis and a line connecting the centre of the orbit, to the point where a line perpendicular to the major axis, passing through the object, intersects a circle inscribing the orbit. The true anomaly is the angle between the point of periastron, the focus, and the orbiting object.

This equation, being transcendental, must be solved by numerical methods, and WD uses the iterative method of Padé approximants

$$x_{i+1} = x_i + \Delta x_i, \quad \Delta x_i = -\frac{f(x)f'(x)}{f'(x)^2 - \frac{1}{2}f'(x)f''(x)} \quad (2.144)$$

$$\Delta E_i = \frac{(E_i - e \sin E_i - M)(1 - e \cos E_i)}{(1 - e \cos E_i)^2 - \frac{1}{2}(E_i - e \sin E_i - M)e \sin E_i} \quad (2.145)$$

Once we have solved for E , ν can be computed by

$$\tan \frac{\nu}{2} = \sqrt{\frac{1+e}{1-e}} \tan \frac{E}{2} \quad (2.146)$$

With the true anomaly computed we can now specify the coordinates of the object as it orbits, given the instantaneous separation of the objects

$$D = \frac{a(1-e)}{1+e \cos \nu} \quad (2.147)$$

We have now fully specified the relative positions of the objects as a function of time.

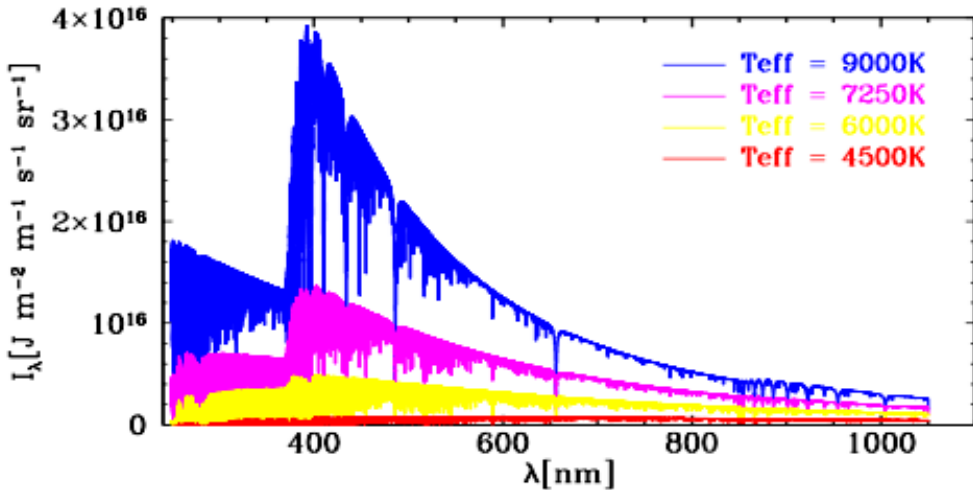


Figure 2.9: Synthetic spectra from Kurucz. We can see that the spectra differ from a simple blackbody spectrum, especially at the Balmer jump. *Image credit: <http://kurucz.harvard.edu/>*

2.6.2 Radiative Properties

In order to compute synthetic light curves for binary systems we must have some knowledge of the radiative properties of the components. In PHOEBE these calculations are performed in general, the radiative properties of the objects are computed in an aspect (observer) independent fashion, and from this the flux in a given direction, at a given time, is computed.

In order to compute the flux, PHOEBE makes use of the model atmospheres developed by Kurucz (1970). These atmospheric models are commonly used, and provide a good estimate of the emergent intensity from a stellar atmosphere (see Fig. 2.9). In close binary systems the assumptions upon which these models rest may be broken, however for a detached system like ζ Aurigae the models should provide reliable results (Siviero *et al.*, 2004).

In order to obtain accurate light curves we must take account of the distribution of flux across the stellar disk. This distribution is not uniform, and is altered by an effect known as limb-darkening. Limb-darkening occurs as a result of the fact that we see to the same optical depth at all points on the disk of a star ($\tau = 2/3$), but this does not correspond to the same physical depth, and hence

temperature/brightness. As such there is a fall off in intensity as we move from disk centre to limb.

Another important effect which must be accounted for is gravity darkening. Gravity darkening arises from the fact that the intensity distribution depends on the energy transfer mechanism in a stellar envelope. The work of von Zeipel (1924) showed that the flux distribution over the surface is proportional to the effective gravity,

$$F_\lambda = -\frac{16\sigma T^3}{3\bar{\kappa}\rho} \frac{dT}{d\Psi} g^\beta \quad (2.148)$$

where σ is the Stefan-Boltzmann constant, T is the local temperature, $\bar{\kappa}$ is the Rosseland mean opacity, ρ is the density of the gas, Ψ is the gravitational potential, and β is the gravity darkening coefficient. von Zeipel (1924) demonstrated that for a radiative envelope $\beta = 1$, and later work by Lucy (1967) derived $\beta = 0.32$ for convective envelopes. This expression can be rewritten for local temperature as

$$T^4(\theta, \phi) = T_{\text{pole}}^4 \left(\frac{g(\theta, \phi)}{g_{\text{pole}}} \right)^\beta \quad (2.149)$$

where θ and ϕ are polar coordinates on the stellar surface.

These radiative properties are phase dependent only as a result of the tidal deformation of the objects, in a circular orbit the face of one star would always appear the same to the other. In PHOEBE these radiative effects are accounted for by the following expression

$$L_{\text{norm}} = \int_{2\pi} \frac{I(\theta)}{I(0)} d\theta \int_{2\pi} \int_{2\pi} T^4(\theta, \phi) d\theta d\phi \quad (2.150)$$

where L_{norm} is normalised luminosity. This normalised luminosity is then used to scale the Kurucz luminosities. These radiative properties are discussed further in the specific instances where they are used in the work.

Finally, in systems where the separation of the objects is $\lesssim 5$ times greater than the radii of the components (i.e. ζ Aurigae) we must take account of the mutual irradiation of the components by one another. This irradiation serves to increase the temperature, and hence the luminosity of the objects, and is usually referred to (somewhat misleadingly) as reflection. This effect was first derived explicitly by Wilson (1990). In order to take account of this effect we must compute the

irradiation of each part of one object due to the second (integrating over the surfaces visible one from another). We define the total reflective excess for each object as

$$\mathcal{R}_1 = 1 + A_1 \frac{F_{2 \rightarrow 1}}{F_1} \quad \mathcal{R}_2 = 1 + A_2 \frac{F_{1 \rightarrow 2}}{F_2} \quad (2.151)$$

where A is the albedo of the star, F is its flux, and $F_{i \rightarrow j}$ is the flux from i falling on j ,

$$F_{i \rightarrow j} = \mathcal{R}_i \int_S F_j \cos \phi d\sigma_j \quad (2.152)$$

where we are integrating over the visible surface of the star, S , F_j is the flux emerging from a surface element $d\sigma_j$, and ϕ is the angle between the surface element and i . Since both stars irradiate one another these equations are solved iteratively until the values for \mathcal{R} have converged. A lengthy discussion of the reflection can be found in Chapter 5.

Now that we have described much of the underlying theory and mathematics which will be used in this thesis we will proceed with discussing the instrumentation we have used.

3

Instrumentation

In this chapter we describe the instruments used to make the observations upon which this thesis is based. We briefly discuss the theory underlying the instruments, their technical construction, and the reduction of their raw output to produce science data. We will begin by discussing ground-based spectroscopy, produced at the Dominion Astrophysical Observatory and other sites, which have been integral in our study of ζ Aurigae. We also describe the Hubble Space Telescope, focusing on the particular instrument we have used, and outlining the reduction pipelines. This work also relies on observations at radio wavelengths, made using CARMA and APEX, and we will describe these telescopes in detail, again providing a description of how the calibrated radio fluxes are produced. In this discussion we also describe the theory and methods underlying the interferometric observations used in this thesis, including observations made at optical, infrared, and radio wavelengths.

In this work we have made use of a number of observational methods in order to study the structure of late-type chromospheres, observations at many wavelengths, encompassing spectrometers — both analogue and digital — radio bolometers, and interferometers. In this chapter we will describe these methods, beginning by discussing spectra, before moving on to radio observations, and finally providing a discussion of optical spectro-interferometers.

3.1 Spectrometers

The results of this work rely heavily on optical spectroscopic observations. We have made use of archival ground-based observations, using the Dominion Astrophysical Observatory (DAO) and other sites, as well as the Hubble Space Telescope (HST). We will discuss each in turn.

3.1.1 Ground-based Observations

In this work we have made use of data collected at a number of ground-based optical telescopes, and as such we will provide a description of how these instruments function in general. In a ground-based spectrometer, light is collected by the main telescope before being sent into the spectrograph, and the amount of light collected by the telescope — hence the spatial resolution and faintness detectable — is dependent on the size of the primary mirror. The main ground-based telescope we have used is the Plaskett telescope at DAO (Plaskett, 1927), which was planned to be, but never was, the largest telescope in the world. This telescope has a 78" primary mirror with a spectrograph mounted at the Cassegrain focus. We have also made use of data collected at the James Lick Telescope (Holden, 2008), a 38" refracting telescope (the largest refracting telescope in the world up to 1897) outside San Jose, California. Finally, we also made use of data collected at Calar Alto Observatory (Elsässer, 1981; Graser & Hopp, 1991), Granada, using the 87" telescope. Most data was collected by R.E.M. Griffin, or in some cases taken from the DAO archive. All observations were reduced, and data provided, by R.E.M. Griffin. An observation log is provided in Chapter 5.

Light from the main telescope, once collected at the primary mirror, is sent into the spectrograph, which is placed at the focus of the instrument. In Fig. 3.1

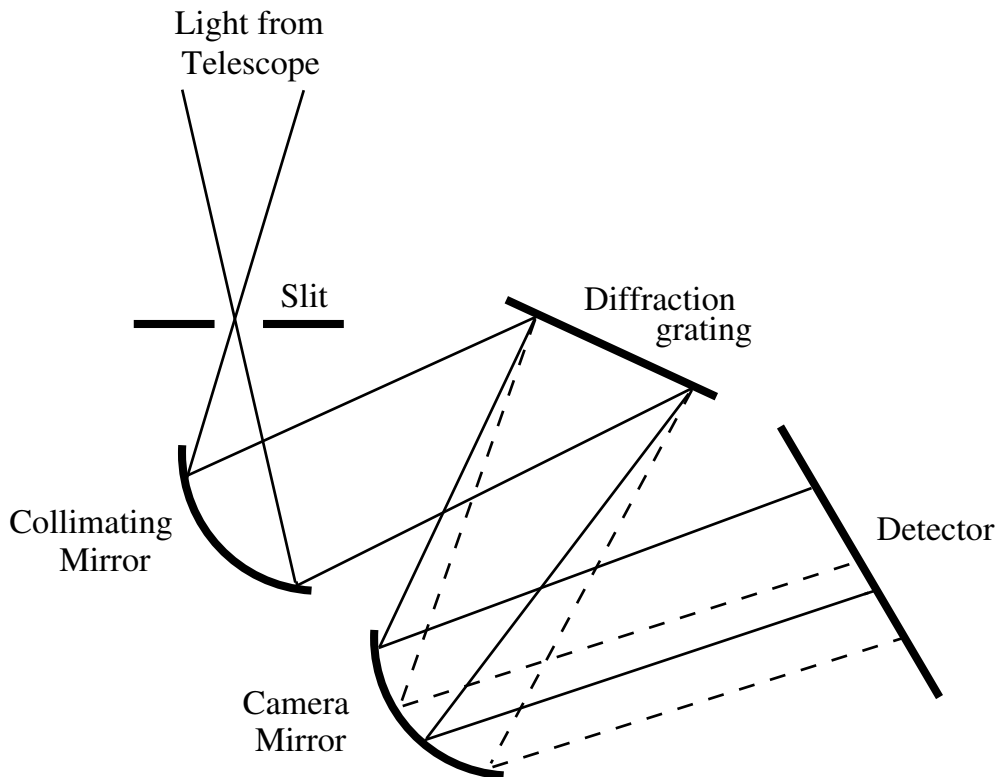


Figure 3.1: Diagram of a spectrograph with a reflecting diffraction grating.

we see a general schematic of a spectrograph. Light enters through a slit, and a collimating mirror transforms the incident beam into parallel rays. At this point, the rays are directed onto a diffractor. A diffraction grating is an optical element with narrow, closely spaced lines at approximately the wavelength of the light, and the grating may transmit the light (a transmission grating), or reflect the light (a reflection grating — as seen in Fig 3.1). An echelle grating may also be used, which is a variant of the diffraction grating with a relatively low groove density, but a groove shape which is optimized for use at a high incidence angle. Echelle gratings are highly blazed, and hence the light is dispersed into high orders, with some overlap. A prism is then required to split the overlapping orders.

Once the light has been split into its spectral components it is focussed onto the detector. Historically, and for some of the observations used in this thesis, the detector was comprised of photographic emulsion (in our case Kodak IIa-0). This photographic exposure has the disadvantage of reacting non-linearly to

incident radiation, making it difficult to calibrate spectra to an absolute flux scale. However the emulsion has the advantage of being physically robust, once the image is chemically fixed, and it is well stored, it will remain unchanged for decades. Hence the archival DAO data used in this thesis, some of which was collected by K.O. Wright in his early observations of ζ Aurigae in the 1950's, has not declined in quality. These data have been digitized by R.E.M. Griffin as part of a long running campaign, and made available for our use. In the modern era photographic plates have been replaced with Charge-Coupled Devices (CCDs). CCDs react linearly to incident radiation, and have a very high quantum efficiency ($\sim 95\%$), allowing high signal-to-noise observations on an absolute flux scale. The CCD is comprised of a photo-reactive layer of silicon divided into columns by insulating boundaries called channel stops, and rows by strips of aluminium, creating the individual pixels. The (p-doped, MOS) silicon layer is biased above the threshold for inversion and hence incoming photons will free electrons as a result of the photoelectric effect. This charge is held in place by the potential well created by positively charged electrodes (the electrode positioning is what defines the position of the pixels). The pixels are then read out row by row, with each pixel passing its charge to its neighbour, and the final pixel in each row of the device passing its charge to a charge amplifier. The resultant voltages are then stored as a digital image.

Traditionally in ground-based spectroscopy line-profiles were very difficult to measure accurately as a result of the limitations of photographic plates, seeing, and the faintness of the object (requiring that the spectrograph's slit be open fully) reducing the spectral resolution. In order to overcome these limitations and perform accurate quantitative spectroscopy astronomers measured the Emission Equivalent Width (EEW) of spectral lines, and the EEW will be the subject of our study. It is computed from the observed spectrum as

$$W = \int_{\lambda_{min}}^{\lambda_{max}} 1 - \frac{F_{\text{cont}}}{F_{\lambda}} d\lambda \quad (3.1)$$

where F_{λ} is the measured flux, and F_{cont} is the local continuum flux. The EEW is the width of a feature (hence it has units of wavelength) whose total intensity is zero, and whose total flux deficit is equal to that of the line. This value is unaffected by the spectral resolution of the instrument as flux in a given wavelength band is

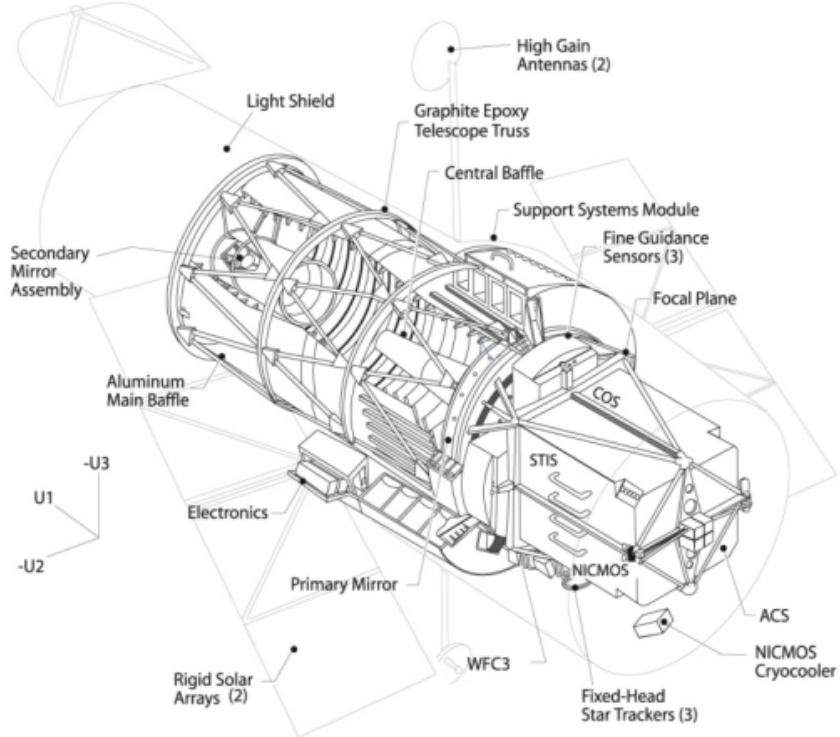


Figure 3.2: Diagram of the Hubble Space Telescope. This diagram is post-installation of the STIS instrument, which took the place of GHRS. *Image Credit: NASA.*

conserved. The EEW is often used in conjunction with curve-of-growth analysis, and this has been a fruitful area in the study of ζ Aurigae binaries. In particular, the analysis of Wilson (1957) of EEW's measured at DAO.

3.1.2 Hubble Space Telescope

The HST is a space telescope mission by NASA launched into low Earth orbit, at a height of \sim 550 km, on the 25th of April 1990, capable of observing at near-ultraviolet, visible, and near-infrared wavelengths. The telescope consists of a 2.4 m primary telescope, and at launch there were five scientific instruments; the Wide Field and Planetary Camera (WF/PC), the Faint Object Spectrograph (FOS), the High Speed Photometer (HSP), the Faint Object Camera (FOC) and the Goddard High-Resolution Spectrograph (GHRS). A diagram of the telescope may be seen

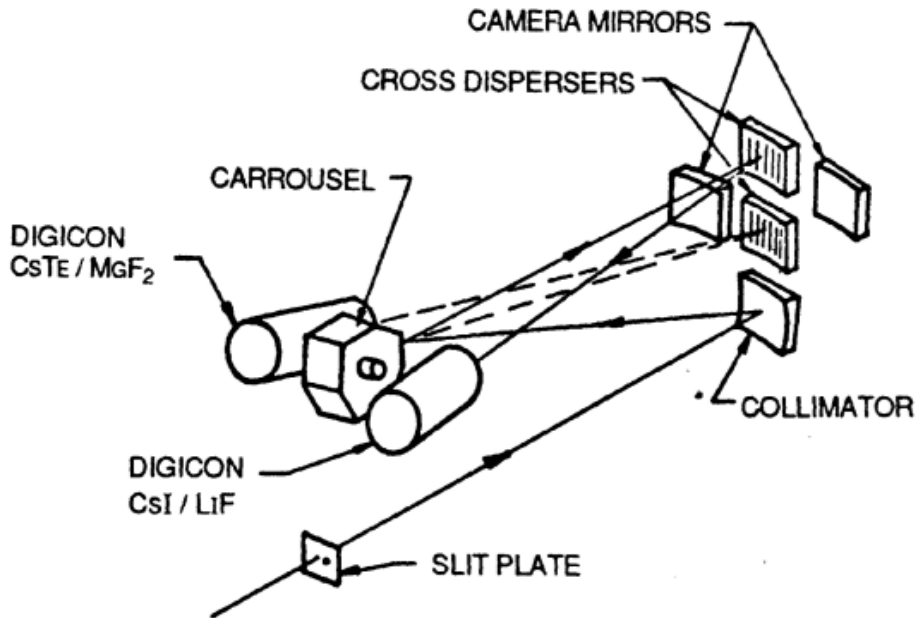


Figure 3.3: A schematic diagram of the GHRS. *Image Credit: Brandt et al. (1994).*

in Fig. 3.2.

The observations in this work make use of the GHRS (Brandt *et al.*, 1994), and as such we will focus our discussion on this instrument. The GHRS was one of the 4 original axial instruments aboard the HST. Owing to an error in the construction of the primary mirror of the HST a spherical aberration was introduced, and in December 1993 HSP was removed in order to fit the Corrective Optics Space Telescope Axial Replacement (COSTAR). With COSTAR in place the spherical aberration which affected the GHRS, the FOC, and the FOS, was corrected allowing these instruments to be used at their highest resolution.

The GHRS¹ is an ultra-violet spectrometer, making observations from 1150 Å–3200 Å. A schematic diagram of the instrument can be seen in Fig 3.3. Light enters the instrument through one of two apertures, labelled LSA and SSA. The LSA has a 2''.0 aperture and is used for faint targets. The SSA has a 0''.25 aperture and is used when the highest spectral resolution is required. Once the light has entered the in-

¹Much of this discussion is based upon, and much more detail can be found in, the GHRS Handbook (Soderblom & et al., 1995).

3.1 Spectrometers

strument a collimator directs it to the rotating carousel which holds the dispersers. By rotating the required element into position spectra can be taken in one of seven modes. Five of these modes are gratings, designated G140L (1100 Å–1900 Å), G140M (1100 Å–1900 Å), G160M (1150 Å–2300 Å), G200M (1600 Å–2300 Å), and G270M (2000 Å–3300 Å). In this naming convention “G” indicates a grating, the number indicates the blaze wavelength (in nm), and the “L” or “M” suffix denotes a “low” or “medium” resolution. The “L” gratings provide a resolution of $R = \lambda/\Delta\lambda = 2,000$, and the “M” grating $R = 20,000 – 35,000$. There are two echelle modes also available, Ech-A, and Ech-B, whereby light from the single echelle grating is directed onto one of the two detectors, D1 and D2. These echelle modes provide the highest resolution, $R = 90,000 – 120,000$. The dispersed light then travels to the camera mirror in the case of the gratings, or the cross-dispersers in the case of the echelles (these are required as the orders coming from the echelle overlap unless separated by the cross-dispersers). Finally, the light is sent to the photocathode of one of the two detectors.

The GHRS makes use of two Digicon detectors, differing only in the wavelengths to which they are sensitive, D1 being sensitive to 1100 Å–1700 Å (CsI photocathode), and D2 being sensitive to 1700 Å–3200 Å (CsTe photocathode). The photoelectrons produced by the photocathodes are accelerated to 22 keV and focussed by a 105 G magnetic field onto one of the 500 science diodes. This produces approximately a 5,600 electron pulse per photoelectron. These pulses are read into buffer memory by each diodes dedicated counter. The diodes have slight response irregularities, which are corrected for by deflecting the spectrum across the diodes in the dispersion direction and adding these spectra, hence averaging out the effect of the diode irregularities. In addition GHRS spectra taken with the SSA, as ours are, are intrinsically undersampled. By substepping, or “dithering”, the electron image in the dispersion direction by 1/2 or 1/4 diode critically sampled spectra are obtained (Gilliland *et al.*, 1992).¹ The background noise in the diodes comes to ~ 0.01 counts/diode/s, with most of this arising from Cerenkov radiation due to cosmic rays.

All of the HST data used in this work was reduced and provided by K. Carpenter (Proposal ID: 6069), however we will provide a brief description of the

¹As such 1/4 diode is often referred to as a pixel.

standard reduction pipeline which was used to construct from the raw detector counts usable science products. The calibration is carried out using the standard CALHRS pipeline developed GHRS Investigation Definition Team (Soderblom & et al., 1995). This pipeline consists of a number of steps,

- Diode non-linearities and non-uniformities are removed by consulting compiled tables for the values associated with each of the 500 diodes.
- Photocathode irregularities arise due to the granulation of the photocathode material, and these are accounted for by determining where on the photocathode each photoelectron measured at the diode arose, and then applying the tabulated photocathode response coefficient for each point.
- Vignetting (reduction of brightness at the edge compared to the centre) is corrected across the photocathode.
- Absolute wavelengths are determined for each diode by solving the dispersion equation relating photocathode sample position to wavelength (the appropriate dispersion equation being chosen for the grating in use). A velocity correction is performed to convert the wavelengths into the heliocentric rest frame.¹ For wavelengths above 2000 Å the wavelength is converted to air wavelengths.
- The background counts are subtracted from the spectrum.
- In the case of the echelles, we must divide the flux value by the normalized echelle efficiency to remove the effect of echelle ripple.
- Finally, the absolute flux is calculated by dividing the flux by the tabulated (pre-calibrated) absolute flux coefficients.

The final, calibrated fluxes are accurate to $\pm 5 - 10\%$ (Carpenter *et al.*, 1999). In this work we are concerned with comparing observed and computed spectra, and as such it is necessary to quantify the relationship between the spectrum

¹Interestingly the Doppler shift caused by the orbital motion of the satellite is compensated for during the data-acquisition process.

Table 3.1: Bandpass and wavelength pixel correspondence for each of the optical elements of the GHRS.

Optical Element	Range (Å)	Å per diode
G140L	1100-1900	0.572-0.573
G140M	1100-1900	0.056-0.052
G160M	1150-2300	0.072-0.066
G200M	1600-2300	0.081-0.075
G270M	2000-3300	0.096-0.087
Echelle A	1100-1700	0.011-0.018
Echelle B	1700-3200	0.017-0.034

emitted by an object, and the broadened spectrum observed by the GHRS. This is known as the Line Spread Function (LSF). The LSF for the GHRS gratings describe the instrumental broadening applied to a delta-function spectral feature by that grating. The SSA, which was used in this work, has a Gaussian LSF with a FWHM of ~ 3.7 pixels, and this is independent of grating and wavelength (Gilliland *et al.*, 1992). Table 3.1 contains the wavelength to diode correspondence for each optical element of the GHRS.

In 1997 the GHRS was decommissioned and removed from the HST, replaced by the Space Telescope Imaging Spectrograph.

3.2 Interferometry

In this thesis we have made use of interferometric observations at both radio and optical wavelengths. In this section we will provide a background to the underlying theory of interferometry, and describe the CHARA optical interferometric array, ahead of a more detailed description of our radio interferometric observations in the next section.

3.2.1 Principles of an Interferometer

An astronomical interferometer is an array of two or more telescopes whose light is combined to provide angular resolution equivalent to a single, larger telescope. An N -element interferometer can be treated as $N(N - 1)/2$ two-element interferometers, and as such we will begin by examining this simple case.

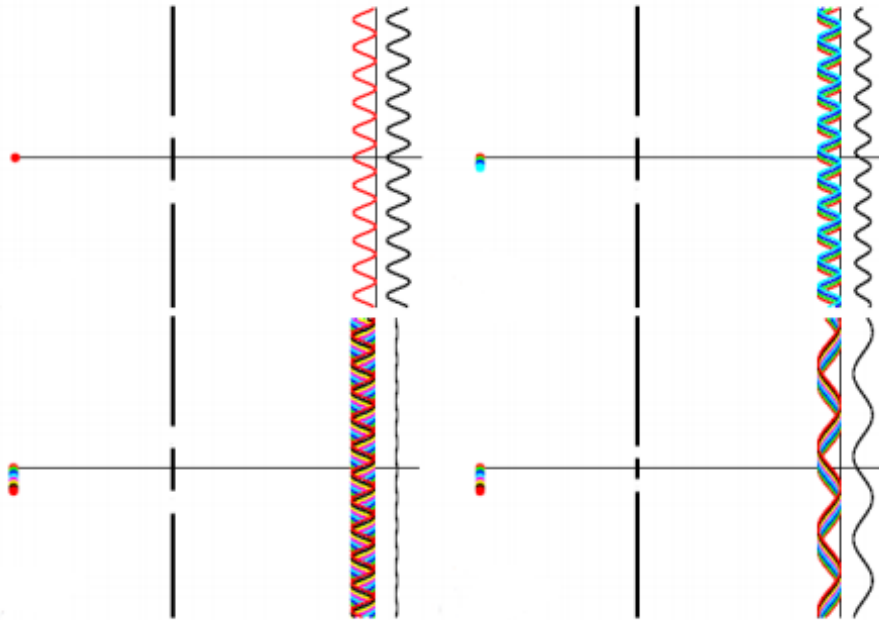


Figure 3.4: Diagram of Young's double slit experiment. On the left-hand side of each image we see the source, and on the right-hand side we see the resultant interference pattern. Note that as the source size and slit separation is varied the interference pattern is modulated. *Image Credit: From Jackson (2008), adapted by E. O'Gorman.*

The two element interferometer is precisely analogous to the Young's double slit experiment. The double slit experiment can be seen in Fig. 3.4. This figure demonstrates a number of key ideas in interferometry. We begin with a point source the light from which passes through the two slits, and we obtain an interference pattern on our detector. This pattern emerges as a result of the different path lengths travelled by the light from each slit in reaching the detector. This causes a phase shift in the wave trains, and hence constructive or destructive interference. This interference is referred to as the fringe pattern in interferometry. We also note that as the source becomes more extended (which we treat as a series of point sources), that the fringe pattern becomes less clear, to the point that we do not see any interference. In the final case we see that reducing the separation of the slits allows us to see the fringe pattern from the more extended source. From

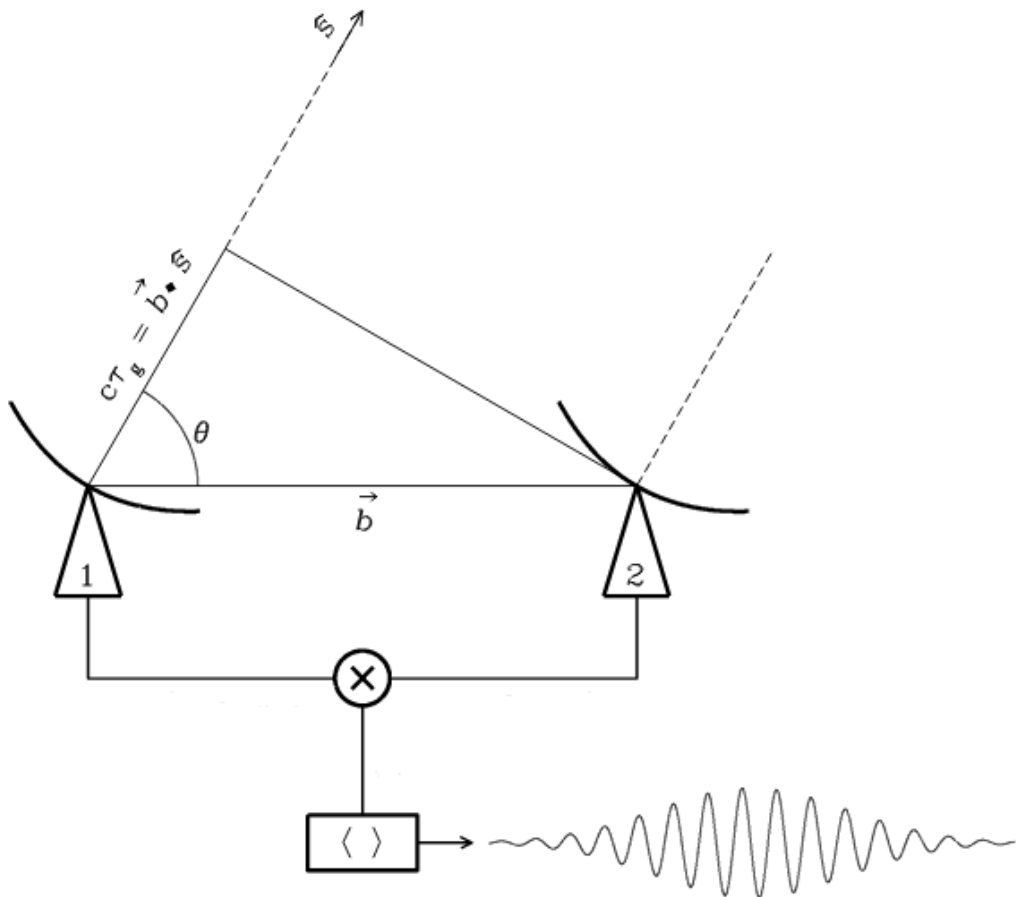


Figure 3.5: Diagram of a two element interferometer. Light enters the two telescopes, labelled 1 & 2, and is combined, resulting in the interference pattern shown.
Image Credit: National Radio Astronomy Observatory.

this we see the spatial resolution to which the fringe pattern is sensitive is inversely related to the separation of the slits,

$$\theta_R = \frac{\lambda}{s} \quad [\text{radians}] \quad (3.2)$$

where θ_R is angular resolution, the minimum angular separation which can be resolved, and s is the separation of the slits.

In Fig. 3.5 we see a diagram of a two-element interferometer, separated by

3.2 Interferometry

a baseline, b . In this configuration the two telescopes are analogous to the slits, and the light from each is combined. In the case that the source is not directly above the telescopes path length of the light to each will be different (by a factor of $b \cos \theta$), causing a fringe pattern (shown in the diagram), as in the double slit experiment. As such, the output of an interferometric instrument is not a direct measure of the magnitude of the incident brightness, but rather a series of fringes of light and dark, corresponding to the interference of the wave trains. This is the principal observable in interferometry, the ratio of maximum to minimum intensity of the fringes, known as the interferometric visibility:

$$V = \frac{I_{\max} - I_{\min}}{I_{\max} + I_{\min}} \quad (3.3)$$

At this point it is convenient to establish a coordinate system for our interferometer. Traditionally the ground coordinates, the positions of the telescopes, are denoted by the coordinates (u, v, w) , where u is oriented East, and v North, and w is the relative height. These coordinates are in units of the observing wavelengths, such that

$$B = \frac{b \cos \theta}{\lambda} = \sqrt{u^2 + v^2 + w^2} \quad (3.4)$$

In the plane-of-sky the coordinates (l, m) are used to describe the brightness distribution, $I(l, m)$, where these are angular coordinates (as we will see they are the Fourier counterparts of (u, w)). In this coordinate system the visibility can be written as

$$V(u, v, w) = \int_{-\infty}^{\infty} \int_{-\infty}^{\infty} I(l, m) e^{-2\pi i (ul + vm + w(\sqrt{1-l^2-m^2}))} \frac{dl dm}{\sqrt{1-l^2-m^2}} \quad (3.5)$$

In the case that the field-of-view, i.e. $|l|$ and $|m|$, is small, and the telescopes are co-planar, i.e. $w = 0$, this equation becomes

$$V(u, v) = \int_{-\infty}^{\infty} \int_{-\infty}^{\infty} I(l, m) e^{-2\pi i (ul + vm)} dl dm \quad (3.6)$$

This is known as the van Cittert–Zernike theorem (van Cittert, 1934; Zernike, 1938), and it states that the visibility measured by an interferometer is the Fourier transform of the brightness distribution on the sky. In our work we will mostly be interested in circularly symmetric objects, and it is useful to recast this equation

in polar coordinates, where θ is the angle coordinate on the sky, ϕ is the angle coordinate on the ground (both with respect to a common reference direction) and,

$$r = \sqrt{l^2 + m^2} \quad (3.7)$$

$$q = \sqrt{u^2 + v^2} \quad (3.8)$$

After some manipulation this gives us (remembering that the source is symmetric in ϕ , and using $\mu = \cos \theta$ as in the previous chapter)

$$V(q) = \frac{1}{A} \int_0^1 I(\mu) J_0(2\pi q R_* \sqrt{1 - \mu^2}) \mu d\mu \quad (3.9)$$

where J_0 is a zeroth order Bessel function. Equations of this type are known as Hankel transforms. Here A is simply a normalising factor, it is the integral evaluated where the $J_0(x) = 1$.

We note that we measure a single visibility for each pair of telescopes, determined by their (u, v) coordinates (other than $u = v = 0$, which returns the flux). In order to reconstruct the brightness distribution by the inverse Fourier transform, we must measure a large number of visibilities. This can be achieved by having a large array of telescopes (recall N telescopes gives $N(N - 1)/2$ unique baselines/pairs), by having an array which can be reconfigured, or by using the rotation of the Earth to alter the projected baseline. This sampling of the (u, v) plane is known as aperture synthesis.

3.2.2 Interferometry with CHARA

The Center for High Angular Resolution Astronomy (CHARA, McAlister *et al.* (2005)) is an optical/near-infrared interferometric array located on Mt. Wilson, California. The array consists of six 1 m telescopes, arranged in Y-shaped configuration (quite common for interferometers, as it provides good (u, v) -plane coverage under rotation while avoiding redundancy), with $(6 \times 5/2 =) 15$ possible baselines. The baselines range from 34 m to 331 m giving a maximum resolution of 1.4 mas at K-Band, and 0.3 mas at V-Band.

CHARA is equipped with three near-infrared instruments (CLASSIC, FLOUR, and MIRC) and two visible, PAVO and the instrument we will be most concerned with in this work, the Visible Spectrograph and Polarimeter (VEGA (Mourard *et al.*, 2009)). VEGA provides spectral resolution up to $R = 30,000$ in the wavelength band 450 nm–850 nm, corresponding to 60 km/s–10 km/s. With this spectrograph it becomes possible to measure the interferometric visibility as a function of a wavelength across a spectral line, hence providing a direct measure of the extent of the line-forming region. We will make use of this diagnostic later in this work.

3.3 Radio Observations

In this work we make use of radio observations taken at using CARMA and APEX. We will describe these instruments in detail in this section, as well as providing details of our observations. All observations in this work were made, reduced, and provided by O’Gorman (2014) (CARMA Proposal Code: c1038, APEX Proposal Code: 094.F-9324).

3.3.1 CARMA

The Combined Array for Millimetre-wave Astronomy (CARMA, Bock (2006)) is a radio interferometer combining the Berkeley-Illinois-Maryland Association array, Caltech’s Owens Valley Radio Observatory, and the Sunyaev-Zel’dovich Array . It is a heterogeneous array of antennae, comprised of nine 6.1 m diameter antennae, six 10.4 m diameter antennae, and the eight additional 3.5 m diameter SZA antennae. The total collecting area of the 15 primary antennae is 772 m^2 , equivalent to a single dish of radius 32 m.

The array observes in two bands, both of which are used in this work, 85 GHz–115 GHz (3 mm), and 215 GHz–270 GHz (1 mm). CARMA is a heterodyne instrument, meaning that the signal which enters the antennae (which is very weak and boosted by a cooled Low-Noise Amplifier), is mixed with a signal from a local oscillator creating a new signal, called the Intermediate Frequency. In interferometry great care must be taken to ensure that the local signals added to the input

Table 3.2: Details of the CARMA observations collected for use in this work.

Name	Date	λ (mm)	Time on Source (min)
α Tau	21.10.2012	3	60
	10.11.2012	1	55
α Boo	19.10.2012	3	70
	30.10.2012	1	96
β And	23.10.2012	3	75
	7.11.2012	1	95
α Cet	15.10.2012	3	240
	6.11.2012	1	130
μ Cet	19.10.2012	3	120
g Her	6.11.2012	3	85

of each antenna be phase locked. This Intermediate Frequency signal is what is mixed and recorded.

The CARMA array is reconfigurable, with 5 possible configurations providing baselines from 8 m to 2 km. In this work we have made use of the D configuration, which is the second most compact, with a maximum baseline of 148 m and a minimum baseline of 10 m. Table 3.2 summarises the observations collected for use in this work. The majority of these observations used planets (Mars, Neptune, and Jupiter) as flux calibrators, providing robust flux calibration.

Images of these objects were computed from the interferometric observations, using the CASA data reduction software package (McMullin *et al.*, 2007), and the point-spread function was deconvolved using the CLEAN algorithm (Högbom, 1974). The flux densities were then computed by fitting a 2D Gaussian to the resultant image. These data are discussed in detail in the subsequent chapter.

3.3.2 APEX

In this thesis we have also made use of the Atacama Pathfinder Experiment (APEX, Güsten *et al.* (2006)). APEX is a radio telescope located at the Llano de Chajnantor Observatory in the Atacama desert, Chile. The telescope is comprised of a single 12.6 m dish with a surface r.m.s. of $17\,\mu\text{m}$. As the name suggests, the APEX telescope is a prototype for the Atacama Large Millimeter/submillimeter Array (ALMA, Wootten & Thompson (2009)). It is also a pathfinder for the

Table 3.3: Details of the APEX observations collected for use in this work. All observations were made at 345 GHz.

Name	Date	Time on Source (min)
α Tau	16.08.2014	60
α Boo	11.10.2014	30
β Gru	16.08.2014	45
γ Cru	16.08.2014	60

Herschel Space Observatory and the Stratospheric Observatory for Infrared Astronomy (SOFIA) as, owing to the favourable atmospheric transmission at the 5100 m altitude site, it observes a band which has to date been poorly studied. ALMA itself consists of 25 APEX-type antennae. APEX was inaugurated in 2005, whereas ALMA began full operation in 2013.

APEX operates at mm and sub-mm wavelengths, from 0.3 mm–1.5 mm, with its primary instrument being the Large APEX Bolometer Camera (LABOCA, Siringo *et al.* (2009)). In this thesis our observations were made at 345 GHz (869 μ m), with a 50% transmission spectral window of 313 GHz – 372 GHz. The LABOCA instrument is a composite bolometer, comprised of 295 individual superconducting substrates, cooled to \sim 285 mK. The bolometer is designed in to operate in an interesting fashion; where most instruments attempt to eliminate sky noise by switching quickly from the source to a blank sky area close to it — known as chopping — at a frequency higher than the variability scale of the sky noise, APEX (and LABOCA) operates differently. As the bolometer is in fact an array of individual elements, it is possible to have some of the array measure the flux of the source, while the other elements measure the blank sky as the telescope scans over the source. The atmospheric contribution (as well as the instrumental noise) will be strongly correlated in all elements and hence analysis of this correlation will make it possible to extract the signals of astronomical interest and greatly reduce the noise. As a result high signal-to-noise observations are possible without the need for chopping.

A summary of the observations collected for use in this work can be seen in Table 3.3. These observations were again reduced using the CASA software package, and provided by E. O’Gorman

3.3 Radio Observations

Now that we have provided the mathematical and observational background to the research undertaken in this work we will proceed to describe the research methods and results.

4

Thermal Continuum Millimetre Emission from non-dusty K and M Giants

In this chapter we discuss the thermal free-free millimetre fluxes expected from the chromospheres of non-dusty K to M giants. In order to compute these fluxes a simple, semi-analytic model is presented. This model, based on our knowledge of the thermodynamic properties of the chromospheres of these objects, along with some simplifying assumptions, is compared with archival flux densities of a large number of late-type stars. By extension of this simple model better agreement can be reached with the existing data. This model is in good agreement with high signal-to-noise observations made with APEX and CARMA, and provided by (O’Gorman, 2014). The extended model can also be used to predict the distribution of intensity across the disk of the object, providing a prediction to be compared with future high resolution interferometric observations. The original radio model is outlined in Harper *et al.* (2013).

4.1 Introduction

Essentially all cool stars possess an atmosphere comprised of material heated above the prediction of radiative equilibrium, the chromosphere. Convective motions beneath the photospheres of these objects agitate the plasma, leading to the excitation of acoustic waves as well as large and small scale magnetic fields. These mechanisms induce the non-radiative heating of the upper photosphere and chromosphere. The roles of acoustic and magnetic waves in heating the chromosphere is the subject of considerable debate (Ayres, 2002; Kalkofen *et al.*, 1999; Vecchio *et al.*, 2009). One line of argument is that the basal heating of the chromosphere arises from the deposition of purely acoustic shock energy generated in the sub-photospheric convection zone (Ulmschneider, 1991), while the absence of spectroscopic signatures of shocks in the chromospheres of inactive red giants (Judge & Carpenter, 1998b) (particularly CII) suggests a magnetic origin. On the Sun both mechanisms are seen to operate: small-scale transient shock heating in the so-called “K grains” and more steady magnetic heating in the large-scale supergranulation network (Schrijver & Zwaan, 2000).

The structures of chromospheres heated by these two mechanisms are likely to be quite different. The acoustic wave picture mechanism would lead to a 3-D network of shocks that is highly time variable. At a given position the gas temperature would fluctuate as it is shocked, with the mean temperature being cool (Wedemeyer-Böhm *et al.*, 2007). Time-independent 1-D semi-empirical models for the Sun that represent regions of different activity are well established (Fontenla *et al.* 1990; Vernazza *et al.* 1976, 1981). Similar models have been constructed for a few cool stars including active and inactive (non-coronal) red giants. These semi-empirical models are designed to reproduce the time-averaged, disk-integrated UV and optical line fluxes. A characteristic of these models is that they require a temperature inversion in the low chromosphere, $T_{\min} \simeq 0.75T_{\text{eff}}$ (Ayres *et al.*, 1976), gradual temperature rise from the top of the photosphere to the upper chromosphere, and then a very steep rise through the transition region in the case of coronal objects (Harper, 1992; Kelch *et al.*, 1978; Luttermoser *et al.*, 1994a; McMurry, 1999).

One might expect that time-dependent acoustic shock models, which do not feature this gradual increase in temperature with height, would not be capable of reproducing the UV and optical line fluxes observed, however this is not the case. In the UV, $h\nu/kT \gg 1$, and the collisionally excited source function ($S_\nu^{\text{UV}} \propto e^{-h\nu/kT}$) is very sensitive to temperature. As a result, the hot, shocked plasma can dominate the temporally and spatially averaged emission from the atmosphere. Thus it is possible for both acoustic shock and semi-empirical models to produce the same UV fluxes even though the temperature structures are profoundly different (Carlsson & Stein, 1995). However, at mm-radio wavelengths, where the source function depends linearly on the temperature, differences between intermittently shocked and time-independent atmospheres will become apparent. This diagnostic should give a more appropriate estimate of the mean radial electron temperature, which controls the ionization balance. At these mm wavelengths the disk averaged emission will be less affected by the local shock peaks, and can hence be used to differentiate between these two methods of heating.

With this in mind we construct a simple semi-analytic model, based on the time-independent 1-D chromospheric models, and use it to compute the expected radio flux density. This chapter will begin by outlining the simplest iteration of this model, discussing the assumptions made and the calibration undertaken (Harper *et al.*, 2013), then explore the extensions made to this model. We will compare the predictions of this model with previous published of mm-flux densities, and with high S/N mm-flux densities obtained with the Atacama Pathfinder Experiment (APEX) and the Combined Array for Research in Millimetre-wave Astronomy (CARMA).

4.2 Initial Model

4.2.1 Semi-Empirical Constraints on Stellar Chromospheres

In order to construct our semi-analytic model we must calculate the mm-radio optical depth, τ_ν ($\propto n_e n_{\text{ion}} ds$), and to do this we turn to previous studies of red giant chromospheres in order to determine some of the atmospheric parameters

upon which the optical depth depends – the electron density, the temperature, and the path length.

Beginning with the electron density, n_e , we note a feature of many time-independent chromospheric models, that the electron density is, to within a factor of ~ 2 , constant throughout the chromosphere (Ayres, 1979; Harper, 1992). At the temperature minimum, the electron density ($\sim 10^{-4}n_{\text{H}}$) is dominated by (photo)ionized low ionization potential metals; but as the temperature increases through the chromosphere hydrogen gradually becomes more ionized until the top of the chromosphere ($\sim 10^4$ K). The ionization of hydrogen in the chromosphere is a two-step process, hydrogen is first collisionally excited to the $n = 2$ state, before being photoionized by the Balmer continuum. At the top of the chromosphere hydrogen is predominantly ionized, hence $n_e \sim n_{\text{H}}$. This provides us with a useful simplification which we will use in our model.

To compute the value of n_e in the chromosphere we turn to Ayres (1979). Ayres (1979) developed a scaling law for the mass column density at the onset of the chromospheric temperature rise (above T_{\min}) which can be rephrased in terms of the chromospheric electron density, n_e , where atmospheric heating is sufficient to overcome H^- cooling, namely

$$n_e \sim \mathcal{A}_{\text{Fe}}^{1/2} \mathcal{F}^{1/2} g_*^{1/2} T_{\text{eff}}^{5/2} \quad (4.1)$$

where \mathcal{A}_{Fe} represents the abundance of low first ionization potential elements relative to solar, \mathcal{F} is the excess “activity” of a particular star relative to the general T_{eff} scaling. In Ayres (1979), $\mathcal{F} = 1$ was taken to represent levels appropriate to inactive stars or the Quiet Sun, and $\mathcal{F} = 10$ for solar plage regions or (fast rotating) stars showing enhanced activity.

To determine the relative enhancement for a given object we consider the ratio of a star’s measured Mg II h & k flux to the *basal-flux*, i.e., a basal-flux star has $\mathcal{F} = 1$. For this work we use the V–K-based expression for the basal-flux ($\text{erg cm}^2 \text{s}^{-1}$) from Pérez Martínez *et al.* (2011),

$$\log F_{\text{basal}} = 6.78 \log T_{\text{eff}} - 19.74 \quad (4.2)$$

which has a very similar T_{eff} -dependence to Linsky & Ayres (1978). We have

chosen specifically their V–K form of the basal-flux, it being more temperature sensitive for cool stars. From the work of Pérez Martínez *et al.* (2011) we collect IUE Mg II h & k flux for 177 cool G, K and M giants and supergiants, which we will later use to calibrate the model. However, we make one important remark on these fluxes. In order to compute the surface Mg II h & k flux, which we then use along with F_{basal} to determine the \mathcal{F} , Pérez Martínez *et al.* (2011) apply the expression of Oranje *et al.* (1982), as corrected by Cox (2000)

$$\log \left(\frac{F_*}{F_\oplus} \right) = 0.35 + 4 \log(T_{\text{eff}}) + 0.4(V + BC) \quad (4.3)$$

where V is the V-band magnitude and BC is a bolometric correction,

$$V - K = \frac{1}{1 - 0.283BC} \quad (4.4)$$

$$BC = -\frac{6.75 \log T_{\text{eff}}}{9500} \quad (4.5)$$

So BC is determined from the $V - K$ value, using the above equation, and with that BC the effective temperature is then determined. However Pérez Martínez *et al.* (2011) apply a general reddening correction to their $V - K$ colour of 1 mag/kpc for all objects. This correction only removes systematic errors, and if we assume a representative differential reddening parameter of $E(V - K) = 0.2$ mag for an individual object, this would correspond to a change of $\sim 10\%$ in the ratio F_*/F_\oplus . This introduces a source of uncertainty in the model.

4.2.2 Scale Height & Chromospheric Extent

It is clearly important in the determination of the mm-flux that we know the angular size of the radio source, particularly its ratio, G , to the photospheric angular diameter, i.e., $\phi_{\text{mm}} = G\phi_*$. As we observe at lower frequency the optical depth increases, meaning that we are seeing higher layers of the stellar atmosphere, and hence the object appears more extended.

The ratio of pressure scale-height, H_{pres} , to stellar radius, R_* , is

$$\frac{H_{\text{pres}}}{R_*} \sim \frac{T_{\text{eff}} R_*}{M_*}, \quad (4.6)$$

so red giants with their much larger radii, but near solar masses, have both intrinsically and relatively thicker chromospheres than the Sun. As a result we should expect the giants to have more extended atmospheres. Eclipse observations of ζ Aurigae (discussed in great detail in the succeeding chapters) indicate that the pressure scale height is determined by both thermal and non-thermal components.

$$H_{\text{pres}} = \frac{v^2 + 2k_b T}{2\langle\mu\rangle m_H g_*} \quad (4.7)$$

where v is a turbulent velocity, $\langle\mu\rangle$ is the chromospheric mean molecular mass in hydrogen masses, m_H , and g_* is the surface gravity. We adopt $\langle\mu\rangle = 1.2$ corresponding to a partially ionized hydrogen ($n_e \simeq 0.1n_H$) and surface helium abundance of $n_{\text{He}} = 0.1n_H$.

The semi-empirical one-component model of α Tau (K5 III) (McMurry, 1999) predicts a 250 GHz (1.2 mm) radial optical depth of unity at $R \simeq 1.03R_*$. The apparent angular diameter of α Boo predicted from a semi-empirical model of (Drake, 1985) is $\phi_{\text{mm}} \simeq 1.06\phi_*$, and for g Her (M6 III) $\phi_{\text{mm}} \simeq 1.08\phi_*$ (Luttermoser *et al.*, 1994a). Although there is a trend of increasing fractional chromospheric extension with later spectral type, in later objects the lower T_{eff} , and thus lower chromospheric heating, should lead to a lower n_e and reduced mm-optical thickness. In light of these competing factors we adopt a typical extension of $1.08\phi_*$ (i.e., $G = 1.08$). This assumption, used in the initial published model, will be addressed and refined in later sections as the model is altered.

4.2.3 Millimetre Optical Depth

When hydrogen is partially ionized, free-free (thermal bremsstrahlung) opacity dominates at mm wavelengths. At low temperatures ($T < 6000$ K), ionization of hydrogen is a two stage process: excitation to the $n = 2$ level by electron collisions or scattered Ly α photons followed by photoionization by the optically thin photospheric Balmer continuum. At higher temperatures, direct collisional ionization becomes important. For the warm chromospheric material in question, in the Rayleigh-Jeans limit, the absorptivity corrected for stimulated emission is

given by Rybicki & Lightman (1979)

$$\kappa_\nu = \frac{0.01772 n_e n_{\text{ion}} Z_{\text{ion}}^2}{T_e^{1.5} \nu^2} g_{\text{ff}} \text{ cm}^{-1} \quad (4.8)$$

where Z_{ion} is the charge of the ions, n_e and n_{ion} are the number densities of the electrons and ions, respectively, and g_{ff} is the free-free Gaunt factor. At mm and sub-mm wavelength the Gaunt factor is

$$g_{\text{ff}}^{\text{sub-mm}} = 24.10 T_e^{+0.26} \nu^{-0.17}, \quad (4.9)$$

as derived using the Gaunt factors from Hummer (1988).

We assume that the majority of abundant species are either neutral or single ionized so that $Z_{\text{ion}} = 1$ and $n_e = n_{\text{ion}}$. This leads to an expression for the mm absorptivity

$$\kappa_\nu = \frac{0.427 n_e^2}{T_e^{1.24} \nu^{2.17}} \text{ cm}^{-1} \quad (4.10)$$

The optical depth of a given increment, ΔL , is $\Delta \tau_\nu = \kappa_\nu \Delta L$.

The assumption that the electron density is approximately constant, as the ionization n_e/n_H goes from $10^{-4} \rightarrow 1$, implies that the hydrogen density has declined by four orders of magnitude and therefore the physical thickness of the layer $\Delta L \simeq 9$ density scale-heights ($e^{-9} \approx 10^{-4}$). To the level of approximation here we set $H_\rho \simeq H_{\text{pres}}$.

For the radial optical depth of the $9H_\rho$ chromosphere we have

$$\Delta \tau_\nu \simeq \frac{0.427 n_e^2}{T_e^{1.24} \nu^{2.17}} \cdot 9 \cdot \frac{2k_b T_e}{\langle \mu \rangle m_H g_*} \simeq \frac{6.4 n_e^2}{T_e^{0.24} \nu^{2.17}} \frac{k_b}{m_H g_*} \quad (4.11)$$

Note that the optical depth is now only a weak function of temperature. The calculation of this optical depth will again be addressed in later sections as the model is altered.

4.2.4 Linear Source Function Method

The key simplification in our semi-analytic model is in the use of the Linear Source Function Method in the calculation of the emergent flux. At radio wavelengths,

in the Rayleigh-Jeans limit, the source function varies linearly with temperature:

$$S_\nu = \frac{2\nu^2 k_b T}{c^2} \quad (4.12)$$

We assume that the temperature increases linearly as a function of radial height through the atmosphere, ΔL , meaning that $S_\nu \propto \Delta L$. As we observed in the preceding section, $\tau_\nu \propto n_e^2 \Delta L$. As n_e^2 is approximately constant throughout this region of the atmosphere, we are left with $\tau_\nu \propto \Delta L$. This means that S_ν is a linear function of τ_ν . In the case that the source function varies linearly in optical depth the integration of the formal solution of the radiative transfer equation can be done analytically by what is known as the short characteristics method.

In our case, the flux, at a given frequency, is linearly proportional to the brightness temperature, T_{Br} , and this is what we will determine from the Linear Source Function Method. T_{Br} is a weighted sum of three temperature parameters, the temperature at the base of the atmosphere, T_{Low} , the temperature above this, T_{Int} , and the temperature at the top of the chromosphere (where the mm optical depth is $\ll 1$), T_{Top} :

$$T_{\text{Br}}(\mu) = \alpha T_{\text{Low}} + \gamma T_{\text{Int}} + \beta T_{\text{Top}} \quad (4.13)$$

and the weighting coefficients are (Olson & Kunasz, 1987b):

$$\alpha = e^{-\Delta\tau} \quad (4.14)$$

$$\beta = 1 - (1 - \alpha) / \Delta\tau \quad (4.15)$$

$$\gamma = 1 - \alpha - \beta. \quad (4.16)$$

From Wiedemann *et al.* (1994) we adopt $T_{\text{Low}} \simeq 0.6 T_{\text{eff}}$ and $T_{\text{Int}} = 4500$ K. The value of T_{Low} is adopted in keeping with observations, in the Sun and in later objects, of CO fundamental bands at $4.6\mu\text{m}$, a CO-mosphere (Ayres, 2002). These observations point to the existence of cool molecular material, with temperatures below T_{min} , and with filling factors close to unity. This cool material will be opaque at mm wavelengths, so this provides the lowest layer of our model atmosphere. We take $T_{\text{Top}} = 10000$ K where hydrogen has become 50% ionized (McMurry, 1999) and any further increase in temperature now leads to a rapid decline in n_e and

Table 4.1: Adopted properties of α Tau.

Quantity	Value	Unit	Reference
Spectral Type		K5 III	
ϕ_*	21.1 ± 0.2	mas	Mozurkewich <i>et al.</i> (2003)
T_{eff}	3871 ± 48	K	Mozurkewich <i>et al.</i> (2003)
[Fe/H]	-0.15 ± 0.20		McWilliam (1990)
$F_{\text{Mg II}}(h+k)$	6.50×10^4	$\text{erg cm}^{-2}\text{s}^{-1}$	Pérez Martínez <i>et al.</i> (2011)
$F_{\text{Mg II}}/F_{\text{basal}}$	1.69		Pérez Martínez <i>et al.</i> (2011)

hence also κ_ν , creating a transparent boundary above T_{Top} .

The stellar flux density can be computed from the integral of $T_{\text{Br}}(\mu)$. We use the plane-parallel approximation in the initial model, and using single-point Gaussian quadrature we can write the brightness temperature as:

$$\langle T_{\text{Br}} \rangle = 2 \int_0^1 T_{\text{Br}}(\mu) \mu d\mu \quad (4.17)$$

$$\langle T_{\text{Br}} \rangle = 2 \sum_{i=1}^n T_{\text{Br}}(\mu_i) \mu_i w_i \quad (4.18)$$

where $n = 1$, $\mu_1 = 1/2$, and $w_1 = 1$.

4.2.5 α Tau Calibration

Next the optical depth expression, Eqn. 4.11, was calibrated. α Tau was used for this calibration, since it is a well studied object with well determined parameters, in order to reduce some of the inherent uncertainties. Using the stellar parameters tabulated in Table 4.1, along with the value of n_e estimated by Robinson *et al.* (1998) from HST observations of the CII] 2325 Å multiplet, $n_e = 10^9 \text{ cm}^{-3}$, we compute an optical depth at 250 GHz of $\tau_\nu = 0.05$. Defining a fictitious star with α Tau's parameters but with solar metallicity, and $F_{\text{Mg II}}/F_{\text{basal}} = 1$, we get $\tau_\nu = 0.04$. This gives us a scalable optical depth, which we note has no explicit gravity dependence:

$$\Delta\tau_\nu(\mu) = 0.04 \frac{A_{\text{Fe}}}{A_{\text{Fe}\odot}} \frac{F_{\text{Mg II}}}{F_{\text{basal}}} \left(\frac{T_{\text{eff}}}{3871 \text{ K}} \right)^{5.54} \left(\frac{\nu}{250 \text{ GHz}} \right)^{-2.17}. \quad (4.19)$$

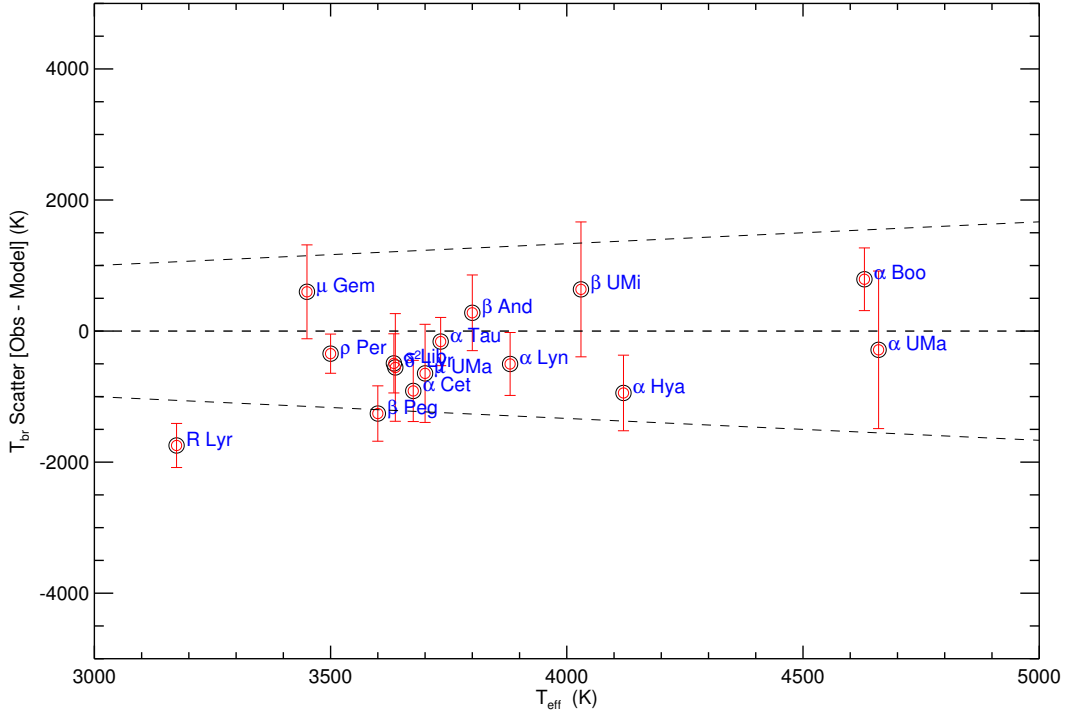


Figure 4.1: Observed minus computed brightness temperatures at 250 GHz. The dotted lines represent $\pm 0.33 T_{\text{eff}}$. Data from the catalogue of Altenhoff *et al.* (1994).

Combining these elements we can compute the brightness temperature at 250 GHz of a collection of objects observed by Altenhoff *et al.* (1994). The results of this calculation can be seen in Fig. 4.1. As we can see the model is generally in good agreement with the data, however there is a scatter of ~ 1000 K, and there appears to be a general trend of overestimation. We will refer to this simple model, published in Harper *et al.* (2013), as Model 1 (M1), and in the coming sections we will discuss additions to this model to improve the flux estimates computed and we will discuss the errors in detail.

4.3 Extensions to the Model

4.3.1 Spherical Geometry

The first alteration made to the model was the adoption of a spherical geometry. Our previous simplification of plane-parallel geometry is only valid in the case that the emitting region is small in extent compared to the radius of the star, an assumption clearly at odds with our adopted extension factor, $G = 1.08$. We cannot use the same methods to compute the optical depth in spherical geometry. This is due to the fact that in general a radiative transfer problem in spherical geometry is not fully characterised without knowledge of the physical extent of the emitting region. It is possible to compute the optical depth of a single scale height, using the expression for optical depth in Section 1.2.3

$$\tau_{\nu}^{H_p} \simeq \frac{k_b \mathcal{A} \mathcal{F} T_{\text{eff}}^{4.4}}{T_e^{0.24} \nu^{2.17} \langle \mu \rangle m_H} \quad (4.20)$$

here T_e is the temperature at a given point in the atmosphere, which, due to it being a very weak power, we will approximate as being ~ 8 ($7000^{0.24} = 8.3$). Though we can determine the optical depth of a single scale height, and we can set the chromospheric thickness to $9H_p$ as before, we cannot determine the extension without knowing the physical extent of a scale height. As a result we must compute the scale height directly from Eqn 4.7, using surface gravity, which will be required as an input to this model.

In spherical geometry, we must take account of two kinds of rays; what we will call “disk rays”, rays which contain a photospheric component, and “grazing rays”, which do not. This can be seen in Fig. 4.2. If we define $\theta_c = R/R_* + 9H_p$, then disk rays are defined as $0 < \theta < \theta_c$, and the grazing rays $\theta_c < \theta < \pi/2$. We must compute the length of the path through the atmosphere, x , for each ray. Beginning with the simpler case of the grazing rays, the length x is:

$$x = \sqrt{(R_* + 9H_p)^2 - \sin^2 \theta (R_* + 9H_p)^2} \quad (4.21)$$

In the case of disk rays this expression is:

$$x = \sqrt{(R_* + 9H_p)^2 - \sin^2 \theta (R_* + 9H_p)^2} - \sqrt{R_*^2 - \sin^2 \theta (R_* + 9H_p)^2} \quad (4.22)$$

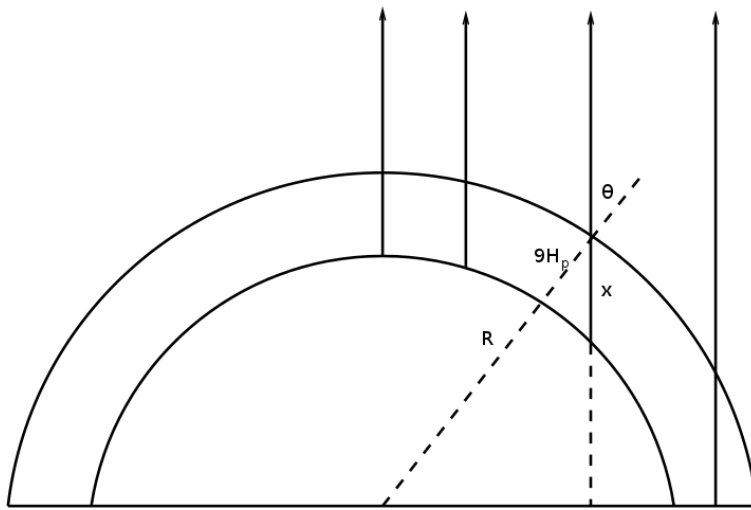


Figure 4.2: Rays in spherical geometry. Note the disk rays, which contain a photospheric component, and “grazing rays”, which do not.

So we can now determine the optical depth along each ray to be:

$$\tau_\nu = \tau_\nu^{H_p} \left(\frac{x}{H_p} \right) \quad (4.23)$$

We use the same linear source function method to compute the brightness temperature, with the addition that the temperature profile of the grazing rays is adapted. The grazing rays will not have the same temperature components as the disk rays, and this is accounted for by having T_{Low} and T_{Int} increase linearly for the grazing ray as the impact parameter of the ray approaches $R_* + 9H_p$. By using spherical geometry we can compute the extension of the star as a function of wavelength. We define the extent of the star by the impact parameter for which the optical depth of a grazing ray drops below 1. This spherical version of the model will be referred to as Model 2 (M2).

4.3.2 Exponential Layer

The model was further adapted by the addition of a layer of exponentially increasing electron density at the base of the atmosphere. This can be seen in Fig. 4.3. In this model we have, between the photosphere and the region of constant n_e from

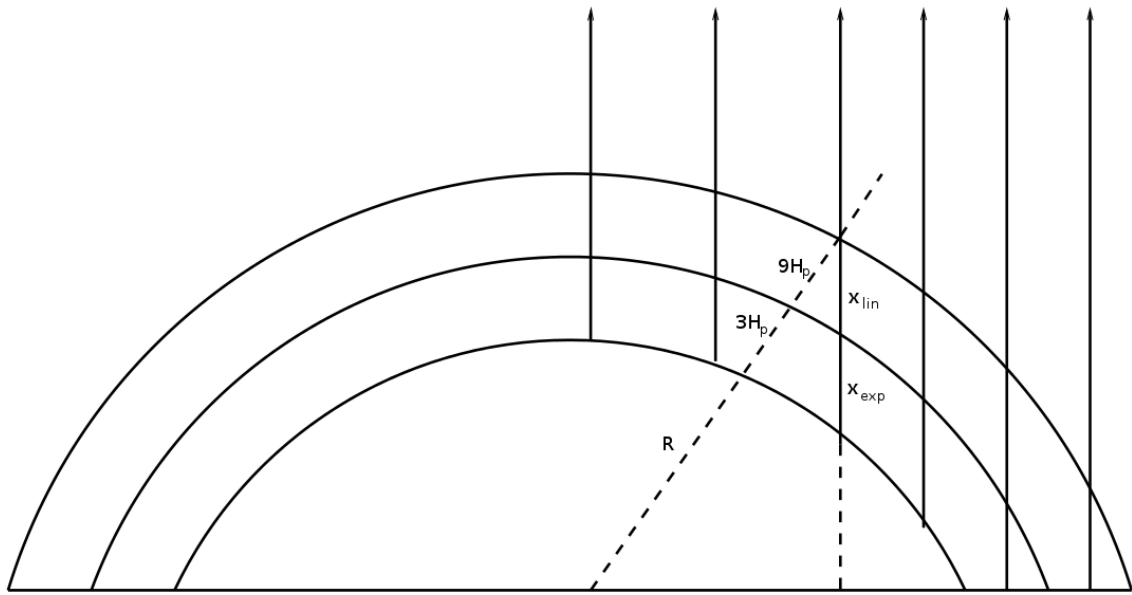


Figure 4.3: Geometry of the atmosphere, featuring the photosphere, with radius R , a layer of exponentially increasing electron density, and the layer of constant electron density.

the previous model, a region $3H_p$ thick where the electron density increases exponentially. This exponential layer was included in order to mitigate the effect of the unphysically sharp interface between the photosphere and the chromosphere in M2. In M2 the situation can arise where the $9H_p$ is optically thin for every grazing ray, and hence we set the radius to the photospheric radius. By including this $3H_p$ exponential layer we ensure that there is always a computed, rather than imposed, radius. We also alter the boundary condition, in that we do not strictly enforce the CO-mosphere as a boundary condition on the brightness temperature. We have the temperature gradient decrease linearly from 8000 K to T_{Low} before increasing, again linearly, to 10000 K at the top of the atmosphere as before. As such, though there is a layer where $T_e = T_{\text{Low}} (= 0.6T_{\text{eff}})$, there is no layer where $T_{\text{Br}} = T_{\text{Low}}$.

In this geometry we have three types of ray; rays with a photospheric component, rays without a photospheric component which pass through both layers, and rays which only pass through the constant n_e layer, much like the grazing rays in

M2. In the first case x_{lin} and x_{exp} , the path lengths in the linear and exponential layers respectively, are:

$$x_{\text{exp}} = \sqrt{(R_* + 3H_p)^2 - \sin^2 \theta(R_* + 12H_p)^2} - \sqrt{R_*^2 - \sin^2 \theta(R_* + 12H_p)^2} \quad (4.24)$$

$$x_{\text{lin}} = \sqrt{(R_* + 12H_p)^2 - \sin^2 \theta(R_* + 12H_p)^2} - \sqrt{(R_* + 3H_p)^2 - \sin^2 \theta(R_* + 12H_p)^2} \quad (4.25)$$

in the second

$$x_{\text{exp}} = \sqrt{(R_* + 3H_p)^2 - \sin^2 \theta(R_* + 12H_p)^2} \quad (4.26)$$

$$x_{\text{lin}} = \sqrt{(R_* + 12H_p)^2 - \sin^2 \theta(R_* + 12H_p)^2} - x_{\text{exp}} \quad (4.27)$$

in the third case

$$x = \sqrt{(R_* + 12H_p)^2 - \sin^2 \theta(R_* + 12H_p)^2} - \sqrt{R_*^2 - \sin^2 \theta(R_* + 12H_p)^2} \quad (4.28)$$

In order to determine the optical depth of the exponential layer we turn to Menzel (1936). In this work Menzel provided a method to calculate the optical depth of a ray travelling tangentially through a spherical atmosphere with an exponentially decreasing density. There are a number of typographical and other errors in the derivation in the literature, and hence the correct derivation is provided here explicitly. A diagram of the ray geometry can be seen below. In an atmosphere of this type the electron density at some height h above the photosphere can be written as:

$$n_e = n_{0e} e^{-h/H_\rho} \quad (4.29)$$

We have the relation:

$$s^2 = (R + h)^2 - (R + h_0)^2 \quad (4.30)$$

$$h = \sqrt{s^2 + (R + h)^2} - R \quad (4.31)$$

Following Menzel's notation we define $a = 1/H_\rho$. The optical depth along our ray,

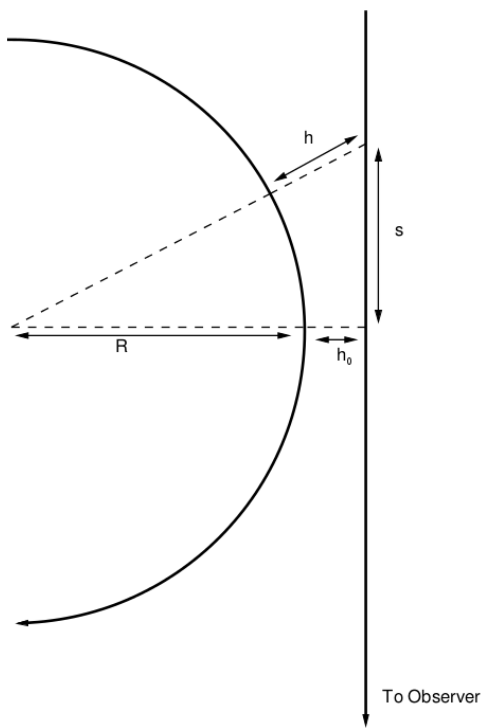


Figure 4.4: Ray passing through the exponential layer.

s , is given by:

$$\tau_\nu = \frac{0.427}{T^{1.24}\nu^{2.17}} \int_0^s n_e^2 ds \quad (4.32)$$

by substitution this integral can be rewritten as:

$$\int_0^s n_e^2 ds = 2n_{0e}^2 \int_0^\infty e^{2aR - 2a(r+h_0)[1 + \frac{s}{r+h_0}]^{1/2}} ds \quad (4.33)$$

To evaluate this integral we set

$$x = s/(R + h_0) \quad (4.34)$$

$$dx = ds/(R + h_0) \quad (4.35)$$

and Taylor expand the $\sqrt{1+x^2}$ term in the exponent we get:

$$= 2(R + h_0)n_{0e}^2 e^{-2ah_0} \int_0^\infty e^{-a(r+h_0)x^2} \left(1 - \frac{1}{4}x^2 + \frac{1}{8}x^4 - \frac{5}{64}x^6 + \dots\right) dx \quad (4.36)$$

This expression is only valid in the limit that $|x| < 1$, though we are integrating over the limits $[0, \infty]$. However

$$\int_0^\infty e^{-Cx^2} dx \approx \int_0^1 e^{-Cx^2} dx \quad (4.37)$$

in the case that $C \gg 1$. In our integral $C = (R + h_0)/H_\rho$, the radius of the object in scale heights, clearly $\gg 1$. As a result we can recast our integral over the domain $[0, 1]$. We will also take only the first term of our expansion. Since this expansion falls away slowly (as $x \rightarrow 1$ the expansion goes to 0.8, so no term will be in error by more than 20%, most will be in error by <5%) and since our function is heavily weighted to values of $x \ll 1$ this approximation will not have a large effect on our result. The approximation gives

$$= 2(R + h_0)n_{0e}^2 e^{-2ah_0} \int_0^1 e^{-a(r+h_0)x^2} dx \quad (4.38)$$

which is a Gaussian integral, and hence we get

$$\int_0^\infty n_e^2 ds = 2n_{0e}^2 e^{-2ah_0} \sqrt{\frac{\pi(R + h_0)}{a}} \quad (4.39)$$

Finally we get an expression for the optical depth

$$\tau_\nu = \frac{0.427}{T^{1.24}\nu^{2.17}} n_{0e}^2 e^{-2ah_0} \sqrt{\frac{\pi(R + h_0)}{a}} \quad (4.40)$$

With this optical depth we now solve for T_{Br} by the same linear method, breaking the exponential layer into increments over which n_e is assumed constant. Again we take care to alter the temperature profile for the grazing rays according to their impact parameter. This model is referred to as M3.

4.4 Calibration and Results

Now that we have outlined the models we will calibrate them using solar observations. This is done in an attempt to reduce the inherent scatter in the model, due to the assumptions made and any unknown biases in the data used. Once the models have been calibrated we will compare them to previous observations.

4.4.1 Solar Brightness Temperature

M2 and M3 are calibrated using two parameters to alter the optical depth, a_1 and a_2 :

$$\tau_{\nu}^{H_p} = a_1 \left(\frac{k_b \mathcal{A} T_{\text{eff}}^{a_2}}{T_e^{0.24} \nu^{2.17} \langle \mu \rangle m_H} \right) \quad (4.41)$$

a_1 allows us to scale the optical depth of a scale height, in effect changing the thickness of the atmosphere, and a_2 allows us to scale the temperature dependence. The a_2 parameter arises from the fact that the relationship of Ayres (1979), Eqn. 4.1, is an empirical scaling relation, derived from observations of the Mg II h & k lines, not an analytic one, and has a scatter of $T_{\text{eff}}^{(5/2)\pm 1}$. Our calibration is performed within these bounds.

Both models are calibrated using the solar data collected in Loukitcheva *et al.* (2004). This paper provides Quiet Sun brightness temperatures for $\lambda = 0.13 - 20.3$ mm. A fit of the model to these data can be seen in Fig. 4.5. We use these data to fit the a_1 and a_2 parameters. Our model is expected to be valid for solar-type stars, since the chromospheric temperature profile is expected to match that of the model. However at lower frequencies where the corona becomes opaque, we would expect to see this hot magnetized plasma.

Gyroresonant opacity in regions of enhanced magnetic field can result in coronal material becoming optically thick, meaning that the coronal material, $T_{\text{Br}} \sim 10^6$ K, will be apparent on the stellar disk. Given the field strength (B , in G) it is possible to compute the gyromagnetic frequency, with emission occurring at harmonics of this frequency:

$$\nu = (2.8 \text{ MHz}) n B \quad (4.42)$$

where n is the harmonic number (Dulk, 1985). From this we see that a field strength of 3 kG, a reasonable value for an active region (Schrijver & Zwaan,

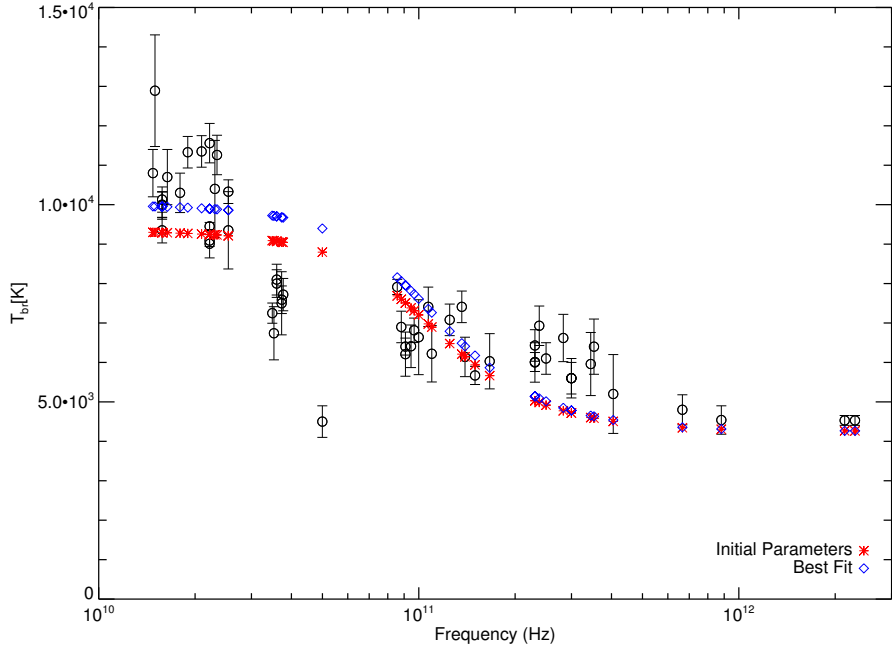


Figure 4.5: A best fit of the M2 model to the solar brightness temperatures of Loukitcheva *et al.* (2004). We see at low frequencies the model fails to reproduce the observations. Best fit values: $a_1 = 1.7$ and $a_2 = 4.55$, Initial parameters: $a_1 = 1$ and $a_2 = 4.4$

2000), would be sufficient to cause gyroresonant emission at 50 GHz from the lower harmonics ($n = 3 - 5$) (Villadsen *et al.*, 2014). It is useful to bear in mind that this emission may well be present in the higher frequency observations we will later examine. At 100 GHz we would see emission from $n = 5$ arising from a field of 7000 G. While this is quite a high field strength, the coronal plasma has a brightness temperature two orders of magnitude above the thermal free-free chromospheric emission, and as a result only a small part of the disk would need to be active for it to have a large effect on the measured flux density.

The model cannot reproduce the coronal brightness temperature, and hence will not be valid for stars to the left of the Linsky-Haisch dividing line with high levels of activity and strong magnetic fields, or active regions on the Sun. We see in Fig. 4.5 that at low frequency the model does not well fit the data; this may be

Table 4.2: The χ^2 and total scatter of the three models for the objects in Table 4.3.

Model	χ^2	χ^2/n	Scatter
M1	82.91	3.77	20006
M2	55.93	2.54	22424
M3	69.29	3.14	19787

due to the effect of the coronal material. This fit provides values of $a_1 = 1.7$ and $a_2 = 4.55$ (with initial parameters of $a_1 = 1$ and $a_2 = 4.4$), which we will adopt for both M2 and M3 going forward.

4.4.2 Stellar Fluxes

The M2 and M3 models were then compared with the flux densities collected by Altenhoff *et al.* (1994). The catalogue of Wendker (1998) was examined for additional objects, however the only suitable observations were made at 50 GHz. The model was found to be unable to reproduce these low frequency observations, perhaps due to the component of gyroresonant emission, described in the preceding section, which may be present at this frequency. This provides a useful indication of the range over which this model is valid. The stellar parameters used in these calculations are presented in Table 4.3. The scatter in the computed flux densities for both models can be seen in Fig. 4.6. The models were computed using the same calibration parameters, $a_1 = 1.7$ and $a_2 = 4.55$, and both were found to have best-fit values in the region $a_1 = 1.6 - 2$ and $a_2 = 4.45 - 4.55$.

In Table 4.2 we present the errors in M1, M2, and M3. We present the χ^2 , given by

$$\chi^2 = \sum_0^n \left(\frac{T_{\text{obs}} - T_{\text{model}}}{T_{\text{err}}} \right)^2 \quad (4.43)$$

the average χ^2 , χ^2/n , and we also present the scatter

$$\text{Scatter} = \sum_0^n (|T_{\text{obs}} - T_{\text{model}}|) \quad (4.44)$$

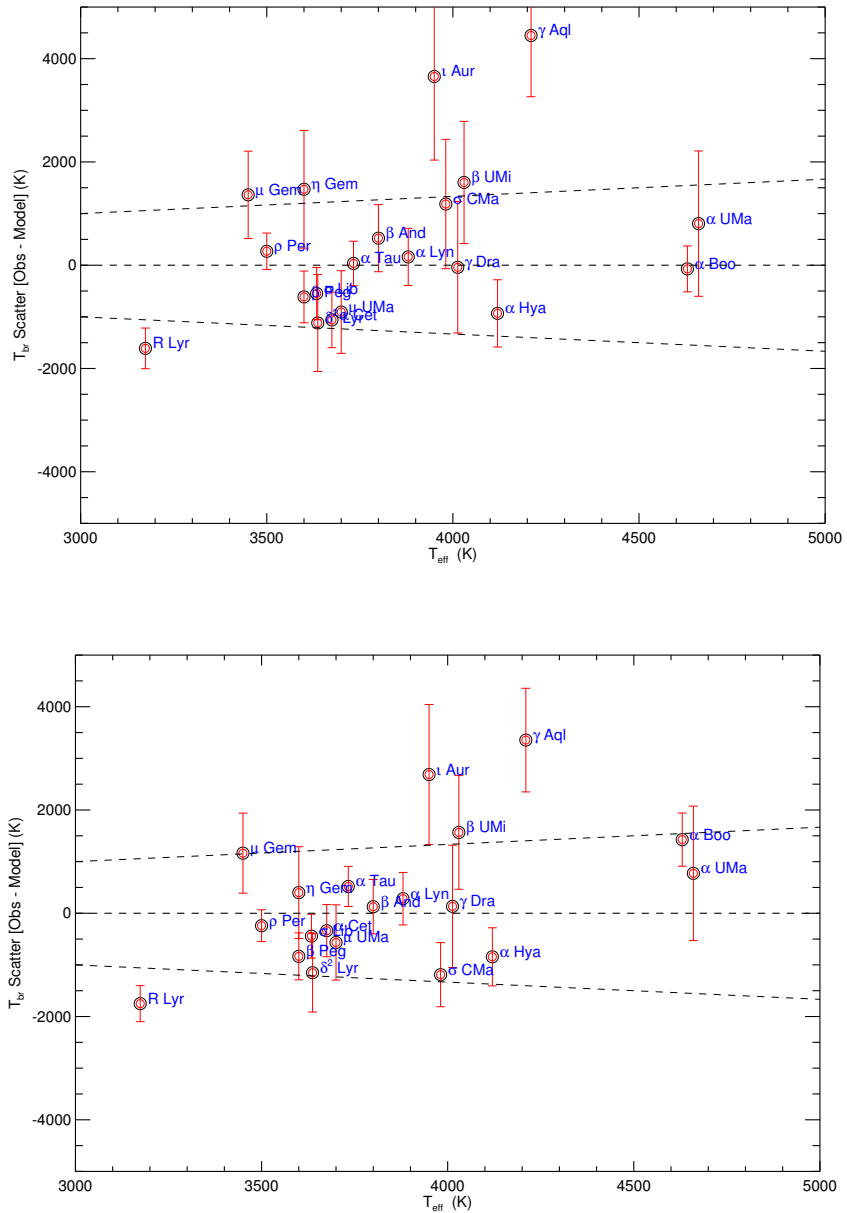


Figure 4.6: Top: Brightness Temperature scatter for the M2 model. Bottom: Brightness Temperature scatter for the M3 model. The dotted lines in both plots represent $\pm 0.33 T_{\text{eff}}$

Note that M1 has the largest χ^2 , and while the χ^2 of M2 is lowest, M3 has the lowest total scatter. In both models, though most particularly in M2, the objects ι Aurigae and γ Aquilae are in error by $\sim 50\%$. There is no clear reason why these two objects should be so greatly underestimated, given that other objects of similar spectral type and effective temperature are well matched, and the error may be attributable to errors in the parameters of these objects. R Lyr is also a clear outlier. The overestimate in the flux density of R Lyr can perhaps be accounted for by its late spectral type. R Lyr is an M5 III object, and there is evidence that the chromospheres of objects of this type are modified by stellar pulsations, which may fundamentally alter their structures (Eaton *et al.*, 1990). Objects of this spectral type are also expected to be highly variable. This provides us with a constraint on the domain of validity of the model. These objects notwithstanding all other objects fall within $\pm 30\%$. This scatter appears to be inherent in the model, resulting from the simplifications made and the errors in the measured parameters – the surface gravity being a particularly large source of error. With the models calibrated and benchmarked, we will now proceed to compare their predictions with high S/N observations made using APEX and CARMA, as well as providing predictions for future observations.

Table 4.3: Stellar parameters and 250 GHz flux densities of objects used to test M2 and M3. The flux densities are from Altenhoff *et al.* (1994), T_{eff} , Fe/H, & $\log(g)$ come from the PASTEL catalogue (bar the marked exceptions)(Soubiran *et al.*, 2010), parallaxes are from van Leeuwen (2007), ϕ from Mozurkewich *et al.* (2003) (bar the marked exceptions), and \mathcal{F} from Pérez Martínez *et al.* (2011)

Name	HD No.	T_{eff} (K)	ϕ (mas)	Parallax (mas)	Fe/H	$\log(g)$	\mathcal{F}	Flux (mJy)	Flux Error (mJy)
β And	6860	3800	13.75	16.52	-0.04	1.5	2.45	25.0	4
α Cet	18884	3675	13.24	13.09	-0.5	0.5	1.73	15.0	3
ρ Per	19058	3500	16.55	10.6	-0.15	0.8	1.7	28.0	3
α Tau	29139	3733	21.1	48.94	-0.1	1.2	1.96	51.0	6
ι Aur	31398	3950	7.5	6.61	-0.18	1.15	1.93	13.0	3
η Gem	42995	3600	11.79	8.48	0.04	1.5	1.81	20.0	5
μ Gem	44478	3450	15.12	14.08	-0.09	1.00	1.75	31.0	6
ϵ Gem	48329	4150	3.38 ^a	3.86	0.20	0.8	1.3	10.0	2
σ CMa	52877	3981	6.94 ^b	2.91	0.16	1.0	2.7	9.0	2
α Lyn	80493	3880	7.54	16.06	-0.26	1.51	1.9	6.0	1
α Hya	81797	4120	9.73	18.09	0.12	1.77	1.52	9.0	2
μ UMa	89758	3700	8.54	14.16	0.00	1.35	2.68	7.0	2
α UMa	95689	4660	6.74	26.54	-0.20	2.46	1.0	6.0	2
α Boo	124897	4200	21.37	88.83	-0.32	1.5	2.7	78.0	8
β UMi	131873	4030	10.3	24.91	-0.29	1.83	1.89	16.0	4
δ^2 Lyr	175588	3637	11.53	4.43	-0.15	0.00	1.9	13.0	4
R Lyr	175865	3174	18.02	10.94	-0.15	0.543 ^c	1.5	14.0	4
α Vul	183439	4750	4.072 ^b	10.97	-0.38	1.4	1.18	14.0	2
γ Aql	186791	4210	7.27	8.26	-0.29	1.63	1.81	13.0	2
β Peg	217906	3600	17.98	16.64	-0.11	1.2	1.6	23.0	5
σ Lib	133216	3634	11.00	11.31	0.00	0.9	2.0	12.1	2
γ Dra	6705	4013	9.86	21.14	-0.08	1.55	1.2	10.1	4

a— value computed from isochrones using PARAM 1. (http://stev.oapd.inaf.it/cgi-bin/param_1.3) (da Silva *et al.*, 2006)

b— value from Lafrasse *et al.* (2010)

c— value computed using radius and an assumed mass of $4M_{\odot}$

4.5 Predictions of the Model

4.5.1 Recent Observations

Table 4.4: *Top:* Stellar parameters of objects recently observed with CARMA, and APEX. The parameters are collected from various sources, as annotated. *Bottom:* The observed flux densities.

Name	HD No.	T_{eff} (K)	ϕ (mas)	Parallax (mas)	Fe/H	$\log(g)$	\mathcal{F}
α Tau ^a	29139	3733	21.1	48.94	-0.1	1.2	1.96
α Boo ^a	124897	4630	21.37	88.83	-0.32	1.5	2.7
β And ^a	6860	3800	13.75	16.52	-0.04	1.5	2.45
μ Gem ^a	44478	3450	15.12	14.08	-0.09	1.00	1.75
α Cet ^a	18884	3675	13.24	13.09	-0.5	0.5	1.73
β Gru	214952	3500 ^b	27.80 ^b	18.43 ^c	0.0 ^d	0.4 ^d	1.0 ^d
γ Cru	108903	3626 ^b	26.37 ^b	36.83 ^c	0.0 ^e	2.0 ^e	1.4 ^f
g Her	148783	3250 ^g	18.4 ^h	9.21 ^c	-0.01 ^g	0.20 ^g	1.0 ^h

^a— Parameters as in Table 4.3 ^b— Engelke *et al.* (2006) ^c— van Leeuwen (2007)

^d— Judge (1986) ^e— Carpenter & Wahlgren (1990) ^f— Pérez Martínez *et al.* (2011) ^g— Soubiran *et al.* (2010) ^h— Luttermoser *et al.* (1994b)

Name	CARMA	CARMA	APEX
	1 mm Flux (mJy)	3 mm Flux (mJy)	345 GHz Flux (mJy)
α Tau	47.6 ± 2.2	13.89 ± 0.32	112.91 ± 12.36
α Boo	51.1 ± 1.8	21.48 ± 0.75	138.97 ± 23.37
β And	14.8 ± 1.2	6.94 ± 0.29	...
μ Gem	...	5.66 ± 0.36	...
α Cet	15.3 ± 1.1	5.15 ± 0.19	...
β Gru	163.59 ± 9.08
γ Cru	132.68 ± 15.87
g Her	...	5.66 ± 0.36	...

Recently observations were made using CARMA and APEX of 8 K and M giants. The CARMA observations were made at two frequencies, 100 GHz and 225 GHz, and the APEX observations were made at 345 GHz. These data were reduced and provided by O’Gorman (2014). The data and the stellar parameters of the targets are tabulated in Table 4.4. The errors included in this table are

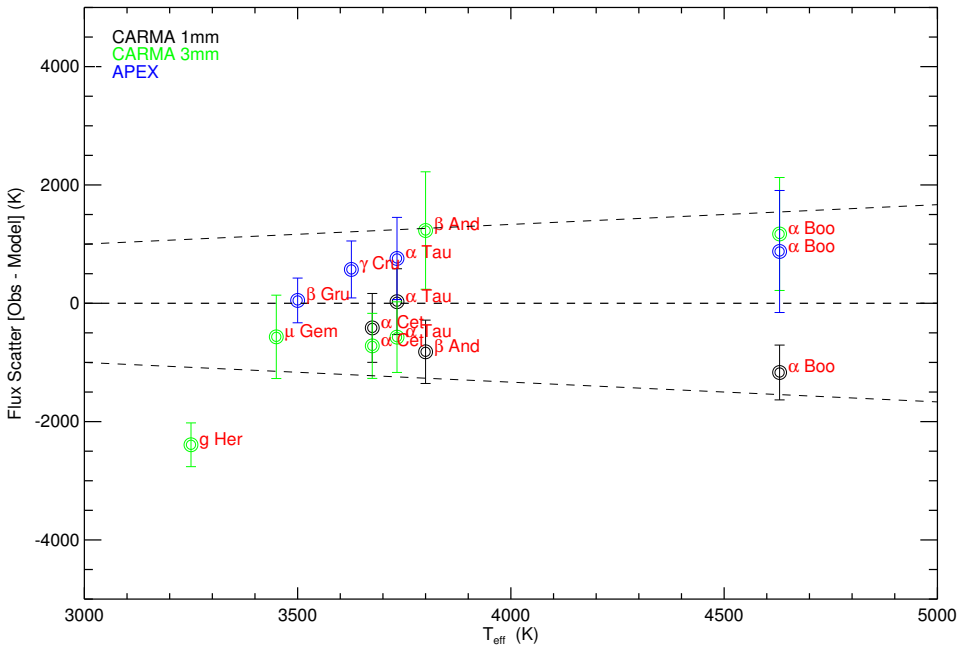


Figure 4.7: M2 model compared with high S/N CARMA and APEX observations. We see that the model again provides a good fit, with most objects falling within $\pm 30\%$ at all frequencies.

1- σ errors and do not include the 10% systematic uncertainty, however all analysis presented hereafter is based on the data with 1- σ errors and the 10% systematic uncertainty due to calibration summed. These data were compared with the M2 model (which we recall had the lowest χ^2), and the results of that calculation can be seen in Fig. 4.7. g Her is a clear outlier in this sample, and this may be accounted for by its spectral type (M6 III), for much the same reasons as R Lyr in the previous sample, noting that Luttermoser *et al.* (1994a) could not construct a time-independent, semi-empirical model for this object.

We see that the model is relatively consistent and reproduces these brightness temperatures quite well, though with the same inherent scatter. It is important to bear in mind that the model may be reaching the limits of its validity for the higher frequency APEX observations (central wavelength = $869 \mu\text{m}$ (Lapkin *et al.*, 2008)). This is another constraint on the model, as we enter the sub-mm/ μm

Table 4.5: Spectral indices from the CARMA observations, and computed from M2.

Name	$\alpha_{1mm-3mm}$	α_{model}
α Tau	1.52 ± 0.33	1.37
α Boo	1.07 ± 0.34	1.60
β And	0.93 ± 0.31	1.47
μ Gem	...	1.27
α Cet	1.34 ± 0.39	1.28
β Gru	...	1.18
γ Cru	...	1.32
g Her	...	1.22

wavelength regime our assumptions may not remain valid. This may be due to bound-free emission-opacity, which are not accounted for in our model, becoming important considerations in the sub-mm regime (Chluba & Sunyaev, 2006). There may be a contribution from dust emission, however the majority of these objects are thought to be relatively dust-free (Sutmann & Cuntz (1995), O’Gorman *et al.* (2013)), and any dust emission would be expected to peak at somewhat shorter wavelengths (peaking closer to 100 μm (Draine, 2011)).

4.5.2 Spectral Indices

The spectral index is the power law exponent which relates the flux density and the frequency; $F_\nu \propto \nu^\alpha$. For an isothermal, non-extended, optically thick atmosphere α will follow the Rayleigh-Jeans tail of the Planck function, $\alpha = 2$, and in the case of an optically thin plasma α will have the same frequency dependence as the Gaunt factor, $\alpha = -0.17$. In a plasma with temperature and density gradients, α will be intermediate between these two values. In reality it is possible to have a value for α which lies outside of this range as a result of the fact that stellar radius varies as a function of frequency. It is due to precisely the effect of seeing a larger, hotter stellar surface at lower frequencies that results in α not simply equalling 2 for the optically thick emission which comprises much of our sample (Kundu, 1965; Newell & Hjellming, 1982).

Spectral indices were computed for CARMA observations and are tabulated in

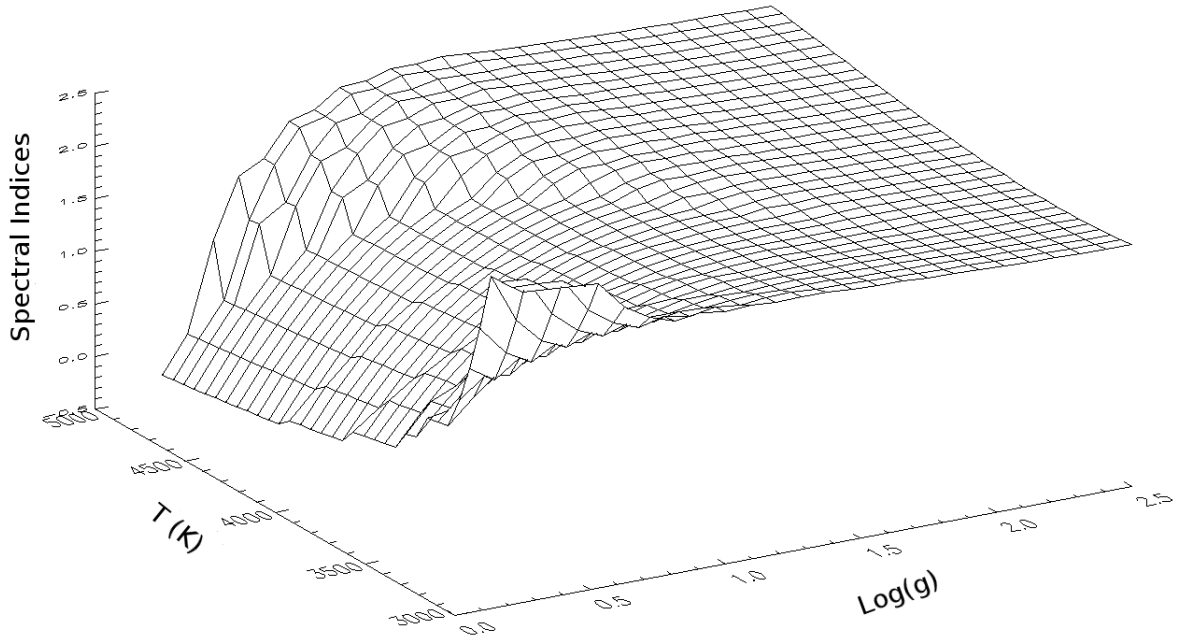


Figure 4.8: Spectral indices, computed at 225GHz and 100GHz, for a range of T_{eff} and $\log(g)$. We see that at high temperature and low gravity the spectral index index matches the optically thin limit, and as $\log(g)$ increases the optically thick case is recovered.

Table 4.5, where:

$$\alpha = \frac{\log_{10}(F_{225}/F_{100})}{\log_{10}(225 \times 10^9 / 100 \times 10^9)} \quad (4.45)$$

The computed values appear to match quite well with observation, indicating that the material probed at different frequencies may have the same temperature variation as our model.

Analytically, we can determine the expected spectral index for given power-law varying temperature and electron density, $n_e \propto r^{-p}$ and $T \propto r^{-n}$ (Sequist & Taylor (1987), O'Gorman *et al.* (2013)):

$$\alpha = \frac{6.2 - 4p + 3.45n}{1 - 2p + 1.35n} \quad (4.46)$$

This relationship was derived for the case of a spherical extended atmosphere. In

our case, where n_e is assumed to be constant, $p = 0$, and T is assumed to be linear in height, $n = -1$. This gives $\alpha = 1.17$, which is generally in agreement with the values measured and computed.

In Fig. 4.8 the values of α returned for a range of T_{eff} and $\log(g)$ are plotted. We can see that our model predicts that for low gravity objects of intermediate temperature α will match the optically thin limit, and as $\log(g)$ increases α reflects the optically thick case. It is interesting to note that this seems to be most strongly a function of $\log(g)$, allowing us to differentiate an object of high gravity from one of low gravity solely by reference to their mm spectral index.

4.6 Summary and Conclusions

In this chapter we presented a simple, semi-empirical model to compute the thermal mm-fluxes from K and M giants. This model was informed by previous semi-empirical atmospheric models of the chromospheres of red giants, coupled with a number of simplifying assumptions. The key assumption is that the source function is linearly proportional to the optical depth, which arises from the fact that the electron density is approximately constant in the chromospheres of these objects. This allows us to solve the radiative transfer equation analytically, and write the observed brightness temperature as a weighted sum of the temperature components of the chromosphere. From these assumptions a spherically symmetric, layered atmospheric model was constructed.

With this model in hand, we made a comparison with the 250 GHz observations of Altenhoff *et al.* (1994). We found the model to be consistent with these data, and we were able to determine the range over which the model appears to be valid. We note that the model overestimates the flux density of later (mid M) type objects, with R Lyr and g Her being clear examples. This is thought to be as a result of the very different chromospheric structure of these objects. We also note that the validity of the model is in question in the case of lower frequency observations. The model was found to be unable to reproduce the flux density of objects observed at 50 GHz (Wendker, 1998). This may be due to the coronal gyroresonant emission at these wavelengths. The model, which we recall is valid in the case of the quiet Sun (and was calibrated using observations of the quiet Sun), also fails to reproduce the

recent observations of Villadsen *et al.* (2014), the first observations of “thermal” emission from solar-type stars. These observations were made using the JVLA, at 34.5 GHz. In the case of τ Cet, a flux density of $25.3 \mu\text{Jy}$ was observed, in comparison with $17 \mu\text{Jy}$ computed by our model, a discrepancy which could be explained by the presence of coronal emission from active regions. At higher frequency, the model appears to be able to reproduce the 345 GHz observations of APEX, with the caveat that as we move to higher frequencies the presence of other emission mechanisms in the sub-mm/far-infrared which are not accounted for in the model, and may lead to inaccuracy. With this considered, the model is found to be valid for objects of type K to mid-M, in the frequency range $\sim 100 \text{ GHz} - 350 \text{ GHz}$, as seen from its comparison to the Altenhoff *et al.* (1994) catalogue, and to the more recent high S/N observations from CARMA and APEX. The model also predicts accurate values for the spectral indices of these objects indicating that the temperature structure probed at different wavelengths may match the linear increase in our model.

Most important to note is that the semi-analytic model presented here is based on time-independent 1-D chromospheric models, and includes all of their inherent assumptions. These models, despite their clear limitations, provide the best available description of chromospheric plasma, and accurately reproduce the optical and UV line emission observed. The capacity of our simple model to predict the observed flux densities at mm-wavelengths, despite the source function’s dependence on temperature being very different in this regime, leads us to believe that the time-independent 1-D chromospheric models provide an accurate reflection of the physical properties of the plasma of the chromosphere. Future observations with ALMA, which will allow imaging of some nearby giants, will be the next test of this model, allowing examination of the disk distribution of flux density (limb-brightening and darkening), and placing constraints on the extension of the emitting regions at these wavelengths.

5

Geometric Modelling of the ζ Aurigae System

In this chapter we discuss modelling the geometry of the eclipsing binary system ζ Aurigae, the construction of an orbital model of the system, and the computation of a synthetic light-curve. This model is constructed to examine periodic emission of neutral silicon observed in the spectra of composite-spectrum binaries. We propose that these features form in the lower chromosphere of the primary due to the irradiation of the secondary. Since this flux illuminates only part of the primary's visible hemisphere at a given phase these lines in effect provide us with spatial information on these otherwise unresolved objects. This unique diagnostic is sensitive to the orbital elements of the system, as well as providing information on stellar properties, for example, the rotational velocity, the local (as opposed to disk-averaged) turbulence. A geometric model of the system yields good agreement with the observed line variation; however a comprehensive radiative transfer calculation is necessary to provide quantitative measures of the emission. The geometric model discussed in this chapter is outlined in O'Riain *et al.* (2015) and Harper *et al.* (2015) (in prep).

5.1 Introduction

ζ Aurigae (K4Ib + B5V) is the eponymous system of a class of detached eclipsing binary systems, which consist of a K supergiant and a hot B-dwarf. Other systems of this type include 31 Cygni, 32 Cygni, and VV Cephei. Non-interacting binaries of this kind provide an opportunity to measure the geometric and atmospheric properties of their individual component stars in considerably more detail than is possible for single stars. Close to its eclipse by the giant the hot secondary acts as a light probe behind the extended chromosphere of the primary and causes the formation of phase-dependent chromospheric absorption lines. When those lines are isolated from the photospheric spectrum of the giant and measured, their variations can provide quantitative information regarding the temperature and density structure of the chromosphere along the lines-of-sight. Furthermore, the information gleaned from the study of these objects, due to the binaries being detached, provides the best constraints on the semi-empirical models of the chromospheres of single stars.

The composite nature of the spectrum of ζ Aurigae, the fact that the spectrum exhibits lines from both a cool and a hot component, has been known since the 19th century (Maury & Pickering, 1897). The observations of Harper (1924) at the Dominion Astrophysical Observatory provided a comprehensive set of radial velocity measurements for the K-star. The orbital elements of the system are also long studied and well determined, with Wood (1951) measuring a period of 972.162 days, and Wright (1970) deriving masses and dimensions for the system. Their values agree well with modern measurement — for instance the period as measured by Bennett *et al.* (1996) is 972.183 days. As a well-studied system with well-determined parameters the study of ζ Aurigae provides useful insight into single stars. Studying the effects of the secondary on the primary provides an invaluable laboratory to examine the atmospheres of late-type stars, and these observations provide useful context for the single star λ Velorum (K4.5 Ib-II), as the primary is a spectral proxy for this object. This parallel will be important in the succeeding chapter as we discuss in greater detail the chromosphere of the K-star.

5.1.1 Spectroscopic Observations

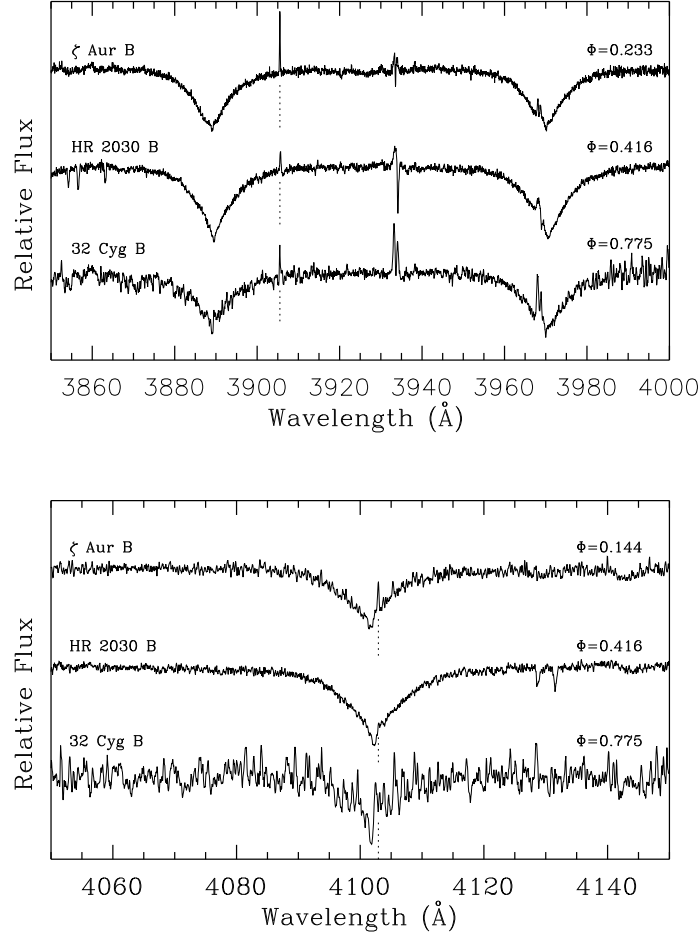


Figure 5.1: Si I in emission in composite-binary systems. The upper panel shows the spectra of three composite-spectrum binaries, with the Ca II K line ($\lambda 3933.7\text{\AA}$) nearly central. Emission appears at $\lambda 3905\text{\AA}$ in the three systems observed at the phases indicated (see Table 5.1). The lower panel shows the emission line at $\lambda 4102\text{\AA}$. It can be seen redward of the core of H- δ , and due to this cannot be measured accurately. It is therefore less useful for quantitative measurements, but its presence is valuable in confirming the identity of the source of the emission. Figure from Harper *et al.* (2015) (REMG).

Due to the diagnostic importance of ζ Aurigae eclipse observations, and with eclipses which are observable throughout the night occurring once every 8 years,

campaigns tend to be clustered around these dates. The eclipse of 1987 was observed in ingress by R. & R. Griffin (Griffin *et al.*, 1990) at high-resolution (2.2 Å/mm) at the Calar Alto Observatory. The same observers, using the same equipment, obtained a spectrum the following year, with the secondary in front of the primary, and discovered (or rather, re-discovered) a strong emission line at $\lambda 3905\text{\AA}$. By subtracting the eclipse spectrum of the primary (Griffin & Griffin, 1986) another emission line was found at $\lambda 4102\text{\AA}$. These two lines were identified as being Si I $\lambda 3905.521\text{\AA}$ and Si I $\lambda 4102.935\text{\AA}$.¹ The line at $\lambda 3905\text{\AA}$ arises from a transition from the (singlet) $^1\text{P}_1$ upper level of Si I to $^1\text{S}_0$, whereas the $\lambda 4102\text{\AA}$ line is from the (triplet) $^3\text{P}_1$ upper level to the same lower level; and hence is an intrinsically weaker intercombination line. These same emission features were noted by R.E.M. Griffin in the ζ Aurigae system 32 Cyg (K4Ib-II + B4V) and 31 Cyg (K4Iab+B4IV-V). They were also noted in the system HR 2030 (K0IIb + B8.5V; (Griffin & Griffin, 2000)), a non-eclipsing binary system.

The original discovery of these features can be attributed to Christie & Wilson (1935), who remarked — in a footnote added in press — on a line noted by W.S. Adams in a plate taken of ζ Aurigae on 16th February 1935 (phase 0.09). They mention that the line is seen to “widen and increase in intensity” but detect no other emission features. They attribute the emission line to the irradiation of the primary by the secondary, an interpretation with which our analysis agrees.

In Figure 5.1 we see the spectra of ζ Aurigae, 32 Cyg, and HR 2030, and the emission features at $\lambda 3905\text{\AA}$ and $\lambda 4102\text{\AA}$. Our efforts will focus on the $\lambda 3905\text{\AA}$ line, as the $\lambda 4102\text{\AA}$ line, being blended with the core of H- δ ($\lambda 4102.86\text{\AA}$), is more difficult to use for quantitative measurement. In ζ Aurigae the emission is sometimes strong enough to be seen by eye on the composite spectrum, as was the case when Adams first noticed it. In the other two systems the emission is less strong even at maximum, as can be seen in the figure. The spectra displayed are created by subtraction of the primary. When an eclipse spectrum of the K supergiant is subtracted from the composite spectrum, the spectrum of the hot star is revealed, together with any other features that were recorded in the composite spectrum but not seen in total-eclipse.

¹These are both air wavelengths, the vacuum wavelengths are $\lambda 3906.629\text{\AA}$ and $\lambda 4104.094\text{\AA}$.

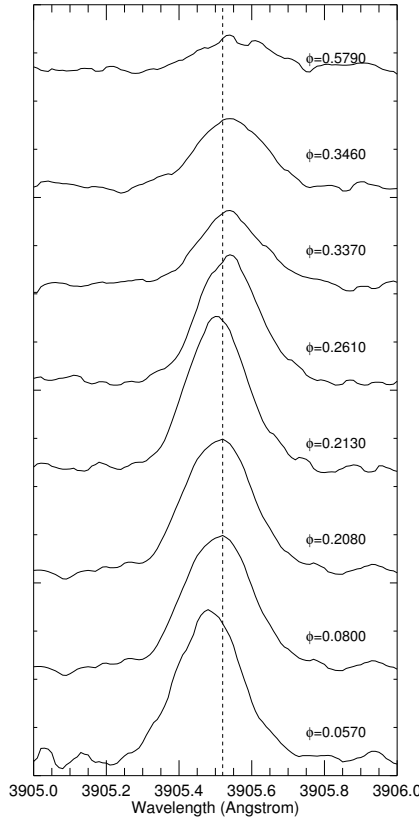


Figure 5.2: Line profiles of the Si I $\lambda 3905\text{\AA}$ obtained at several different phases, ϕ , where ϕ is the fractional orbit elapsed from periastron, which occurs shortly after second contact of the secondary's eclipse. They are offset vertically for clarity. The phase dependency of the line can be clearly seen.

The database of observations of the $\lambda 3905\text{\AA}$ region used in this analysis, provided by R.E.M. Griffin, includes several high-dispersion spectra each of ζ Aur and 32 Cyg, and HR 2030. Four different instruments were involved in these observations: the Mount Wilson 100" telescope and coudé spectrograph (used photographically), the Calar Alto 2.2 m telescope and coudé spectrograph (f/12 and f/3 systems, both used in photographic mode), the Lick 120" CAT telescope and Hamilton coudé echelle spectrograph + CCD, and the Dominion Astrophysical Observatory 1.2 m telescope, coudé spectrograph, 96" camera + CCD. There is sufficient observational material on ζ Aur to conduct an analysis of the Si I emission in considerable detail, and this system will be the subject of our efforts. Selected

spectra of ζ Aur are listed in Table 5.1. In total we have 71 spectra, between them covering some 18 cycles of the 972-day orbit of the system, demonstrating that this feature appears over multiple orbits.

In Figure 5.2 we see the line profiles of the $\lambda 3905\text{\AA}$ line at a series of phases. We can clearly see the phase variation of the feature in this figure. In assessing the line profiles we see that:

1. The flux of the Si emission is phase dependent, being visible from the Earth when the face of the supergiant is illuminated by the B star.
2. The width of the emission profile (Doppler width $\sim 15 \text{ km/s}$) implies that the lines are formed deep in the atmosphere of the K supergiant, probably near the temperature minimum. The Doppler widths are above those given by Gray (2008) for the photosphere of an object of this type, $< 10 \text{ km/s}$, and below the chromospheric values measured by Schroeder *et al.* (1990), Eaton (1993), & Wilson & Abt (1954) $\sim 20 - 25 \text{ km/s}$. The wind lines are typically $\sim 50 \text{ km/s}$ and lines formed in the photosphere of the B-star are broadened rotationally, since $v \sin i \approx 200 \text{ km/s}$ for ζ Aur B. Neutral silicon is readily photoionized by the UV continuum of the hot companion shortward of the ground state ionization edge at $\lambda 1521\text{\AA}$. Therefore, the presence of Si I in the K supergiant must necessarily be restricted to depths below which this ionizing radiation cannot penetrate: the upper photosphere.

These facts suggest that the emission in Si I $\lambda 3905\text{\AA}$ and $\lambda 4102\text{\AA}$ originates in the atmosphere of the K supergiant when it is irradiated by the ultraviolet flux of its hot companion, and our analysis is based on this assumption. We propose that the UV radiation of the B-star photoionizes Si I, which, following recombination and a radiative cascade, emits a photon in the singlet and triplet system lines. Since only a fraction of the face of the K-star is illuminated at a given phase this line will be formed in a localized area, or “hot spot”.

The observed spectra of ζ Aurigae will form the focus and motivation of this chapter. In order to examine the phase variation of the emission a geometric model of the binary system was produced, and the reflection effect was simulated. We will begin by discussing the modelling of the orbit, and the calculation of a

5.1 Introduction

synthetic light-curve for this system. We will then discuss the phase variation of the emission, and compare this with the reflection predicted by our model.

Table 5.1: Log of observations of the emission-line region near $\lambda 3905\text{\AA}$ in ζ Aur.

Data source and ID	UT Date	Detector	Recip. Disp. ($\text{\AA}/\text{mm}$)	Phase	Estimated EEW (m \AA) [*]
MW Ce 10341	1956 Mar. 18	Kodak IIa-O	10	.011	51 10 21
DAO 19986	1998 Oct. 23	CCD	2.2	.015	49 11 16
MW Ce 12246+12247	1958 Nov. 26+27	Kodak IIa-O	10	.022	83 12 23
MW Ce 10424	1956 Apr. 21	Kodak IIa-O	10	.046	82 10 21
MW Ce 12400+12406	1959 Jan. 17+18	Kodak IIa-O	10	.076	192 11 18.5
MW Ce 12452	1959 Feb. 22	Kodak IIa-O	10	.112	180 12 22
Lick 9011	1991 Feb. 12	CCD	:	.126	101
CA S4539	1991 Mar. 3	Kodak IIa-O	8.8	.145	178 12 21
CA L3980	1988 Sept. 27	Kodak IIa-O	2.2	.233	130 7 14
CA S3985	1988 Sept. 28	Kodal IIa-O	8.8	.233	132 10 15
DAO 9952+10032	1999 Aug. 26+27	CCD	2.2	.332	71 11 16
DAO 10609	1999 Sept. 7	CCD	2.2	.344	62 11 16
DAO 10943+10944	1999 Sept. 13	CCD	2.2	.350	44 4 14
DAO 13783+13989	1999 Oct. 15+18	CCD	2.2	.384	52 5 17
MW Ce 9396	1954 Sept. 15	Kodak IIa-O	4.5	.445	48 10 21
MW Ce 9491	1954 Oct. 15	Kodak IIa-O	4.5	.476	36: 8 15
MW Ce 24156	1984 Mar. 23	Kodak IIa-O	10	.536	34 11 26
CA L4038	1989 Sept. 16	Kodak IIa-O	2.2	.596	34 11 23
MW Ce 10039	1955 Sept. 5	Kodak IIa-O	4.5	.810	9: 4 :
MW Ce 12176+12180	1958 Oct. 17+18	Kodak IIa-O	10	.982	0
MW Ce 10305	1956 Feb. 20	Kodak IIa-O	10	.983	0

*EEW is the equivalent emission width.

Note: This log does not include the large numbers of spectra of both systems observed photographically and with a CCD during phases very close to total eclipse. No emission in the Si line was ever detected in any of those observations.

5.2 Geometric Model & Light Curve

5.2.1 Stellar Parameters & Orbital Elements

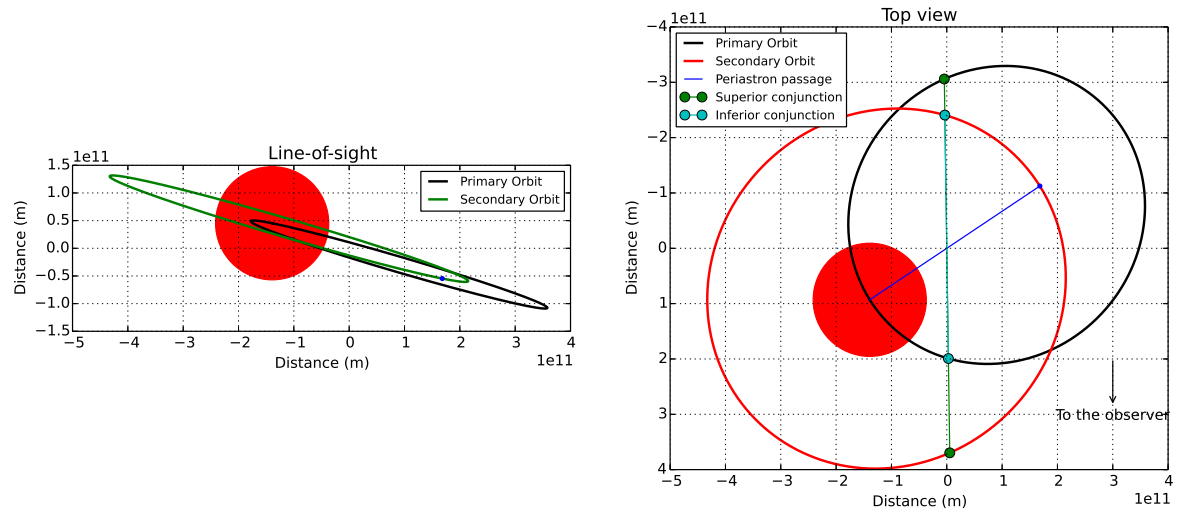


Figure 5.3: The orbits of the ζ Aurigae system. We see the objects at periastron, $\phi = 0$. In the top down plot the inferior conjunction (secondary is eclipsed as viewed from Earth) and superior conjunction (primary is eclipsed as viewed from Earth) are marked. The objects are plotted to scale.

Initially a geometric model of the system was constructed in order to model the orbits of the stars. The model was constructed using the Physics Of Eclipsing Binaries¹ (PHOEBE) suite of code. This is an extension of the widely used Wilson-Devinney code (Wilson & Devinney, 1971). Written in Python, PHOEBE 2.0 builds upon the WD code and provides additional functionality for modelling the light-curves of binary systems (Prša & Zwitter (2005), Degroote *et al.* (2013)).

The model constructed is based on the orbital parameters listed in Table 5.2. The orbital solution produced can be seen in Figure 5.3. The orbital elements used to compute this solution are those of Griffin (2005). The elements tabulated, those of Bennett *et al.* (1996) and Eaton *et al.* (2008), were used to compute light-curve

¹<http://www.phoebe-project.org/>

5.2 Geometric Model & Light Curve

Table 5.2: Orbital Elements and Stellar Parameters of ζ Aur.

	Bennett <i>et al.</i> (1996)	Griffin (2005)	Eaton <i>et al.</i> (2008)
Period (days)	972.183 ^a	972.164 ± 0.041	972.162
Eccentricity	0.37 ± 0.2	0.393 ± 0.0023	0.3973 ± 0.0007
Systemic Velocity (km/s)	12.21 ± 0.07^a	12.11 ± 0.04	10.81 ± 0.01
Longitude of Periastron, ω (degrees)	328.5 ^a	327.5 ± 0.4	328.9 ± 0.13
Passage of Periastron (+JD 2,400,000)	$41,373.6 \pm 1.8^a$	$47,204.8 \pm 0.9$	$53,039.9 \pm 0.1$
Inclination, i (degrees)	87.3 ± 1.0
Semimajor Axis (m)	$6.32 \pm 0.07 \times 10^{11}$
Mass (M_{\odot})			
ζ Aur A	5.8 ± 0.2		
ζ Aur B	4.8 ± 0.2		
Radius (R_{\odot})			
ζ Aur A	147 ± 3		
ζ Aur B	4.5 ± 0.3		
T_{eff} (K)			
ζ Aur A	$3,960 \pm 100$		
ζ Aur B	$15,200 \pm 200$		

^a These values appear in Bennett *et al.* (1996) but are credited to a private communication from R.F. Griffin (1995).

solutions which were found to differ from those computed from the elements of Griffin (2005) by $<0.1\%$.

The stellar parameters adopted are also presented in Table 5.2, those of Bennett *et al.* (1996). In this work the K-star radius is measured by the Mark III optical interferometer at Mt. Wilson. This same instrument is used to measure the dimensions of the orbit. With these dimensions the total mass of the system is computed from Kepler's third law, and the component masses are determined using the mass ratio, as derived from radial velocity measurements. The radius of the B-star is found by fitting a stellar flux model to the flux-calibrated GHRS data. The T_{eff} of the B-star is then determined by fitting the GHRS spectroscopic

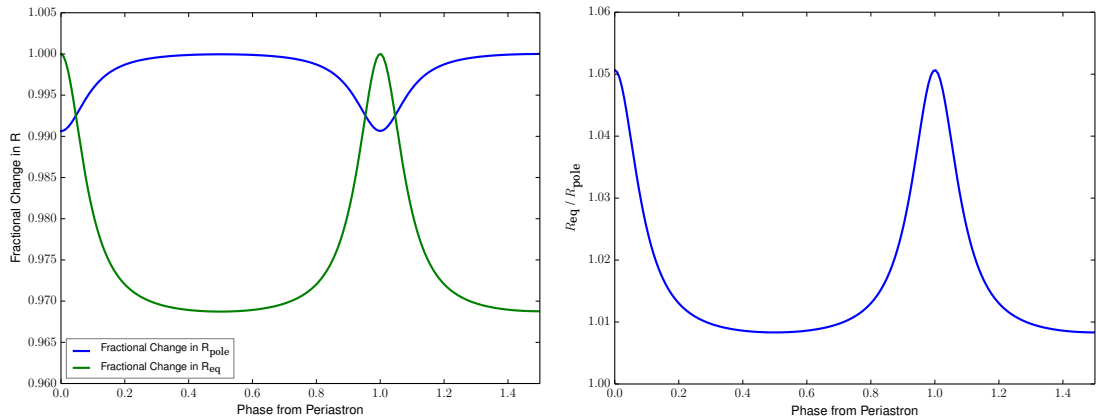


Figure 5.4: *Left:* Fractional change in the K-star equatorial radius, R_{eq} , and the polar radius, R_{pole} , as a function of phase over 1.5 periods. *Right:* $R_{\text{eq}}/R_{\text{pole}}$, demonstrating that even far from periastron the K-star is slightly oblate, with $R_{\text{eq}} = 1.008R_{\text{pole}}$. Note that in the figure on the left both curves are normalised to unity, and in the figure on the right the curve presented is $R_{\text{eq}}/R_{\text{pole}}$ at each phase.

data (Hubeny & Lanz, 1995), using the radius to determine g_* . The K-star's T_{eff} is determined using the measured radius, and the integrated IRAS flux (measured at 12, 25, and 60 μm) and RIJK magnitudes used to compute the bolometric flux at Earth. This provides a mutually consistent set of stellar parameters. These values are in good agreement with those previously published. The T_{eff} of the K-star agrees very well with the survey of McWilliam (1990), who derived a temperature of 3,920 K. Further the measured K-star radius agrees with the value of di Benedetto & Ferluga (1990), who measured the radius to be $154 \pm 13R_{\odot}$ using the I2T optical interferometer. It is important for the analysis to follow, in this and subsequent chapters, that these parameters be reliably known so this agreement is reassuring.

The power of the PHOEBE model is its capacity to take account of the ellipsoidal variation, or tidal distortion, of the K-star. Though this is a detached binary system, around perisastron the gravity of the B-star appreciably distorts the K-star, making it more oblate. This effect greatly influences the light-curve, and is of great importance in accurately modelling the phase dependency of reflection. In Figure 5.4, we see the fractional change of the equatorial radius along the line connecting the centres of the stars, R_{eq} , and the polar radius, R_{pole} . We see

that around periastron R_{eq} increases as the K-star is drawn towards the B-star, and a commensurate decrease in R_{pole} . We also note that even far from periastron the K-star is not a perfect sphere, but is slightly oblate, with $R_{\text{eq}} = 1.008R_{\text{pole}}$. This figure can be compared with a simple distortion calculation:

$$\frac{R_{\text{eq}}}{R_{\text{pole}}} \propto \frac{F_{\text{eq}}}{F_{\text{pole}}} \quad (5.1)$$

$$F_{\text{pole}} = \frac{GM_*}{R_*^2} \quad (5.2)$$

$$F_{\text{eq}} = \frac{GM_*}{R_*^2} - \frac{v^2}{R_*} \quad (5.3)$$

Here we relate the ratio of the equatorial to polar radius with the forces in those directions. The force in the polar direction is simply the gravitational force, and the force in the equatorial direction is the gravitational force minus the centrifugal force. This equates to a ratio of $R_{\text{eq}} = 1.006R_{\text{pole}}$, which is quite close to the value provided by the ellipsoidal variation calculation.

The PHOEBE orbital model presented is in good agreement with observations of this system. In Figure 5.5 we see the agreement between the computed radial velocity of ζ Aurigae A and the values measured by Eaton *et al.* (2008). The model also predicts the phase of mid-eclipse to very good agreement with previous studies, a value of $\phi = 0.92938$, in comparison with the value of $\phi = 0.9294$ given by Griffin (2005).

5.2.2 Synchronicity

In Hut (1981) the concept of pseudo-synchronicity is introduced. A binary system with a circular orbit will tend to an equilibrium where the rotational period matches the orbital period, $P_{\text{rot}} = P_{\text{orb}}$. This is known as tidal locking or a synchronous orbit. In an eccentric system equilibrium is reached where the rotational period is less than the orbital period, and their ratio is determined solely by the eccentricity. This was observed by Hall (1986), and earlier by Boyd *et al.* (1983) in λ Andromeda, and by Shen *et al.* (1985) in α Aurigae. Hut (1981) provides the

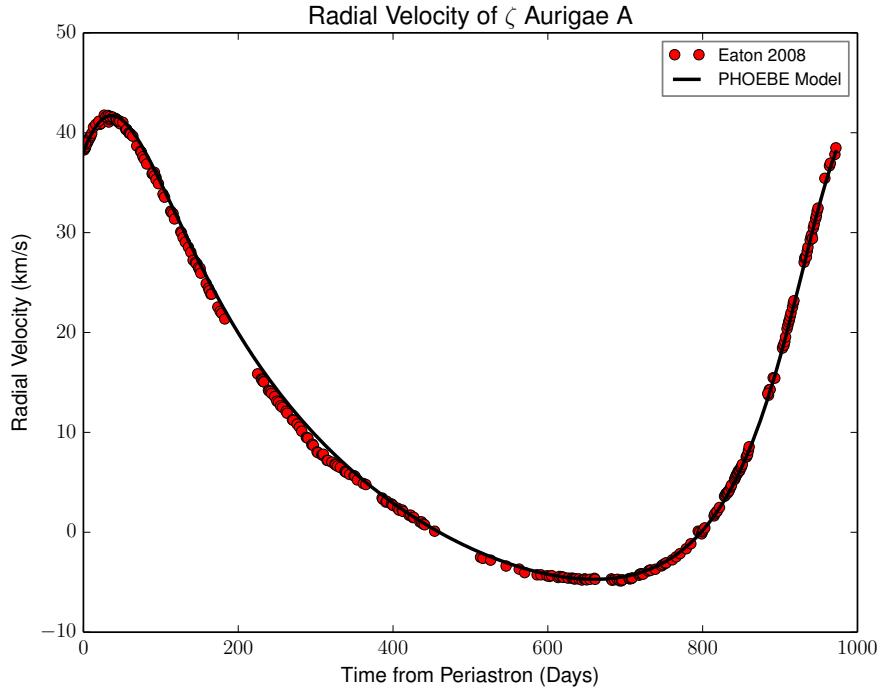


Figure 5.5: Radial velocity curve of the primary of ζ Aurigae. The data presented are those of Eaton *et al.* (2008).

following expression:

$$\frac{\Omega_{ps}}{n_p} = \frac{1 + \frac{15}{2}e^2 + \frac{45}{8}e^4 + \frac{15}{6}e^6}{(1 + 3e^2 + \frac{3}{8}e^4)(1 + e)^2} \quad (5.4)$$

where Ω_{ps} is the rotational angular velocity of pseudo-synchronization, n_p is the orbital angular velocity at periastron, and e is the eccentricity. n_p can be written in terms of the mean orbital angular velocity n ,

$$n_p = \frac{1 - e^2}{(1 - e^2)^{3/2}} n \quad (5.5)$$

In the case of ζ Aurigae $n_p = 2.53n = 1.89 \times 10^{-7}$ rad/s. This means that $\Omega_{ps} = 0.803n_p \rightarrow v_{rot} = 15.5$ km/s. This corresponds to $P_{rot} \approx P_{orb}/2$.

Hut (1981) also provides a time scale for pseudo-synchronization:

$$t_{ps} = \frac{1}{3(\alpha - 3)} T^* \quad (5.6)$$

$$T^* = (kq(1+q))^{-1} \left(\frac{a_o}{R_*} \right)^8 T \quad (5.7)$$

$$\alpha = \frac{1}{r_g} \left(\frac{q}{1+q} \right) \left(\frac{a_o}{R_*} \right)^2 \quad (5.8)$$

where k is the apsidal motion constant (here assumed to be of order 0.1; Chandrasekhar (1933), Brooker & Olle (1955), Lecar *et al.* (1976)), q is the mass ratio, a_o is the semimajor axis, R_* is the radius of the primary, T is the period, and r_g is the radius of gyration, given by $I = M_* R_*^2 r_g^2$ where I is the moment of inertia. With these equations we can estimate the order of magnitude of the time scale for pseudo-synchronization to be 10^6 yrs. Given the age of this system, 8×10^7 yrs (Bennett *et al.*, 1996), we might expect pseudo-synchronicity. However, the parameters used to compute this time scale are not constant over the life of the binary system (R_* being a clear example), and so this time scale may be misleading.

The rotational velocity computed from the pseudo-synchronous model is very large, larger than the value of 8.5 ± 0.14 km/s found by Griffin (2005) by measuring the velocity shift of spectral lines formed in the chromosphere with respect to the photosphere in the rest-frame of the K-star, and the values of ~ 9 km/s found by Gray & Toner (1987) for Ib supergiants. De Medeiros *et al.* (2002) find a value of $v \sin i = 6.9 \pm 1$ km/s for ζ Aurigae A, comparable to the value of $v \sin i = 5.6 \pm 2$ km/s for λ Velorum (de Medeiros & Mayor, 1999). Eaton *et al.* (2008) argues that a rotational velocity this large would lead to measurably broader, shallower lines (Eaton, 1995), however his observations, with $R \sim 30,000$, may not have sufficient resolving power to definitively measure this effect. Hence, a rotational velocity of $v \sin i = 6.9 \pm 2$ km/s is not ruled out by his observations.

We conclude that the system is not rotating pseudo-synchronously, and adopt a synchronicity parameter of 0.5; setting $P_{rot} = P_{orb}/2$. It has been found that the synchronicity parameter assumed does not have a large effect on the light-curve.

5.2.3 Limb-Darkening & Gravity Darkening

To compute a synthetic light-curve for this system intensities from Kurucz model atmospheres¹ were used (Kurucz, 1970), based on the stellar parameters given in Table 5.2. A linear limb-darkening law was applied to the intensities (Milne, 1921);

$$I_\mu = I_{\mu=0}[1 - u(1 - \mu)] \quad (5.9)$$

where u is the limb-darkening coefficient, and $I_{\mu=0}$ is the intensity of the central ray. In the case of the K-star a value of $u = 0.85$ was used, and for the B-star $u = 0.3$. These values are the limb-darkening coefficients of Claret (2000) for the Johnson V-band, taken from observations of field objects.

In addition to limb-darkening, the model must also take account of gravity darkening. von Zeipel (1924) demonstrates that the distribution of intensity across the disk of a star is proportional to the local effective gravity, g_{eff} , and provides us with the expression

$$F_\lambda = -\frac{16\sigma T^3}{3\bar{\kappa}\rho} \frac{dT}{d\Psi} g^\beta \quad (5.10)$$

where σ is the Stefan-Boltzmann constant, T is the local temperature, $\bar{\kappa}$ is the Rosseland mean opacity, ρ is the density of the gas, Ψ is the gravitational potential, and β is the gravity darkening coefficient (Kippenhahn, 1977).

For non-spherical, oblate objects the difference in gravity between the equator and the poles results in the poles having a higher surface gravity and hence brightness. In fast-rotating objects, such as Be-stars, this can be measured by optical interferometry (van Belle *et al.*, 2006). The temperature distribution follows a power-law, determined by the gravity darkening coefficient:

$$T_{\text{eff}}^4 = T_{\text{pole}}^4 \left(\frac{g}{g_{\text{pole}}} \right)^\beta \quad (5.11)$$

For radiative stars, where $T_{\text{eff}} > 8,000K$, $\beta = 1.00$ (von Zeipel (1924), Espinosa Lara & Rieutord (2012)). For cooler, convective stars $T_{\text{eff}} < 5,000K$, $\beta = 0.32$, as first proposed by Lucy (1967), observed in binary systems by Rafert & Twigg (1980), and simulated by Alencar & Vaz (1997). These values were assumed for

¹<http://kurucz.harvard.edu/grids.html>

the B-star and the K-star respectively. As one would expect the gravity darkening parameters have a large effect on the synthetic light curve, and the values selected do indeed provide the best fit to the data.

5.2.4 Light Curve

Using these parameters a PHOEBE model and synthetic light curve was computed for the Johnson V-band. This light curve is shown, superimposed on the orbit, in Figure 5.6. We see that the V-band flux decreases when the hot B-star is eclipsed by the K-star ($\phi = 0.95$), as we would expect. We also see, at periastron ($\phi = 0.0$), a hint of the tidal distortion discussed in Section 5.2.1. This synthetic V-band light curve is compared with the photometric data of Eaton *et al.* (2008) in Figure 5.6.

The light curve computed is in good agreement with observation. With this model in hand we will now examine the phase dependence of the reflection effect in order compare it with the periodic Si I emission observed.

5.3 Reflection Effect

We examined the possibility that the phase dependence of the Si I emission may be due to reflection, but the inadequacy of this explanation can be demonstrated by recourse to the geometry of the system. Following Eddington (1926) we can calculate the magnitude of the reflection effect. Given two stars, their centres separated by a , as shown in Figure 5.7 below, we examine the light falling on, and then re-emitted by, the annulus shown. We assume that all of the light that falls on the annulus will be reflected (re-emitted).

If we take L_1 as the total luminosity of the star on the left, then the amount of light shining on the annulus is:

$$L_{\text{in}} = L_1 \int_0^{2\pi} \sin \psi d\psi d\mu \quad (5.12)$$

$$= \frac{1}{2} L_1 \sin \psi d\psi \quad (5.13)$$

Here we begin with the surface area element $\sin \psi d\psi d\mu$, where μ is the angle around the annulus (out of the page), and integrate for the annular area. The result is

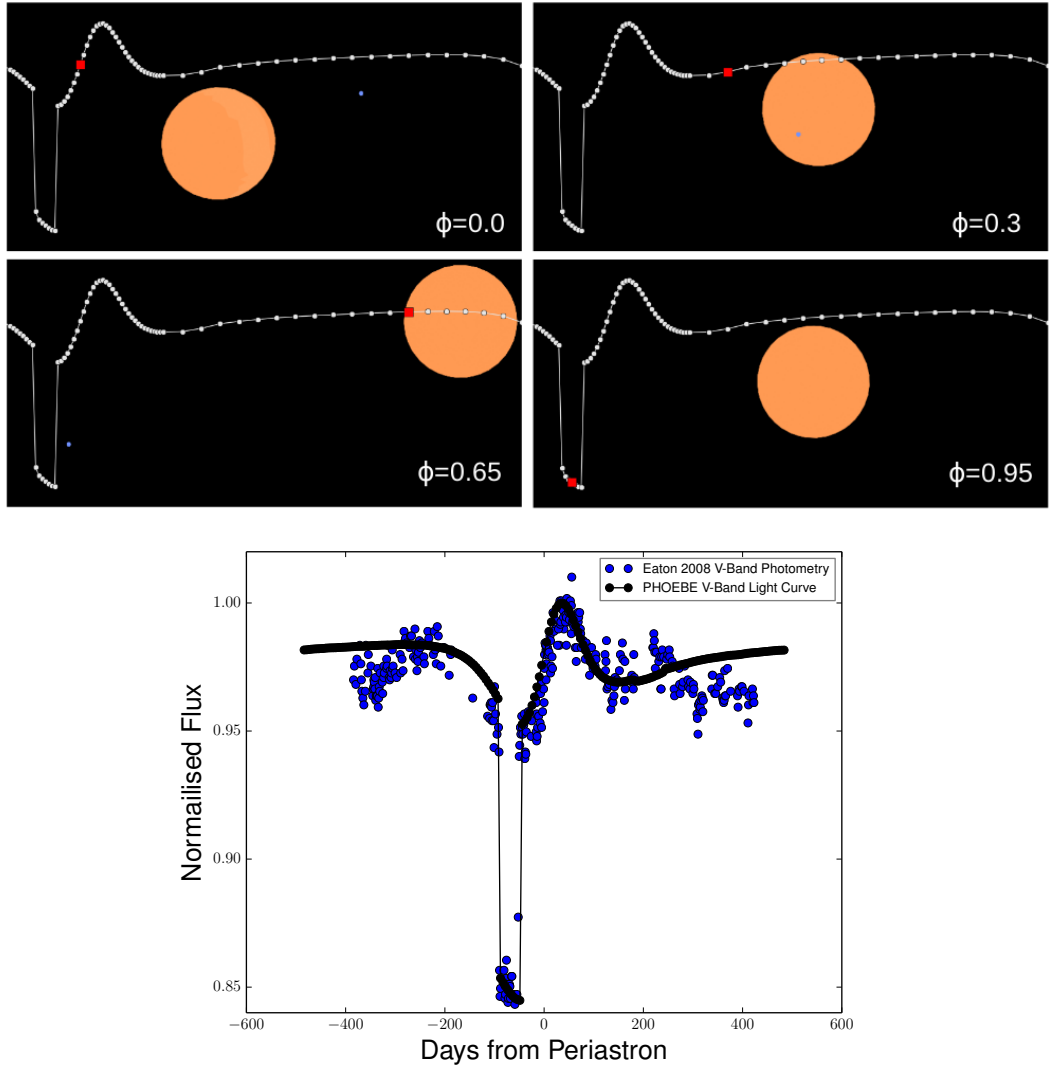


Figure 5.6: *Upper panel:* The orbit of the ζ Aurigae system at various phases from periastron, ϕ , with the Johnson V-Band light curve superimposed. *Lower Panel:* V-Band light curve of the ζ Aurigae system. The PHOEBE synthetic light curve, in black, is in good agreement with the photometric data of Eaton *et al.* (2008).

expressed as a fraction of the total solid angle of the star. By the same method we can get the fraction of the reflecting star's luminosity, L_2 , through the annulus:

$$L_{\text{emitted}} = \frac{1}{2} L_2 \sin \theta d\theta \quad (5.14)$$

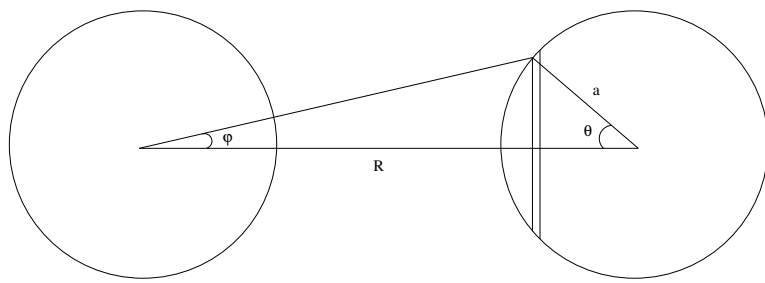


Figure 5.7: Diagram of two stars, separated by a .

To keep the net luminosity through the annulus constant the total luminosity from it must be $L_{\text{emitted}} + L_{\text{in}}$; $L_{\text{in}} = L_{\text{reflected}}$.

To find the luminosity seen by an observer at a great distance (distantly along the line of centres) we multiply the luminosity by $\cos \theta$ (to account for foreshortening) and integrate the annuli. The ratio of reflected radiation to emitted radiation is:

$$\frac{1}{2}L_1 \int_0^{\psi_0} \sin \psi \cos \theta d\psi : \frac{1}{2}L_2 \int_0^{\pi/2} \sin \theta \cos \theta d\theta \quad (5.15)$$

where $\sin \psi_0 = R/a$. ψ_0 is the maximum angles at which reflection will occur.

By taking the triangle defined by R , a , and ψ we see that there are two possible values for θ . We want to find an expression for value which is less than $\pi/2$. To do this we first apply to sine rule, then the cosine rule, and find the roots of the resulting quadratic equation in $\cos \theta$. This gives us the following expression:

$$\cos \theta = \frac{\sin^2 \psi + \cos \psi \sqrt{\cos^2 \psi - \cos^2 \psi_0}}{\sin \psi_0} \quad (5.16)$$

Subbing this expression for $\cos \theta$ into Eqn. 5.15 and performing the integral the ratio becomes:

$$\frac{L_{\text{reflected}}}{L_{\text{emitted}}} = \frac{2}{3} \frac{L_1}{L_2} \left(\sin^2 \psi_0 + \frac{2 + \cos^3 \psi_0 - 3 \cos \psi_0}{\sin \psi_0} \right) \quad (5.17)$$

In the case that the star are separated by a large distance, ψ_0 is small and the

second term of the sum becomes small. In this case we are left with:

$$\frac{L_{\text{reflected}}}{L_{\text{emitted}}} = \frac{2}{3} \frac{L_1}{L_2} \left(\frac{R}{a} \right)^2 \quad (5.18)$$

For ζ Aur $a \sim 6R_A$, giving a flux increase of the order of 1%. The emission in $\lambda 3905\text{\AA}$ and $\lambda 4102\text{\AA}$, being far stronger than this, must therefore be due to a line formation mechanism that channels the radiative energy effectively from the broadband UV flux falling on the K-star into the specific lines observed. Though the reflection argument is inadequate to explain the observed emission, the emission should, however, have the same phase variation as reflection; being dependent only on the separation of the components and the amount of the visible K-star hemisphere being illuminated.

5.3.1 Sobolev Reflection

In order to examine the phase variation of reflection we turn to Sobolev (1975, p. 175). Figure 5.8 outlines the coordinate system that will be in use. α denotes the phase angle, the angle at the reflector between the source and the observer. ϕ and ω are the latitude as measured from intensity equator (the great circle passing through the sub-source and sub-observer points), and the longitude measured from the sub-observer point, respectively.

We also designate the angles $\cos^{-1} \eta$, $\cos^{-1} \zeta$ (which is to say η and ζ are ratios of lengths, not angles), and φ . These angles can be seen in Figure 5.8 (b) & (c). For a given point on the surface of the reflector the angles $\cos^{-1} \eta$ and $\cos^{-1} \zeta$ are the angle between the point, the origin, and the sub-observer point, and the point, the origin, and the sub-stellar point, respectively. Taking a point and the tangential normal plane φ is the angle between the projection on the plane of the vectors to the source and the observer. This is shown in Figure 5.8 (c).

Applying the spherical law of cosines we get the following relations:

$$\zeta = \cos \psi \cos(\alpha - \omega) \quad (5.19)$$

$$\eta = \cos \psi \cos \omega \quad (5.20)$$

The intensity passing through an area element on the surface, into a unit solid

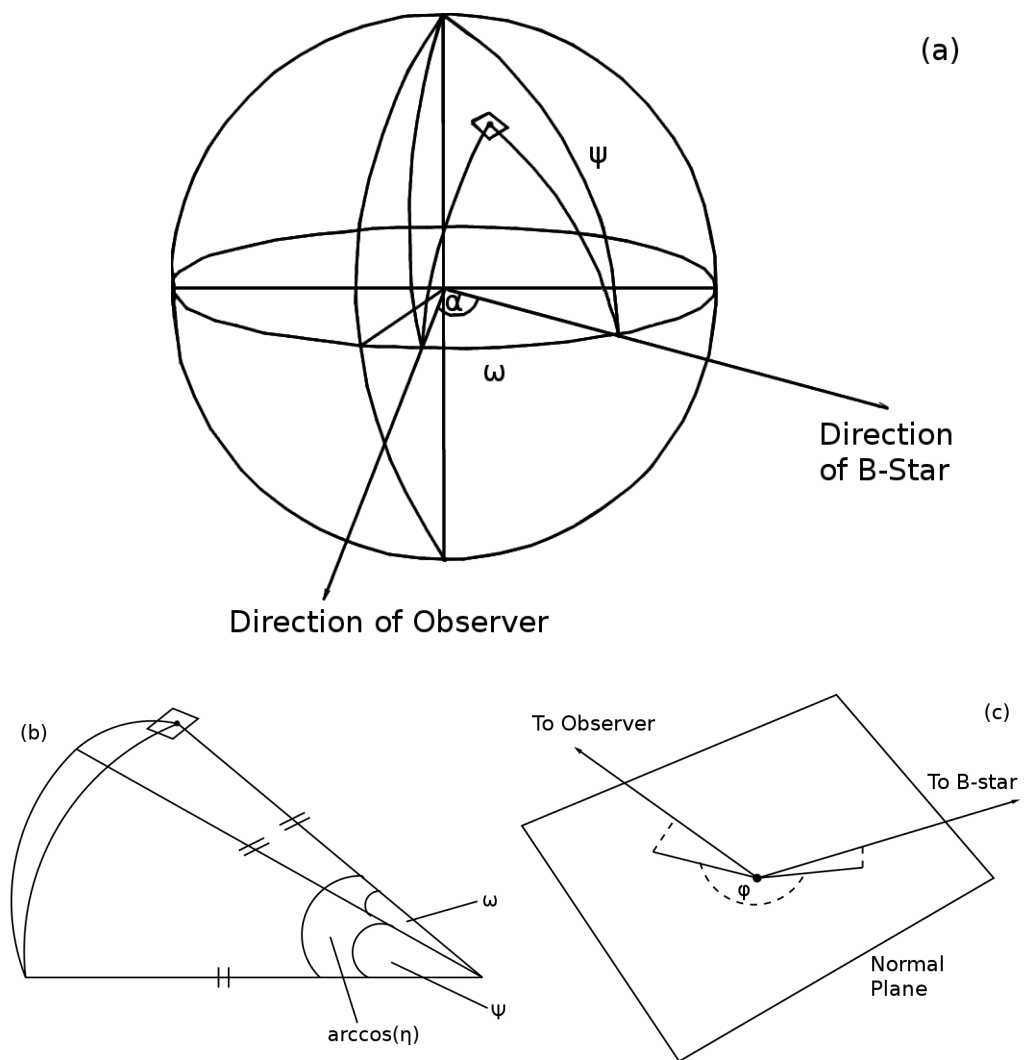


Figure 5.8: Diagrams outlining the coordinate system in use.

angle, will be $Sa_r\eta\zeta d\sigma$. Here πS is the flux through an area at the surface of the reflector oriented perpendicular to the source, ζ is the cosine of the angle between the perpendicular and the reflector, η the cosine of the angle between the reflector and the observer, a_r is the reflection coefficient, and $d\sigma$ is an area element on the reflector's surface into a unit solid angle (assuming the star is spherical this is $R^2 \cos \psi d\psi d\omega$).

Combining these elements we get:

$$R^2 S a_r \cos(\alpha - \omega) \cos \omega \cos^3 \psi d\psi d\omega \quad (5.21)$$

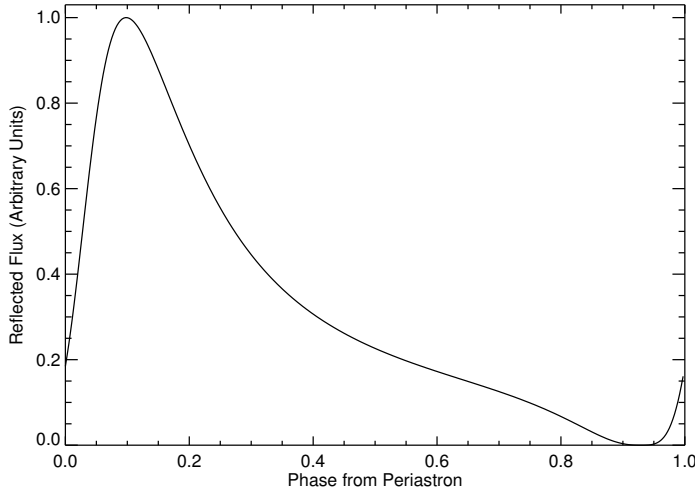


Figure 5.9: Flux reflected from the K-star as a function of phase as predicted by Eqn. 5.25.

In order to get the total flux in the direction of Earth we integrate this expression over ψ between $-\psi_0$ and ψ_0 (note that ψ_0 has the same meaning as in Section 1.3) and over ω between $\alpha - \pi/2$ (the angle of the terminator) and $\pi/2$. this yields:

$$F(\alpha) = 2SR^2a_r \int_{\alpha-\pi/2}^{\pi/2} \cos(\alpha - \omega) \cos \omega d\omega \int_0^{\psi_0} \cos^3 \psi d\psi \quad (5.22)$$

We assume that the reflection coefficient is constant with longitude and latitude. S is the energy falling on an area element perpendicular to the source at a point on the reflector. We could take a simple radial dilution of the B-star's flux (assuming, as Eddington does, that the B-star is a point source) and write this as:

$$S = \frac{\pi F_B}{d^2} \quad (5.23)$$

here d is the distance from the B-star to the point on the surface of the K-star. This can be written, using the same law of cosines as was used to derive relations 2 & 3, as:

$$d = \sqrt{R_K^2 + d^2 - 2dR_K \cos \omega \cos \psi} \quad (5.24)$$

Table 5.3: Sensitivity of the phase variation of the reflection curve to various model parameters.

Parameter	Order of change in phase variation of reflection
Orbital Parameters:	
Bennett 1996 — Griffin 2005	~ 0.1%
K star Radius:	
$147R_{\odot}$ (Bennett 1996)	
$160R_{\odot}$ (Schroder 1990)	~ 0.1%
Stellar Masses:	
$M_B = 4.8 \pm 0.2M_{\odot}$	
$M_K = 5.8 \pm 0.2M_{\odot}$ (Bennett 1996)	~ 0.1%
Synchronicity Parameter:	
$P_{rot} = CP_{orb}$ $C = [0, 1]$	~ 1%
Limb Darkening:	
Gravity Darkening Parameter:	Does not alter the phase variation
	Does not alter the phase variation

This gives us the final relation:

$$F(\alpha) = 2\pi R_K^2 F_B a_r \int_{\alpha-\pi/2}^{\pi/2} \int_0^{\psi_0} \frac{\cos(\alpha - \omega) \cos \omega \cos^3 \psi}{R_K^2 + d^2 - 2dR_K \cos(\alpha - \omega) \cos \psi} d\psi d\omega \quad (5.25)$$

This expression gives the flux reflected from the K-star as a function of phase angle. This is plotted in Figure 5.9. This reflection curve is only valid in the case of a spherical star, and, as discussed in Section 1.2.2, this is not a valid assumption in the case of the K-star. However, we can use the light curve computed by PHOEBE to determine the phase variation of reflection while taking account of the ellipsoidal variation of the K-star.

5.3.2 PHOEBE Reflection Curve

The PHOEBE model allows us to compute a reflection curve which takes account of the oblateness of the K-star. This is done by computing one light curve, like the one in Figure ??, which takes account of reflection, another which does not, and subtracting one from the other. The reflection is Lambertian (directly proportional to the cosine of the angle between the direction of the incident light and the surface normal — isotropic reflectance). We see, in the upper images of Figure 5.10, the

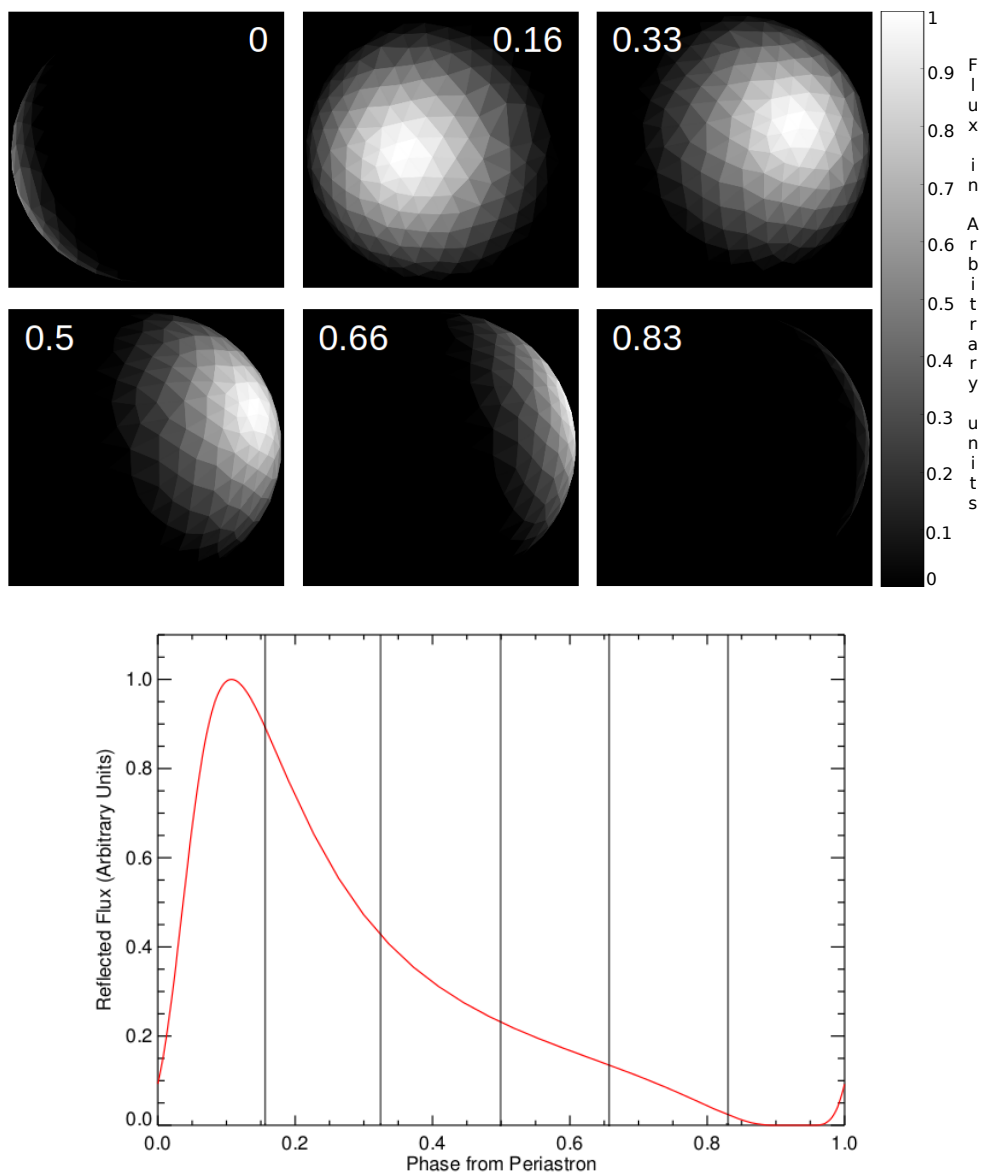


Figure 5.10: *Top:* Six images of the surface of the K-star and the reflected B-star flux. The images show (from top left to bottom right) 0, 0.16, 0.33, 0.5, 0.66 and 0.83 phase from periastron, respectively. *Bottom:* The reflected V-band flux as a function of phase, as calculated by PHOEBE. The black lines mark the phases shown in the above images.

surface of the K-star, and the reflected B-star flux. In the lower plot of Figure 5.10, we see the phase variation of the reflected flux. In Table 5.3 we see the

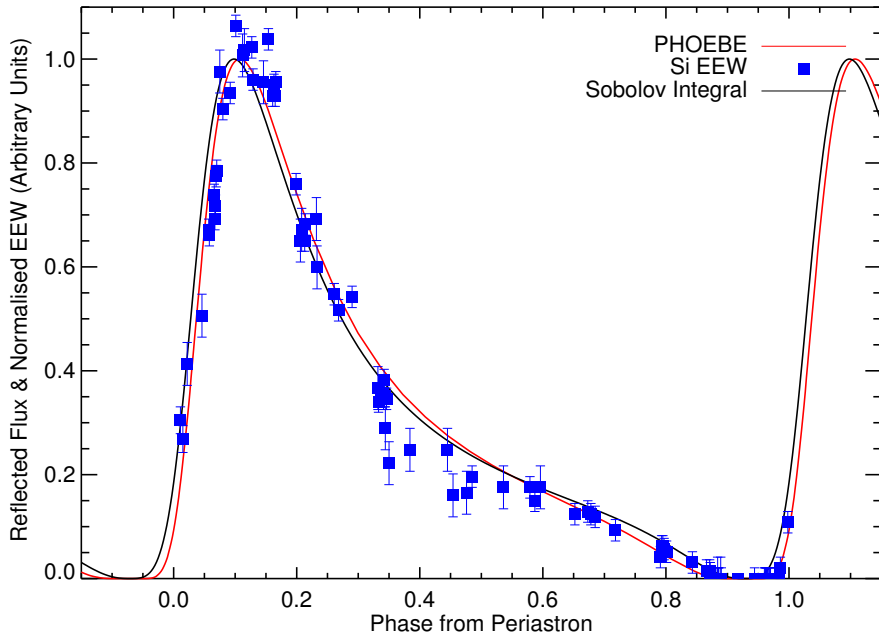


Figure 5.11: PHOEBE model output (red), the Sobolev spherical approximation (black), and the observed Si I EEW (blue).

sensitivity of the phase variation of reflection curve to various model parameters. We stress that the values given only refer to the phase variation of the curve, all of the parameters listed have a large effect on the magnitude of the effect, and on the light-curve itself, however they do not effect the shape of the reflection curve in the same manner.

Figure 5.11 shows the PHOEBE model output, the Sobolev spherical approximation, and the observed Si I EEW. We see that the PHOEBE model is a good fit to the data, and a better fit than the spherical approximation. This is particularly clear in the rise phase. Where the Sobolev integral predicts a rise earlier than we see in the data, this is not present in the PHOEBE model. Discrepancies remain between the PHOEBE model and the data. The data appear to peak more sharply than the model. This may be an effect of the data reduction, however. The two highest points are from photographic plates exposed at Mount Wilson in the 1950's, and if the peaks of the spectrum were over-exposed, the tendency will have been for the calibration to over-estimate their corresponding EEW (Griffin,

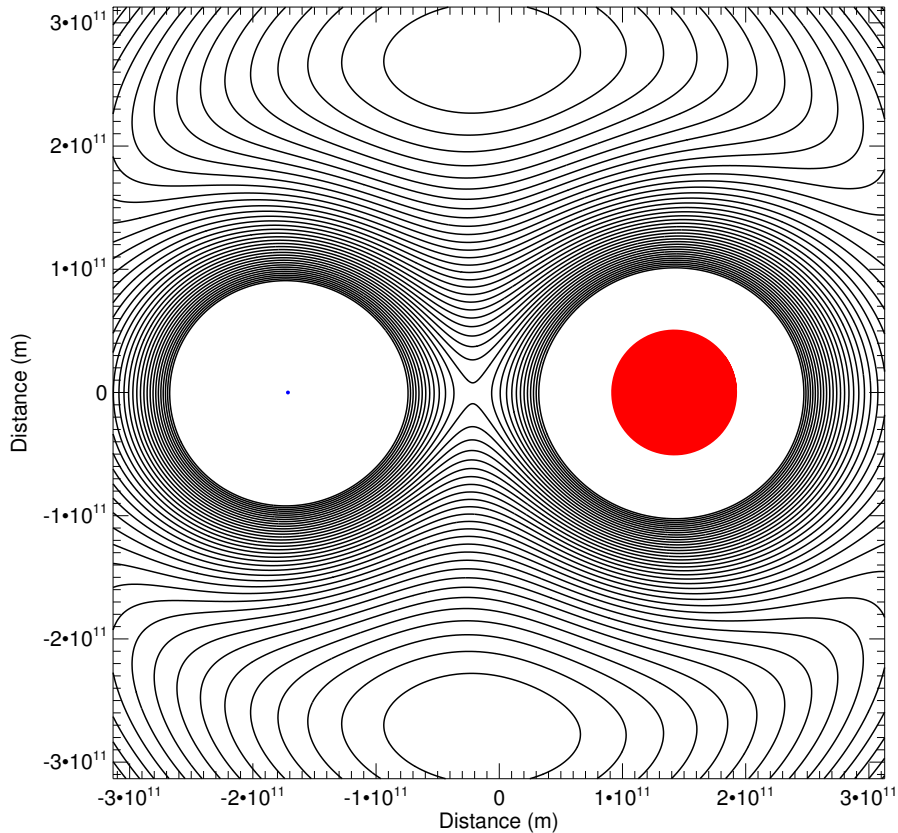


Figure 5.12: Contours of equal gravitational potential for the ζ Aurigae system, a slice through the plane of the orbit. The objects are plotted to scale.

private communication). The dip at ~ 0.35 phase is not predicted. This dip appears across many orbits, and is present in the CCD data. We also note that there appears to be a very small discrepancy between our radial velocity curve and the data at the same phase. We posit that this may be due to excess material collected at the Lagrange point 4 crossing our line of sight. In Fig 5.12 we see the contours of equal potential for the system. We note that, as a result of the objects being of similar mass, L4 and L5, the Lagrange points which lie along the path of the orbit, are very large and extended. L4 will pass between the observer and the primary

at $\phi = 0.45$, which coincides with the dip in the Si I flux. We note that no excess of material was found in the hydro-dynamical modelling of Harper *et al.* (2005), however these models only examined the evolution of the circumstellar environment over two orbits, and given that Lagrange points are stable nulls rather than attractors, this timescale may not have been sufficient to allow for the build up of material.

Other than the discrepancies mentioned above the PHOEBE model provides a good fit to the data.

5.3.3 Line Reflection

We can analyse the reflection effect in greater detail by examining the spectral data. Maintaining our assumption that the Si I lines form on the portion of the visible hemisphere of the K-star illuminated by the B-star, we can determine the velocity of the portion of the K-star where the line is formed by measuring the Doppler shift of the lines, and hence the rotational velocity of the star. In order to construct a simple analytic model we return to our assumption of sphericity, and compute the reflection of a Gaussian line as a function of phase.

We will use a Gaussian line-profile with a turbulent velocity, v_t . Our line profile can be written as

$$I_\lambda = e^{-\left(\frac{\lambda_c - \lambda}{\lambda_t}\right)^2} \quad (5.26)$$

where λ_c is the central wavelength of the line, and λ_t is the turbulent width of the line, given by

$$\lambda_t = (1 + v_t/c)\lambda_c - \lambda_c \quad (5.27)$$

$$\lambda_t = \frac{\lambda_c v_t}{c} \quad (5.28)$$

This gives a line profile of

$$I_\lambda = e^{-\left(\frac{c}{v_t}\left(1 - \frac{\lambda}{\lambda_c}\right)\right)^2} \quad (5.29)$$

Returning to the geometry of Section 1.3.1, for each longitude and latitude, ω

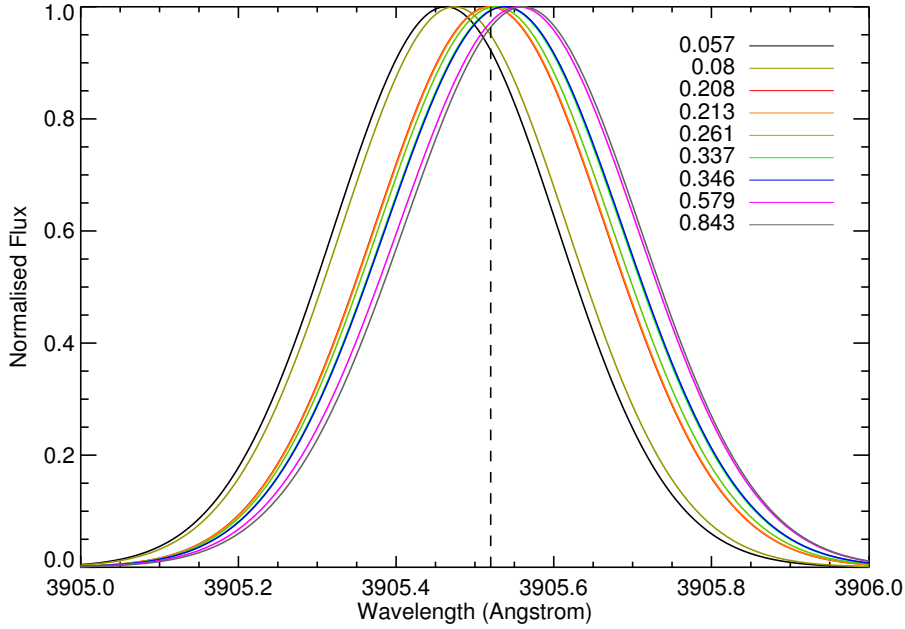


Figure 5.13: Reflected line profiles at given phases for a rotational velocity of $v_{\text{rot}} = 6 \text{ km/s}$. The dotted line represents line centre.

and ψ , we compute the component of velocity in the direction of the observer:

$$v_{\text{proj}} = v_{\text{rot}} \sin \omega \cos \psi \quad (5.30)$$

Then for each point we apply a Doppler shift and compute the intensity from the Gaussian:

$$\lambda_m = (1 + v_{\text{proj}}/c)\lambda_e \quad (5.31)$$

$$I_{\lambda_m} = e^{-\left(\frac{c}{v_t} - \frac{c\lambda_e}{v_t\lambda_c} + \frac{\lambda_e v_{\text{proj}}}{\lambda_c v_t}\right)^2} \quad (5.32)$$

where λ_m is the measured wavelength, and λ_e is the emitted wavelength. This is

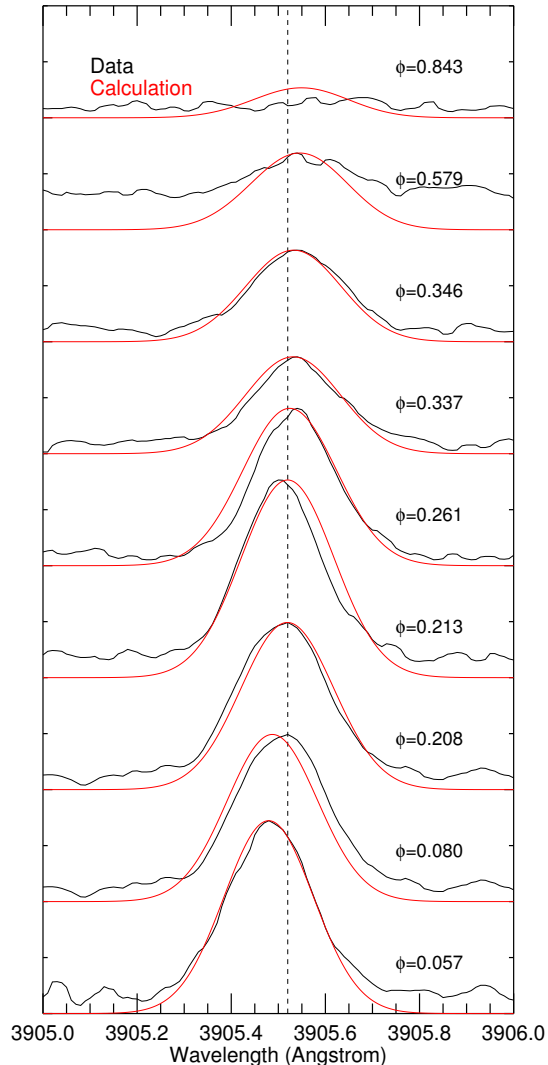


Figure 5.14: Left: Reflected line profiles at given phases for a rotational velocity of $v_{\text{rot}} = 6 \text{ km/s}$ and a turbulent velocity of $v_{\text{turb}} = 10 \text{ km/s}$ overplotted with observation.

then used as a weighting factor for Eqn. 5.25.

$$\begin{aligned}
 F_{\lambda_m}(\alpha) = & \\
 2\pi R_K^2 F_B a_r \int_{\alpha-\pi/2}^{\pi/2} \int_0^{\psi_0} & \frac{\cos(\alpha - \omega) \cos \omega \cos^3 \psi}{R_K^2 + d^2 - 2dR_K \cos(\alpha - \omega) \cos \psi} e^{-\left(\frac{c}{v_t} - \frac{c\lambda_e}{v_t \lambda_c} + \frac{\lambda_e v_{\text{proj}}}{\lambda_c v_t}\right)^2} d\psi d\omega
 \end{aligned} \tag{5.33}$$

This equation gives us the rotationally Doppler shifted line profile at each phase. This is shown in Fig. 5.13. These line profiles were then fit to the spectral data in order to find a best fit for the rotational velocity. The best fit to the data can be seen in Fig. 5.14. This best fit provides values of $v_{\text{rot}} = 6 \text{ km/s}$ and $v_{\text{turb}} = 10 \text{ km/s}$. The lines are all fit with the same v_{turb} , which may not be the case. Since the lines form in a localized spot on the K-star at a given phase they will have a local turbulent velocity, which will vary as the emission moves across the disk. The value of v_{rot} agrees well with the values discussed in Section 5.2.2, however we must be aware of the low resolution and S/N of these data, making the centroid difficult to track, particularly at the intrinsically weak later phases.

5.4 Conclusions

In this chapter we have examined the periodic emission of Si I observed in ζ Aurigae. We have proposed that the phase-modulated emission observed in the $\lambda 3905\text{\AA}$ and $\lambda 4102\text{\AA}$ lines originates in the deep chromosphere of the K-star, and is due to the photoionization and recombination of Si I. This photoionization, being caused by the UV radiation of the B-star, occurs only on the portion of the K-star which is illuminated at any given phase, hence the phase modulation.

The emission cannot be due to simple reflection. As described in Section 5.3 this mechanism is inadequate to account for the strength of the lines, which must be due to a mechanism which effectively channels the broadband UV radiation falling on the atmosphere into these two lines. Despite not being sufficient to explain the strength of the lines, the phase variation should be the same as in the case of broadband reflection; only being dependent on the separation of the two objects and the amount of the visible K-star hemisphere being illuminated. To fully explore this a model of the system was produced, as detailed in Section 5.2. This model agrees well with the known orbital parameters of the system, the radial velocity observations, and the synthetic light curve it predicts agrees well with photometric observation.

With this model in hand the broadband (specifically V-band) reflection effect could be computed, taking account of the distortion of the K-star caused by the gravity of the B-star. This reflection curve is in very good agreement with the

data, and is a better fit than a model which assumes a spherical K-star. There is no appreciable shift between the model and the data as there would be if the “hot spot” from which the emission originates lagged behind the substellar point, i.e. if the Si I recombination timescale was of the order of days. There are a couple of small discrepancies between the model and the data, the most obvious being the dip seen in the data at $\phi \approx 0.35$ which is not predicted by the model. However for the most part, the phase variation of the emission is explained solely by recourse to the geometry of the system, without need to introduce elements of atomic physics or radiative transfer.

Employing an adapted form of the analytic spherical reflection expression we could predict the expected Doppler shift of a spectral line formed locally by the B-star irradiation. This allowed us to compute a value for the rotational velocity of the star which is in good agreement with the values in the literature.

In order to fully exploit this unique and powerful diagnostic higher resolution spectra are required, with greater S/N. These data would allow us to examine in far greater detail the phase variation, and could, particularly around the peak of the emission, allow us the put constraints on the oblateness of the K-star. They would allow us to measure the change in line width to greater accuracy, and examine its variation as the location of the emission moves across the disk of the K-star. Further they would allow us to more robustly compute the rotational velocity from the shift in the line centroid. This is exceedingly difficult to do with the current S/N. This line emission effectively provides spatial resolution on an otherwise unresolved object, being a locally formed line in a disk-averaged spectrum, and gives an opportunity for novel insights into the chromospheres of late-type stars. With the geometric model providing an explanation for its phase variation we are now free to move forward with modelling the chromosphere and examining in detail the line formation mechanism in order to glean as much information as possible from this unique diagnostic.

6

Chromospheric Model of ζ Aurigae A

In this chapter we discuss the construction of a model chromosphere for the primary of the ζ Aurigae system (ζ Aurigae A — K4Ib). This semi-empirical model is based on the large archive of optical and ultraviolet observations of the system, and the model is fit to Hubble Space Telescope observations of the C II] $\lambda 2325\text{ \AA}$ quintet, and Al II] $\lambda 2669\text{ \AA}$ line. Despite the long history of observation of ζ Aurigae A a full semi-empirical model of its chromosphere has not previously been attempted. The model is constructed with its application to other objects in mind, particularly λ Velorum, a single star and close spectral proxy, and the model is used to comment on the structure and extent of giant chromospheres generally. The model is also constructed with a view to more accurately characterise the periodic Si I emission discussed in the previous chapter, and the effect of irradiation by the B-star on the chromosphere of ζ Aurigae A. The model described in this chapter is the subject a paper in prep, O’Riain & Harper (2015).

6.1 Introduction

Studies of the eclipsing binary system ζ Aurigae provide a unique opportunity to observe the properties of stellar chromospheres. During eclipse the secondary acts as a light source shining through the K giant's chromosphere, allowing the physical properties — mass column density, excitation temperature, turbulent velocities — of the chromosphere to be determined along the lines of sight. These values are particularly useful as they should be representative of the chromospheric conditions of single stars (Eaton, 1992, 1993; Schröder, 1988), and they provide the best constraints on the properties of stellar chromospheres.

Owing to the value of the ζ Aurigae systems in determining the structure of stellar atmospheres, they have been long studied. Study of these systems, ζ Aurigae, 31 & 32 Cyg, begins with the optical observations of the 1950's by Wilson & Abt (1954) and Wright (1959). Studies like these probed the inner chromospheres of these objects, deriving temperatures, ionization balances, in the case of ζ Aurigae pointed to inhomogeneity in the atmosphere. Since this early work there has been evidence for inhomogeneity and asymmetry, as well as evidence for an underlying constant atmosphere (McKellar & Petrie, 1952). Optical observations probed the chromosphere below a height of $h \sim 0.5R_*$, and in the 1970's the International Ultraviolet Explorer (IUE) provided observations of the UV part of the spectrum, where the lines are intrinsically stronger, allowing a study of the more extended envelope of ζ Aurigae; see the series of papers "A study of UV spectra of ζ Aur/VV Cep systems" (Hempe, 1982). Despite the unique insight that can be gleaned from the study of ζ Aurigae A, and the large archive of observation, no attempt has been made to construct a full semi-empirical model of its chromosphere. Other ζ Aurigae systems have been modelled previously, with full semi-empirical models for HR 6902 (G9IIb + B8V) and 22 Vul (G4I + B9V) having been computed by Marshall (1996).

In this chapter we will discuss the construction of a spherical, one-component, non-LTE, semi-empirical model chromosphere for ζ Aurigae A. The model constructed is based on empirically measured temperatures and mass column densities, and it is fit to HST observations of the C II] $\lambda 2325\text{\AA}$ quintet, and the Al II]

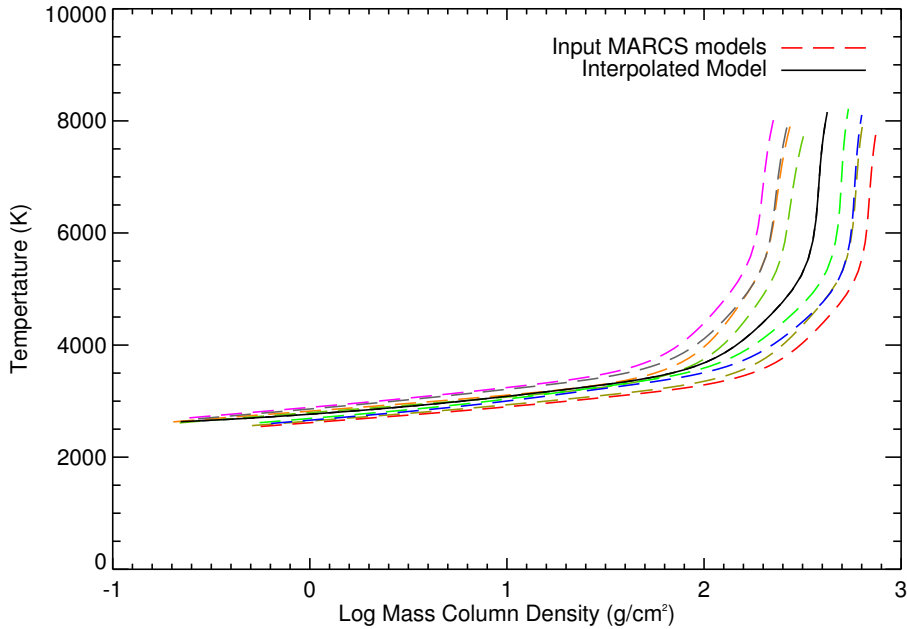


Figure 6.1: The run of temperature with mass column density for interpolated MARCS model photosphere, as compared with the models used to produce it.

$\lambda 2669 \text{ \AA}$ line. We will discuss the implications of the model for single stars, in particular λ Velorum, a close spectral proxy for ζ Aurigae, and an object for which we have complementary data.

6.2 Construction of the Initial Model

6.2.1 MARCS Model Photosphere

The construction of our model atmosphere begins with the photosphere. The photospheric model employed is interpolated from the grid of Model Atmospheres in Radiative and Convective Scheme (MARCS) model photospheres (Gustafsson *et al.*, 1975, 2008). MARCS provides a grid of spherical, hydrostatic, LTE, one-component model photospheres which specify the column density, temperature, electron density, and opacities as a function of height. The models have parameters $2500 \text{ K} < T_{\text{eff}} < 8000 \text{ K}$; $-1 < \log(g) < 5$ (for various masses and radii); $-5 <$

$[\text{Fe}/\text{H}] < 1$; $[\alpha/\text{Fe}] = 0.0$ and 0.4 and different choices of C and N abundances (corresponding to chemically evolved giants, and R, S, & N stars); and $1 \text{ km/s} < v_{\text{turb}} < 5 \text{ km/s}$.

From this grid a model photosphere was interpolated for the parameters of ζ Aurigae A. This was done using the interpolation routine which is provided by MARCS,¹ which computes a model for a given set of parameters using a 3-dimensional (T_{eff} , $\log(g)$, $[\text{Fe}/\text{H}]$ space) cubic spline interpolation. The parameters of ζ Aurigae A were specified as, $T_{\text{eff}} = 3960 \text{ K}$, $\log(g) = 1.33$ (Bennett *et al.*, 1996), $\text{Fe/H} = -0.26$ (McWilliam, 1990), and solar abundances — in the absence of clear evidence that the object has undergone a dredge-up (Luck, 1977). The run of temperature with mass column density, $\log(m_{\text{col}})$, for the interpolated photosphere, and the models used to produce it, can be seen in Fig. 6.1.

This model photosphere is used as the lower part of the model atmosphere constructed, its domain of validity, the region where the plasma is in LTE, is taken to be up to the temperature minimum ($T_{\min} = 0.75T_{\text{eff}}$).

6.2.2 Empirical Mass Column Densities

Eaton (1993) makes use of archival IUE observations to measure the column densities, temperatures, and turbulent velocities along a number of lines of sight, from the photosphere, $h = 0$, to a height of $h \approx 1R_*$. This is done by fitting the observed spectra, specifically the wings of Ly- α and various metals (e.g. Fe I/II, Mg I/II, Ni/II), with one set of parameters ($\log(m_{\text{col}})$, T , v_{Doppler}) per line-of-sight (Eaton, 1988). These parameters will be used in the construction of our model atmosphere, and will be discussed each in turn. We begin with the $\log(m_{\text{col}})$.

Eaton (1993) computes $\log(m_{\text{col}})$ along 14 lines of sight and we collect a further 4 values covering the inner chromosphere from Wilson & Abt (1954). These tangential column densities are converted to radial column densities, and the densities are fit by the following expression:

$$\rho(r) = \rho_0 e^{-R_*/H} e^{R_*^2/H\rho h} \quad (6.1)$$

¹<http://marcs.astro.uu.se/software.php>

where ρ is the mass density, R_* is the stellar radius, H_ρ is the isothermal density scale height, and h is the radial height above the photosphere. This is simply an atmosphere with a density decreasing exponentially with scale height, including a term to account for the decrease in gravity as we move higher into the atmosphere. Eaton (1993) provides best fit values to the data of $H_\rho = 8R_*$, and $\rho_0 = 2.3 \times 10^{-13} \text{ g/cm}^{-3}$. With this expression we can determine the run of radial column density to the photosphere, above the region wherein we use the column density from the MARCS model. With the column density defined in this way, we use Eqn. 6.1 to convert between mass column density and height. In general observations will be compared by reference to their height above the photosphere, as this can be defined based on the date of the observation without recourse to the author's own adopted parameters (radii, ephemerides, etc.), however radiative transfer calculations are performed using mass column density as this allows us to directly control the distribution of mass in the atmosphere.

6.2.3 Empirical Temperatures and Turbulent Velocities

We collect the empirically determined excitation temperatures from the work of Eaton (1993), Wilson & Abt (1954), and Schroeder *et al.* (1990). In Fig. 6.2 we see these values, plotted with respect to their height above the photosphere. The upper scale denotes the corresponding $\log(m_{\text{col}})$ (cgs) at each height. The scale covers the range from the photosphere to $h = 1R_*$. We also plot the lower portion of the wind temperature law given by Harper *et al.* (2005). We note in this plot the extent of the atmosphere, these data pointing to a temperature $\sim 10000 \text{ K}$ being reached at $h \sim 1R_*$. The values from Eaton (1993) are determined by the method discussed in the preceding section, the values in Harper *et al.* (2005) come from a combination of HST and VLA observations (the data points plotted coming from HST, the wind law being informed by both), the values from Wilson & Abt (1954) and Schroeder *et al.* (1990) come from the ionization balance of FeI and TiII, and the ratios of FeII/FeI and MgII/MgI respectively. In our initial model we adopt the temperature-height relation in Harper *et al.* (2005) (provided by P.D.

6.2 Construction of the Initial Model

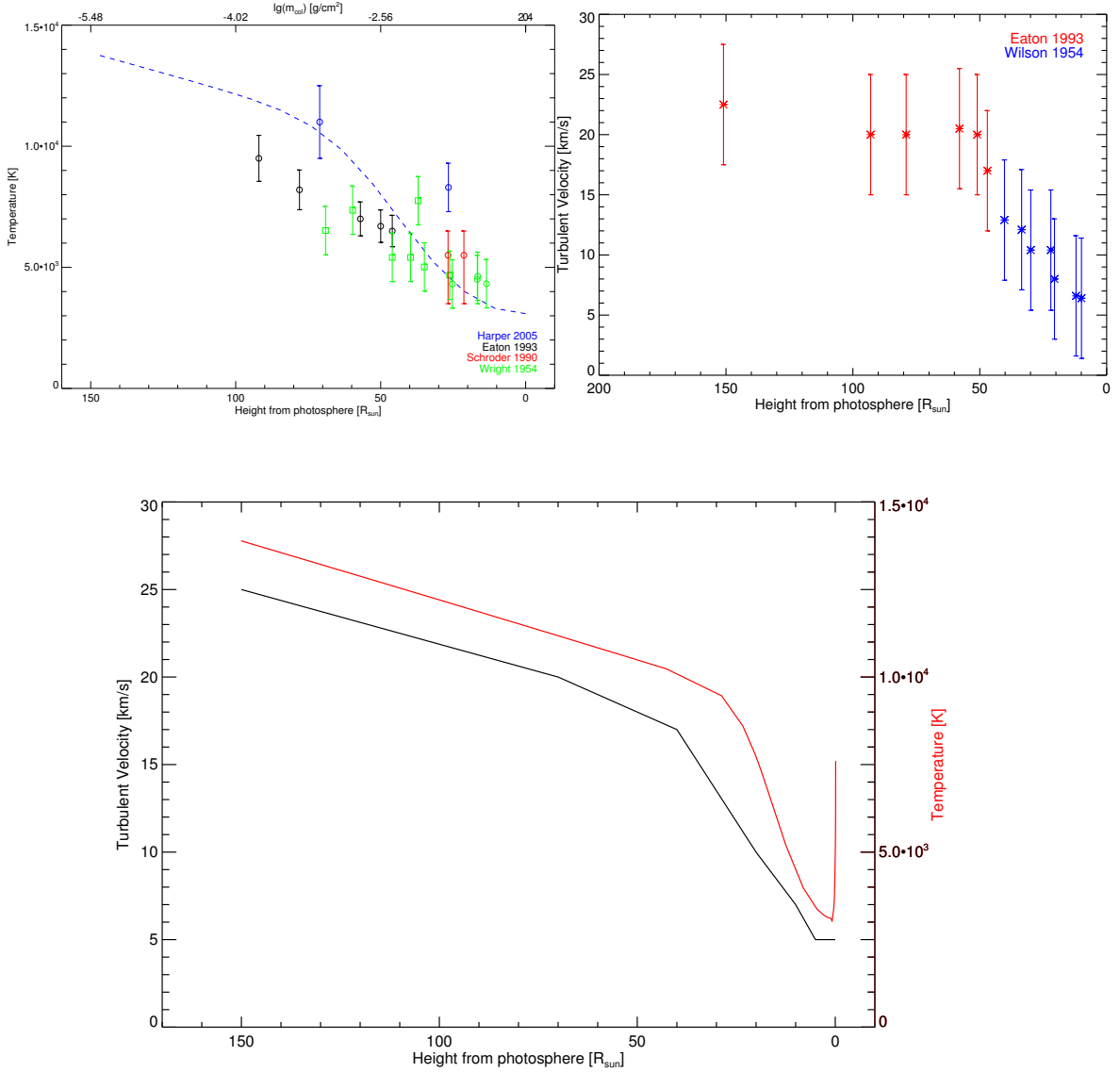


Figure 6.2: *Top Left:* Empirically measured temperatures as a function of height and column density through the atmosphere. We note the extent of the atmosphere. *Top Right:* Empirically determined turbulent velocities as a function of height. We note the large errors on these data. *Bottom:* The temperature and v_{turb} profiles for the model atmosphere, constructed from the empirical data, and the MARCS model.

Bennett),

$$T(r) = 3085.4 + 5656.9 \left(\frac{r}{R_*} \right)^{0.9198} \tanh \left(\frac{r/R_* - 1}{0.1413} \right)^2 \quad (6.2)$$

where r here is defined as photospheric radius plus the height above the photosphere, $r = R_* + h$. We note that this relation does appear to overestimate the temperature points, as plotted in Fig. 6.2, we will address this in succeeding sections.

Turbulent velocities were also collected from the literature, and are plotted in Fig. 6.2. These values are determined from the measured line-widths, and we note that the errors on these measurements are quite large. We also note, however, the clear trend of increasing turbulent velocity with height, as we might expect. These values match those from the work of Baade *et al.* (1996) and references therein, which gives $v_{\text{turb}}(r) = 20 - 15 \text{ km/s}$ $1 < r/R_* \leq 2$. The measured values also chime well with the photospheric turbulent velocities, decreasing toward values we might anticipate in the photosphere (Gray, 2008). Again we combine these values with those of the MARCS model (5 km/s), giving us $v_{\text{turb}}(r)$.

Finally in Fig. 6.2 we see the temperature and turbulent velocity profiles used in the initial model. The temperature model is constructed from the MARCS model and the empirical temperature relation of Harper *et al.* (2005), the turbulent velocity comes from a cubic spline interpolation over the data points provided, again joined with the MARCS model at the temperature minimum. In the coming sections we will discuss how this model was refined in order to better fit spectral observations.

6.2.4 Electron Densities

There are a small number of empirically measured electron densities in the literature, specifically coming from the sources of the temperatures and turbulent velocities. In order to construct a fully self-consistent model atmosphere we will compute the electron density from the other empirical parameters, and compare these with the measured values.

The method by which we will use to compute the electron densities is based on that outlined by Vernazza *et al.* (1973). If we make the assumption of charge

6.2 Construction of the Initial Model

neutrality the electron density will be given by:

$$n_e = n_p + n_H \sum_{\xi} A_{\xi} n_{\xi} \quad (6.3)$$

where n_p is the proton number density, n_H is the total hydrogen number density, A_{ξ} is the abundance of other constituent elements, and n_{ξ} is their degree of ionization. We let

$$\psi(T) = \left(\frac{h^2}{2\pi m k_b T} \right)^{3/2} e^{E_{\kappa}/k_b T} \quad (6.4)$$

where E_{κ} is the ionization energy. For the first level of hydrogen, n_1 , we can write

$$n_1 = n_e n_p b_1 \psi(T) \quad (6.5)$$

Here b_1 is the departure coefficient of the first level, as defined by Menzel (1937)

$$b_i = \frac{n_i/n_i^*}{n_{\kappa}/n_{\kappa}^*} \quad (6.6)$$

where n_{κ} is the number density of ionized atoms, and the asterisk denotes the population values as computed in LTE.

Hence we break up the total hydrogen number as

$$n_H = n_1 \left(1 + \sum_{l=2}^n \frac{n_l}{n_1} \right) \quad (6.7)$$

From which we construct the following quadratic equation in n_e

$$dn_e^2 + n_e - n_e n_h Z d - n_H - n_H Z = 0 \quad (6.8)$$

where

$$Z = \sum_{\xi} A_{\xi} n_{\xi} \quad (6.9)$$

$$d = b_1 \psi(T) \left(1 + \sum_{l=2}^n \frac{n_l}{n_1} \right) \quad (6.10)$$

this quadratic equation has the root¹

$$n_e = \frac{\sqrt{(1 - Zdn_{\text{H}})^2 + 4dn_{\text{H}} + 4dZn_{\text{H}}} - (1 - Zdn_{\text{H}})}{2d} \quad (6.11)$$

The ionization fraction of the elements is computed by

$$n_{\xi} = \frac{1}{1 + n_e \psi_{\xi}(T)} \quad (6.12)$$

where

$$\psi_{\xi}(T) = \left(\frac{h^2}{2\pi m k_b T} \right)^{3/2} \left(\frac{U_I}{2U_{II}} \right)_{\xi} e^{E_{\xi}/k_b T} \quad (6.13)$$

where U_I and U_{II} are the partition functions of the first and second ionization stages of the relevant element. The abundances of the elements are taken from Asplund *et al.* (2006), partition functions from Irwin (1981), and ionization threshold energies from NIST Kramida *et al.* (2015). We note here that due to Eqn 6.12 we have an equation for n_e written in terms of n_{ξ} . Hence we must solve the equation iteratively by substitution. In practice this converges in a small number of iterations.

As part of this iterative process we solve the hydrogen ionization in detail, using RH. This gives us the correct hydrogen departure coefficient b_1 . Hydrogen will be the primary contributor to the electron density through much of the atmosphere, with metals only contributing substantially at lower temperatures, and hence we account only for hydrogen in detail.

The ionization of hydrogen in the chromosphere is a two-step process, excitation to the $n = 2$ level by electron collisions or scattered Ly α photons followed by photoionization by the photospheric Balmer continuum. In order to accurately treat the hydrogen radiation field, since the Balmer and Lyman continua will control the ionization fraction, we compute the hydrogen solution using the assumption of Partial Redistribution (PRD — discussed at length in the introductory chapters) for Ly- α , Ly- β , and H- α .

We turn to the empirically measured electron densities of Schroeder (1986); Schroeder *et al.* (1990). These values are computed from the ionization balance of

¹The root provided by Vernazza *et al.* (1973) is written in a slightly different form, but is equivalent.

6.2 Construction of the Initial Model

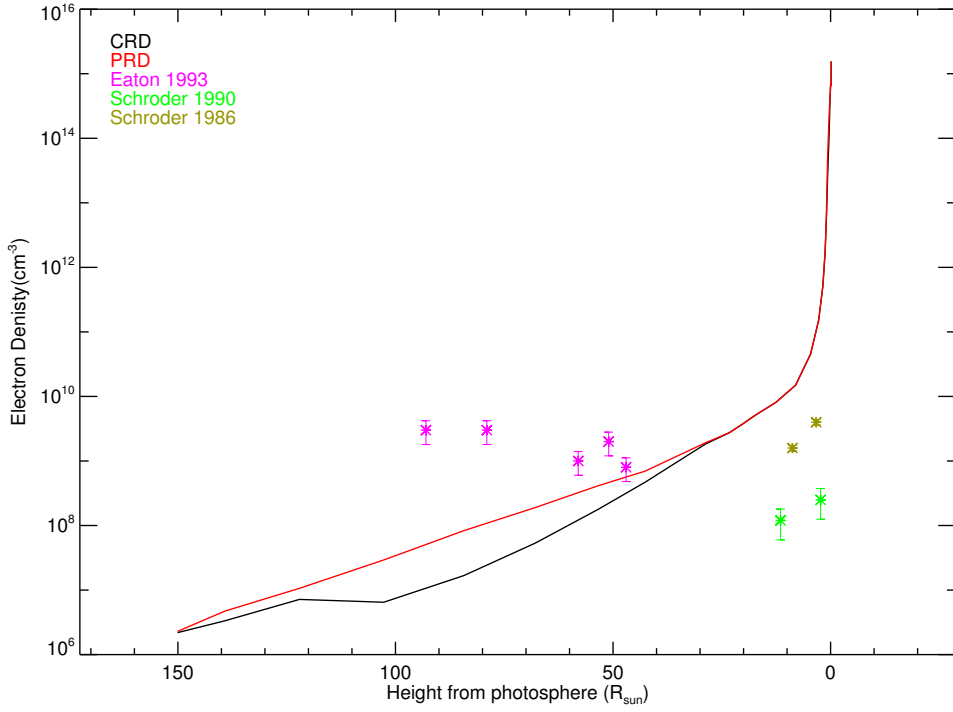


Figure 6.3: Electron density as a function of height above the photosphere. We see the electron density computed using the the assumptions of CRD and PRD, compared with the empirically measured electron densities.

Fe II/Fe I. This is achieved by assuming that the ionization to Fe II is controlled by the B-star radiation field, and this is balanced by recombination to Fe I, giving:

$$n_e = \frac{n_{\text{FeI}}}{n_{\text{FeII}}} \frac{\Gamma_B}{\alpha(T)} \quad (6.14)$$

where Γ_B is the photoionization rate due to the B-star and $\alpha(T)$ is the recombination coefficient. The photoionization rate due to the B-star is given by:

$$\Gamma_B = \frac{W 4\pi}{hc} \int_0^{1576\text{\AA}} F_B \lambda a_\lambda d\lambda \quad (6.15)$$

where W is the dilution factor, and a_λ is the photoionization cross-section, F_B

Table 6.1: Electron density as computed by Schroeder (1986); Schroeder *et al.* (1990) and recomputed using updated atomic data.

Height (m)	n_e (cm^{-3}) (Schroeder)	n_e (cm^{-3}) (Recomputed)
2.3×10^9	3.55×10^9	1.22×10^9
6.1×10^9	1.31×10^9	3.88×10^8
8×10^9	1.2×10^8	2.45×10^8
1.6×10^{10}	2.5×10^8	4.35×10^8

comes from Castelli *et al.* (1997). The atomic data relating to Fe have changed considerably in the past 20 years – the key ratio here, $\Gamma_B/\alpha(T)$ has changed by a factor of ~ 2 – and as a result we recompute the electron density based on the updated atomic data of Bautista (1997). The values of electron density can be seen in Table 6.1. The values are computed given a temperature of 5000 K which, as well as being of similar magnitude as the measured temperatures at these heights, is also the minimum of $\alpha(T)$ and hence provides an upper limit on the electron density. As we can see the values have changed by a factor of $\sim 2 - 3$, and this has the effect of decreasing the upper limit on the electron density in this region by an order of magnitude. Eaton (1993) provides a number of electron densities derived from the Fe ionization balance, which our calculation also revise down by a factor of 50% from $\sim 10^9 \text{ cm}^{-3}$, though this has less of an effect on the electron densities presented by Eaton (1993) as they are averaged between the ionization balance of number of elements. We will discuss the relation between these empirically measured values and our computed values in the discussion of the final atmospheric model.

In Fig. 6.3 we see contrast the results using Complete Redistribution (CRD), and PRD, along with the small number of empirically measured electron densities. We see that both the PRD and the CRD case agree well in the lower chromosphere (where the plasma is well approximated by the assumption of LTE), before diverging in the middle chromosphere, and finally converging again at the top of the chromosphere, as $n_e \rightarrow n_H$ for both cases. It is difficult to make general qualitative statements about the differences between the CRD and PRD electron densities, as one would expect as we change the atmospheric parameters the differences between the two computed values change, however it does appear to be

the case that electron density is generally lower for the CRD case. We note that there appears to be disagreement between the electron densities as analytically computed, and those values presented in the literature. We will discuss the details of this disagreement when we present the final model.

To summarise the method used to compute n_e :

1. We begin by computing the total hydrogen number density from the mass column density and the abundance.
2. Then, using the temperature profile, the LTE hydrogen balance is computed, including the proton number.
3. We compute n_e from this n_H using Eqn 6.11, and proceed to compute the NLTE hydrogen solution using RH.
4. From this hydrogen solution we compute a new electron density, n_e^{new} , again using Eqn 6.11, which we then use to compute a new hydrogen solution.
5. We continue this process until $(n_e^{new} - n_e^{old})/n_e^{old} < 10^{-4}$ for every point in the atmosphere.

Now we have the mass column density, temperature profile, turbulent velocity, and electron density, we have specified the required thermodynamic parameters of the atmosphere. Next we must address the microphysics, and construct the relevant atomic models.

6.3 Atomic Models

In the coming sections we will be examining HST spectra of ζ Aurigae, with an emphasis on optically thin lines, which allow us to probe the structure of the atmosphere. In particular we will be looking at the C II] $\lambda 2325 \text{ \AA}$ quintet, and the Al II] $\lambda 2669 \text{ \AA}$ line, and as such we will need to construct models of these atoms. In this section we will begin by discussing the H model used in the electron densities calculation, followed by the Al model, and the C model. These models are provided in the Appendix.

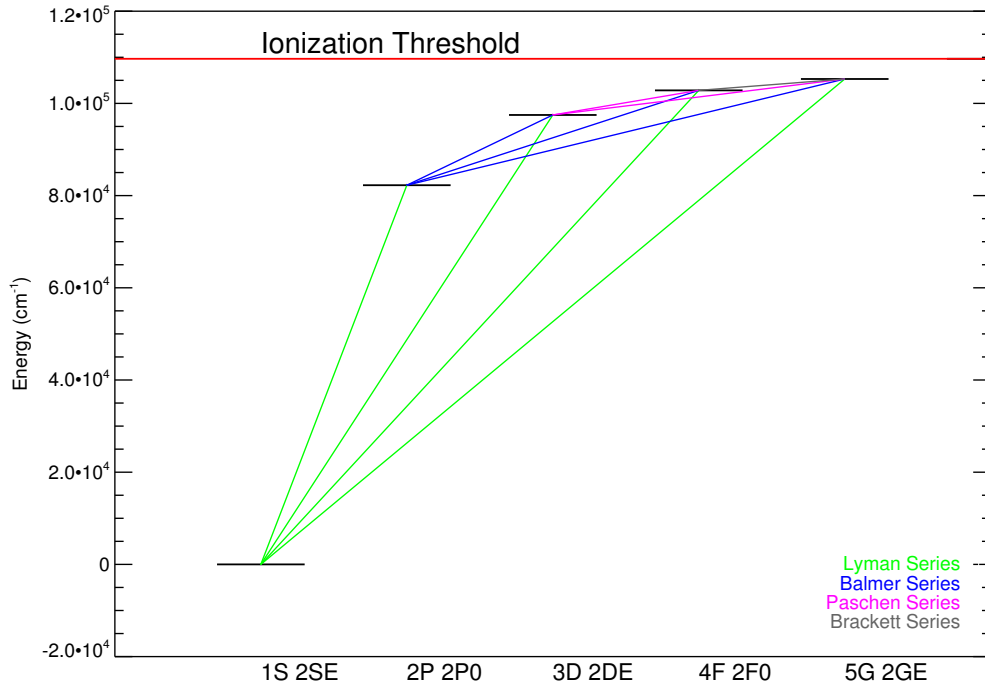


Figure 6.4: Grotrian Diagram of the H model constructed. This model consists of 5 HI levels and one HII ionization level. The transition series (Lyman, Balmer, etc.) are colour coded.

6.3.1 Hydrogen Model

In the case of the H it is possible to use a number of hydrogenic simplifications to construct a model atom. The H model used is a 6 level atom, based on that used in the Vernazza *et al.* (1973) series of papers, and can be seen in the Grotrian diagram in Fig. 6.4. The energy levels in this Grotrian were computed from the Rydberg Equation

$$E_n = -13.6 \left(1 - \frac{1}{n^2}\right) \text{eV} \quad (6.16)$$

where n is the principal quantum number. We compute the oscillator strengths, the collisional excitation, and the collisional ionization rates by the method of Johnson (1972), as follows.

The oscillator strength of a transition from j to i is given by

$$f_{ij} = \frac{32}{3\sqrt{3}\pi} \frac{n_i}{n_j^3} x^{-3} g(n, x) \quad (6.17)$$

$$x = 1 - \left(\frac{n_i}{n_j} \right)^2 \quad (6.18)$$

$$g(n, x) = g_0(n) + g_1(n)x^{-1} + g_2(n)x^{-2} \quad (6.19)$$

Here x is the ratio of the transition energy to the ionization energy (E_k), and $g(n, x)$ is the Gaunt factor, approximated as the given polynomial, with the coefficients tabulated in Johnson (1972).

The collisional excitation cross-section is provided by the expression

$$\begin{aligned} q_{ij} = & \frac{2n^2}{x} U_{ij}^{-1} (1 - e^{-r_{ij} U_{ij}}) \left(A_{ij} \left(\ln(U_{ij}) + \frac{1}{2U_{ij}} \right) + \right. \\ & \left. + B_{ij} - A_{ij} \ln \left(\frac{2n^2}{x} \right) \left(1 - \frac{1}{U_{ij}} \right) \right) \pi a_0^2 \end{aligned} \quad (6.20)$$

where $U_{ij} = E_k/E_{ij}$, a_0 is the Bohr radius, A_{ij} and B_{ij} are polynomial approximations to the integrals introduced by Bethe (1930), and r_{ij} is a fitting parameter such that

$$r_{ij} = r_i x \quad (6.21)$$

$$r_1 = 0.45 \quad n = 1 \quad (6.22)$$

$$r_n = 1.94n^{-1.57} \quad n \geq 2 \quad (6.23)$$

The collisional ionization cross-section is given by a similar expression

$$q_{ik} = \frac{2n^2}{U_i} (1 - e^{-r_i U_i}) \left(A_i \ln(U_i) + (B_i - A_i \ln(2n^2)) \left(1 - \frac{1}{U_i} \right)^2 \right) \pi a_0^2 \quad (6.24)$$

Finally we compute the photoionization cross sections by the expression of Menzel & Pekeris (1935) (see also Hubeny & Mihalas (2014, p. 188))

$$\alpha_{ik}(n, \nu) = \frac{64\pi^4 Z^4 e^{10} m_e}{3\sqrt{3} c h^6} \frac{g_{bf}(n, \nu)}{n^5 \nu^3} \quad (6.25)$$

where $Z = 1$, e is the electron charge, m_e is the electron mass, and $g_{bf}(n, \nu)$ is the bound-free Gaunt factor tabulated in Karzas & Latter (1961).

6.3.2 Aluminium Model

In Fig. 6.5 we see the Grotrian Diagram of the Al model atom constructed. The model, based on the model atoms presented in Harper (1992) and Vernazza *et al.* (1976), consists of 12 levels and 7 radiative transitions, over the first two ionization states – Al I & Al II – and a continuum Al III level. The full atomic model is published in the Appendix. In Fig. 6.5 we see the levels and the radiative transitions of the atom constructed. The Al II] $\lambda 2669 \text{ \AA}$ line, for which we have HST observations, is marked.

The energies of the levels were collected from the NIST Atomic Database (Kramida *et al.*, 2015). The data for the radiative transitions – the $\log(gf)$ values, the radiative damping constants, the Stark damping constants – were collected from Kurucz & Bell (1995)¹.

The photoionization cross-sections are collected from TOPBASE² (Cunto & Mendoza, 1992). TOPBASE ignores fine structure levels, providing the total photoionization cross-section of a “super-level” summed over the fine-structure levels, as a function of frequency, $\sigma_T(\nu)$.

From this we want to determine the cross-section of each of the N fine-structure levels such that the total photoionization rate (s^{-1}) is preserved. Hubeny & Michalas (2014, p. 680) provide the expression used to sum the photoionization cross-sections of levels:

$$\sigma_T(\nu) = \frac{\sum_i g_i w_i \sigma_i(\nu) e^{-E_i/k_b T}}{\sum_i g_i w_i e^{-E_i/k_b T}} \quad (6.26)$$

where g_i is the statistical weight of a given level, w_i is the occupation probability and σ_i is the photoionization cross-section. Here we will make the assumption that $w_i = 1$ (w_i accounts for the effect of neighbouring particles on the ionization energy, which we will here assume, as it is in the classical treatment, to be negligible), and that the energies of the levels is approximately equal $E = E_i$ (since we are dealing

¹<http://kurucz.harvard.edu/>

²<http://cdsweb.u-strasbg.fr/topbase/topbase.html>

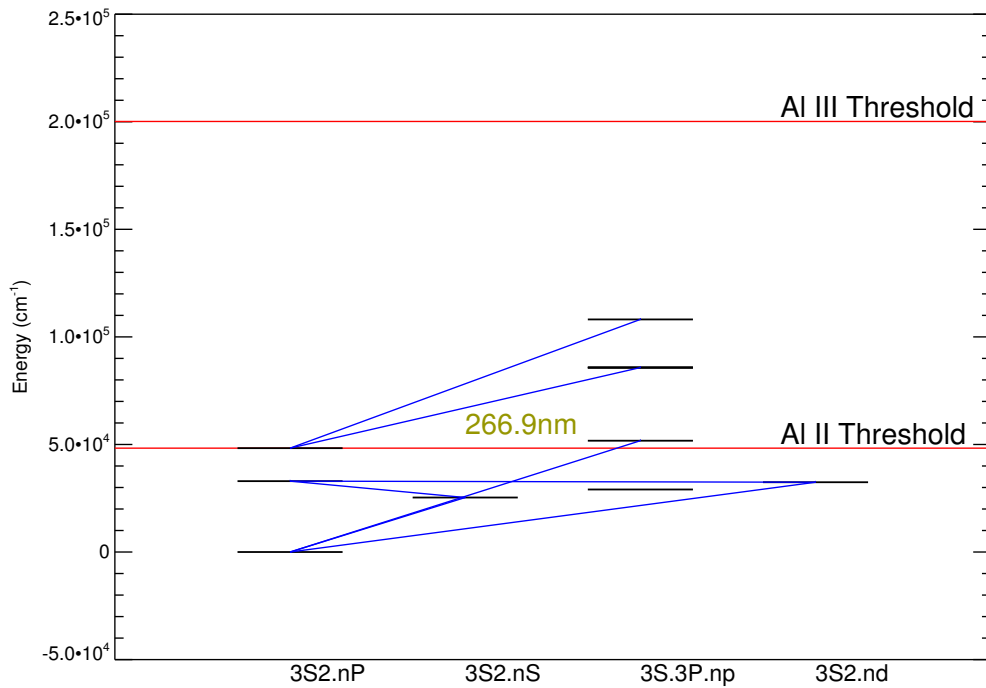


Figure 6.5: Grotrian Diagram of the Al I-III model constructed. The Al II] $\lambda 2669\text{ \AA}$ line, for which we have HST spectra, is marked.

with fine-structure this is a reasonable assumption). This gives us:

$$\sigma_T(\nu) = \frac{\sum_i g_i \sigma_i(\nu)}{\sum_i g_i} \quad (6.27)$$

We aim to preserve the photoionization rate

$$n_T \int_0^\infty \sigma_T(\nu) J_\nu d\nu = \sum_i \int_0^\infty n_i \sigma_i(\nu) J_\nu d\nu \quad (6.28)$$

where

$$n_T = \sum_i n_i \quad (6.29)$$

A solution which will preserve the rate is clearly obtained by setting each of the photoionization cross-sections to the total, $\sigma_i = \sigma_T$, however it is important

to note that this may not be reflective of the *true* rate out of each level.

Finally we compute the collisional cross-section. To compute the collisional excitation cross-sections, a commonly used method is that of van Regemorter (1962), which expresses the collisional excitation cross-section for a dipole-permitted transition in terms of the oscillator strength, f_{ij}

$$q_{ij}(T) = C_0 T^{1/2} 14.5 f_{ij} (E_H/E_{ij})^2 u_0 e^{-u_0} \Gamma(u_0) \quad (6.30)$$

where

$$\Gamma(u_0) = \max[\bar{g}, 0.276 e^{u_0} E_1(u_0)] \quad (6.31)$$

where $C_0 = \pi a_0^2 (8k_b/m\pi)^{1/2}$, E_H is the ionization energy of hydrogen, E_{ij} is the energy of the level, $u_0 = E_{ij}/k_b T$, \bar{g} is the effective Gaunt coefficient, and E_1 is the first exponential integral.

For collisional ionizations we use the formula provided by Seaton (Hubeny & Mihalas, 2014)

$$q_{ik} = 1.55 \times 10^{13} T^{-1/2} \bar{g}_i \sigma_{ik}(\nu_0) \frac{e^{-u_0}}{u_0} \quad (6.32)$$

where $\sigma_{ik}(\nu_0)$ is the threshold photoionization cross-section, and \bar{g}_i is the Gaunt factor for an ion of given charge – of order 0.1 for $Z = 1$, and 0.2 for $Z = 2$.

6.3.3 Carbon Model

In Fig. 6.6 we see the Grotrian diagram of the C model atom constructed. This model comprises 3 CI levels, which are not radiatively linked, 8 C II levels, whose transitions we see in the Grotrian diagram, and a continuum C III level. In the Grotrian diagram we have plotted in red the $\lambda 2325 \text{ \AA}$ quintet transitions, which are then plotted in more detail in the schematic Grotrian in the right hand panel of Fig. 6.6. The flux ratios of the quintet transitions are density-sensitive, they provide a direct measure of the electron density in the line-forming region, and hence are very powerful chromospheric diagnostics (Stencel *et al.*, 1981). The

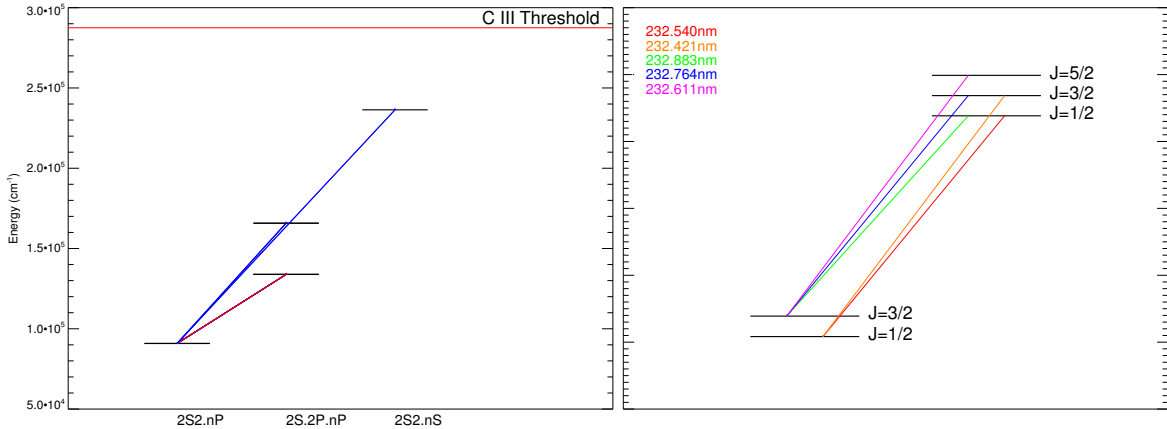


Figure 6.6: *Left:* Grotrian diagram of the radiative transitions in the C II-III model constructed. The quintet transitions are marked in red. *Right:* A schematic Grotrian diagram of the CII electron density sensitive quintet transitions.

density sensitive flux ratios are

$$R_1 = \frac{F(2326.11\text{\AA})}{F(2328.83\text{\AA})} \quad (6.33)$$

$$R_2 = \frac{F(2326.11\text{\AA})}{F(2327.64\text{\AA})} \quad (6.34)$$

$$R_3 = \frac{F(2325.40\text{\AA})}{F(2327.64\text{\AA})} \quad (6.35)$$

These ratios are sensitive to electron densities in the range $n_e \sim 10^6 - 10^{10} \text{ cm}^{-3}$. This system also gives rise to the ratios:

$$R_4 = \frac{F(2326.11\text{\AA})}{F(2324.21\text{\AA})} \quad (6.36)$$

$$R_5 = \frac{F(2328.83\text{\AA})}{F(2325.40\text{\AA})} \quad (6.37)$$

$$(6.38)$$

which sensitive to the oscillator strengths of the lines, and also the optical depth.

Due to their diagnostic importance, care was taken to select accurate atomic

Table 6.2: Atomic data for the electron density sensitive C II] quintet.

Level	Energy (cm ⁻¹)	g
2s ² 2p ² P _{1/2}	90832.1	2
2s ² 2p ² P _{3/2}	90895.62	4
2s2p ² ⁴ P _{1/2}	133835.5	2
2s2p ² ⁴ P _{3/2}	133857.5	4
2s2p ² ⁴ P _{5/2}	133885.8	6

Transition	2J - 2J'	λ (Å)	A_{ij} (s ⁻¹)
2s ² 2p ² P - 2s2p ² ⁴ P	1 - 1	2325.4	52
	1 - 3	2324.21	1.711
	3 - 1	2328.83	61.07
	3 - 3	2327.64	8.606
	3 - 5	2326.11	34.45

data for the model, particularly the collision rates. We collect the energies of the levels, the oscillator strengths, and the collision strengths from Tayal (2008). These values have the advantage of being self-consistently computed, with all of the values coming from the same R-matrix wave function calculation, and so we avoid any conflict that may arise from selecting values from different sources with different unknown biases. As with the previous model the radiative parameters (with the exception of the oscillator strengths) are taken from Kurucz & Bell (1995), and the photoionization cross-sections from TOPBASE (Cunto & Mendoza, 1992).

In order to quantify the sensitivity of the flux ratios to the atomic data the mean escape probability method was used to compute the flux ratios (Judge, 1990; Osterbrock, 1962). The formalism used is the frequency- and angle-averaged one-sided mean escape probability which is described in the introduction. While this approximation is inadequate to model the full, non-local radiative transfer problem, it can provide useful qualitative insight into the dependency of the fluxes on the atomic parameters. In Fig. 6.7 we can see the result of the calculation, holding the temperature constant at 6500 K and the hydrogen column density ($\int n_H dz$) at 10^{23} cm⁻², and varying the electron density. The sensitivity to electron density is clear.

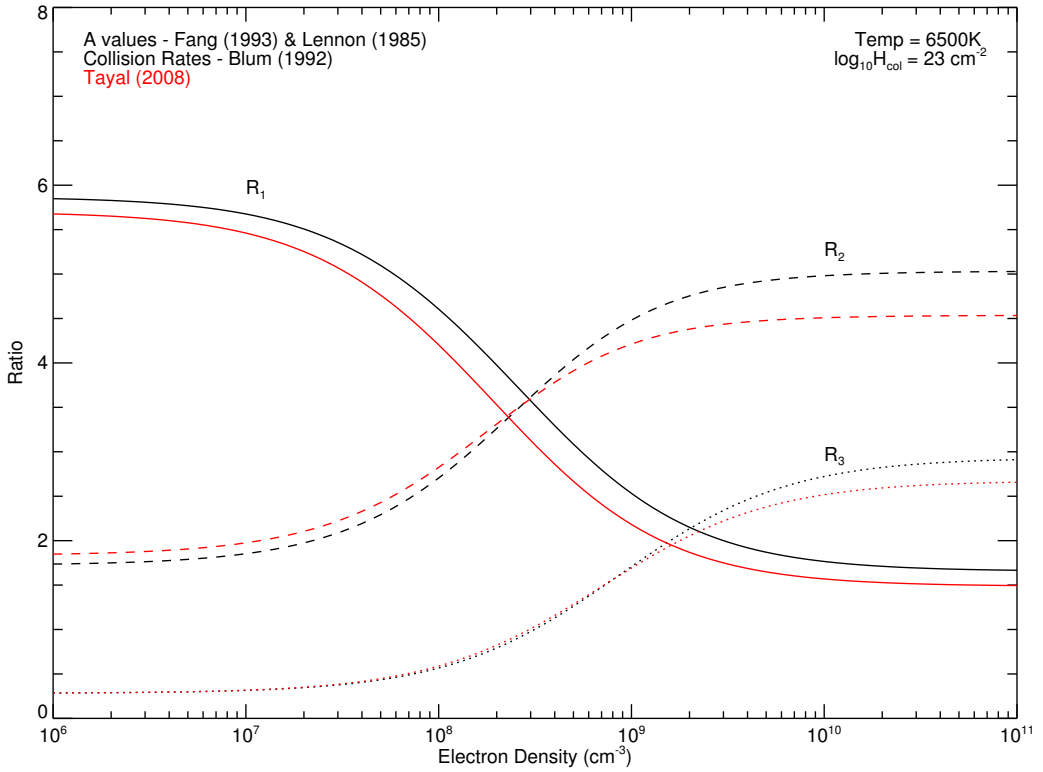


Figure 6.7: Line ratios as a function of electron density for a fixed column density (10^{23} cm^{-2}) and temperature (6500 K). The ratios for the atomic data used in our model can be seen in red, and are contrasted with atomic parameters used in the analysis Judge & Carpenter (1998a).

The calculation is performed using the atomic parameters of our model, as collected from Tayal (2008). These results are compared results for the atomic parameters collected from Fang *et al.* (1993) and Lennon *et al.* (1985) (A values), and Blum & Pradhan (1992) (collision strengths). These values are used by Judge & Carpenter (1998a), who made use of this diagnostic to determine the electron density of a number of evolved stars – γ Dra, α Tau, γ Cru, μ Gem, g Her, λ Vel, and α Ori.

The accuracy of our calculation can be checked against the analytically calculable ratios in the high and low (electron) density limits. In the high density limit the relative level populations are given by Boltzmann statistics and hence

the ratios are determined solely by the A values.

$$\frac{n_i}{n_j} = \frac{g_i}{g_j} e^{-E_{ij}/kT} \quad (6.39)$$

$$F_\nu \propto n_i A_{ij} \nu_{ij} \quad (6.40)$$

$$R_{ij/kj} = \frac{n_i A_{ij} \nu_{ij}}{n_k A_{kj} \nu_{kj}} \quad (6.41)$$

In the low density limit we can ignore collisional de-excitation, so the level populations are determined by collisional excitation, and radiative decay. We begin with the populations of the lower doublet relative to the total (in this brief derivation we will label the levels 1 – 5 in increasing energy)

$$\frac{n_1}{n_{\text{tot}}} = g_1 \frac{e^{-E/kT}}{U} \quad (6.42)$$

and similarly for n_2 , where U is the partition function. Hence the populations of the upper triplet relative to the total (noting that level 5 can only decay to 2, a transition to 1 is spin-forbidden) will be given by

$$\frac{n_3}{n_{\text{tot}}} = \frac{n_1/n_{\text{tot}} C_{13} + n_2/n_{\text{tot}} C_{23}}{A_{32} + A_{31}} \quad (6.43)$$

$$\frac{n_4}{n_{\text{tot}}} = \frac{n_1/n_{\text{tot}} C_{14} + n_2/n_{\text{tot}} C_{24}}{A_{42} + A_{41}} \quad (6.44)$$

$$\frac{n_5}{n_{\text{tot}}} = \frac{n_1/n_{\text{tot}} C_{15} + n_2/n_{\text{tot}} C_{25}}{A_{52}} \quad (6.45)$$

where C_{ij} is the collisional rate is

$$C_{ij} = \left(\frac{8.63 \times 10^{-6}}{g_i \sqrt{T}} \right) \gamma_{ij} e^{-E_{ij}/kT} \quad (6.46)$$

where γ_{ij} is the collision strength. From these populations we can then determine the flux ratios as before. In Table. 6.3 we tabulate the high and low density limit line ratios. As we can see these values are in reasonable agreement with the results of our mean escape probability calculation.

Comparing the results of this calculation for the two sets of atomic parameters used we see that they show the same trends, but there is a clear offset between

Table 6.3: Analytic and computed (by the mean escape probability method) values for the flux ratios in the high and low density limits, from the values of Tayal (2008).

Ratio	Low Density		High Density	
	Computed	Analytic	Computed	Analytic
R_1	5.67	5.65	1.49	1.68
R_2	1.85	1.82	4.53	5.00
R_3	0.29	0.27	2.65	3.03

them. This is most evident for R_1 , the ratio which we will examine most extensively in our subsequent analysis. For R_1 we see our atomic model predicts a consistently lower n_e than the model used by Judge & Carpenter (1998a), by a factor of ~ 3 in the region with which we are most concerned. It is important to keep in mind the sensitivity of the estimated electron density to the atomic parameters as we make use of this diagnostic.

6.4 Spectral Observations

6.4.1 HST Data

HST observations of ζ Aurigae were made using the Goddard High Resolution Spectrograph (Brandt *et al.*, 1994) at 8 epochs between April 1993 and December 1996. In this work we will use data obtained on the 16th October 1995 (Proposal ID: 6069), which we will refer to as Epoch 8, maintaining the convention of previous publications (Bennett *et al.*, 1996; Harper *et al.*, 2005). These epochs can be seen overlaid on the orbit in Fig. 6.8. This observation is made very close to mid-eclipse, when the B-star is behind the K-star, giving the best opportunity to measure the undiluted K-star spectrum. As mentioned in previous sections, we will focus in particular on two sets of observations: those of C II] $\lambda 2325 \text{ \AA}$ quintet, and Al II] $\lambda 2669 \text{ \AA}$ line. These observations were made using the ECH-B grating (2323 \AA -2335 \AA & 2663 \AA -2675 \AA) providing a resolution of $R = 85,000$. These spectra are plotted in Fig. 6.9.

The spectra have been converted to stellar surface flux using an angular diameter of $\phi = 5.66 \text{ mas}$ (Bennett *et al.*, 1996; di Benedetto & Ferluga, 1990). They

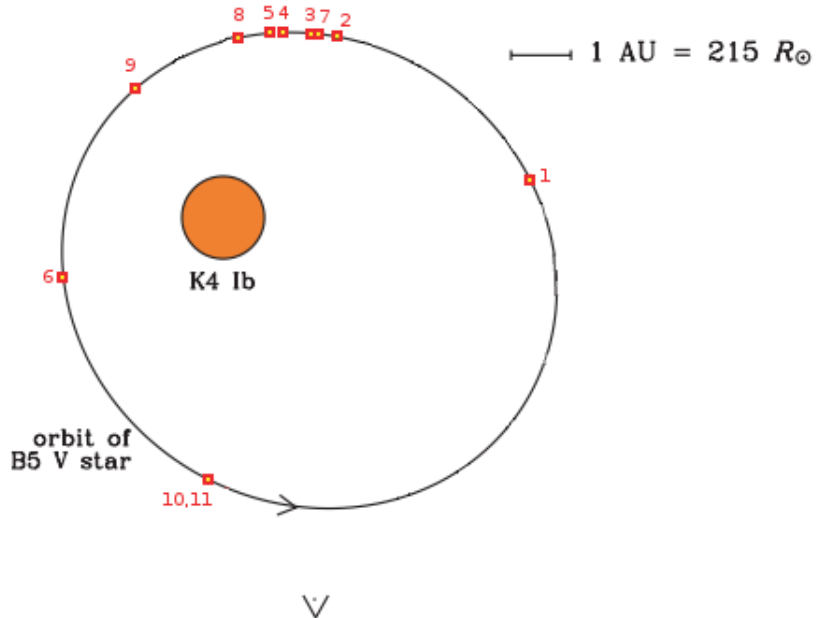


Figure 6.8: Orbit of ζ Aurigae with the HST GHRS observation epochs annotated.
Image adapted from Harper *et al.* (2005).

have also been converted to the stellar rest frame using a systemic velocity of 10.8 km/s (Eaton *et al.*, 2008) (this is the value annotated on the figure), as well as an additional 6.5 km/s to account for the stellar orbital motion at the phase of observation. This value was determined from the radial velocity curve presented in the preceding chapter. Note that these spectra have been converted to vacuum wavelength (it is common for spectra above 2000 Å to be given in air wavelength) using the following relation (Morton, 1991):

$$\lambda_{\text{vac}} = \lambda_{\text{air}} \left(1 + 2.73 \times 10^{-4} + \frac{131.4182}{\lambda_{\text{air}}^2} + \frac{2.76249 \times 10^8}{\lambda_{\text{air}}^4} \right) \quad (6.47)$$

We note the very bright features which dominate both spectra, these are wind-scattering features (the bright line at 2328 Å, for instance, is an Fe II line). These lines arise due to the influence of the B-star, which, despite being in eclipse, will contribute to the UV spectrum due to the scattering of photons in the wind. These

6.4 Spectral Observations

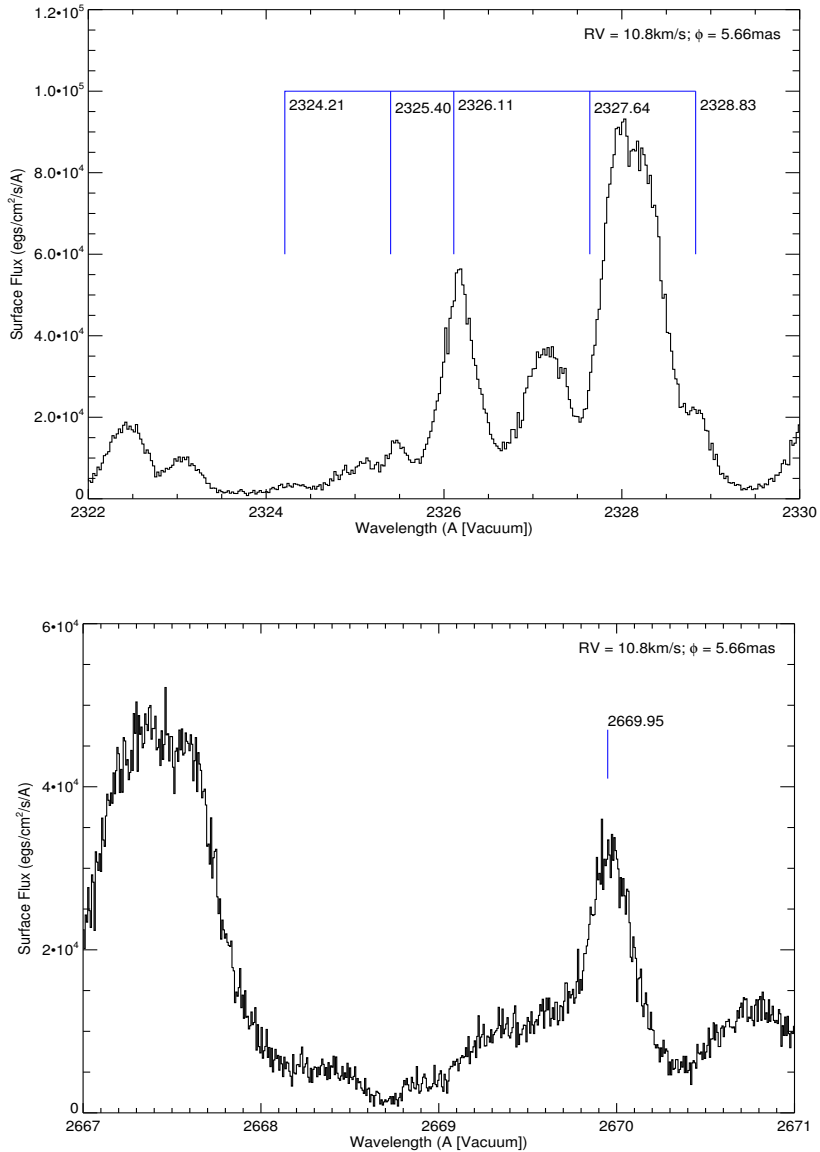


Figure 6.9: HST GHRS ζ Aurigae Epoch 8 spectra. *Top:* Spectrum covering the region of the CII] $\lambda 2325 \text{ \AA}$ quintet with the lines annotated. *Bottom:* Spectrum of the AlII] $\lambda 2669 \text{ \AA}$ region, again annotated. Note that both spectra have been converted to stellar surface flux using the angular diameter given, ϕ . Further note the very bright wind scattering features which dominate the spectra.

wind scattering features stand out more clearly when we plot the spectrum of λ Velorum.

HST GHRS spectra of λ Velorum were obtained on September 3rd 1994 (Carpenter *et al.*, 1999). These spectra cover the same spectral regions as those of ζ Aurigae, however they were collected at a lower spectral resolution ($R \approx 25000$), using the G200M and G270M gratings. Nevertheless these spectra provide an important counterpoint to our study of ζ Aurigae. As previously discussed λ Velorum is a single star and a close spectral proxy for ζ Aurigae, hence a careful examination of the chromosphere of one object may provide insight into the structure of the other. In Fig. 6.10 the spectra of both objects are plotted. The spectra of λ Velorum were scaled in the same way as those of ζ Aurigae, using a radial velocity of 18.4 km/s. (Wilson, 1953), and an angular diameter of 11.7 mas¹. In this figure, with the spectra of λ Velorum for comparison, we can more clearly see the effect of the wind scattering lines on the spectrum of ζ Aurigae. The spectrum of λ Velorum is provided here primarily for illustrative purposes, demonstrating the similarity between the objects and allowing us to more clearly identify the lines in question.

In order to more accurately quantify the line ratios in ζ Aurigae we attempt to remove the wind-scattering lines from the spectrum. An analysis was performed by Bennett (2015) (private communication) in order to quantify the effect of wind-scattering in the spectrum. This was achieved by fitting a power-law to the relationship between the ratio of emission to continuum flux, and the line optical depth for a number of species,

$$F_{\text{scattered}} \propto (NS)^\alpha \quad (6.48)$$

where N is the number of atoms in the lower level of the scattering line, and S is a measure of the line transition strength. This fit provides $\alpha = 0.37$. From the fit scattered light spectra were produced for the C II] quintet and Al II] 2669Å regions, these can be seen in Fig. 6.11. Examining these figures we can clearly see

¹This value is taken from Lafrasse *et al.* (2010) and is slightly larger than the older value of 11.1 ± 0.8 mas used in Carpenter *et al.* (2014). Their value was taken from Blackwell & Shallis (1977), and may be modestly in error due to a lack of an accurate model atmosphere for their analysis

6.4 Spectral Observations

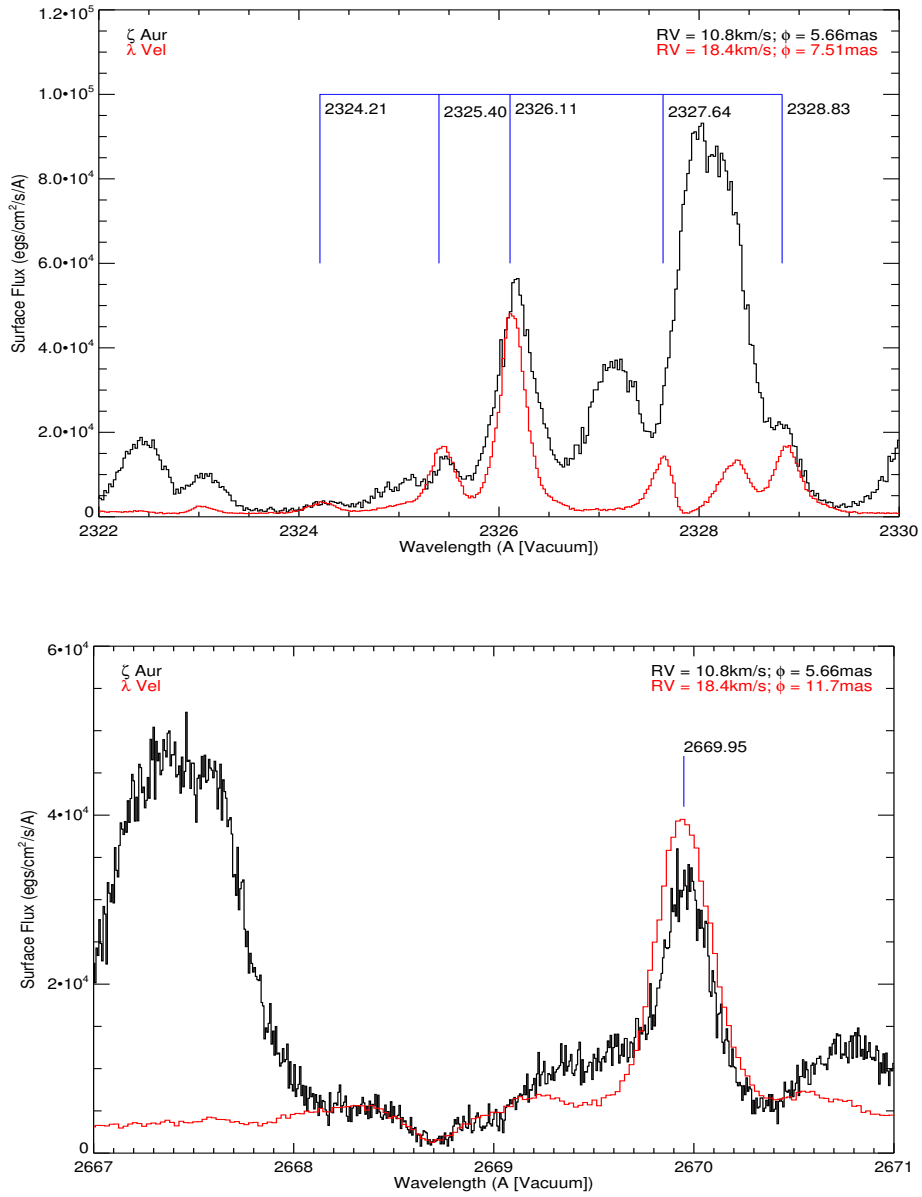


Figure 6.10: HST GHRS ζ Aurigae Epoch 8 spectra with the spectra of λ Velorum over plotted. We can see how closely the surface fluxes of these objects match, and we also note the wind scattering features in the spectra of ζ Aurigae which are clearly absent in those of λ Velorum.

6.4 Spectral Observations

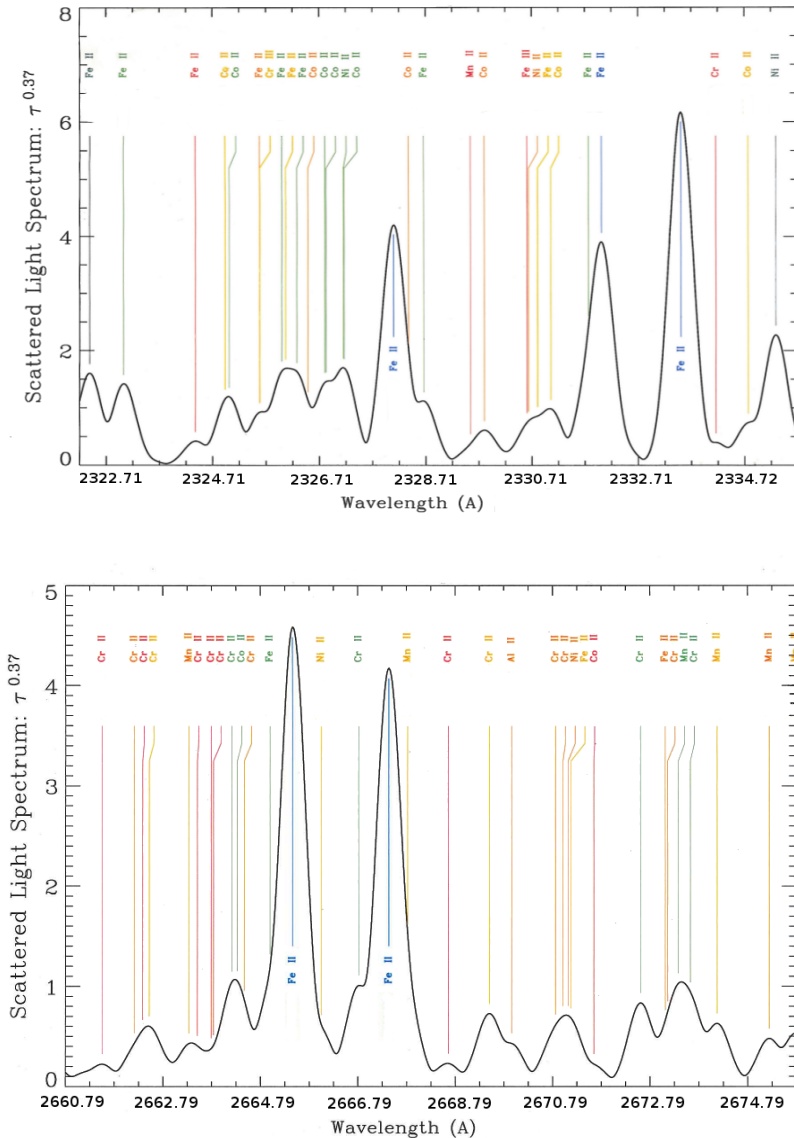


Figure 6.11: Scattered light spectra, as computed by Bennett (2015), for the regions of the C II] quintet and Al II] 2669Å.

the prominent wind scattering Fe II lines which dominate our ζ Aurigae spectra. In order to remove the wind-scattering component from the C II] quintet region we select 5 of the brightest lines from the Bennett (2015) spectrum — Fe II 2322.4 Å,

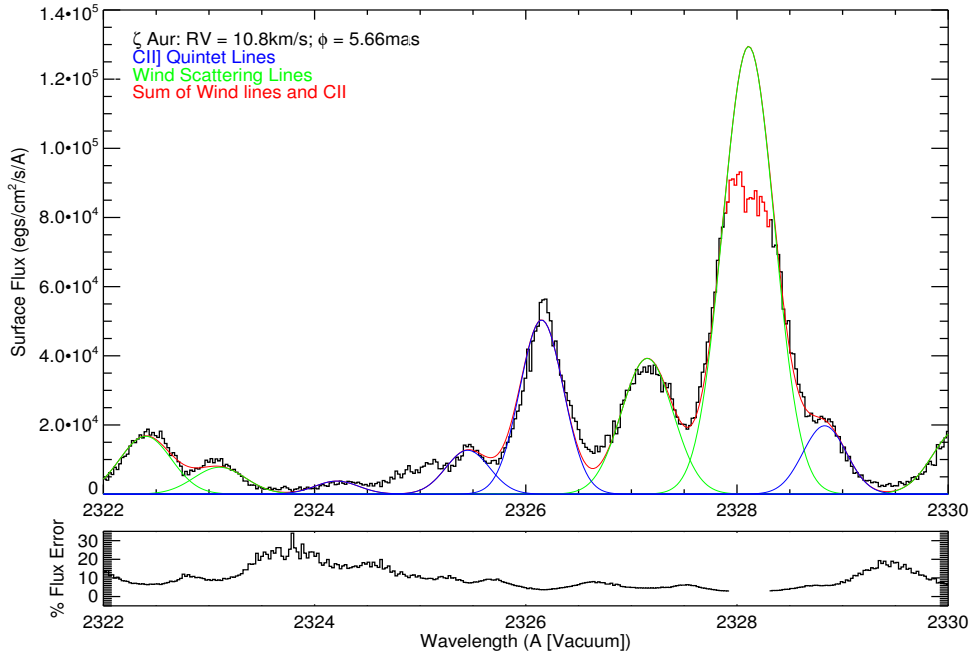


Figure 6.12: Gaussian fits to five of the most prominent wind-scattered lines, and four of the lines of the C II] 2325Å quintet. The observed spectrum can be seen in black, the Gaussian fits to the contaminants in green, and the C II] lines in blue. The sum is plotted in red. The region of the 2328Å feature marked in red is removed from the fit. In the lower panel the percentage error in the spectrum is plotted. Note that the region excised from our fit is flagged with NaN values in the error array.

Fe II 2323.04 Å, Ni II/Co II 2327.16 Å, Fe II 2328.11 Å, Co II 2329.82 Å. We fit these lines and the C II] lines with Gaussians, the fit can be seen in Fig. 6.12. In this fit the FWHM of the wind-scattering lines is fixed to 0.14 Å (measured from the lines) and the FWHM of the C II lines is fixed to 0.1 Å. This leaves ten free parameters in the fit, the relative intensities of the nine lines, and any systematic offset in the line-centres (this effect is found to be negligibly small). The peak of the feature at 2328.11 Å is removed from the fit, this is coloured red in Fig. 6.12. We note, as can be seen in the lower panel of Fig. 6.12, that this region is flagged in the error array associated with this observation. This region corresponds to an interstellar

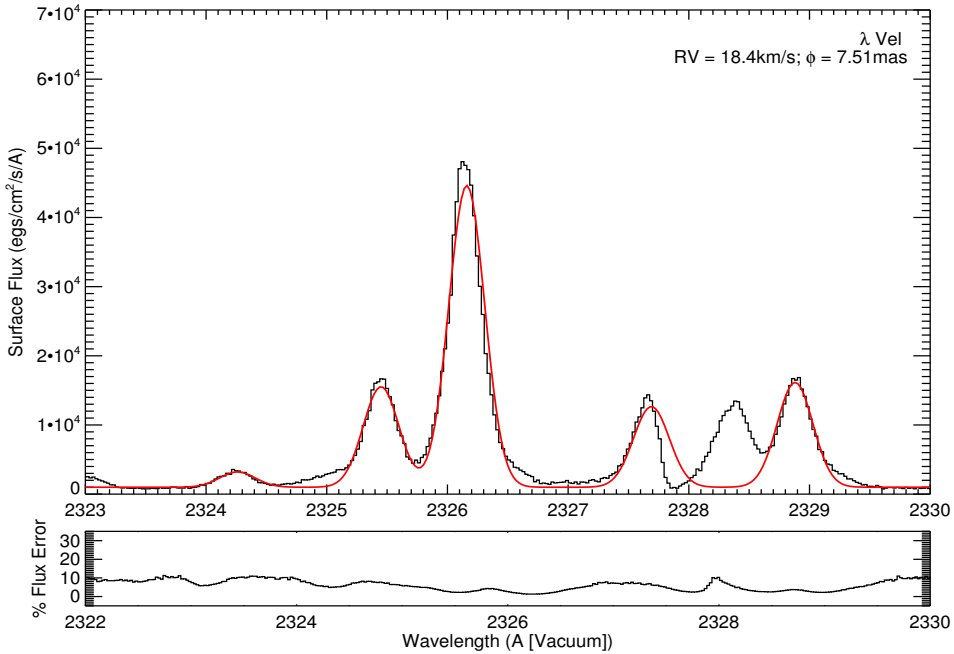


Figure 6.13: Gaussian fits to the lines of the C II] quintet in the spectrum of λ Velorum. The observed spectrum can be seen in black, and the Gaussian fits in red. The continuum is fitted, and offset from zero by 1×10^3 ergs/cm²/s/Å. The lower panel shows the percentage error in the observed fluxes.

absorption line, Fe II 2328.112Å.¹ As a result we removed this region from the fit in order to better match the width of the feature.

With Gaussians fit to the C II] quintet lines we can then quantify the flux ratios. In the ζ Aurigae spectrum we only fit four lines, as the line at 2327.64 Å is removed in the deblending. In the λ Velorum spectrum we fit all five lines of the quintet, any systematic offset in the line-centres (which is found to be negligible), and the level of the continuum. The λ Velorum fit can be seen in Fig. 6.13. We use these Gaussians to compute the flux ratios, for both spectra the ratios are tabulated in Table. 6.4. In Fig. 6.14 we have plotted the density sensitive ratios on the isothermal curves, computed by the mean-escape probability method (see Fig. 6.7). We see that in for both objects these ratios match well, and we note that

¹This was corroborated by another absorption line of Fe II at 2333.5156Å.

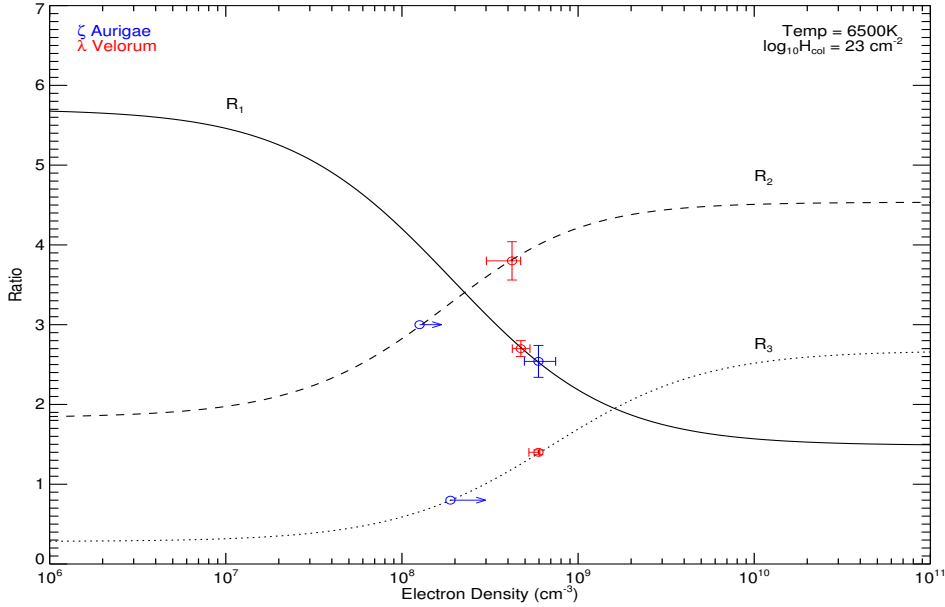


Figure 6.14: The density-sensitive CII] ratios, as computed from the Gaussian fits to the spectra, plotted on the line ratios as a function of electron density (for a fixed column density (10^{23}cm^{-2}) and temperature (6500 K)). The points with arrows denote upper limits. The line ratios are computed using the mean-escape probability method using the data of Tayal (2008), see Fig. 6.7

Table 6.4: The electron densities predicted from the measured HST GHRS CII] line ratios. We note that this diagnostic predicts similar electron densities for both λ Velorum and ζ Aurigae. Neither R_4 nor R_5 is density-sensitive, they are sensitive to the optical depth. We note that these ratios also match one another.

Ratio	ζ Aurigae	n_e (cm^{-3})	λ Velorum	n_e (cm^{-3})
R_1	2.54 ± 0.24	$5_{-1}^{+1.5} \times 10^8$	2.7 ± 0.1	$4_{-0.5}^{+0.6} \times 10^8$
R_2	> 3	$> 1 \times 10^8$	3.8 ± 0.24	$3.5_{-1.2}^{+2.3} \times 10^8$
R_3	> 0.8	$> 1.8 \times 10^8$	1.4 ± 0.029	$6.3_{-0.7}^{+0.01} \times 10^8$
R_4	12.7 ± 0.85	—	12.3 ± 2.3	—
R_5	1.5 ± 0.13	—	1.1 ± 0.04	—

the density-sensitive lines predicts similar electron densities for both λ Velorum and ζ Aurigae. Neither R_4 nor R_5 is density-sensitive, they are sensitive to the optical depth. We note that these ratios also match one another.

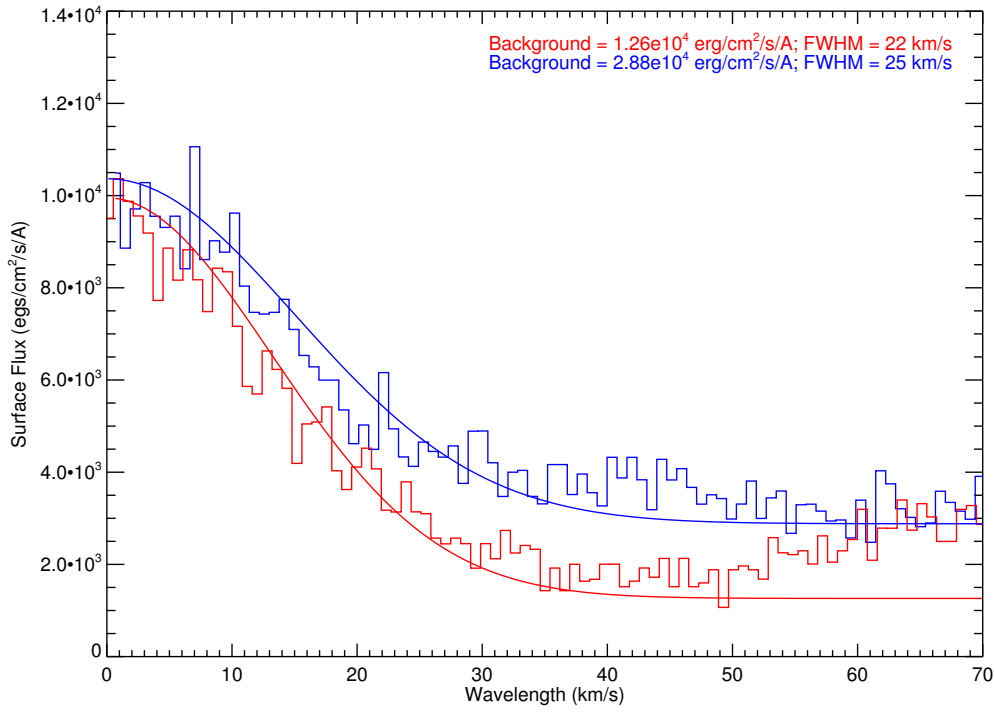


Figure 6.15: Asymmetry in the ζ Aurigae Al 2669Å line profile. Here we see the line plotted, on a velocity scale with the red-ward and blue-ward fluxes plotted (coloured accordingly). We see a clear excess on the blue side of the line (shorter wavelength, higher frequency, than line center). Both are fitted with Gaussians to quantify the asymmetry. The background and the FWHM of the Gaussians are annotated.

Another important remark about these spectra is the asymmetry in the Al II] 2669Å feature in ζ Aurigae. This can be seen more clearly in Fig. 6.16. In this figure we see the line on a velocity scale with the red-ward and blue-ward fluxes plotted, and we can see the obvious excess in flux shortward of line centre. This may be due to a large scale outward flow in the line-forming region, perhaps the acceleration of the stellar wind. We see the excess most prominently at velocities of ~ 40 km/s. However the wind velocity relation given by Baade *et al.* (1996), in the acceleration region $r < 2R_*$,

$$v(r) = v_\infty \left(1 - \frac{R_*}{r}\right)^\beta \quad (6.49)$$

where $v_\infty = 70 \text{ km/s}$ and $\beta = 3.5$, gives $v < 7 \text{ km/s}$. The wind acceleration argument is also weakened by the fact that the CII] 2326.11Å line displays a similar asymmetry, however it is reversed, with a prominent red-ward excess, indicating a down-flow. The CII] 2326.11Å line asymmetry is perhaps a more complex matter than the case of AlII] 2669Å. The observations of α Tau made by Judge (1994) showed red-shifted emission which was interpreted as a down-flow of dense material, and a later set of HST observations made by Judge & Carpenter (1998b) showed this red-shift to be ubiquitous among the objects studied. This could be evidence of anisotropy in the chromosphere. This unusual effect was propagated through to the measurement of electron densities by this diagnostic (Judge, 1994). By measuring the density sensitive ratios across the line profiles higher electron densities were found in down-flowing material, which may be evidence of “physically separate packets of emitting gas on the star with different electron densities” – a multi-component atmosphere. This idea of “clumping” in the chromosphere is also invoked by Eaton (2008), again as an attempt to reconcile observation with the inferred electron densities. This is discussed in more detail later in this chapter and in the final chapter.

In our case it may be that the asymmetry in the lines can be attributed to the scattered flux of the B-star. Returning to the scattered light spectra of Bennett (2015) (Fig. 6.11), we see that there appear to be wind-scattering lines which match with the asymmetries in our profiles. There is a Cr II line at $\lambda 2669.5\text{\AA}$ which may explain the blue-ward asymmetry in our AlII] 2669Å profile, and a number of Fe II and Cr II lines red-ward of the CII] 2326.11Å line which may explain its asymmetry.

6.4.2 Synthetic Spectra

We use these HST spectra to improve our atmospheric model. Beginning with the initial model atmosphere outlined in Section 1.2, and the atomic model described in Section 1.3, synthetic spectra were computed using RH. Comparing these calculations to the observations they were found to overestimate the flux of both spectra

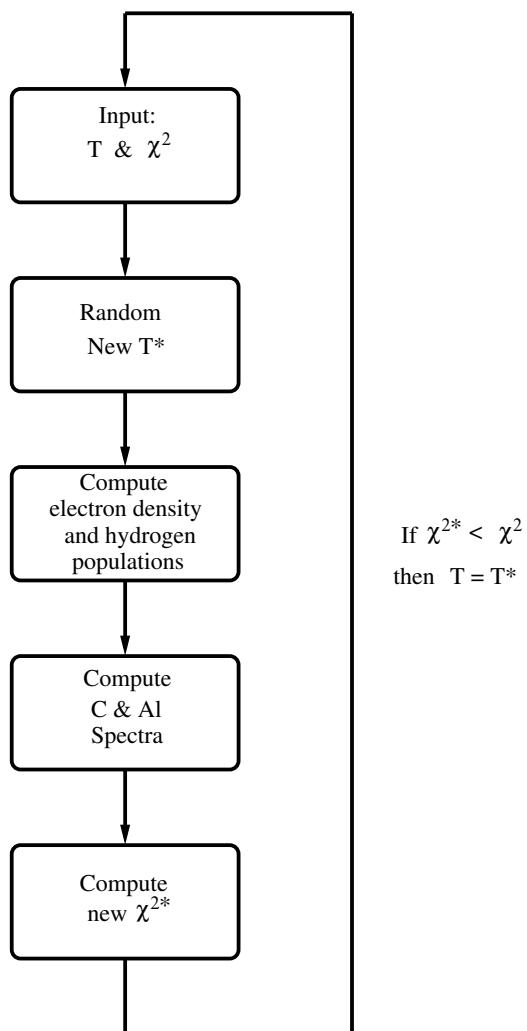


Figure 6.16: Flowchart describing the Markov Chain process by which the atmosphere is adapted to better fit the HST spectra.

by an order of magnitude. Hence it was necessary to alter the model atmosphere in order to better fit the HST observations. To do this a simple Markov Chain algorithm was constructed. The algorithm is described in the flowchart in Fig. 6.16, it operates as follows:

1. We begin with the initial model atmosphere outlined in Section 1.2, and use RH compute synthetic spectra for C & Al. These fluxes are compared to the HST fluxes and a χ^2 value is calculated.

2. A new temperature grid is then randomly generated from the input grid. The grid is only altered above the temperature minimum (since our diagnostics provide us no information below T_{\min} it is fixed from the MARCS model), and is done in such a way as to be smooth, preserve monotonicity, and such that the temperature at the top of the atmosphere does not exceed 15000 K.
3. For this new temperature grid, T^* , we then compute a self-consistent electron density and NLTE hydrogen populations by the iterative method outlined in Section 6.2.4.
4. Using this new model we compute new synthetic spectra for C & Al using RH, and a new χ^2 value, χ^{2*} .
5. If $\chi^{2*} < \chi^2$ then the new model atmosphere is used as the initial model for the next iteration, if not we retain the old model. We return to step 2, and the loop begins again.

This loop is continued until the model is sufficiently close to the data. In practice, given our initial model, < 100 iterations are required to find an atmosphere which well fits the data, corresponding to < 1 hr of computing time on 4 Intel Xeon (2.4 GHz) cores. This method has the benefit of allowing us to vary the input parameters and quickly search the solution space for models which well fit the observations.

We must also take care to broaden the synthetic spectra according to the instrumental effects present in the HST data, and the line broadening which arises due to the rotation of the objects. The rotational broadening is computed by a similar method to that described in the case of line reflection in the previous chapter; the only difference being that we do not assume a Gaussian line profile, but rather use the computed line-profile from RH. We use a rotational velocity of $v_{\text{rot}} = 6.9$ km/s for ζ Aurigae A, as discussed in the preceding chapter. To account for the instrumental broadening we apply the line spread function of Ech-B. The effect of HST line broadening is discussed in detail in the Instrumentation chapter.

We must also take account of interstellar reddening. This is achieved by the method outlined by Cardelli *et al.* (1988, 1989). This method allows us to compute

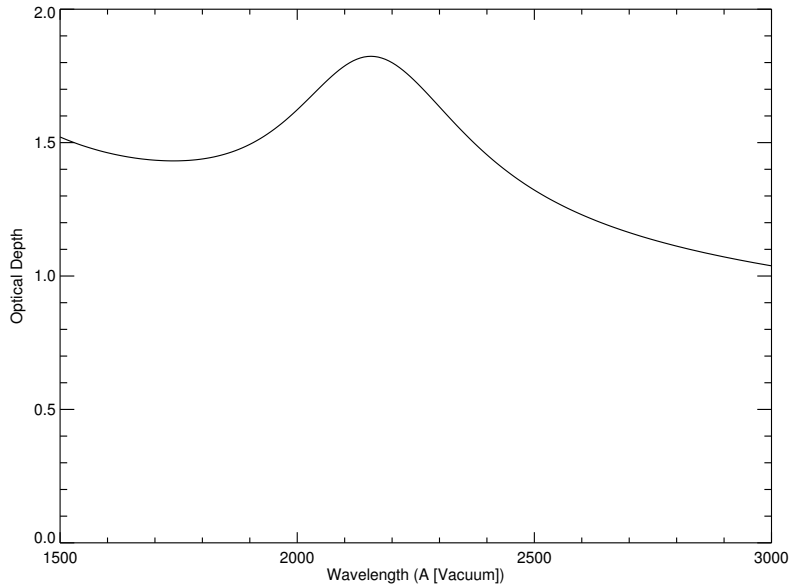


Figure 6.17: The optical depth due to interstellar dust as a function of wavelength. We can prominently see the well-known 2175Å feature (Stecher & Donn, 1965).

the coefficients $a(\lambda)$ and $b(\lambda)$, which are in turn used to compute

$$\frac{A_\lambda}{A_V} = a(\lambda) + \frac{b(\lambda)}{R_V} \quad (6.50)$$

where A_λ is the extinction at a given wavelength, A_V is the extinction in the V-band, and R_V is equal to

$$R_V = \frac{A_V}{E(B - V)} \quad (6.51)$$

We set $R_V = 3.1$ (Cardelli *et al.*, 1988), and $E(B - V) = 0.2$ mag (Schlegel *et al.*, 1998). Finally we can determine the optical depth by

$$A_\lambda = 2.5 \log_{10}(e) \tau_\lambda \quad (6.52)$$

In Fig. 6.17 we see the optical depth as a function of frequency. As we are working with narrow wavelength regions the interstellar material introduces very

6.4 Spectral Observations

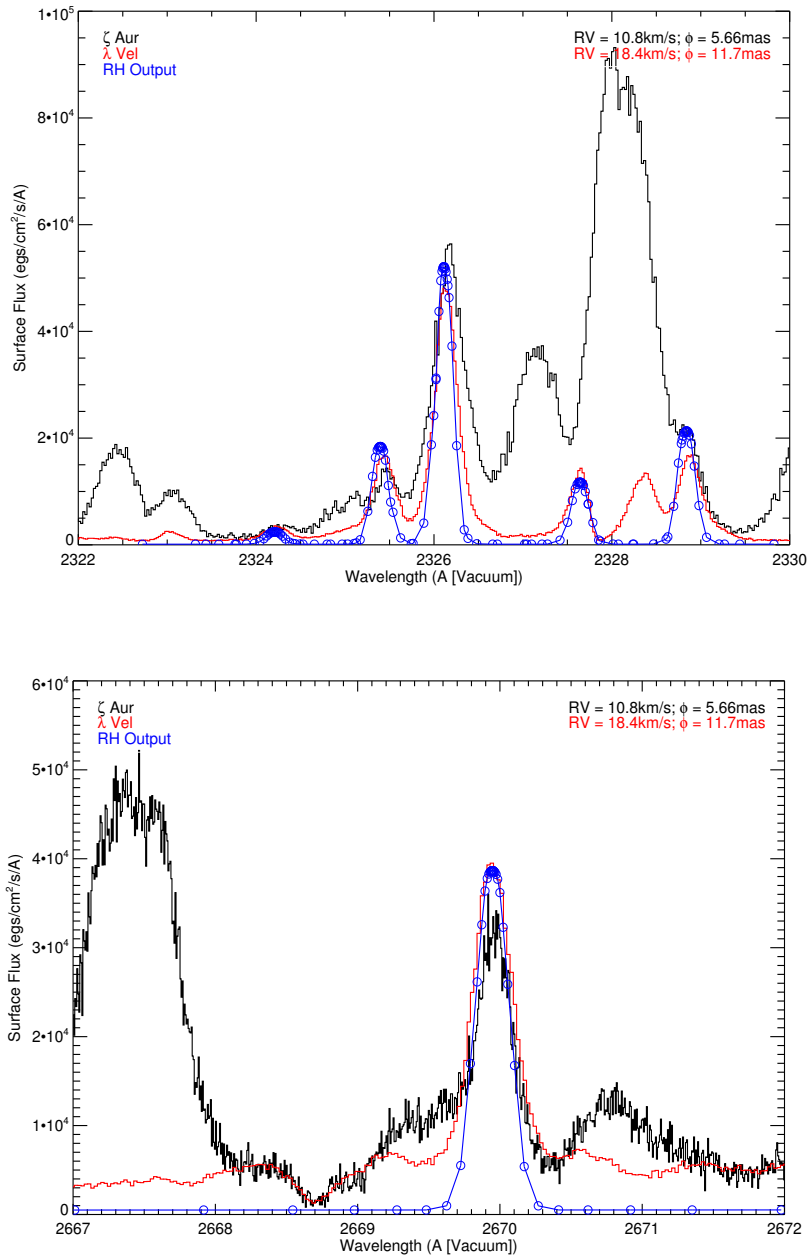


Figure 6.18: Synthetic spectra from the best fit ζ Aurigae atmosphere plotted with the HST GHRS ζ Aurigae Epoch 8 spectra and the HST spectra of λ Velorum.

little reddening or asymmetry, and solely acts to reduce the flux.

The synthetic spectra resulting from the best fit model atmosphere can be seen in Fig. 6.18. As we can see the model atmosphere provides a good fit for both the CII] quintet and the AlII] emission line. We will discuss this model in detail in the next section.

6.4.3 Contribution Function

In Fig. 6.19 we show the radial contribution function, as a function of height, for the CII] quintet and the AlII] 2669Å line. The contribution function is a measure of the contribution to the emission from a given height in the atmosphere, given by

$$C_\nu(r) = S_\nu(r)e^{-\tau_\nu} \quad (6.53)$$

where $C_\nu(r)$ is the contribution function as a function of radius, $S_\nu(r)$ is the source function at a given radial height, and τ is the optical depth at a given height. This is the integrand of intensity. We construct the optical depth from the background and line opacities

$$\tau_\nu = \int_0^r (\chi_l + \chi_b) ds \quad (6.54)$$

and the source function is given by

$$S_\nu = \frac{\eta_b + \eta_l + J_\nu \epsilon_\nu}{\chi_b + \chi_l} \quad (6.55)$$

where η_b and η_l are the background and line emissivities, respectively, J_ν is the mean intensity, and ϵ_ν is the scattering cross-section. These values are extracted from the model, for the final, converged solution of the radiation field.

We can see from these contribution functions that the lines form at similar radial heights, at the lower end of our model atmosphere, at a height of $h \approx 50R_\odot$ ($\sim 0.3R_*$). It is important to consider the broad region over which the CII] quintet lines form. As a result of their forming across this region, which encompasses material of different temperatures and electron densities, the ratios of these lines will not provide a density representative of a single point in the chromosphere, but rather a weighted average of the electron density across the line forming region.

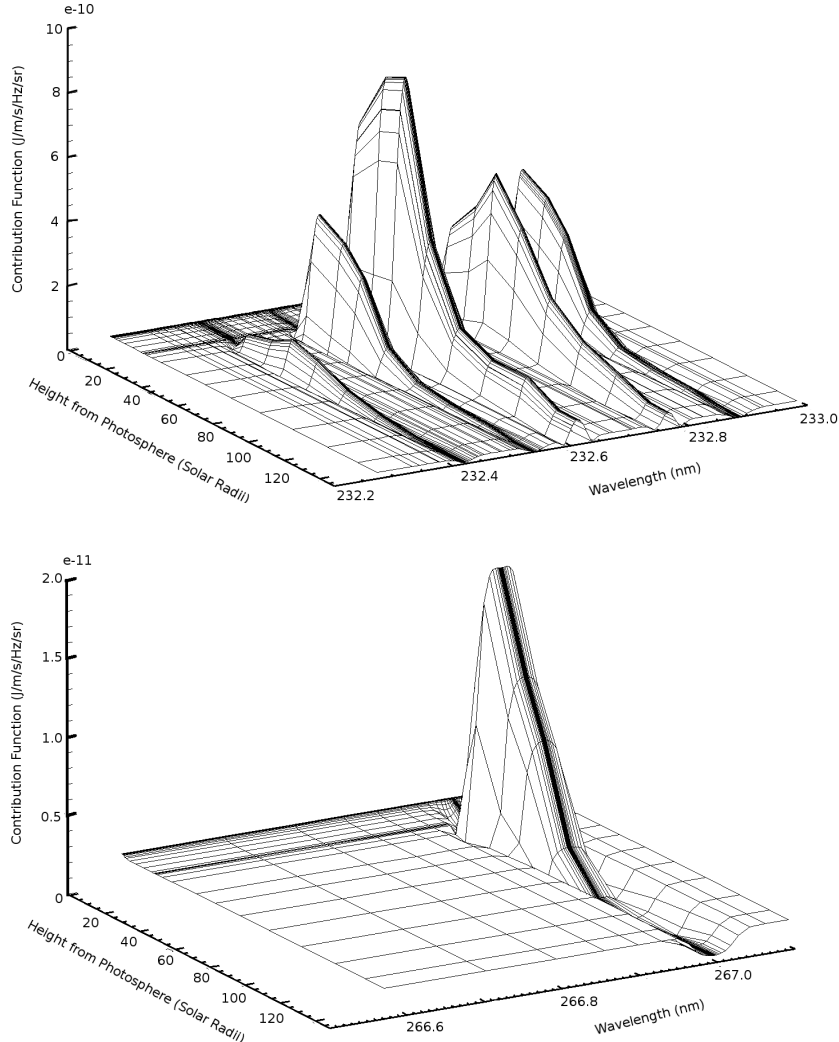


Figure 6.19: Top: Contribution function of the C II] quintet. Bottom: Contribution function of the Al II] line. We note that both of these features appear to form at similar heights in the atmosphere.

6.4.4 λ Velorum Ca K & H- α Profiles

To conclude our analysis of spectra, we will briefly discuss the H- α and Ca II K profiles of λ Velorum. Observations of these profiles were made by Zarro & Rodgers (1983) as part of an atlas of 85 objects. In Fig. 6.20 we see their observations, as well as the computed profiles. In both of these figures the H- α profile is normalised

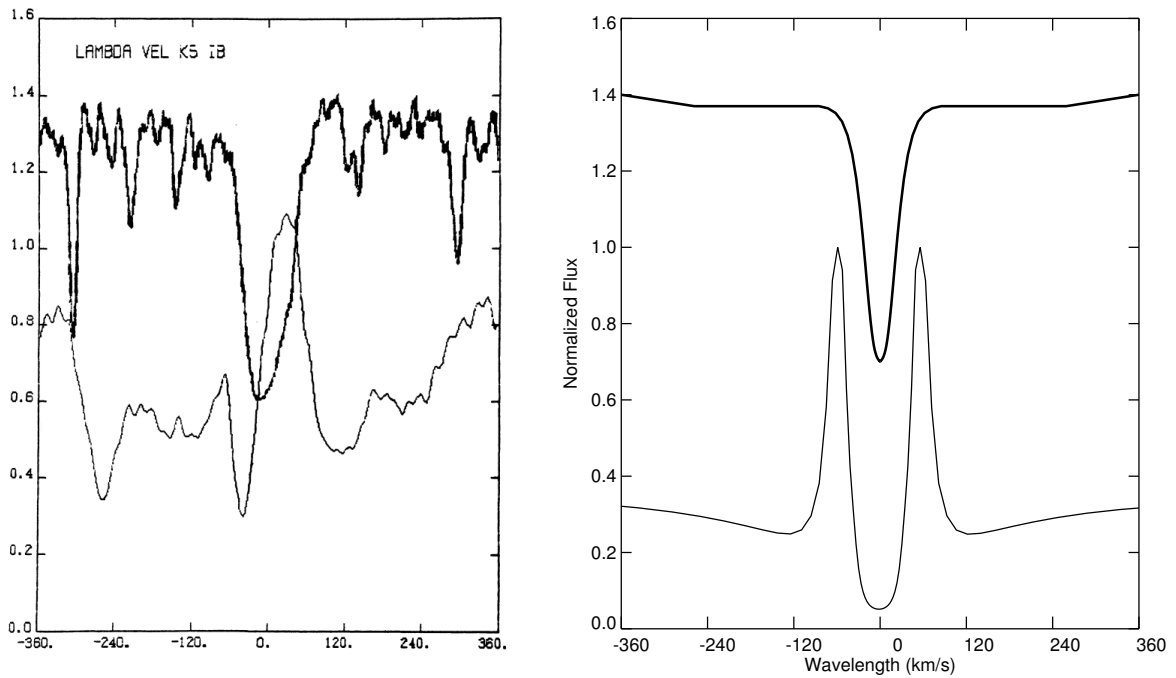


Figure 6.20: *Left:* H- α and Ca II K profiles of λ Velorum taken from the atlas of Zarro & Rodgers (1983). The H- α is on top, and in the thinner line style, the Ca II below. *Right:* The computed H- α and Ca II K profiles, using the same line styles.

to its continuum, and then offset by 0.4 (i.e. the continuum is set to 1.4). The Ca II K of Zarro & Rodgers (1983) is normalised to the continuum flux at $\lambda = 3939.682\text{\AA}$. Since this normalising factor is not provided we simply normalise ours to the peak of the K_{2v} feature. These profiles were computed using the same H atom as used in the n_e calculation, and a Ca atomic model provided by Han Uitenbroek (Uitenbroek, 1990, 2014). Both sets of calculations were performed using the assumption of PRD, which is vital in providing accurate line widths. The profiles are again rotationally broadened, and the instrumental broadening is accounted for by convolution with a Gaussian with FWHM = 13.5 km/s, as it is by Zarro & Rodgers (1983). These profiles allows us to make some simple, qualitative comparisons to the data. The H- α profile appears to reproduce the contrast between continuum and line core. The contrast between K_3 and K_{2r} in the Ca II K profile does not appear to be reproduced well, however given the

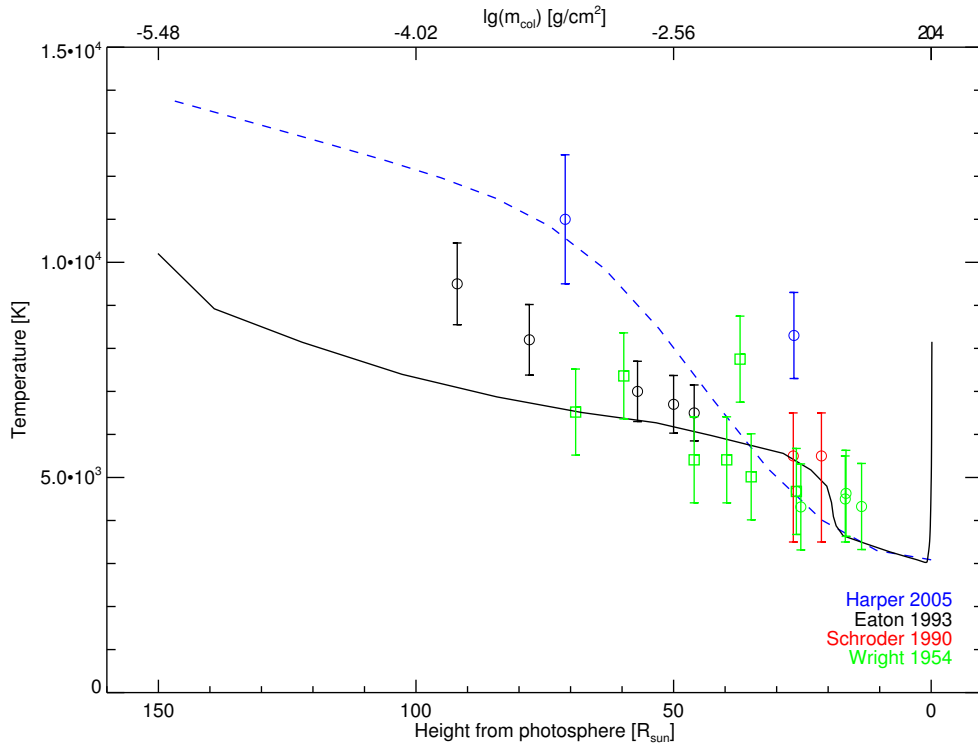


Figure 6.21: The run of temperature with height, and mass column density, for the best fit model atmosphere. The model is plotted in black, with the empirical data points plotted as annotated, and the empirical wind law – which was used as the initial temperature – is plotted in blue.

clear asymmetry in the profile (which as before, given the absence of flows in our atmosphere, cannot be reproduced), and in the absence of a true flux scale it is difficult to comment on this inaccuracy. In both cases the line widths appear to be consistent with observation.¹

6.5 Chromospheric Model

6.5.1 Best-fit Chromospheric Model

By the method outlined above a chromospheric model was constructed which fits well with the HST observations. The temperature structure of this atmospheric model, plotted as a function of height¹ and mass column density, can be seen in Fig. 6.21. In this figure we see, plotted in blue, the empirical temperature relation of Harper *et al.* (2005), which was used as the initial input temperature of the model. As we see, this temperature relation lies above the empirical data points for heights above $h \approx 30R_\odot$ ($\sim 0.2R_*$). It was found that the synthetic spectra computed using this temperature grid overestimated the line flux by over an order of magnitude. We can see that in order to bring the synthetic spectra into agreement with observation it was necessary to reduce the temperature of the atmosphere, and we see that the best fit temperature grid in fact falls below the temperature points higher in the atmosphere, in particular those of Eaton (1993). While examining these data we must remember that the temperatures measured by Eaton (1993) are excitation temperatures, T_{exc} , while the values that we use in our calculation are electron temperatures, T_e . These values are likely to be equal, given that many of the lines analysed by Eaton (1993) are metastable and would be expected to be collisionally excited and hence in thermal equilibrium with the electrons (Jordan & Avrett, 1973; Judge *et al.*, 1992; Thomas, 1957). However this assumption breaks down in the higher chromosphere, where, as the optical depth and, vitally, the electron density decrease, the radiation of the B-star will cause the excitation temperature to exceed the electron temperature (Eaton, 2008). This may explain why, as we move higher in the chromosphere, our electron temperature is below the measured excitation temperature.

It was also necessary to reduce the turbulent velocities higher in the atmosphere in order to reproduce the observed line widths. We see, in Fig. 6.22, the run of turbulent velocity with height which fits the line widths observed. The initial

¹In the case of the CaII K profile the line width is measured between the violet and red edges of the emission components (Wilson & Vainu Bappu, 1957).

¹We note here that the upper photosphere is defined, in our radiative transfer model, as the height where the optical depth at 5000Å drops below unity, $\tau_{5000} = 1$

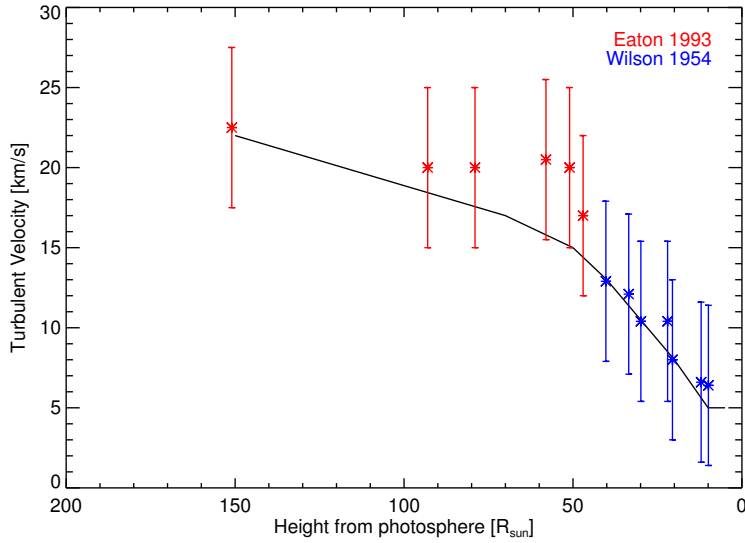


Figure 6.22: The run of turbulent velocity with height for the best fit model atmosphere. Note that it was necessary to reduce the turbulent velocity in the line-forming region ($h \sim 10 - 40 R_{\odot}$) to reproduce the observed line widths.

turbulent velocities adopted, which attributed equal weight to the observed points of Eaton (1993) and Wilson & Abt (1954), overestimated the line widths, and as a result it was necessary to reduce the values in the line-forming region ($\sim 10 - 40 R_{\odot}$) to better fit the observations. This brings the turbulent velocities into closer agreement with those of Wilson & Abt (1954).

Finally in Fig. 6.23 we see the temperature grid plotted along with the electron density computed from it. We also show the empirically measured temperatures (black) and electron densities, (red — these values are the same as those plotted in preceding sections, please refer to those plots for annotation.)

The greatest source of disagreement between our model and the data is in the electron density measurements in the mid-chromosphere. At a height of $\sim 100 R_{\odot}$ Eaton (1993) measures an electron density of $9 \times 10^9 \text{ cm}^{-3}$ and $2 \times 10^9 \text{ cm}^{-3}$, where our model predicts an electron density in the region of 10^7 cm^{-3} . We must bear in mind however that the values measured by Eaton (1993) were based on the ionization balance of only two elements at these heights, the ratios of CI/CII and NI/NII (at other heights 5 elements are used to determine the electron density).

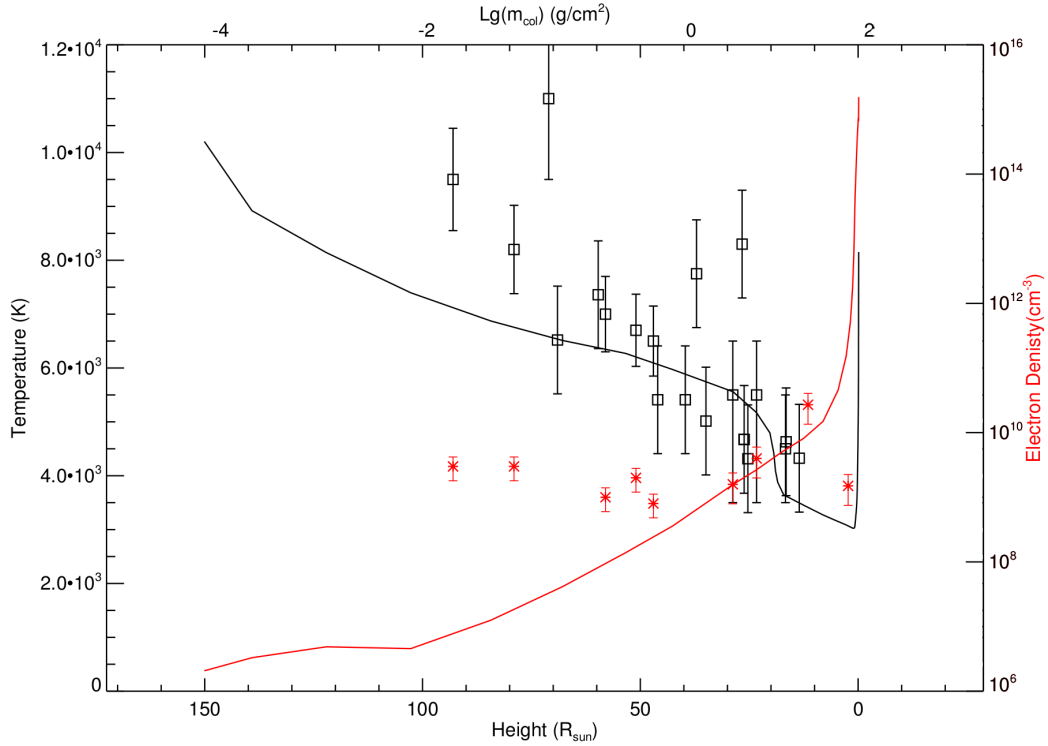


Figure 6.23: The best fit temperature grid, with the resultant electron densities, plotted against height. the empirically measured temperatures, black, and electron densities, red. The values plotted are the same as those used in preceding sections, where the plots are fully annotated.

These values also appear to be too large to fully agree with the measured temperature and hydrogen densities at this height (particularly the higher point), given the determined temperature is 10000 K we should expect that H be fully ionised and be the main contributor to the electron density. However at this height Eaton (1993) predicts a H density of order 10^8 cm^{-3} , insufficient to provide an electron density of $9 \times 10^9 \text{ cm}^{-3}$ predicted by the CI/CII ratio¹.

Interestingly, the detection by IUE of the wings of Ly- α high in the chromosphere, as well as the similarity of the mass column densities derived from H with those derived from Fe II (these points are also true of 31 Cyg, as observed in the

¹It is observed by Eaton (2008) that the electron densities determined from photoionization are “rather crude and may be systematically wrong”.

doctoral thesis of K.P. Marshall (1995)) point to H being neutral through the chromosphere. This is in direct contradiction to the standard assumption of semi-empirical models, an assumption made in the first chapter of this work, that as we move higher in the chromosphere the ionisation of H compensates for the declining density, resulting in the electron density remaining roughly constant throughout the chromosphere. This point is examined by Eaton (2008), who seeks to explain this discrepancy between the electron densities computed from the ionisation balance and the neutrality of H by invoking clumping in the chromosphere. This clumping is also invoked to explain the abundance of more highly ionised species in the chromosphere. There may well be a degree of clumping present in the chromospheres of these objects, though the complications introduced through the inclusion of such clumped material fall outside the domain of most semi-empirical models attempted, including this work. The question raised by this clumping argument, whether the chromosphere is a time-independent, homogeneous structure covering the face of the star, is at the core of the work presented in this thesis. While these matters are of great relevance to all the work undertaken in this thesis and will later be addressed in detail in the context of all the evidence presented, based on the analysis of this chapter we believe it is possible to construct a one-component, time-independent model chromosphere which is consistent with observations of ζ Aurigae. We conclude that, while there is evidence of clumping in the chromosphere (particularly in the electron densities), it is possible to reconcile most of the observations of this object with the existence of the homogeneous chromosphere presented in this work.

This atmospheric model is provided in the Appendix.

6.5.2 Chromospheric Extent

One important point on this chromospheric model is its extent, the model outlined here extend to a height of $h \approx 1R_*$ ($\sim 150R_\odot$) above the stellar surface. This extent is in keeping with the IUE data presented by Eaton (1993) which, owing to the chromospheric eclipse, measure column densities far above the photosphere. This is also in keeping with observations of the chromospheric extent of other supergiants (Eaton, 1988; Harper *et al.*, 2001; Lim *et al.*, 1998). It further agrees with the

extent predicted by Carpenter *et al.* (1985) for λ Velorum. There is, however, some debate on the subject of chromospheric extent of late-type stars. For instance, in the case of the McMurry (1999) model of α Tau (K5III), a chromospheric extent of $R \approx 1.2R_*$ is predicted. This matter is further complicated by the findings of Ohnaka (2013), whose VLTI spectro-interferometric observations of α Tau points to a layer of CO, a MOLsphere, at approximately $2R_*$. These findings have since been reproduced for a number of other objects.

A recent study by Berio *et al.* (2011) made spectro-interferometric observations of the Ca II infra-red triplet lines (849 nm, 854 nm & 866 nm) for a sample of coronal and non-coronal giants. Berio *et al.* (2011) found that all of the objects studied showed chromospheric extents of $\sim 1.4R_*$ regardless of spectral type, in direct contradiction of the findings of Carpenter *et al.* (1985) who predict $R \approx 2R_*$ for non-coronal giants, and $R \approx 1.001R_*$ for coronal giants. In particular the results of Berio *et al.* (2011) are in opposition to the semi-empirical model chromosphere of β Ceti constructed by Eriksson *et al.* (1983). Berio *et al.* (2011) measure a chromospheric extent of $\sim 1.16 - 1.47R_*$ for this object, in comparison with the extent, $R \approx 1.02R_*$, of the semi-empirical model of Eriksson *et al.* (1983).

A collaborative visit was spent at the Observatoire de la Côte d’Azur, funded by an award from the Fizeau Optical Interferometry Initiative, to work with P. Berio and other members of the group based at OCA. To examine their results in more detail synthetic spectra were computed for the Ca II infra-red triplet using MULTI (Carlsson, 1986). These calculations were performed using the model chromosphere of Eriksson *et al.* (1983), and a model Ca atom provided by with the MULTI distribution. There are a number of subtle complications in this radiative transfer problem which must be addressed. Of principle importance is treating the Ca II H & K transitions in PRD, as described in Section 1.4.4. Another key matter is the ionisation of Ca II to Ca III by Ly- α & β (Rowe, 1992). This will have the effect of depleting the number of Ca II ions. Finally we must take account of Cross Re-Distribution (XRD - the theory of which is described in the introduction), as both the Ca II H & K lines and the Ca II infrared triplet share a common upper level. MULTI allows us to solve the radiative transfer problem including these subtle effects, at the expense of requiring that the geometry be plane-parallel.

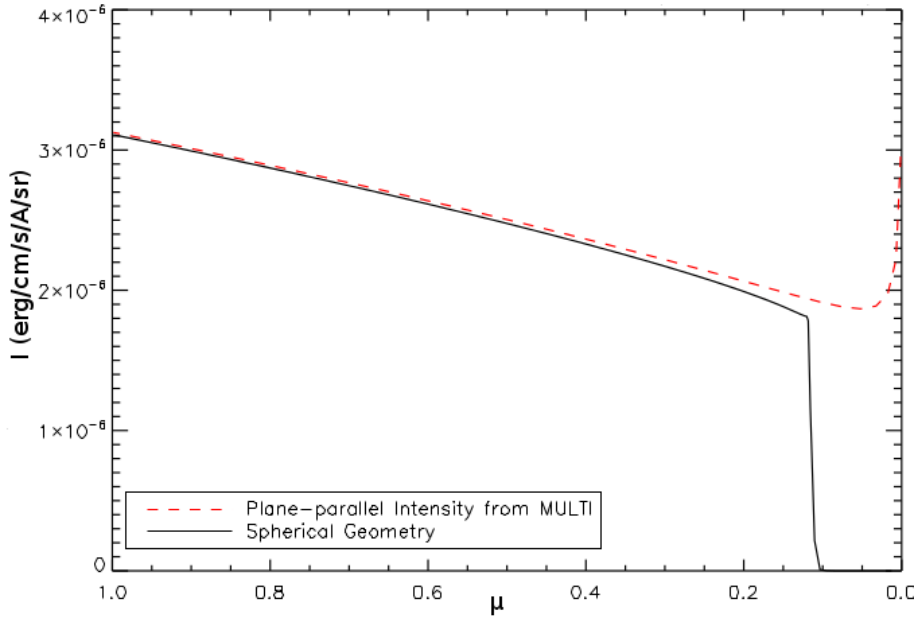


Figure 6.24: Limb darkening curve for β Ceti, computed using MULTI, for the plane-parallel and the spherical case. Note that in the plane-parallel case we see increasing intensity as we move to the limb.

This limitation is important, as in this case we are particularly interested in the rays which emerge from the extended atmosphere (what we called limb rays in the Chapter 4). To overcome this limitation, albeit approximately, we take the emissivities and absorptivities as computed by MULTI, and using a Feautrier solver compute the emergent intensity from a spherical atmosphere with those properties. The results of this calculation can be seen in Fig. 6.24. As we can see there is a great difference between the limb-darkening curves computed for these different geometries, and recall that this function, $I_\nu(\mu)$, is what determines the observed visibility.

Computing $I_\nu(\mu)$ across the Ca II infrared triplet lines, it was found that it was not possible to reproduce the observed visibility using the atmospheric model of Eriksson *et al.* (1983). This leads us to the conclusion that an atmosphere of a very different nature than has previously been assumed may be required for coronal giants such as β Ceti, perhaps with an extent closer to that found in the case of ζ Aurigae A.

6.6 Conclusions

In this chapter we have seen the construction of a semi-empirical, spherical, time-independent model of the chromosphere of ζ Aurigae A. The construction of this model is motivated by the unique importance of the ζ Aurigae system as a laboratory for studying the chromospheres of late-type stars. Due to the eclipsing nature of the binary system it provides extraordinary diagnostic insights into determining the thermodynamic properties of stellar chromospheres. Despite this importance no full model of the system has previously been attempted.

In the construction of this model we collected archival data from many sources, providing a large number of mass column densities, temperatures, and turbulent velocities as a function of height through the stellar atmosphere. An interpolated MARCS model photosphere provides the lower boundary of the atmosphere. These values were then used to compute the electron density throughout the atmosphere, specifying a complete thermodynamic model.

This model was then compared with high spectral resolution HST observations of this object. These observations cover the C II] $\lambda 2325 \text{ \AA}$ density sensitive quintet, as well as the optically thin Al II] $\lambda 2669 \text{ \AA}$ line. In order to compute synthetic spectra for comparison with these observations it was necessary to construct model atoms of C, Al, and H. The spectra computed using our initial model atmosphere and these model atoms was found to overestimate the observed line flux by over an order of magnitude.

In order to bring the computed flux into closer agreement with observation a Markov chain algorithm was employed to quickly adapt the model atmosphere. Using this algorithm it was possible to construct a model atmosphere whose spectra well matched observation. It was found that in order to match the UV line observations the atmosphere must be cooler than the initial model. We also find some discrepancy between the computed and observed electron densities. While it is possible that the observed electron densities are systematically in error (far more so than the temperatures or column densities), this may be evidence of clumping in the chromosphere, or perhaps large scale inhomogeneity. The final model presented is in good agreement with many of the observations of this object, and we suggest that while there surely is a degree of inhomogeneity in the chromosphere

it is of second-order importance, and that much of the evidence can be reconciled with the chromosphere being a single, homogeneous structure of the type outlined in this chapter.

The model atmosphere we have constructed can also be used to comment on single stars. λ Velorum is a close spectral proxy for ζ Aurigae A, and using our model atmosphere we have computed spectra which compare well with observations of the Ca II H and H- α lines from λ Velorum. Furthermore the chromospheric heating of λ Velorum is known to be similar to that of ζ Aurigae A (Eaton, 1992). We suggest that the chromospheric structure of these objects may be very similar.

We find that the chromosphere is quite extended, $h \approx 1R_*$, which agrees well with estimates of Carpenter *et al.* (1985), however it is somewhat larger than the estimates of Judge (1986) and McMurry (1999) for similar objects. Importantly our results are also in opposition to those of Cuntz (1990) ($h \approx 0.05R_*$) for chromospheres of time-dependent, acoustically shocked plasma. As a further counterpoint to our study we examine briefly the recent observations of coronal giants which point to their being more extended (perhaps by a factor of ~ 5) than previously thought. We find in the case of β Ceti that the atmospheric model constructed for this object by Eriksson *et al.* (1983) which well reproduces the UV/optical line spectrum cannot reproduce the spectro-interferometric visibility measured for these lines. This may be due to the atmosphere having a very different structure than was assumed, and perhaps being considerably extended.

7

Conclusions & Future Work

In this final chapter we summarise the work presented in this thesis. We begin by describing the methods and results of each chapter, and outlining the conclusions of each. We discuss how the work of this thesis can be expanded and built upon, both through future observations and further modelling. We then discuss the results of the thesis in aggregate, drawing together the work of each chapter. The principal motivation of this work rests on questions regarding the thermodynamic structure and geometric extents of late-type stellar chromospheres. We discuss the results of the chapters as they comment generally on these thematic questions and form coherent conclusions from the evidence presented.

7.1 Radio Model

In Chapter 4 a simple model for computing the thermal bremsstrahlung, mm-radio flux from the chromospheres of late-type stars was presented. The model described has been published in Harper *et al.* (2013). This model makes use of a number of simplifying assumptions, and is based on previously constructed semi-empirical model atmospheres. In addition to the implicit assumptions of these semi-empirical models, which we address shortly, the primary assumptions of the model are;

- The temperature is approximately linear in radial height throughout the chromospheres of both coronal and non-coronal stars, as it rises from the temperature minimum to 10,000K.
- Due to increasing ionization of hydrogen counteracting the declining density, the electron density remains approximately constant in this region.
- The geometric extent of this region, which is region from which the mm-flux arises, is approximately $9H_\rho$. This corresponds to a height of $\lesssim 0.2R_*$.

These simplifications provide the key to our model. By making these simplifications we state that $S_\nu \propto \tau_\nu$, and in this case the equation of radiative transfer can be solved analytically. We solve the equation of radiative transfer, using the assumption of a spherical atmosphere, and compare the resultant flux with published 250 GHz flux densities (Altenhoff *et al.*, 1994). We see that our model compares favourably with these observations, reproducing the observed values to within $\pm 30\%$. We also compare our model with high signal-to-noise observations taken by E. O’Gorman for this work using CARMA and APEX. Again our model compares well with these values, accurately predicting their fluxes and spectral indices.

From comparison with these samples we can determine the range of validity of our model. We find that the model is most accurate for objects of spectral type K to mid-M, in the frequency range $\sim 100 - 350$ GHz. At lower frequencies, as we enter the $\mu\text{m}/\text{IR}$ region of the spectrum the model begins to break down, perhaps as a result of other emission mechanisms (other than thermal bremsstrahlung)

beginning to become important. At higher frequencies the model again becomes inaccurate, as non-thermal emission from magnetically active regions begins to effect the flux. This is particularly true for stars of an earlier spectral type or coronal giants, hence our caveat that the model is most robust in predicting the flux from K type objects. We find that our model is capable of reproducing the mm-flux from quiet regions on the Sun, and is in fact calibrated using these values, however it is found to underestimate the observed flux from τ Ceti, a solar-type star whose thermal mm-flux was recently measured. This may be as a result of active regions on τ Ceti enhancing the flux. We also find that for objects of later spectral type than mid-M the model is incapable of providing accurate predictions, as the chromospheres of these objects may be of a very different structure, being modified by stellar pulsations. Within its region of validity however, the model is capable of accurately reproducing the observed flux. In addition the model provides a good estimate of the spectral indices of these objects, which is in effect a measure of the temperature as a function of optical depth.

The model also allows us to make predictions regarding the distribution of flux across the stellar disk, which could be compared with results from the current generation of interferometers. The angular resolution of a two-element interferometer is:

$$\theta = 1.22 \left(\frac{\lambda}{B} \right) 4.84 \times 10^{-9} \quad [\text{mas}] \quad (7.1)$$

where θ is the angular resolution, λ is the wavelength of the observation, and B is the baseline. In the case of CARMA, observing at 225 GHz with a baseline of 1883 m, an angular resolution of 140 mas can be achieved, insufficient to image the disks of the objects discussed in this chapter. In the case of ALMA, observing at the same wavelength, with a baseline of 16 km an angular resolution of 17 mas is possible, sufficient to begin to probe the flux density distribution and chromospheric extents of these objects. The JVLA can offer similar resolutions, however it is limited to frequencies lower than 50 GHz and as established, the validity of the model at these frequencies is uncertain. However, despite the model being unable to reproduce the flux at these wavelengths, perhaps due to coronal emission, the geometric extents predicted may be reliable.

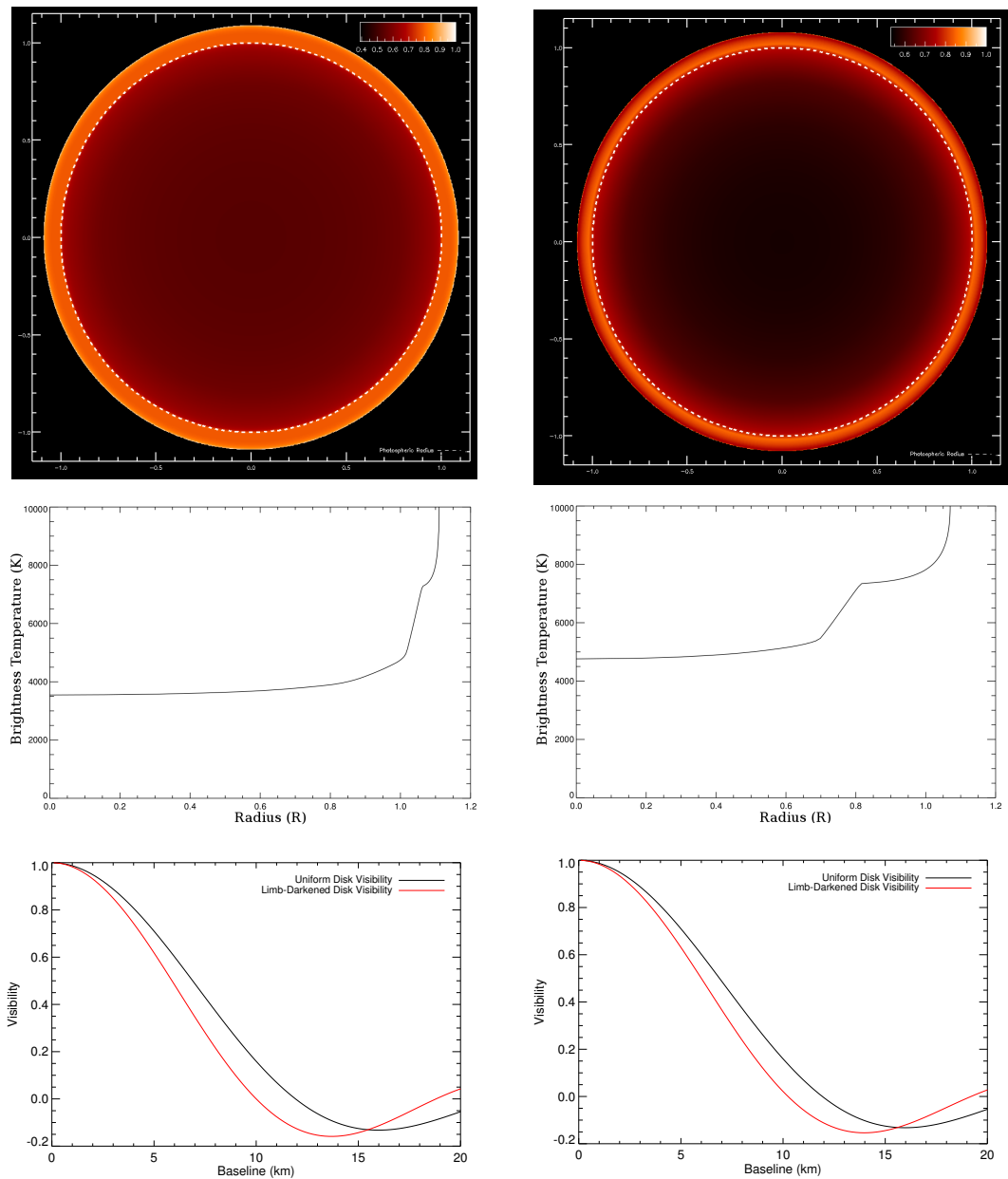


Figure 7.1: *Top Panels:* The computed normalised brightness temperature distribution of α Tau (left) and α Boo (right) at 250 GHz. The photospheric radius is denoted by a dotted line. *Middle Panels:* Limb-darkening curves computed which were used to produce the images. *Lower Panels:* Visibility curves for both objects, showing the uniform disk visibility (black), and the visibility given the computed limb-darkening curve (red).

Two promising candidates for interferometric imaging are α Boo and α Tau. α Boo is the closest and brightest non-coronal red giant, and with an angular diameter of $\phi = 21.37$ mas is the best example of a red giant whose atmosphere can be studied in detail with ALMA. α Tau, despite being almost twice as far away as α Boo, has a comparable angular diameter, $\phi = 21.1$ mas, and is another candidate for interferometric imaging. In Fig. 7.1 images are presented of both objects. These computed model images display the brightness temperature, which can be readily converted to flux, at 250 GHz for both objects. The middle panels of this figure display the computed limb-darkening curves used to produce the images. We can readily see limb-brightening in both cases, more particularly in the case of α Tau. This is due to the limb rays passing through material with a different, hotter temperature profile than radial or on disk rays. We can also see the extension of the atmosphere above the photospheric radius, 11% in the case of α Tau, and 8% in the case of α Boo.

The lower panels show the visibility curves for the two objects, where the visibility is given by

$$V = \frac{1}{A} \int_0^1 I_\nu(\mu) J_0(2\pi\phi q) \mu d\mu \quad (7.2)$$

where $I_\nu(\mu)$ is the monochromatic limb-darkening curve, ϕ is the radius in radians, J_0 is the zeroth-order Bessel function, q is the baseline in units of the observing wavelength, and A is a normalising factor, the value of the integral evaluated at $J_0(2\pi\phi q) = 1$. The theory underlying this is discussed in detail in the introductory chapters. We can readily see from these curves how, using ALMA, an atmosphere of the structure and extent outlined in our models can be differentiated from an atmosphere which does not feature a chromospheric temperature rise, and as a result has a more uniform brightness temperature. Observations of this type would allow us to test the validity of our model, and place direct constraints on the temperature and distribution of plasma in stellar chromospheres.

7.2 Periodic Si I Emission

In Chapter 5 of this thesis we examined the phenomenon of periodic Si I emission from ζ Aurigae binaries. Emission was observed by R.E.M. Griffin in two lines of Si I, $\lambda 3905\text{\AA}$ and $\lambda 4102\text{\AA}$, in the spectrum of ζ Aurigae. This emission was seen to vary periodically throughout the orbit of the system, being at its strongest when the B-star is between the K-star and the observer, and at its weakest when the B-star is eclipsed. The phase modulated emission was also seen in other binary systems, 31 Cyg, 32 Cyg, and HR 2030. We propose that this emission arises from the lower chromosphere of the K-star, and is due to the UV flux of the B-star photoionising Si I, which then undergoes recombination, and after radiative cascade, emission in one of the two observed lines. As the portion of the K-star visible hemisphere illuminated by the B-star radiation varies as a function of phase the Si I emission is periodic.

We determine the strength of this emission can not be explained by simple reflection, however we expected that it will have the same phase variation as broadband reflection. In order to examine the reflection effect we constructed a model of the ζ Aurigae system using PHOEBE. PHOEBE models both the orbit geometry, taking account of the morphology of the component stars, and the radiative properties, allowing us to produce a synthetic V-band light curve. The model constructed compares very well with observations of this system. We use this model to compute the phase variation of the broadband reflection effect, and compare this to the phase variation of the EEW of the Si I $\lambda 3905\text{\AA}$ line. Our model was found to match the observation very well, indicating that our line-formation hypothesis is accurate, and that the line's periodicity can be well explained by the system geometry, without appeal to the effects of more complex radiative transfer or atomic physics.

We make use of the novel diagnostic properties of this spectral line to compute the rotational velocity of the K-star. As this line is formed on only a portion of the K-star's surface at a given phase it effectively provides us with spatial resolution on this otherwise unresolved object. By studying the Doppler shift of the line, as the "hot spot" where it forms moves across the stellar surface, we computed a rotational velocity for the K-star which agrees well with the values in the literature.

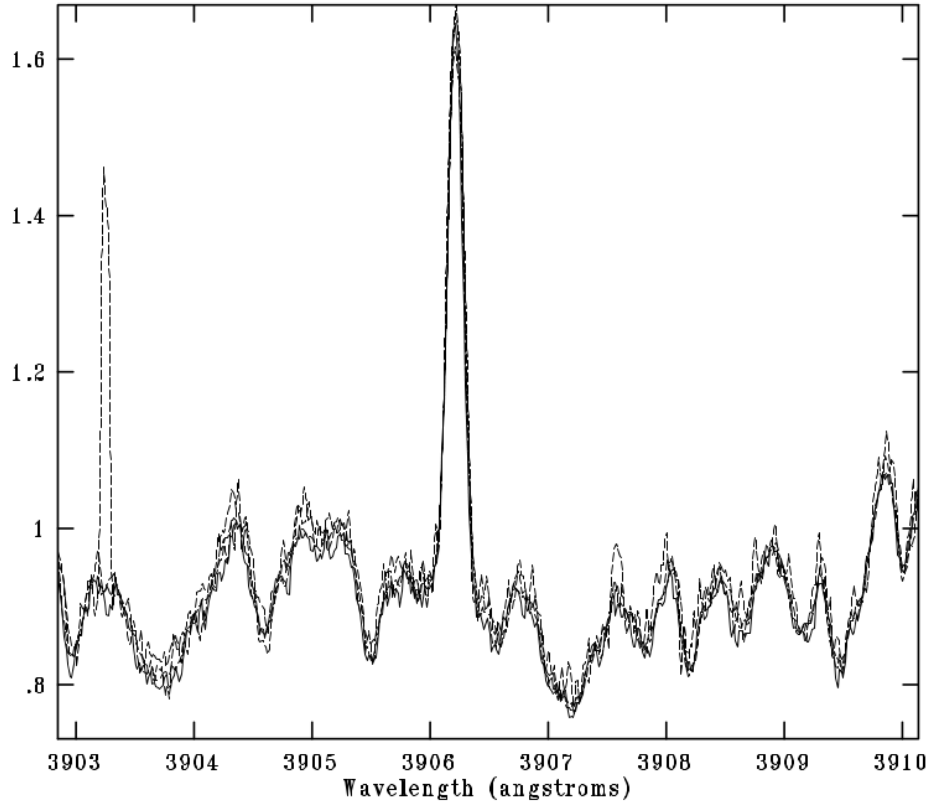


Figure 7.2: Spectra of ζ Aurigae, collected by O. Hashimoto using the Gunma Astronomical Observatory Echelle Spectrograph. Wavelengths are given in air.

In order to make best use of this unique and powerful diagnostic high spectral resolution observations are required. In April 2015 (phase, $\phi = 0.197$) spectra were collected by O. Hashimoto using the Gunma Astronomical Observatory Echelle Spectrograph (GAOES). These spectra can be seen in Fig. 7.2. These spectra were collected at very high resolution, $R = 100,000$, with a number of other spectra collected at $R = 70,000$. They were collected as part of an ongoing programme to study the formation of this emission feature in the spectrum of ζ Aurigae. By making observations such as these as a function of phase we can greatly improve our understanding of this object. At high resolution, this diagnostic can be used to place constraints on the oblateness of the K-star, determine the

local turbulent velocity across the disk of the star, and establish whether or not pseudo-synchronization and rotational alignment have occurred in this system. By carefully studying the line-formation mechanism these observations can be further used to glean unique insights into the thermodynamic structure of the K-star's chromosphere.

7.3 Chromospheric Model of ζ Aurigae A

In Chapter 6 of this thesis the construction of a one-component, spherical, semi-empirical model atmosphere for the primary of the ζ Aurigae system was described. This model was based on archival eclipse observations of this object, which provide us with mass column densities, temperatures, and turbulent velocities as a function of height above the photosphere. In addition to these empirical quantities a MARCS model photosphere was interpolated to provide the lower boundary. Using these atmospheric parameters, values of electron density throughout the atmosphere were computed, hence specifying all of the required thermodynamic properties.

This model chromosphere was compared with high spectral resolution HST observations of ζ Aurigae. These observations cover the C II] $\lambda 2325\text{\AA}$ density sensitive quintet, and the Al II] $\lambda 2669\text{\AA}$ line. In order to compute synthetic spectra for comparison with these observations it was necessary to construct model atoms of C, Al, and H. The spectra computed using our initial model atmosphere and these model atoms was found to overestimate the observed line flux by over an order of magnitude. The model atmosphere was altered to bring it into better agreement with observation, and this was achieved through a simple Markov chain algorithm.

In order to fit the spectral observations it was necessary to lower the temperature in the mid-chromosphere. The final model was found to be in good agreement with previous observations of ζ Aurigae, though there appears to be some discrepancy between our computed electron densities and those determined from the ionization balance. This may be due to systematic errors in the measured electron densities, or perhaps evidence of clumping in the atmosphere. There is some evidence of inhomogeneity in the atmosphere of ζ Aurigae, however we suggest

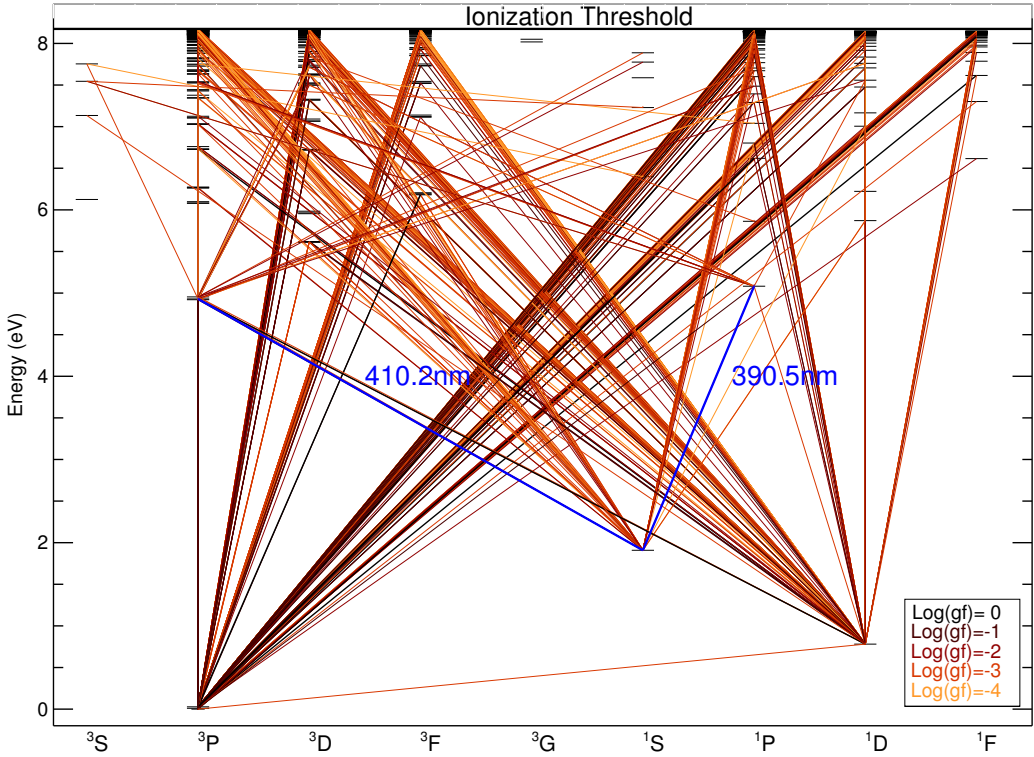


Figure 7.3: Si I Grotrian diagram. The lines are colour-coded according to $\log(gf)$, thicker, darker lines have a higher value. The $\lambda 3905\text{\AA}$ and $\lambda 3905\text{\AA}$ transitions of interest are highlighted in blue.

that this inhomogeneity is of second-order importance, as most of the observations can be reconciled with a homogeneous, time-independent atmosphere of the type presented in this work.

To expand on this work we aim to use this model atmosphere to examine the formation of the periodic Si I emission described in Chapter 5. While the geometric model presented in that chapter does accurately describe the phase periodicity of the EEW, we have no model to describe the line formation process. In order to gain a quantitative understanding of this effect we construct a Si I model atom. A Grotrian diagram of this model atom can be seen in Fig. 7.3. This model atom has 600 levels and approximately 2000 transitions. The energies of the levels were

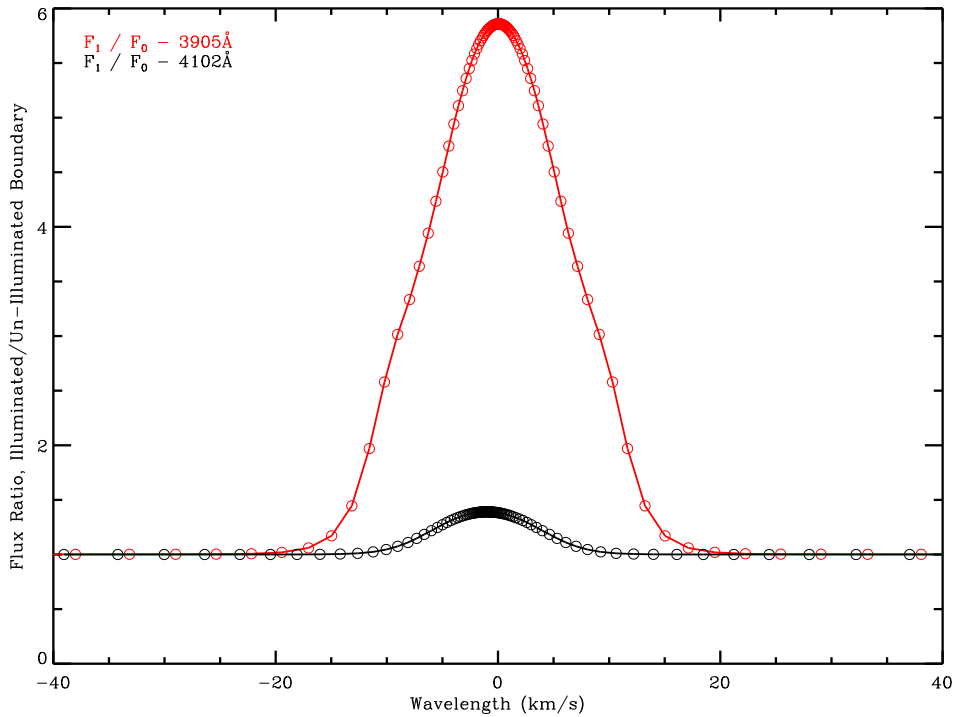


Figure 7.4: Ratio of the emergent flux in the SiI $\lambda 3905\text{\AA}$ and $\lambda 4102\text{\AA}$ lines for an illuminated and un-illuminated boundary.

collected from the NIST Atomic Database (Kramida *et al.*, 2015), and data for the radiative transitions — the $\log(gf)$ values, the radiative damping constants, the Stark damping constants — were collected from Kurucz & Bell (1995)¹. An atomic model of this size is required in order to accurately account for recombination to the upper levels. Using the method of Seaton (1959) for computing the recombination cross-section of hydrogenic atoms as an approximation, we found a Si I model with 20 levels underestimates the recombination by $\sim 25\%$ at 5000 K when compared with the values of Verner *et al.* (1996). Once the recombination has taken place the electron will cascade through the levels before finally emitting a photon in one of the two observed lines.

¹<http://kurucz.harvard.edu/>

In order to quantify this effect an alteration was made to the RH code, allowing us to make use of an illuminated boundary condition for the atmosphere. This is done using the Feautrier boundary condition formalism described in Chapter 2. In this case we used a plane-parallel version of the atmospheric model developed in Chapter 6, as the problem of illumination, and calculation using the very large Si atomic model, is far simpler in this geometry. Since the Si I line-formation problem only concerns a small “hot spot” on the stellar surface the full spherical atmosphere is not required, and the plane-parallel atmosphere should provide an accurate approximation. The flux of the B-star was taken from a Kurucz model atmosphere (Castelli *et al.*, 1997). The emergent flux in the Si I $\lambda 3905\text{\AA}$ and $\lambda 4102\text{\AA}$ lines was computed using a plane-parallel form of the ζ Aurigae model atmosphere, for both an illuminated and un-illuminated boundary. The ratios of these emergent fluxes can be seen in Fig. 7.4. This work is at an early stage, and we have yet to undertake a detailed quantitative analysis of the line formation, however it is encouraging to note that the width of the $\lambda 3905\text{\AA}$ line matches well with observation, as does the ratio of the two lines with respect one another.

7.4 Concluding Remarks

In this thesis the thermodynamic structures and geometric extents of late-type stellar chromospheres have been addressed using two complementary approaches. While Chapter 5 is a case study of a novel phenomenon observed in a specific class of object, Chapters 4 and 6 are strongly thematically linked, and by taking their results in aggregate we can attempt to make some general statements about the chromospheres of late-type objects.

We begin by examining the assumptions and results of our radio model. This model assumes that the chromosphere, or more specifically the thermal mm flux emitting region, is described by an approximately constant electron density, a linear increase of temperature in radial height, and a geometric extent on the order of 10% of the stellar radius. Furthermore it assumes that the chromosphere is a single structure which covers the entire face of the star. We find that a model based on these assumptions can reproduce the thermal mm flux, and the spectral index, and we suggest that the underlying assumptions reflect the physical properties

of chromosphere. This is compounded by the fact that the model breaks down for objects which are thought to have chromospheres of a different structure, i.e. g Her (Luttermoser *et al.* (1994a) could not construct a time-independent, semi-empirical model for this object). The fact that models of this kind can reproduce the observed flux at mm wavelengths is interesting, and is in direct opposition to the results from time-dependent, inhomogeneous shock models. We contend that while granulation as a result of convection will introduce a time-varying dimension to the atmosphere, it will tend introduce quite small variability, as the number of granules scales as (assuming that the granule size is $\sim 10H_\rho$ (Chiavassa *et al.*, 2009; Freytag *et al.*, 2002))

$$N_{\text{gran}} = 4 \times 10^6 \left(\frac{R_\odot}{R_*} \right)^2 \left(\frac{T_{eff,\odot}}{T_{eff,*}} \right)^2 \left(\frac{M_*}{M_\odot} \right)^2 \quad (7.3)$$

which implies $\sim 10^4$ granules on the visible disk. If the brightness of these granules is uncorrelated this corresponds to a fractional variability in the flux of $1/\sqrt{10^4} = 1\%$. Variability above this level may be attributable to larger scale (magnetic) structure, though quite close monitoring may be required to observe this effect. In the absence of such variability we restate the validity of our time-independent, homogeneous atmospheric model.

Contrasting the radio model with our model of ζ Aurigae based on UV/optical observations we see that there is some common ground. The empirical data of this object, taken on the whole, lead us to a number of conclusions,

- The density decreases with radial height.
- The excitation temperature and turbulent velocity increase with height.
- Hydrogen appears to be predominantly neutral.
- Electron densities appear to be higher than would be possible given an isotropic distribution of material.
- The extent of the chromosphere is, $h \sim 1R_*$.

The first two points here agree well with the findings of our radio model, the final three however give us pause, as they appear to be in opposition to our previous

assumptions and perhaps point to a larger, and perhaps more complex atmosphere than is assumed in our radio model.

Extreme inhomogeneity, such as an inverted density gradient, which would cause the splitting of spectral lines is absent in ζ Aurigae (though some evidence of line splitting is found by Schroeder (1983) in 32 Cyg), with the exception of occasional splitting of the K line high in the chromosphere, observed by R.E.M. Griffin (Griffin & Ake, 2015). The inhomogeneity seen in the electron densities in the chromosphere could be attributable to material confined along magnetic flux tubes, as in the Sun, and this may be the cause of the K line splitting, however the infrequent observation of this splitting points to this clumping not being particularly prevalent. Clumping which is not magnetic in nature was examined by Eaton (2008), who created a semi-empirical model for the chromosphere and wind of 31 Cyg based on the proposition that the force which led to clumping was also responsible for extending the chromosphere and driving the wind. Using this model however he derived modest clumping factors, which were in fact revised *down* by Harper (2010) in order to match the cm-radio emission from the wind of ζ Aurigae.

In the case of global inhomogeneity, where the large-scale structure of the chromosphere is asymmetric, we do note the long-standing observation (Baade *et al.*, 1996; Wilson & Abt, 1954; Wright, 1959) that the chromosphere appears different at ingress and egress, though McKellar & Petrie (1952) determined that a single “minimum” model could be constructed which underlies the inhomogeneity. To some extent the difference at egress and ingress may be attributable to the relative distance to the B-star (which is closer at egress), and its distortion of the K-star chromosphere.¹ In general it is assumed that the chromospheres and winds from supergiants are a single structure, and Baade *et al.* (1996) presented evidence of anisotropy/asphericity in the wind of ζ Aurigae A, perhaps indicating that the wind and chromosphere may consist of isolated structures anchored to different parts of the photosphere. This is contradicted by observations of H- α which imply

¹That said we must point out that the Strömgren sphere of the B-star is quite small, so outside of this gravitational distortion the total/electron densities of the K-star should, on the whole, be unaffected by the B-star.

that the chromosphere must cover the face of the star quite uniformly (Eaton, 1995; Griffin & Ake, 2015).

Though the evidence for large- and small-scale inhomogeneity is itself patchy, the atmosphere is clearly not static and isotropic. However we believe that on balance the model for ζ Aurigae A presented in this work, despite its relative simplicity, can account for much of the observation of this object, crucially the line spectra, and is an accurate reflection of the physical conditions in the chromosphere. We also believe that owing to the similarity of this object to others, λ Velorum in particular, much of what we have concluded can be generalised.

The extent of our model of ζ Aurigae A is comparable to the extents of other supergiants (Eaton, 1988; Harper *et al.*, 2001; Lim *et al.*, 1998) and specifically agrees with the extent predicted by Carpenter *et al.* (1985) for λ Velorum. This is in disagreement with the expectation for time-dependent, acoustically shocked chromospheres, which are modelled as being significantly more compact (Cuntz, 1990). We briefly examine the extents of coronal giants and find some evidence that the traditional models of these objects, which determine them to be quite compact also, may be inaccurate as they cannot reproduce the profiles of spectral lines and their interferometric visibilities. This is a fruitful avenue of study, and the direct constraints placed on line-forming regions by spectro-interferometry appears to lead us toward reconsidering the current models of geometric extent.

As this relates to our radio model, it is possible to compute the apparent extent of our chromospheric model when observed at mm wavelengths. At these wavelengths, owing to the low electron density in the high chromosphere, the apparent radius is $\sim 0.15R_*$, which is in keeping with the computed extents from our radio model. Below this height the chromosphere loosely satisfies the condition that the electron density remain approximately constant to within an order of magnitude, though the upper temperature is somewhat lower than is assumed in our model.

To conclude, in this thesis we presented two models of late-type stellar chromospheres, both assuming time-independence, homogeneity, as well as comparable geometric extents and temperature/density profiles. We find that these models reproduce well the emission from these objects at multiple wavelengths. At the mm-radio wavelengths our model is capable of reproducing the thermal emission from

7.4 Concluding Remarks

the chromosphere of these objects in a general sense. In the UV/optical a specific model of ζ Aurigae A is presented which matches closely observations of this object, and is used to comment generally on late-type chromospheres. Despite their simplicity these models are found to agree with observations of late-type stars, and we contend that to a good approximation they reflect the thermodynamic properties of these objects.

Using the diagnostic methods discussed in this work great insights can be gleaned into the structures of stellar atmospheres. With modern observational methods it is now possible to determine the basic parameters of late-type stars to a higher degree of accuracy than ever before. With knowledge of parameters such as effective temperature, distance, and photospheric radius, we can begin to answer questions of chromospheric structure for objects other than the Sun for the first time. Through interferometric observation at multiple wavelengths, novel diagnostics such as the periodic Si I lines presented in this work, and careful attention to the unique vantage provided by ζ Aurigae binaries, as well as a host of other recent advances, we can begin to effectively spatially resolve distant objects, and disentangle the complex problem of understanding their atmospheres.

A

Atomic Models

Here we provide the atomic models developed in the course of this work, as formattted for RH.

A.1 H atom

```

H
# Nlevel Nline Ncont Nfixed
 6      10      5      0
#   E[cm^-1]    g          label[20]      stage   levelNo
#           ,|----|----|----|----,
#   0.000  2.00  'H I 1S 2SE      ,     0     0
82258.211  8.00  'H I 2P 2P0      ,     0     1
37491.219 18.00  'H I 3D 2DE      ,     0     2
10232.46   50.00  'H I 4F 2F0      ,     0     3
105290.508 50.00  'H I 5G 2GE      ,     0     4
109677.617 1.00  'H II continuum  ,     1     5
# j i f type Nlambda symmetr qcore quing vdWapprx      vdWaals      radiative Stark
# Lyman series
1 0 4.162E-01 PRD  100  SYMM 15.0  600.0  UNSOLD 1.000 0.000 1.000 0.000 4.70E+08 1.0E+00
2 0 2.895E-02 PRD  50   SYMM 10.0  250.0  UNSOLD 1.000 0.000 1.000 0.000 9.98E+07 1.0E+00
3 0 2.895E-02 VOIGT 20   SYMM 3.0   100.0  UNSOLD 1.000 0.000 1.000 0.000 3.02E+07 1.0E+00
4 0 1.394E-02 VOIGT 20   SYMM 3.0   100.0  UNSOLD 1.000 0.000 1.000 0.000 1.15E+07 1.0E+00
# Balmer series
2 1 6.407E-01 PRD  70   SYMM 1.0   250.0  UNSOLD 1.000 0.000 1.000 0.000 9.98E+07 1.0E+00
3 1 1.193E-01 VOIGT 40   SYMM 3.0   250.0  UNSOLD 1.000 0.000 1.000 0.000 3.02E+07 1.0E+00
4 1 4.467E-02 VOIGT 40   SYMM 3.0   250.0  UNSOLD 1.000 0.000 1.000 0.000 1.15E+07 1.0E+00
# Paschen series
3 2 0.606E-01 VOIGT 20   SYMM 2.0   30.0   UNSOLD 1.000 0.000 1.000 0.000 3.02E+07 1.0E+00
4 2 0.506E-01 VOIGT 20   SYMM 2.0   30.0   UNSOLD 1.000 0.000 1.000 0.000 1.15E+07 1.0E+00
# Brackett series
4 3 1.036E+00 VOIGT 20   SYMM 1.0   30.0   UNSOLD 1.000 0.000 1.000 0.000 1.15E+07 1.0E+00
# Photoionization Cross Sectionss
# j i alpha [m^-2]  Nlambda      Wavel. Dep.  lamb_min [nm]
#
# H I 1S 2SE
5 0 6.152E-22  20  HYDROGENIC  22.794
# H I 2P 2P0
5 1 3.79E-21  20  HYDROGENIC  91.176
# H I 3D 2DE
5 2 5.149E-21  20  HYDROGENIC  205.147
# H I 4F 2F0
5 3 2.923E-21  20  HYDROGENIC  364.705
# H I 5G 2GE
5 4 3.699E-21  20  HYDROGENIC  569.852
# Fixed Transitions
# j i Strength Trad Option
# Collisional rate coefficients
TEMP 6      3000.0  5000.0  7000.0  10000.0  20000.0  30000.0
CE   1 0    9.750e-16 6.098e-16 4.535e-16 3.365e-16 2.008e-16 1.560e-16 (Johnson)
CE   2 0    1.437e-16 9.069e-17 6.798e-17 5.097e-17 3.118e-17 2.461e-17 (Johnson)

```

A.2 Al atom

```

GE      3   0    4.744e-17  3.001e-17  2.255e-17  1.696e-17  1.044e-17  8.281e-18  (Johnson)
GE      4   0    2.154e-17  1.364e-17  1.026e-17  7.723e-18  4.772e-18  3.791e-18  (Johnson)
GE      2   1    1.127e-14  8.077e-15  6.716e-15  5.691e-15  4.419e-15  3.890e-15  (Johnson)
CE      3   1    1.360e-15  1.011e-15  8.617e-16  7.482e-16  6.068e-16  5.482e-16  (Johnson)
CE      4   1    4.040e-16  3.041e-16  2.612e-16  2.287e-16  1.887e-16  1.726e-16  (Johnson)
CE      3   2    3.114e-14  2.629e-14  2.434e-14  2.290e-14  2.068e-14  1.917e-14  (Johnson)
CE      4   2    3.119e-15  2.700e-15  2.527e-15  2.400e-15  2.229e-15  2.130e-15  (Johnson)
CE      4   3    7.728e-14  7.317e-14  7.199e-14  7.109e-14  6.752e-14  6.310e-14  (Johnson)

# Collisional rate coefficients
TEMP     6    3000.0    5000.0    7000.0    10000.0   20000.0   30000.0
CI      0   5    2.638e-17  2.864e-17  3.075e-17  3.365e-17  4.138e-17  4.703e-17  (Johnson)
CI      1   5    5.309e-16  6.595e-16  7.544e-16  8.583e-16  1.025e-15  1.089e-15  (Johnson)
CI      2   5    2.215e-15  2.792e-15  3.169e-15  3.518e-15  3.884e-15  3.828e-15  (Johnson)
CI      3   5    6.182e-15  7.576e-15  8.370e-15  8.992e-15  9.252e-15  8.752e-15  (Johnson)
CI      4   5    1.342e-14  1.588e-14  1.710e-14  1.786e-14  1.743e-14  1.601e-14  (Johnson)
#
END

```

A.2 Al atom

```

AL
# Nlevel Nline Ncont Nfixed
# 13      9       11      0
# Energy levels from NIST
# E[cm^-1]   g          label[20]      stage      levelNo
#           ,|---|---|---|---|---|---|---|---|---|---|---|---|---|---|---|---|---|---|---|---|
# 0.000    2.00   'AL I 3S2 3P 2P0 1/2'   0        0
121.061   4.00   'AL I 3S2 3P 2P0 3/2'   0        1
25347.756  2.00   'AL I 3S2 4S 2SE'      0        2
25066.960  1.00   'AL I 3S2 3P 2D5'      0        3
25435.593  15.00  'AL I 3S2 3P 2D5'      0        4
32949.807  6.00   'AL I 3S2 4P 2P0'      0        5
37689.407  2.00   'AL I 3S 5S 2SE'      0        6
48278.480  1.00   'AL II 3S2 1SE'      1        7
85651.510  1.00   'AL II 3S 3P 3P0'    1        8
85720.400  1.00   'AL II 3S 3P 3P1'    1        9
85856.300  5.00   'AL II 3S 3P 3P0'    1        10
108130.482 3.00   'AL II 3S 3P 1P0'    1        11
200141.281 2.00   'AL III Ground Term'  2        12
# j i f type Nlambda symmetr qcorder quing vdWapprx      vdWaals      radiative  Stark
# j i f type Nlambda symmetr qcorder quing vdWapprx      vdWaals      radiative  Stark
# 0   0  1.160e-01 VOIGT  30  ASYMM  1.0  30.0  UNSOLD  1.000  0.000  1.000  0.000  1.82e+08  0.0e+00
3  0  1.160e-01 VOIGT  30  ASYMM  1.0  30.0  UNSOLD  1.000  0.000  1.000  0.000  1.82e+08  0.0e+00
4  0  1.1670e-01 VOIGT  30  ASYMM  1.0  30.0  UNSOLD  1.000  0.000  1.000  0.000  1.14e+08  0.0e+00
4  1  1.1670e-02 VOIGT  30  ASYMM  1.0  30.0  UNSOLD  1.000  0.000  1.000  0.000  1.14e+08  0.0e+00
5  0  2.4130e-02 VOIGT  30  ASYMM  1.0  30.0  UNSOLD  1.000  0.000  1.000  0.000  1.34e+08  0.0e+00
6  0  1.5100e-02 VOIGT  30  ASYMM  1.0  30.0  UNSOLD  1.000  0.000  1.000  0.000  5.75e+08  0.0e+00
6  1  1.510e-02 VOIGT  30  ASYMM  1.0  30.0  UNSOLD  1.000  0.000  1.000  0.000  5.75e+08  0.0e+00
9  7  1.054e-05 VOIGT  60  ASYMM  0.3  60.0  UNSOLD  1.000  0.000  1.000  0.000  6.45e+03  0.0e+00
11 7  1.770e+00 VOIGT  30  ASYMM  1.0  30.0  UNSOLD  1.000  0.000  1.000  0.000  1.73e+08  0.0e+00
# Photoionization rates
# j i alpha [m^-2]  Nlambda      Wavel. Dep.  lamb_min [nm]
# AL I 3S2 4S 2SE
# 7   1  9.408e-24  50      EXPLICIT  13.832144
# 212.70817  2.03000e-21
# 204.89078  2.03000e-21
# 200.53208  1.59267e-21
# 196.47339  1.59267e-21
# 192.41469  4.22300e-21
# 188.45600  1.43700e-21
# 184.29731  1.43700e-21
# 180.23861  9.12333e-22
# 176.17934  9.12333e-22
# 172.12022  9.12333e-22
# 168.06253  9.12333e-22
# 164.00383  5.99333e-22
# 159.94514  5.99333e-22
# 155.88645  5.99333e-22
# 151.82775  2.52667e-22
# 147.76906  2.52667e-22
# 143.71036  3.10967e-23
# 139.65167  6.21333e-23
# 135.59297  4.49667e-22
# 131.53428  2.49676e-22
# 127.47559  3.15267e-22
# 123.41690  7.12763e-23
# 119.35820  7.07000e-23
# 115.29950  2.01200e-22
# 111.24081  1.96067e-22
# 107.18211  8.61657e-23
# 103.12342  1.09000e-22
# 99.064725  6.31667e-23
# 95.006030  4.26333e-23
# 90.947336  4.47333e-23
# 86.888645  4.47333e-23
# 82.829947  3.30633e-23
# 78.771253  1.89333e-23
# 74.712559  1.32767e-23
# 70.652970  1.32767e-23
# 66.594270  3.34000e-23
# 62.536476  3.18533e-21
# 58.477781  9.26333e-24
# 54.419087  7.28657e-24
# 50.351393  4.51000e-24
# 46.301698  4.51000e-24
# 42.243004  3.54667e-24
# 38.184310  2.62733e-24
# 34.125610  1.52970e-24
# 30.066521  1.52970e-24
# 26.008227  8.40333e-25
# 21.949532  4.89667e-25
# 17.890838  2.68733e-25
# 13.832144  1.23200e-25
# AL I 3S2 4S 2SE
# 7   2  1.05408e-24  50      EXPLICIT  13.832144
# 212.70817  2.03000e-21
# 208.64947  4.06000e-21
# 204.59078  4.06000e-21
# 200.53208  3.18533e-21
# 196.47339  1.09000e-21
# 192.41469  8.42400e-21
# 188.35600  2.87400e-21
# 184.29731  2.87400e-21
# 180.23861  1.43700e-21
# 176.17934  1.43700e-21
# 172.12022  1.82467e-21
# 168.06253  1.82467e-21
# 164.00383  1.19867e-21
# 159.94514  1.19867e-21
# 155.88645  1.19867e-21

```

A.2 Al atom

151.82775	5.05333e-22
147.76906	5.05333e-22
143.71036	6.21933e-23
139.65167	1.26267e-21
135.59297	6.99333e-22
131.53428	1.09333e-22
127.47559	6.30533e-22
123.41689	5.94267e-22
119.35820	1.41400e-22
115.30050	1.04200e-22
111.24081	3.92133e-22
107.18211	1.72333e-22
103.12342	1.87667e-22
99.06473	8.26533e-23
95.00613	8.26533e-23
90.947336	8.94667e-23
86.888642	5.71800e-23
82.829547	6.61267e-23
78.770853	1.09333e-22
74.712559	2.65533e-23
70.653864	2.18800e-23
66.595170	2.68000e-23
62.536476	2.18800e-23
58.477781	6.85267e-23
54.419087	1.45733e-23
50.360393	1.21733e-23
49.308749	9.09333e-24
45.243004	5.09333e-24
38.184310	5.28467e-24
34.125615	3.66600e-24
30.066521	2.55800e-24
29.010777	1.09333e-23
24.949532	9.79333e-25
17.890838	5.37467e-25
13.832144	2.46400e-25
# AL I 3S 3P2 4P	
7 3 3.664e-21	50
EXPLICIT	16.488866
453.70773	1.76900e-23
449.65167	1.04200e-23
435.60206	4.05000e-23
426.93923	5.75900e-24
418.01639	2.87600e-24
406.19556	1.52600e-24
400.13639	1.09333e-24
391.247789	5.85200e-29
382.32506	1.46700e-25
373.40223	1.17700e-24
369.47856	1.09333e-24
355.55656	6.42200e-24
346.63373	9.97900e-24
337.71089	9.97900e-24
320.78560	1.09333e-24
319.86522	2.67000e-23
310.94239	2.67000e-23
302.01956	3.82400e-23
293.09672	5.36700e-23
284.17399	5.36700e-23
275.25106	1.54200e-22
266.32822	5.86000e-22
257.40539	1.33200e-22
246.48256	1.09333e-22
239.55972	1.98300e-23
230.63689	4.50100e-23
221.71406	7.14400e-23
212.79122	1.09333e-23
203.86839	1.59400e-22
194.94556	8.89400e-23
186.02272	2.32800e-22
177.09996	3.09333e-22
168.17706	1.04200e-20
159.25422	1.46900e-21
150.33139	2.23500e-22
141.41655	1.48900e-22
132.49372	1.09333e-23
123.56289	2.44400e-23
114.64005	4.43100e-24
105.71722	3.56300e-22
96.79437	1.09333e-22
87.871554	2.13700e-23
78.948720	1.31400e-23
70.025887	7.97100e-24
61.113153	5.23700e-24
52.180220	1.09333e-24
43.257386	1.88900e-24
34.334553	9.76100e-25
25.411719	3.96800e-25
16.408686	1.06000e-20
# AL I 3S2 3D 2DE	
7 4 3.70328e-21	50
EXPLICIT	15.164350
176.47530	3.66400e-21
173.18630	3.66400e-21
169.89417	3.66400e-21
166.60205	3.66400e-21
163.31093	3.66400e-21
160.01780	1.99300e-21
156.72568	1.99300e-21
153.43355	1.99300e-21
150.14132	1.99300e-21
146.84931	1.99300e-21
143.55718	1.99300e-21
140.26506	1.45800e-21
136.97483	1.45800e-21
133.68381	1.88900e-21
130.38869	1.11000e-21
127.09665	1.11000e-21
123.80444	1.11000e-21
120.51222	1.09333e-21
117.22019	8.55200e-22
113.92807	6.13800e-22
110.63594	6.79500e-22
107.34381	4.04200e-22
104.05170	3.96800e-22
100.75957	2.39400e-22
97.467447	2.70700e-22
94.17531	1.09333e-22
90.883200	9.43000e-22
87.591076	1.51700e-22
84.298952	1.26100e-22
81.006528	9.89200e-23
77.71434	1.09333e-22
74.422580	6.69400e-23
71.130456	6.69400e-23
67.838332	5.93700e-23
64.546206	4.04200e-23
61.254084	3.98000e-23
57.961960	3.67400e-23
54.669836	3.06900e-23
51.377789	2.56300e-23
48.085689	2.02000e-23
44.793465	1.68400e-23
41.501341	1.32500e-23
38.209217	1.04200e-23
34.917093	8.07300e-24
31.624969	8.07300e-24
28.332848	4.23700e-24
25.040721	2.95600e-24
21.746197	1.09333e-24
18.455253	2.02000e-24
15.164350	6.59500e-25
# AL I 3S2 4P 2P	

A.2 Al atom

```

7   5      1.810e-21      50      EXPLICIT      16.853651
 670.80263  3.02900e-21
 657.45673  3.02900e-21
 644.11083  3.02900e-21
 630.76493  3.02900e-21
 617.41503  2.17500e-21
 604.07314  2.17500e-21
 590.72724  2.17500e-21
 577.38134  2.17500e-21
 564.04545  2.17500e-21
 550.68955  2.17500e-21
 537.34365  1.53900e-21
 523.99775  1.53900e-21
 510.65186  1.53900e-21
 497.31596  1.53900e-21
 483.96006  1.53900e-21
 470.61416  1.53900e-21
 457.26527  1.10900e-21
 443.91737  1.10900e-21
 430.57647  1.10900e-21
 417.23057  1.10900e-21
 403.88468  8.34000e-22
 390.54878  8.34000e-22
 377.19288  8.34000e-22
 363.84698  7.00700e-22
 350.50109  7.07500e-22
 337.15519  8.19100e-22
 325.80529  5.40700e-21
 310.46339  5.72500e-22
 297.11750  4.12900e-22
 283.77160  3.44500e-22
 270.42570  3.05000e-22
 257.07980  3.19100e-22
 243.73391  2.78100e-22
 230.38801  2.59500e-22
 217.04211  2.07000e-22
 203.69622  2.07000e-22
 190.35032  2.84400e-21
 177.00442  8.71700e-21
 163.65852  1.36600e-21
 150.31663  1.85500e-22
 136.96673  5.80400e-22
 123.62083  2.98700e-22
 110.27493  3.26300e-22
 98.93303  3.05000e-22
 83.583138  5.87500e-23
 70.237241  3.82300e-23
 56.891343  2.09800e-23
 43.551346  9.07600e-24
 30.199548  0.07600e-24
 16.853651  5.39900e-25

# AL I 3S2 5S 2SE      6      1.139e-22      50      EXPLICIT      18.680428
 687.88779  1.75400e-21
 674.19189  1.45400e-21
 660.53483  1.75400e-21
 646.87836  1.86900e-21
 633.22188  1.86900e-21
 619.57541  1.45400e-21
 605.30893  1.86900e-21
 592.25245  1.86900e-21
 578.59597  1.74400e-21
 564.94940  1.74400e-21
 551.28302  1.74400e-21
 537.62654  1.74400e-21
 523.97007  1.65200e-21
 510.31651  1.49700e-21
 496.25711  1.49700e-21
 483.00064  1.61900e-21
 469.34416  1.61900e-21
 455.68768  1.61900e-21
 442.03120  1.61900e-21
 428.37473  9.73900e-22
 414.71828  9.73900e-22
 401.06178  9.73900e-22
 391.40528  9.73900e-22
 375.74882  4.98000e-22
 360.09235  6.49400e-22
 346.43587  6.49400e-22
 332.77539  6.49400e-22
 319.11891  5.16000e-22
 305.46644  4.31600e-22
 291.80996  2.25600e-22
 278.15348  2.25600e-22
 264.49699  2.25600e-22
 250.84053  1.90200e-22
 237.18405  1.70700e-22
 223.52758  7.81400e-23
 209.87101  5.92900e-23
 196.21462  3.32200e-23
 182.55815  2.99900e-22
 168.90167  8.76100e-21
 155.24515  9.18600e-21
 141.58862  6.69400e-22
 127.93224  9.04700e-23
 114.27576  7.20300e-23
 100.61929  6.15900e-22
 86.96271  4.98000e-22
 73.306334  5.93700e-24
 59.649858  3.25800e-24
 45.993381  1.49400e-24
 32.336504  5.07200e-25
 18.680428  1.00400e-25

# AL II 3S2 1SE      6      1.148e-24      50      EXPLICIT      4.2902021
 67.710071  9.25400e-23
 66.415791  2.24000e-23
 65.121508  2.87200e-25
 63.827228  2.87200e-25
 62.538749  2.05700e-23
 61.238659  1.87100e-23
 59.944376  1.87100e-23
 58.650093  2.70200e-23
 57.361610  5.16000e-23
 56.061526  5.45400e-23
 54.767243  2.97300e-23
 53.472960  3.45200e-25
 52.188664  9.73900e-23
 50.886664  9.73900e-23
 49.590111  2.39800e-23
 48.295828  3.10000e-23
 47.001545  3.43800e-23
 45.712262  3.43800e-23
 44.412978  3.19300e-23
 43.118698  3.79300e-23
 41.824412  3.30500e-23
 40.535846  3.45200e-23
 39.235846  3.45200e-23
 37.941563  3.76600e-23
 36.647280  3.15800e-23
 35.360843  3.45200e-23
 34.085714  3.26600e-23
 32.764431  3.24600e-23
 31.470147  3.16600e-23
 30.175864  3.16600e-23
 28.889581  3.16600e-23
 27.587298  3.92900e-23
 26.293015  2.92900e-23
 24.998732  2.92900e-23
 23.712449  2.49800e-23
 22.410166  2.49800e-23
 21.115883  2.48300e-23

```

A.2 Al atom

```

19.821599 2.48300e-23
18.527316 2.22600e-23
17.233033 1.84000e-23
15.938750 1.44800e-23
14.644467 0.07200e-23
13.611944 8.00000e-24
12.055901 6.25000e-24
10.761618 4.36000e-24
9.4673346 3.04200e-24
8.112057 2.00000e-24
6.8737684 1.16500e-24
5.5848582 6.02000e-25
4.2902021 2.76000e-25

# AL II 3S 3P0      6.671e-23          50      EXPLICIT      3.4334352
# AL II 3S 3P1      6.671e-23          50      EXPLICIT      3.4334352
# AL II 3S 3P2      6.671e-23          50      EXPLICIT      3.4334352

```

The output shows three sets of data for the Al II 3S 3P atomic system. Each set includes the atomic number (12), the state identifier (AL II 3S 3P0, 3P1, or 3P2), the principal quantum number (6.671e-23), the angular momentum quantum number (50), the calculation method (EXPLICIT), and the energy value (3.4334352). The data lists numerous numerical values representing energy levels and transitions.

A.2 Al atom

```

51.470600 2.21333e-23
49.691446 2.11333e-23
47.91292 2.13333e-23
46.133137 2.33167e-23
44.353983 2.23722e-23
42.59259 2.23722e-23
40.795674 2.33333e-23
39.016520 2.29556e-23
37.237365 2.26333e-23
35.455365 2.29167e-23
33.679057 2.29167e-23
31.899903 2.29167e-23
30.120749 2.29167e-23
28.341595 2.29167e-23
26.561400 2.29167e-23
24.783286 1.42556e-23
23.004132 1.42556e-23
21.224978 1.42556e-23
19.446833 2.45000e-23
17.666669 1.42556e-23
15.887515 1.32222e-23
14.108361 9.84445e-24
12.331565 8.01674e-24
10.550052 6.01674e-24
8.7708980 2.33167e-24
6.9917437 1.20500e-24
5.2125654 4.90000e-25
3.4333552 3.39000e-25

# AL II SS 3P 1PO
# 12 11 2.7886e-22 50 EXPLICIT 3.7803974
115.27886 4.45000e-22
113.00338 4.45000e-22
110.73000 2.45000e-22
108.45242 2.80700e-22
106.17694 1.17400e-22
103.90146 1.17400e-22
101.62540 4.33333e-23
99.35005 2.45000e-23
97.075026 1.47800e-22
94.799548 1.71200e-22
92.524069 1.20800e-22
90.24710 1.19000e-22
87.973111 8.41000e-23
85.697632 4.55100e-23
83.422154 2.10900e-23
81.146664 4.55100e-23
78.87199 2.45000e-23
76.595717 2.49700e-23
74.320239 1.93500e-23
72.044760 1.75100e-23
70.768591 1.19000e-23
67.493802 5.89500e-23
65.218324 2.73300e-23
62.942845 2.34100e-23
60.666368 2.34100e-23
58.391887 3.07900e-23
56.116409 2.08900e-23
53.840930 5.17000e-23
51.564470 2.08900e-23
49.289372 3.05200e-23
47.014494 3.07600e-23
44.739015 3.36600e-23
42.463857 3.41300e-23
40.186557 3.51000e-23
37.912879 3.53000e-23
35.637100 3.53000e-23
33.351614 3.53000e-23
31.069142 3.52000e-23
28.810664 3.05200e-23
26.535185 3.05200e-23
24.259705 3.05200e-23
21.978327 3.05200e-23
19.708749 2.43000e-23
17.433270 2.19000e-23
15.157791 1.83400e-23
12.882541 1.52000e-23
10.600334 6.61400e-24
8.3313549 3.21900e-24
6.0558762 1.23300e-24
3.7803974 2.92100e-25

# Collisional rate coefficients
TEMP 13 1000.0 3000.0 5000.0 7000.0 10000.0 20000.0 40000.0 70000.0 126491.0 224936.0 400000.0 711312.0 1264910.0
CE 1 0 4.051E-12 2.850E-12 2.420E-12 2.173E-12 1.939E-12 1.553E-12 1.244E-12 1.040E-12 8.608E-13 7.160E-13 5.955E-13 4.953E-13 4.120E-13 (van Regemorter)
CE 2 0 2.346E-14 7.913E-14 4.804E-15 3.472E-15 2.472E-15 1.303E-15 7.104E-16 4.479E-16 2.820E-16 1.828E-16 1.194E-16 7.798E-17 5.064E-17 (Seaton IP)
CE 3 0 1.869E-14 6.297E-15 3.820E-15 2.758E-15 1.962E-15 1.031E-15 5.607E-16 3.533E-16 2.227E-16 1.450E-16 9.530E-17 6.270E-17 4.103E-17 (Seaton IP)
CE 4 0 2.234E-14 7.523E-15 4.560E-15 3.291E-15 2.339E-15 1.226E-15 6.654E-16 4.189E-16 2.644E-16 1.727E-16 1.141E-16 7.552E-17 4.974E-17 (Seaton IP)
CE 5 0 3.289E-16 2.314E-16 1.965E-16 1.764E-16 1.574E-16 1.261E-16 1.010E-16 8.445E-17 6.988E-17 5.812E-17 4.835E-17 4.021E-17 3.345E-17 (van Regemorter)
CE 6 0 1.546E-16 5.203E-16 3.152E-16 2.273E-16 1.613E-16 8.433E-17 4.561E-17 2.867E-17 1.811E-17 1.188E-17 7.908E-18 5.282E-17 3.512E-18 (Seaton IP)
CE 2 1 5.151E-16 3.624E-16 3.078E-16 2.763E-16 2.465E-16 1.975E-16 1.582E-16 1.323E-16 1.095E-16 1.040E-17 7.572E-17 6.298E-17 5.239E-17 (van Regemorter)
CE 3 1 4.088E-16 2.877E-16 2.443E-16 2.193E-16 1.957E-16 1.568E-16 1.256E-16 1.050E-16 8.687E-17 7.226E-17 6.010E-17 4.999E-17 4.158E-17 (van Regemorter)
CE 4 1 2.241E-15 7.548E-16 4.576E-16 3.302E-16 2.347E-16 1.231E-16 6.679E-17 4.206E-17 2.655E-17 1.734E-17 1.146E-17 7.587E-18 4.997E-18 (Seaton IP)
CE 5 1 3.309E-16 2.328E-16 1.977E-16 1.775E-16 1.584E-16 1.269E-16 1.016E-16 8.497E-17 7.031E-17 5.849E-16 4.865E-17 4.046E-17 3.365E-17 (van Regemorter)
CE 6 1 1.560E-16 5.251E-16 3.180E-16 2.293E-16 1.628E-16 8.512E-17 4.604E-17 2.895E-17 1.830E-17 1.200E-17 7.989E-18 5.337E-18 3.549E-18 (Seaton IP)
CE 3 2 1.284E-14 9.036E-15 7.673E-15 6.890E-15 6.147E-15 4.924E-15 3.945E-15 3.298E-15 2.729E-15 2.270E-15 1.888E-15 1.570E-15 1.306E-15 (van Regemorter)
CE 4 2 4.347E-15 3.058E-15 2.597E-15 2.332E-15 2.080E-15 1.667E-15 1.335E-15 1.116E-15 9.236E-16 7.683E-16 6.390E-16 5.315E-16 4.421E-16 (van Regemorter)
CE 5 2 1.293E-13 4.872E-14 3.251E-14 2.548E-14 2.010E-14 1.326E-14 8.768E-15 6.137E-15 4.126E-15 2.812E-15 1.854E-15 1.197E-15 7.639E-16 (Seaton IP)
CE 6 2 1.712E-15 1.205E-15 1.023E-15 9.185E-16 8.194E-16 6.564E-16 5.258E-16 4.396E-16 3.638E-16 3.026E-16 2.517E-16 2.093E-15 1.741E-16 (van Regemorter)
CE 4 3 1.517E-14 1.067E-14 9.063E-15 8.137E-15 7.260E-15 5.818E-15 4.659E-15 3.895E-15 3.232E-15 2.681E-15 2.230E-15 1.855E-15 1.543E-15 (van Regemorter)
CE 5 3 1.195E-14 8.405E-15 7.138E-15 6.409E-15 5.718E-15 4.580E-15 3.669E-15 3.068E-15 2.539E-15 2.111E-15 1.756E-15 1.461E-15 1.215E-15 (van Regemorter)
CE 6 3 3.127E-15 2.200E-15 1.868E-15 1.678E-15 1.497E-15 1.199E-15 9.605E-16 8.030E-16 6.645E-16 5.527E-16 4.597E-16 3.824E-16 3.180E-16 (van Regemorter)
CE 5 4 3.565E-13 2.509E-13 2.130E-13 1.913E-13 1.706E-13 1.367E-13 1.095E-13 9.155E-14 7.576E-14 6.301E-14 5.241E-14 4.359E-14 3.626E-14 (van Regemorter)
CE 6 4 7.188E-15 5.057E-15 4.295E-15 3.856E-15 3.440E-15 2.756E-15 2.208E-15 1.846E-15 1.527E-15 1.270E-15 1.057E-15 8.789E-16 7.310E-16 (van Regemorter)
CE 6 5 8.546E-15 6.013E-15 5.106E-15 4.585E-15 4.090E-15 3.277E-15 2.625E-15 2.195E-15 1.816E-15 1.510E-15 1.256E-15 1.045E-15 8.692E-16 (van Regemorter)
OMEGA 8 7 8.535E-01 (van Regemorter)
OMEGA 9 7 8.950E-05 (van Regemorter)
OMEGA 10 7 8.468E-01 8.488E-01 (van Regemorter)
OMEGA 11 7 9.433E+00 (van Regemorter)
OMEGA 9 8 3.943E+02 (van Regemorter)
OMEGA 10 8 1.558E+02 (van Regemorter)
OMEGA 11 8 1.419E+00 (van Regemorter)
OMEGA 12 8 7.723E+02 (van Regemorter)
OMEGA 11 9 4.272E+00 (van Regemorter)
OMEGA 11 10 7.160E+00 (van Regemorter)
CI 7 1 2.105E-18 2.105E-18
CI 7 2 4.420E-18 4.420E-18
CI 7 3 2.058E-15 2.058E-15
CI 7 4 1.838E-15 1.838E-15
CI 7 5 1.272E-15 1.272E-15
CI 7 6 1.159E-16 1.159E-16
CI 12 7 4.879E-17 4.879E-17
CI 12 8 1.255E-17 1.255E-17
CI 12 9 1.256E-17 1.256E-17
END

```

A.3 C atom

```

C
# Nlevel Nline Ncont Nfixed
# 12 11 6 0
# Energy levels
#   E[cm-1]   g      label[20]      stage    levelNo
#
#   29.578  0.00  'C I 2S2 2P2 3PE' , 0 0
10192.635  8.00  'C I 2S2 2P2 1DE' , 0 1
21648.018  1.00  'C I 2S2 2P2 1SE' , 0 2
90832.100  2.00  'C II 2S2 2P 2P0 1/2' , 1 3
90895.620  4.00  'C II 2S2 2P 2P0 3/2' , 1 4
133835.500  2.00  'C II 2S 2P2 4P 1/2' , 1 5
133857.500  4.00  'C II 2S 2P2 4P 3/2' , 1 6
133879.500  6.00  'C II 2S 2P2 5D 5/2' , 1 7
165762.300  6.00  'C II 2S 2P2 5D 7/2' , 1 8
165764.820  4.00  'C II 2S 2P2 5D 3/2' , 1 9
236381.470  4.00  'C II 2S2 3D 2DE 3/2' , 1 10
287492.726  1.00  'C III 2S2 1SE 0' , 2 11
# j i f type Nlambda symmetr qcore qwing vdWapprx vdwAals radiative Stark
# 4 3 1.707E-09 VOIGT 30 ASYMM 1.0 30.0 UNSOLD 0.000 0.000 0.000 0.000 6.87E-06 0.00E+00
5 3 4.270E-08 VOIGT 30 ASYMM 1.0 30.0 UNSOLD 0.000 0.000 0.000 0.000 2.31E+02 0.00E+00
6 3 2.987E-09 VOIGT 30 ASYMM 1.0 10.0 UNSOLD 0.000 0.000 0.000 0.000 3.71E+08 0.00E+00
10 3 3.170E-01 VOIGT 30 ASYMM 1.0 10.0 UNSOLD 0.000 0.000 0.000 0.000 7.17E+09 0.00E+00
5 4 2.510E-08 VOIGT 30 ASYMM 1.0 30.0 UNSOLD 0.000 0.000 0.000 0.000 2.31E+02 0.00E+00
6 4 7.040E-08 VOIGT 30 ASYMM 1.0 30.0 UNSOLD 0.000 0.000 0.000 0.000 1.32E+09 0.00E+00
7 4 1.240E-08 VOIGT 30 ASYMM 1.0 30.0 UNSOLD 0.000 0.000 0.000 0.000 4.32E+01 0.00E+00
9 4 1.281E-02 VOIGT 30 ASYMM 1.0 10.0 UNSOLD 0.000 0.000 0.000 0.000 7.71E+08 0.00E+00
8 4 1.159E-01 VOIGT 30 ASYMM 1.0 10.0 UNSOLD 0.000 0.000 0.000 0.000 2.89E+08 0.00E+00
10 4 3.187E-02 VOIGT 30 ASYMM 2.0 10.0 UNSOLD 0.000 0.000 0.000 0.000 7.17E+09 0.00E+00
# Photoionization Cross Sections
# j i alpha [m-2] Nlambda Wavel. Dep. lamb_min [nm]
#
# C I 2S2 2P2 3PE 4'
3 0 -9.000E+00 17 EXPLICIT 49.000
110.300 1.720E-21
101.300 1.670E-21
91.300 1.630E-21
88.100 1.600E-21
86.900 1.820E-21
86.000 1.190E-21
84.200 1.390E-21
81.400 1.120E-21
80.400 1.750E-21
79.800 1.340E-21
78.000 1.650E-21
77.700 1.480E-21
75.300 1.480E-21
70.100 1.260E-21
65.100 1.080E-21
59.100 5.900E-22
49.000 5.050E-22
# C I 2S2 2P2 1DE 2'
3 1 0.000E+00 19 EXPLICIT 50.600
123.890 1.050E-21
122.000 1.020E-21
121.000 1.020E-21
121.000 1.020E-21
117.100 9.660E-22
113.900 1.080E-21
107.400 2.400E-21
104.400 3.500E-21
100.000 3.500E-21
93.000 2.260E-21
91.100 5.100E-21
89.500 5.910E-21
89.300 5.300E-21
82.800 1.550E-21
75.900 1.090E-21
70.100 2.160E-21
65.100 9.660E-22
57.000 7.660E-22
50.600 6.400E-22
# C I 2S2 2P2 1SE 0'
3 0 -9.000E+00 13 EXPLICIT 57.000
144.320 1.430E-21
130.200 1.270E-21
122.000 1.040E-21
121.000 1.020E-21
113.900 8.440E-22
104.000 8.570E-22
101.300 3.020E-21
99.300 1.380E-20
98.900 1.350E-21
91.100 2.160E-21
82.800 1.430E-21
70.100 3.020E-21
57.000 5.050E-22
# C I 2S2 2P2 3PE 4'
4 0 0.000E+00 17 EXPLICIT 49.000
110.000 1.720E-21
101.300 1.670E-21
91.300 1.630E-21
88.100 1.690E-21
86.900 1.820E-21
86.000 1.190E-21
84.200 1.390E-21
81.400 1.480E-21
80.400 1.750E-21
79.800 1.340E-21
78.000 1.650E-21
77.700 1.480E-21
75.300 1.480E-21
70.100 1.260E-21
65.100 1.080E-21
59.100 5.900E-22
49.000 5.050E-22
# C I 2S2 2P2 1DE 2'
4 1 0.000E+00 19 EXPLICIT 50.600
123.890 1.050E-21
122.000 1.020E-21
121.500 1.020E-21
121.000 1.020E-21
117.100 9.660E-22
113.900 1.080E-21
107.000 2.400E-21
104.400 3.500E-21
100.000 3.500E-21
93.000 2.260E-21
91.100 5.100E-21
89.500 5.910E-21
89.300 5.300E-21
82.800 1.550E-21
75.900 1.090E-21
70.100 2.160E-21
65.100 9.660E-22
57.000 7.660E-22
# C I 2S2 2P2 1SE 0'
4 2 0.000E+00 13 EXPLICIT 57.000

```

A.3 C atom

```

144.320 1.430E-21
130.200 1.370E-21
122.000 1.040E-21
121.000 1.040E-21
113.900 6.440E-22
104.900 2.020E-22
101.300 3.020E-21
99.700 1.390E-20
95.900 3.950E-21
91.100 2.430E-21
82.800 1.430E-21
70.100 1.020E-21
57.000 7.580E-22

# Collisional data
TEMPO 17 1.199E-03 3548 6 63095 6 11220 2 19952 6 35481 4 63095 8 112202 0 199526 0 354814 0 630958 0 1122020 1995260 0 3548140 0
OMEGA 1 0 1.000E+00 1.000E+00
OMEGA 2 0 1.000E+00 1.000E+00
OMEGA 4 3 1.640E+00 1.770E+00 1.980E+00 2.190E+00 2.270E+00 2.270E+00 2.230E+00 2.200E+00 2.170E+00 2.160E+00 2.150E+00 2.150E+00 2.140E+00 2.140E+00 2.140E+00
OMEGA 5 3 2.550E-01 2.850E-01 2.910E-01 2.915E-01 2.920E-01 2.920E-01
OMEGA 6 3 2.410E-01 2.430E-01 2.430E-01
OMEGA 7 3 2.400E-01 2.320E-01 2.280E-01 2.280E-01 2.450E-01 2.420E-01 2.370E-01 2.330E-01 2.300E-01 2.290E-01 2.280E-01 2.270E-01 2.270E-01 2.270E-01 2.270E-01
OMEGA 9 3 1.290E+00 1.310E+00 1.340E+00 1.410E+00 1.530E+00 1.660E+00 1.810E+00 2.010E+00 2.300E+00 2.720E+00 3.260E+00 3.900E+00 4.630E+00 5.410E+00
OMEGA 8 3 5.140E-01 5.130E-01 5.260E-01 5.480E-01 5.600E-01 5.530E-01 5.360E-01 5.200E-01 5.100E-01 5.030E-01 4.990E-01 4.970E-01 4.960E-01 4.950E-01
OMEGA 6 4 4.617E-01 4.823E-01 4.932E-01 4.932E-01 5.030E-01 5.129E-01 5.035E-01 4.700E-01 4.145E-01 4.530E-01 4.510E-01 4.500E-01 4.490E-01
OMEGA 6 4 4.127E-00 4.111E-01 4.112E-00 4.114E-01 4.084E-00 4.077E+00 4.077E+00 4.077E+00 4.077E+00 4.077E+00 4.077E+00 4.077E+00 4.077E+00 4.077E+00 4.077E+00
OMEGA 7 4 4 1.136E+00 1.127E+00 1.111E+00 1.112E+00 1.114E+00 1.084E+00 1.077E+00 9.709E-01 9.588E-01 9.530E-01 9.510E-01 9.490E-01 9.460E-01
OMEGA 9 4 8.750E-01 8.840E-01 9.010E-01 9.360E-01 9.790E-01 9.940E-01 9.670E-01 9.310E-01 9.200E-01 9.540E-01 1.030E+00 1.140E+00 1.280E+00 1.430E+00
OMEGA 8 5 2.610E+00 2.610E+00
OMEGA 6 5 2.6100E-01 2.61220E-01 2.61220E-01
OMEGA 7 5 6.710E-01 6.940E-01 7.650E-01 8.800E-01 9.650E-01 9.970E-01 9.90E+00 9.820E-01 9.810E-01 9.800E-01 9.800E-01 9.800E-01 9.800E-01 9.800E-01 9.800E-01 9.800E-01
OMEGA 9 5 4.280E-01 4.380E-01 4.530E-01 4.760E-01 5.040E-01 5.260E-01 5.400E-01 5.480E-01 5.530E-01 5.560E-01 5.580E-01 5.590E-01 5.600E-01 5.600E-01 5.600E-01 5.600E-01
OMEGA 8 5 2.6100E-01 2.6100E-01
OMEGA 6 5 6.820E+00 6.820E+00
OMEGA 7 6 6.810E-01 6.790E-01 7.040E-01 7.430E-01 7.890E-01 8.240E-01 8.450E-01 8.580E-01 8.650E-01 8.700E-01 8.720E-01 8.740E-01 8.750E-01
OMEGA 8 6 6.690E-01 6.910E-01 7.210E-01 7.650E-01 8.150E-01 8.550E-01 8.810E-01 8.970E-01 9.070E-01 9.120E-01 9.160E-01 9.170E-01 9.190E-01 9.190E-01
OMEGA 9 7 5.000E+00 5.000E+00
OMEGA 6 7 4.490E+00 4.490E+00
CI 1 3 1.320E-16 1.320E-16
CI 1 2 3 1.790E-16 1.790E-16
CI 3 11 1.000E-17 1.000E-17
CI 4 11 1.000E-17 1.000E-17
CI 5 11 1.000E-17 1.000E-17
CI 6 11 1.000E-17 1.000E-17
CI 7 11 1.000E-17 1.000E-17
CI 8 11 1.000E-17 1.000E-17
CI 9 11 1.000E-17 1.000E-17
CI 10 11 1.000E-17 1.000E-17
END

```

B

Atmospheric Model

Here we provide the atmospheric models developed in the course of this work, as formatted for RH.

```
ZETA_AUR
Mass Scale
*
* lg g [cm s^-2] Radius [km]
    1.33  1.022e8
*
* Ndep      Ncore      Ninter
    63          8            0
*
*lg column Mass      Temperature      Ne      V(no v-field)      Vturb
-5.47596E+00  8.3169E+03  2.18646E+06  0.0000000  2.2500E+01
-4.99033E+00  8.0605E+03  3.34179E+06  0.0000000  2.1776E+01
-4.50471E+00  7.5314E+03  7.14857E+06  0.0000000  2.1175E+01
-4.01908E+00  7.0556E+03  6.45903E+06  0.0000000  2.0697E+01
-3.53346E+00  6.5688E+03  1.66903E+07  0.0000000  2.0342E+01
-3.04783E+00  6.1920E+03  5.31015E+07  0.0000000  2.0110E+01
-2.56220E+00  5.7151E+03  1.78146E+08  0.0000000  2.0000E+01
-2.18110E+00  5.3249E+03  4.66758E+08  0.0000000  2.0000E+01
-1.56273E+00  5.0103E+03  1.82788E+09  0.0000000  2.0500E+01
-1.34243E+00  4.6795E+03  2.70919E+09  0.0000000  2.0000E+01
-1.21302E+00  4.3421E+03  3.69200E+09  0.0000000  1.7000E+01
-1.17426E+00  4.1150E+03  4.07477E+09  0.0000000  1.6556E+01
-1.15816E+00  3.8396E+03  4.24612E+09  0.0000000  1.6374E+01
-1.13515E+00  3.6200E+03  4.49933E+09  0.0000000  1.6116E+01
-1.07558E+00  3.4643E+03  5.19206E+09  0.0000000  1.5463E+01
-8.75079E-01  3.3203E+03  8.09428E+09  0.0000000  1.3410E+01
-6.64063E-01  3.2042E+03  1.48501E+10  0.0000000  1.1491E+01
-4.15972E-01  3.1448E+03  4.49847E+10  0.0000000  5.0000E+00
-1.67881E-01  3.1013E+03  1.50474E+11  0.0000000  5.0000E+00
8.02095E-02  3.0722E+03  5.06123E+11  0.0000000  5.0000E+00
3.28300E-01  3.0566E+03  1.66908E+12  0.0000000  5.0000E+00
5.76391E-01  3.0556E+03  5.05295E+12  0.0000000  5.0000E+00
8.24482E-01  3.0630E+03  1.23400E+13  0.0000000  5.0000E+00
9.02006E-01  3.0755E+03  1.60005E+13  0.0000000  5.0000E+00
9.77661E-01  3.0933E+03  1.99560E+13  0.0000000  5.0000E+00
```

1.05157E+00	3.1150E+03	2.41065E+13	0.0000000	5.0000E+00
1.12388E+00	3.1397E+03	2.80591E+13	0.0000000	5.0000E+00
1.19475E+00	3.1666E+03	3.26036E+13	0.0000000	5.0000E+00
1.26435E+00	3.1950E+03	3.78573E+13	0.0000000	5.0000E+00
1.33282E+00	3.2246E+03	4.39442E+13	0.0000000	5.0000E+00
1.40029E+00	3.2553E+03	5.08707E+13	0.0000000	5.0000E+00
1.46684E+00	3.2874E+03	5.88898E+13	0.0000000	5.0000E+00
1.53251E+00	3.3211E+03	6.82013E+13	0.0000000	5.0000E+00
1.59727E+00	3.3572E+03	7.90396E+13	0.0000000	5.0000E+00
1.66100E+00	3.3962E+03	9.19261E+13	0.0000000	5.0000E+00
1.72353E+00	3.4391E+03	1.07261E+14	0.0000000	5.0000E+00
1.78462E+00	3.4866E+03	1.25646E+14	0.0000000	5.0000E+00
1.84397E+00	3.5399E+03	1.46858E+14	0.0000000	5.0000E+00
1.90128E+00	3.6000E+03	1.73022E+14	0.0000000	5.0000E+00
1.95631E+00	3.6680E+03	2.02286E+14	0.0000000	5.0000E+00
2.00887E+00	3.7452E+03	2.35828E+14	0.0000000	5.0000E+00
2.05901E+00	3.8329E+03	2.74326E+14	0.0000000	5.0000E+00
2.10699E+00	3.9326E+03	3.13128E+14	0.0000000	5.0000E+00
2.15334E+00	4.0460E+03	3.53073E+14	0.0000000	5.0000E+00
2.19888E+00	4.1750E+03	3.96673E+14	0.0000000	5.0000E+00
2.24477E+00	4.3217E+03	4.37932E+14	0.0000000	5.0000E+00
2.29223E+00	4.4882E+03	4.83849E+14	0.0000000	5.0000E+00
2.34225E+00	4.6766E+03	5.38836E+14	0.0000000	5.0000E+00
2.39474E+00	4.8882E+03	6.04222E+14	0.0000000	5.0000E+00
2.44687E+00	5.1231E+03	6.74465E+14	0.0000000	5.0000E+00
2.49294E+00	5.3797E+03	7.19679E+14	0.0000000	5.0000E+00
2.52827E+00	5.6542E+03	7.30922E+14	0.0000000	5.0000E+00
2.55254E+00	5.9405E+03	7.15925E+14	0.0000000	5.0000E+00
2.56828E+00	6.2308E+03	7.08392E+14	0.0000000	5.0000E+00
2.57825E+00	6.5165E+03	6.52621E+14	0.0000000	5.0000E+00
2.58492E+00	6.7898E+03	7.02588E+14	0.0000000	5.0000E+00
2.59053E+00	7.0443E+03	8.07886E+14	0.0000000	5.0000E+00
2.59585E+00	7.2770E+03	8.99456E+14	0.0000000	5.0000E+00
2.60113E+00	7.4864E+03	1.01901E+15	0.0000000	5.0000E+00
2.60659E+00	7.6777E+03	1.13498E+15	0.0000000	5.0000E+00
2.61238E+00	7.8479E+03	1.24359E+15	0.0000000	5.0000E+00
2.61860E+00	8.0257E+03	1.39414E+15	0.0000000	5.0000E+00
2.62544E+00	8.1530E+03	1.55013E+15	0.0000000	5.0000E+00

*	HYDROGEN POPULATIONS	NH(1)	NH(2)	NH(3)	NH(4)	NH(5)	NP	
2.85304E+06	2.59313E-04	7.65127E-09	1.81208E-09	1.56683E-09	1.51051E+05			
4.46855E+06	1.14557E-03	2.58375E-08	3.77614E-09	3.38976E-09	2.21654E+05			
9.91626E+06	4.08894E-03	1.05265E-07	1.57775E-08	1.43918E-08	4.47248E+05			
3.01213E+07	1.70403E-02	4.91639E-07	4.07129E-08	2.55709E-08	1.20522E+05			
1.00361E+08	1.01992E-01	3.76523E-06	2.92169E-07	1.78502E-07	2.20130E+05			
3.47278E+08	7.37277E-01	3.91103E-05	2.73115E-06	1.60785E-06	5.97705E+05			
1.20292E+09	6.20077E+00	7.07870E-04	3.56668E-05	1.87208E-05	1.86921E+06			
3.16967E+09	3.27946E+01	9.49798E-03	3.82765E-04	1.62800E-04	4.83148E+06			
1.50596E+10	1.67481E+02	1.75523E-01	8.16340E-03	2.77371E-03	9.92606E+06			
2.59977E+10	6.69241E+01	9.56696E-02	5.34857E-03	1.71428E-03	2.84664E+06			
3.65019E+10	1.55315E+01	2.38933E-02	1.43994E-03	4.54036E-04	4.88609E+05			
4.04424E+10	2.26764E+00	3.50423E-03	2.13026E-04	6.71899E-05	4.78261E+04			
4.21552E+10	6.26833E-01	9.69069E-04	5.90738E-05	1.86690E-05	1.17833E+04			
4.46726E+10	7.84605E-02	1.21331E-04	7.42578E-06	2.35628E-06	1.38833E+03			
5.15509E+10	8.42350E-03	1.30327E-05	8.06567E-07	2.58679E-07	1.30606E+02			
8.03666E+10	1.27372E-03	1.97419E-06	1.28088E-07	4.25869E-08	1.24357E+01			
1.47444E+11	1.83944E-04	2.85694E-07	1.97203E-08	6.85068E-09	1.00374E+00			
4.46644E+11	1.09775E-04	1.71144E-07	1.27257E-08	4.64669E-09	2.14043E-01			
1.49403E+12	1.03794E-04	1.62186E-07	1.29147E-08	4.97633E-09	6.64421E-02			
5.02520E+12	2.03040E-04	3.18296E-07	2.777470E-08	1.14816E-08	4.46970E-02			
1.65719E+13	6.26509E-04	9.88106E-07	1.00747E-07	4.61427E-08	5.36090E-02			
5.01698E+13	1.88663E-03	2.99242E-06	3.62360E-07	1.75726E-07	6.15171E-02			
1.22521E+14	4.60104E-03	7.28870E-06	9.77014E-07	4.72419E-07	5.36984E-02			
1.58866E+14	8.67479E-03	1.47075E-05	2.05474E-06	1.00343E-06	8.47753E-02			
1.98139E+14	1.56012E-02	2.83004E-05	4.09875E-06	2.02174E-06	1.34281E-01			
2.39348E+14	2.71232E-02	5.26259E-05	7.86241E-06	3.91868E-06	2.16013E-01			
2.78594E+14	4.50189E-02	9.32721E-05	1.43154E-05	7.20932E-06	3.51260E-01			
3.23715E+14	7.40188E-02	1.63529E-04	2.57166E-05	1.30851E-05	5.65970E-01			
3.75878E+14	1.20423E-01	2.83198E-04	4.55548E-05	2.34139E-05	8.99751E-01			
4.36314E+14	1.94916E-01	4.87473E-04	8.01430E-05	4.16024E-05	1.42126E+00			
5.05086E+14	3.13118E-01	8.32050E-04	1.39741E-04	7.32591E-05	2.23535E+00			
5.84706E+14	5.03408E-01	1.42166E-03	2.43895E-04	1.29128E-04	3.52545E+00			

6.77157E+14	8.14543E-01	2.44733E-03	4.29073E-04	2.29457E-04	5.62010E+00
7.84769E+14	1.33325E+00	4.27015E-03	7.65613E-04	4.13681E-04	9.12721E+00
9.12717E+14	2.23262E+00	7.65030E-03	1.40442E-03	7.67218E-04	1.52744E+01
1.06497E+15	3.84656E+00	1.41665E-02	2.66719E-03	1.47411E-03	2.65893E+01
1.24752E+15	6.88970E+00	2.74496E-02	5.31230E-03	2.97379E-03	4.88582E+01
1.45812E+15	1.28504E+01	5.58271E-02	1.11361E-02	6.32197E-03	9.61063E+01
1.71791E+15	2.53041E+01	1.20904E-01	2.49338E-02	1.43750E-02	2.02201E+02
2.00846E+15	5.23416E+01	2.77957E-01	5.94825E-02	3.48843E-02	4.64351E+02
2.34149E+15	1.14227E+02	6.81247E-01	1.51832E-01	9.07355E-02	1.15681E+03
2.72373E+15	2.64434E+02	1.79150E+00	4.17496E-01	2.54706E-01	3.13842E+03
3.10899E+15	6.37315E+02	4.95871E+00	1.21298E+00	7.56750E-01	9.25261E+03
3.50559E+15	1.61119E+03	1.45578E+01	3.75219E+00	2.39842E+00	2.95310E+04
3.93849E+15	4.29700E+03	4.55661E+01	1.24216E+01	8.14827E+00	1.01371E+05
4.34815E+15	1.19305E+04	1.50073E+02	4.34296E+01	2.92882E+01	3.75148E+05
4.80404E+15	3.50736E+04	5.28853E+02	1.63069E+02	1.13250E+02	1.49275E+06
5.34999E+15	1.09926E+05	2.00771E+03	6.62017E+02	4.74253E+02	6.39418E+06
5.99920E+15	3.66127E+05	8.18016E+03	2.89451E+03	2.14240E+03	2.94518E+07
6.69659E+15	1.27207E+06	3.50757E+04	1.33599E+04	1.02301E+04	1.44754E+08
7.14532E+15	4.38587E+06	1.50259E+05	6.17465E+04	4.89789E+04	7.49997E+08
7.25590E+15	1.47860E+07	6.32618E+05	2.81007E+05	2.31062E+05	4.04251E+09
7.10119E+15	4.88603E+07	2.61896E+06	1.25876E+06	1.07357E+06	2.23584E+10
6.99414E+15	1.62962E+08	1.09431E+07	5.69373E+06	5.03703E+06	1.24213E+11
6.27964E+15	4.71533E+08	3.93411E+07	2.20764E+07	2.02269E+07	6.33501E+11
6.35340E+15	1.11341E+09	1.08689E+08	6.44370E+07	6.05613E+07	1.98387E+12
6.73034E+15	2.09823E+09	2.27871E+08	1.40198E+08	1.34086E+08	4.15368E+12
6.75687E+15	3.29149E+09	3.88230E+08	2.45954E+08	2.38361E+08	7.08566E+12
6.89455E+15	4.80745E+09	6.06000E+08	3.92916E+08	3.84905E+08	1.06631E+13
6.88747E+15	6.49521E+09	8.65892E+08	5.72516E+08	5.65947E+08	1.47498E+13
6.72392E+15	8.29583E+09	1.16204E+09	7.81964E+08	7.79254E+08	1.93304E+13
6.78860E+15	1.07004E+10	1.56931E+09	1.07243E+09	1.07661E+09	2.47751E+13
6.78235E+15	1.34609E+10	2.06009E+09	1.42909E+09	1.44461E+09	3.10011E+13

References

- ALENCAR, S.H.P. & VAZ, L.P.R. (1997). The gravity-brightening effect and stellar atmospheres. I. Results for models with $3700\text{K} < T_{eff} < 7000\text{K}$. *Astronomy & Astrophysics*, **326**, 257–262. (Cited on page 124.)
- ALTENHOFF, W.J., THUM, C. & WENDKER, H.J. (1994). Radio emission from stars: A survey at 250 GHz. *A&A*, **281**, 161–183. (Cited on pages xiii, xx, 91, 100, 103, 108, 109 and 189.)
- ASPLUND, M., GREVESSE, N. & SAUVAL, A.J. (2006). The new solar abundances - Part I: the observations. *Communications in Asteroseismology*, **147**, 76–79. (Cited on page 148.)
- AUER, L. (1967). Improved Boundary Conditions for the Feautrier Method. *Astrophysical Journal Letters*, **150**, L53. (Cited on page 54.)
- AUER, L.H. & MIHALAS, D. (1969). Non-Lte Model Atmospheres. III. a Complete-Linearization Method. *Astrophysical Journal*, **158**, 641. (Cited on page 47.)
- AVRETT, E.H. & HUMMER, D.G. (1965). Non-coherent scattering, II: Line formation with a frequency independent source function. *Monthly Notices of the Royal Astronomical Society*, **130**, 295. (Cited on page 51.)
- AYRES, T.R. (1979). Chromospheric scaling laws, width-luminosity correlations, and the Wilson-Bappu effect. *ApJ*, **228**, 509–520. (Cited on pages 85 and 98.)
- AYRES, T.R. (2002). Does the Sun Have a Full-Time COmosphere? *ApJ*, **575**, 1104–1115. (Cited on pages 83 and 89.)
- AYRES, T.R., LINSKY, J.L., RODGERS, A.W. & KURUCZ, R.L. (1976). Stellar model chromospheres. V - Alpha Centauri A /G2 V/ and Alpha Centauri B /K1 V/. *Astrophysical Journal*, **210**, 199–210. (Cited on page 83.)
- BAADE, R., KIRSCH, T., REIMERS, D., TOUSSAINT, F., BENNETT, P.D., BROWN, A. & HARPER, G.M. (1996). The Wind Outflow of zeta Aurigae: A Model Revision Using Hubble Space Telescope Spectra. *Astrophysical Journal*, **466**, 979. (Cited on pages 146, 170 and 200.)
- BATES, D. (1962). *Atomic and molecular processes*. Pure and applied physics, Academic Press. (Cited on page 38.)
- BAUTISTA, M.A. (1997). Atomic data from the IRON Project. XX. Photoionization cross sections and oscillator strengths for Fe I. *Astronomy & Astrophysics Supplemental*, **122**, 167–176. (Cited on page 150.)

REFERENCES

- BEDDING, T.R., MOSSER, B., HUBER, D., MONTALBÁN, J., BECK, P., CHRISTENSEN-DALSGAARD, J., ELSWORTH, Y.P., GARCÍA, R.A., MIGLIO, A., STELLO, D., WHITE, T.R., DE RIDDER, J., HEKKER, S., AERTS, C., BARBAN, C., BELKACEM, K., BROOMHALL, A.M., BROWN, T.M., BUZASI, D.L., CARRIER, F., CHAPLIN, W.J., DI MAURO, M.P., DUPRET, M.A., FRANDSEN, S., GILLILAND, R.L., GOUPIL, M.J., JENKINS, J.M., KALLINGER, T., KAWALER, S., KJELDSEN, H., MATHUR, S., NOELS, A., AGUIRRE, S.V. & VENTURA, P. (2011). Gravity modes as a way to distinguish between hydrogen- and helium-burning red giant stars. *Nature*, **471**, 608–611. (Cited on page 5.)
- BEER, A. (1934). The recent eclipse of ζ Aurigae. *Monthly Notices of the Royal Astronomical Society*, **95**, 24. (Cited on page 17.)
- BENNETT, P. (2015). (Cited on pages xvii, 164, 166 and 171.)
- BENNETT, P.D., HARPER, G.M., BROWN, A. & HUMMEL, C.A. (1996). The Masses and Radii of the Eclipsing Binary ζ Aurigae. *Astrophysical Journal*, **471**, 454. (Cited on pages 111, 118, 119, 123, 143 and 161.)
- BERIO, P., MERLE, T., THÉVENIN, F., BONNEAU, D., MOURARD, D., CHESNEAU, O., DELLA, O., LIGI, R., NARDETTO, N., PERRAUT, K., PICHON, B., STEE, P., TALLON-BOSC, I., CLAUSSE, J.M., SPANG, A., MCALISTER, H., TEN BRUMMELAAR, T., STURMANN, J., STURMANN, L., TURNER, N., FARRINGTON, C. & GOLDFINGER, P.J. (2011). Chromosphere of K giant stars. Geometrical extent and spatial structure detection. *Astronomy & Astrophysics*, **535**, A59. (Cited on page 184.)
- BETHE, H. (1930). Zur Theorie des Durchgangs schneller Korpuskularstrahlen durch Materie. *Annalen der Physik*, **397**, 325–400. (Cited on page 153.)
- BLACKWELL, D.E. & SHALLIS, M.J. (1977). Stellar angular diameters from infrared photometry - Application to Arcturus and other stars; with effective temperatures. *Monthly Notices of the Royal Astronomical Society*, **180**, 177–191. (Cited on page 164.)
- BLUM, R.D. & PRADHAN, A.K. (1992). Rate coefficients for the excitation of infrared and ultraviolet lines in C II, N III, and O IV. *Astrophysical Journal Supplemental Series*, **80**, 425–452. (Cited on page 159.)
- BOCK, D.C.J. (2006). CARMA: Combined Array for Research in Millimeter-Wave Astronomy. In D.C. Backer, J.M. Moran & J.L. Turner, eds., *Revealing the Molecular Universe: One Antenna is Never Enough*, vol. 356 of *Astronomical Society of the Pacific Conference Series*, 17. (Cited on page 78.)
- BOYD, R.W., EATON, J.A., HALL, D.S., HENRY, G.W., GENET, R.M., LOVELL, L.P., HOPKINS, J.L., SABIA, J.D., KRISCIUNAS, K. & CHAMBLISS, C.R. (1983). Five years of photometry of Lambda Andromedae. *Astrophysics & Space Science*, **90**, 197–206. (Cited on page 121.)
- BRADSTREET, D.H. (1993). Binary Maker 2.0 - an interactive graphical tool for preliminary light curve analysis. "Double stars for the masses". *IAU Commission on Close Binary Stars*, **21**, 151–166. (Cited on page 57.)

REFERENCES

- BRANDT, J.C., HEAP, S.R., BEAVER, E.A., BOGESS, A., CARPENTER, K.G., EBBETS, D.C., HUTCHINGS, J.B., JURA, M., LECKRONE, D.S., LINSKY, J.L., MARAN, S.P., SAVAGE, B.D., SMITH, A.M., TRAFTON, L.M., WALTER, F.M., WEYMAN, R.J., AKE, T.B., BRUHWEILER, F., CARDELLI, J.A., LINDLER, D.J., MALUMUTH, E., RANDALL, C.E., ROBINSON, R., SHORE, S.N. & WAHLGREN, G. (1994). The Goddard High Resolution Spectrograph: Instrument, goals, and science results. *Publications of the Astronomical Society of the Pacific*, **106**, 890–908. (Cited on pages xiii, 70 and 161.)
- BROOKER, R.A. & OLLE, T.W. (1955). Apsidal-motion constants for polytropic models. *Monthly Notices of the Royal Astronomical Society*, **115**, 101. (Cited on page 123.)
- CANNON, C.J. (1973). Frequency-Quadrature Perturbations in Radiative-Transfer Theory. *Astrophysical Journal*, **185**, 621–630. (Cited on page 44.)
- CARDELLI, J.A., CLAYTON, G.C. & MATHIS, J.S. (1988). The determination of ultraviolet extinction from the optical and near-infrared. *Astrophysical Journal Letters*, **329**, L33–L37. (Cited on pages 173 and 174.)
- CARDELLI, J.A., CLAYTON, G.C. & MATHIS, J.S. (1989). The relationship between infrared, optical, and ultraviolet extinction. *Astrophysical Journal*, **345**, 245–256. (Cited on page 173.)
- CARLSSON, M. (1986). A computer program for solving multi-level non-LTE radiative transfer-problems in moving or static atmospheres. *Uppsala Astronomical Observatory Reports*, **33**. (Cited on page 184.)
- CARLSSON, M. & STEIN, R.F. (1995). Does a nonmagnetic solar chromosphere exist? *ApJ*, **440**, L29–L32. (Cited on page 84.)
- CARPENTER, K.G. & WAHLGREN, G.M. (1990). Modeling the ultraviolet photospheric spectrum of cool giant stars. I - Arcturus. II - Gamma Crucis. In G. Wallerstein, ed., *Cool Stars, Stellar Systems, and the Sun*, vol. 9 of *Astronomical Society of the Pacific Conference Series*, 64–69. (Cited on page 104.)
- CARPENTER, K.G., BROWN, A. & STENCEL, R.E. (1985). The geometric extent of C II (UV 0.01) emitting regions around luminous, late-type stars. *Astrophysical Journal*, **289**, 676–680. (Cited on pages 184, 187 and 201.)
- CARPENTER, K.G., ROBINSON, R.D., HARPER, G.M., BENNETT, P.D., BROWN, A. & MULLAN, D.J. (1999). GHRS Observations of Cool, Low-Gravity Stars. V. The Outer Atmosphere and Wind of the Nearby K Supergiant λ Velorum. *Astrophysical Journal*, **521**, 382–406. (Cited on pages 72 and 164.)
- CARPENTER, K.G., AYRES, T.R., HARPER, G.M., KOBER, G., NIELSEN, K.E. & WAHLGREN, G.M. (2014). An HST COS "SNAPshot" Spectrum of the K Supergiant λ Vel (K4Ib-II). *Astrophysical Journal*, **794**, 41. (Cited on page 164.)
- CASTELLI, F., GRATTON, R.G. & KURUCZ, R.L. (1997). Notes on the convection in the ATLAS9 model atmospheres. *Astronomy & Astrophysics*, **318**, 841–869. (Cited on pages 150 and 198.)

REFERENCES

- CAYREL, R. (1964). On the Temperature of Radiative Equilibrium in a Layer of Optically Thin Gas in the Radiation Field of the Solar Photosphere. *SAO Special Report*, **167**, 169. (Cited on page 8.)
- CHAMEL, N., HAENSEL, P., ZDUNIK, J.L. & FANTINA, A.F. (2013). On the Maximum Mass of Neutron Stars. *International Journal of Modern Physics E*, **22**, 30018. (Cited on page 6.)
- CHANDRASEKHAR, S. (1931). The highly collapsed configurations of a stellar mass. *Monthly Notices of the Royal Astronomical Society*, **91**, 456–466. (Cited on page 6.)
- CHANDRASEKHAR, S. (1933). The equilibrium of distorted polytropes. IV. the rotational and the tidal distortions as functions of the density distribution. *Monthly Notices of the Royal Astronomical Society*, **93**, 539–574. (Cited on page 123.)
- CHIAVASSA, A., PLEZ, B., JOSSELIN, E. & FREYTAG, B. (2009). Radiative hydrodynamics simulations of red supergiant stars. I. interpretation of interferometric observations. *Astronomy & Astrophysics*, **506**, 1351–1365. (Cited on page 199.)
- CHLUBA, J. & SUNYAEV, R.A. (2006). Free-bound emission from cosmological hydrogen recombination. *Astronomy & Astrophysics*, **458**, L29–L32. (Cited on page 106.)
- CHRISTIE, W.H. & WILSON, O.C. (1935). ζ Aurigae: the Structure of a Stellar Atmosphere. *Astrophysical Journal*, **81**, 426. (Cited on page 113.)
- CLARET, A. (2000). A new non-linear limb-darkening law for LTE stellar atmosphere models. Calculations for $-5.0 < \log[M/H] < +1$, $2000 \text{ K} < T_{\text{eff}} < 50000 \text{ K}$ at several surface gravities. *Astronomy & Astrophysics*, **363**, 1081–1190. (Cited on page 124.)
- COX, A.N. (2000). *Allen's astrophysical quantities*. (Cited on page 86.)
- CUNTO, W. & MENDOZA, C. (1992). The Opacity Project - the Topbase Atomic Database. *Revista Mexicana de Astronomia y Astrofisica*, **23**, 107. (Cited on pages 154 and 158.)
- CUNTZ, M. (1990). Chromospheric extents predicted by time-dependent acoustic wave models. *Astrophysical Journal*, **349**, 141–149. (Cited on pages 187 and 201.)
- DA SILVA, L., GIRARDI, L., PASQUINI, L., SETIAWAN, J., VON DER LÜHE, O., DE MEDEIROS, J.R., HATZES, A., DÖLLINGER, M.P. & WEISS, A. (2006). Basic physical parameters of a selected sample of evolved stars. *Astronomy & Astrophysics*, **458**, 609–623. (Cited on page 103.)
- DE MEDEIROS, J.R. & MAYOR, M. (1999). A catalog of rotational and radial velocities for evolved stars. *Astronomy & Astrophysics Supplemental*, **139**, 433–460. (Cited on page 123.)
- DE MEDEIROS, J.R., UDRY, S., BURKI, G. & MAYOR, M. (2002). A catalog of rotational and radial velocities for evolved stars. II. Ib supergiant stars. *Astronomy & Astrophysics*, **395**, 97–98. (Cited on page 123.)
- DEGROOTE, P., CONROY, K., HAMBLETON, K., BLOEMEN, S., PABLO, H., GIAMMARCO, J. & PRŠA, A. (2013). PHOEBE 2.0 - Where no model has gone before. In K. Pavlovski, A. Tkachenko & G. Torres, eds., *EAS Publications Series*, vol. 64 of *EAS Publications Series*, 277–284. (Cited on pages 56 and 118.)

REFERENCES

- DI BENEDETTO, G.P. & FERLUGA, S. (1990). Angular diameters of Zeta Aurigae-type supergiants by Michelson interferometry. *Astronomy & Astrophysics*, **236**, 449–454. (Cited on pages 120 and 161.)
- DRAINE, B.T. (2011). *Physics of the Interstellar and Intergalactic Medium*. (Cited on page 106.)
- DRAKE, S.A. (1985). Modeling lines formed in the expanding chromospheres of red giants. In J. E. Beckman & L. Crivellari, ed., *NATO ASIC Proc. 152: Progress in Stellar Spectral Line Formation Theory*, 351–357. (Cited on page 87.)
- DULK, G.A. (1985). Radio emission from the sun and stars. *Annual Review of Astronomy & Astrophysics*, **23**, 169–224. (Cited on page 98.)
- EATON, J.A. (1988). The atmospheric eclipse of 31 Cygni in the ultraviolet. *Astrophysical Journal*, **333**, 288–299. (Cited on pages 143, 183 and 201.)
- EATON, J.A. (1992). Intrinsic chromospheric emission from Zeta Aurigae binaries. *Monthly Notices of the Royal Astronomical Society*, **258**, 473–475. (Cited on pages 141 and 187.)
- EATON, J.A. (1993). On the chromospheric structure of Zeta Aurigae. *Astrophysical Journal*, **404**, 305–315. (Cited on pages 115, 141, 143, 144, 150, 180, 181, 182 and 183.)
- EATON, J.A. (1995). H-alpha measurements for cool giants. *Astronomical Journal*, **109**, 1797–1783. (Cited on pages 123 and 201.)
- EATON, J.A. (2008). A Model for the Chromosphere/Wind of 31 Cygni and Its Implications for Single Stars. *Astronomical Journal*, **136**, 1964–1979. (Cited on pages 171, 180, 182, 183 and 200.)
- EATON, J.A., JOHNSON, H.R. & CADMUS, R.R., JR. (1990). Chromospheric variability of M giant semiregular variables. *Astrophysical Journal*, **364**, 259–265. (Cited on page 102.)
- EATON, J.A., HENRY, G.W. & ODELL, A.P. (2008). Orbits and Pulsations of the Classical ζ Aurigae Binaries. *Astrophysical Journal*, **679**, 1490–1498. (Cited on pages xv, 118, 119, 121, 122, 123, 125, 126 and 162.)
- EDDINGTON, A.S. (1926). The reflection effect in eclipsing variables. *Monthly Notices of the Royal Astronomical Society*, **86**, 320–327. (Cited on page 125.)
- EINSTEIN, A. (1916a). Strahlungs-Emission und Absorption nach der Quantentheorie. *Deutsche Physikalische Gesellschaft*, **18**, 318–323. (Cited on page 28.)
- EINSTEIN, A. (1916b). Zur Quantentheorie der Strahlung. *Physikalische Gesellschaft Zürich*, **18**, 47–62. (Cited on page 28.)
- ELSÄSSER, H. (1981). Calar Alto - bisherige Erfahrungen, zukünftige Entwicklung. *Mitteilungen der Astronomischen Gesellschaft Hamburg*, **54**, 15. (Cited on page 66.)
- ENGELKE, C.W., PRICE, S.D. & KRAEMER, K.E. (2006). Spectral Irradiance Calibration in the Infrared. XVI. Improved Accuracy in the Infrared Spectra of the Secondary and Tertiary Standard Calibration Stars. *Astronomical Journal*, **132**, 1445–1463. (Cited on page 104.)

REFERENCES

- ERIKSSON, K., LINSKY, J.L. & SIMON, T. (1983). Outer atmospheres of cool stars. XIV - A model for the chromosphere and transition region of Beta Ceti (G9.5 III). *Astrophysical Journal*, **272**, 665–677. (Cited on pages 184, 185 and 187.)
- ESPINOSA LARA, F. & RIEUTORD, M. (2012). Gravity darkening in binary stars. *Astronomy & Astrophysics*, **547**, A32. (Cited on page 124.)
- EWEN, H.I. & PURCELL, E.M. (1951). Observation of a Line in the Galactic Radio Spectrum: Radiation from Galactic Hydrogen at 1,420 Mc./sec. *Nature*, **168**, 356. (Cited on page 27.)
- FANG, Z., KWONG, V.H.S., WANG, J. & PARKINSON, W.H. (1993). Measurements of radiative-decay rates of the $2s^22p(^2P) - 2s2p(^4P)$ intersystem transitions of C⁺. *Physical Review A*, **48**, 1114–1122. (Cited on page 159.)
- FEAUTRIER, P. (1964). A Procedure for computing the Mean Intensity and the Flux. *SAO Special Report*, **167**, 80. (Cited on pages 13 and 52.)
- FELDMAN, U. & DOSCHEK, G.A. (1979). The N III and O IV intersystem multiplets as density indicators for solar plasmas. *Astronomy & Astrophysics*, **79**, 357–359. (Cited on page 42.)
- FLOWER, D.R. & NUSSBAUMER, H. (1975). On the extreme ultraviolet solar emission of B-like ions - O IV. *Astronomy & Astrophysics*, **45**, 145–150. (Cited on page 42.)
- FONTENLA, J.M., AVRETT, E.H. & LOESER, R. (1990). Energy balance in the solar transition region. I - Hydrostatic thermal models with ambipolar diffusion. *ApJ*, **355**, 700–718. (Cited on page 83.)
- FREYTAG, B., STEFFEN, M. & DORCH, B. (2002). Spots on the surface of Betelgeuse – Results from new 3D stellar convection models. *Astronomische Nachrichten*, **323**, 213–219. (Cited on page 199.)
- GILLILAND, R.L., MORRIS, S.L., WEYMANN, R.J., EBBETS, D.C. & LINDLER, D.J. (1992). Resolution and noise properties of the Goddard High-Resolution Spectrograph. *Publications of the Astronomical Society of the Pacific*, **104**, 367–382. (Cited on pages 71 and 73.)
- GRASER, U. & HOPP, U. (1991). Pointing models for the Calar Alto 2.2 M and 3.5 M telescopes. *Astronomy & Astrophysics*, **251**, 737–742. (Cited on page 66.)
- GRAY, D.F. (2008). *The Observation and Analysis of Stellar Photospheres*. (Cited on pages 115 and 146.)
- GRAY, D.F. & TONER, C.G. (1987). An analysis of the photospheric line profiles in F, G, and K supergiants. *Astrophysical Journal*, **322**, 360–367. (Cited on page 123.)
- GRiffin, R. & GRIFFIN, R. (1986). Composite spectra. I - HR 6902. *Journal of Astrophysics and Astronomy*, **7**, 195–223. (Cited on page 113.)
- GRiffin, R.E. & AKE, T.B. (2015). The Zeta Aurigae Binaries. In *Astrophysics and Space Science Library*, vol. 408 of *Astrophysics and Space Science Library*, 1. (Cited on pages 17, 200 and 201.)

REFERENCES

- GRiffin, R.E.M. & GRIFFIN, R.F. (2000). Composite spectraPaper 10: the equal-mass binary HR 2030 (K0IIb+B8IV). *Monthly Notices of the Royal Astronomical Society*, **319**, 1094–1108. (Cited on page 113.)
- GRiffin, R.E.M., GRIFFIN, R.F., SCHROEDER, K.P. & REIMERS, D. (1990). Optical spectra of Zeta Aurigae binary systems. I - The 1987 eclipse of Zeta Aurigae. *Astronomy & Astrophysics*, **234**, 284–298. (Cited on page 113.)
- GRiffin, R.F. (2005). Spectroscopic binary orbits from photoelectric radial velocities. Paper 180: zeta Aurigae. *The Observatory*, **125**, 1–22. (Cited on pages 118, 119, 121 and 123.)
- GUSTAFSSON, B., BELL, R.A., ERIKSSON, K. & NORDLUND, A. (1975). A grid of model atmospheres for metal-deficient giant stars. I. *Astronomy & Astrophysics*, **42**, 407–432. (Cited on page 142.)
- GUSTAFSSON, B., EDVARDSSON, B., ERIKSSON, K., JØRGENSEN, U.G., NORDLUND, Å. & PLEZ, B. (2008). A grid of MARCS model atmospheres for late-type stars. I. Methods and general properties. *Astronomy & Astrophysics*, **486**, 951–970. (Cited on page 142.)
- GÜSTEN, R., NYMAN, L.Å., SCHILKE, P., MENTEN, K., CESARSKY, C. & BOOTH, R. (2006). The Atacama Pathfinder EXperiment (APEX) - a new submillimeter facility for southern skies -. *Astronomy & Astrophysics*, **454**, L13–L16. (Cited on page 79.)
- GUTHNICK, P. (1934). Das bevorstehende Bedeckungsminimum von ζ Auriage. *Astronomische Nachrichten*, **252**, 13. (Cited on page 17.)
- HALL, D.S. (1986). Pseudosynchronization found in binaries with eccentric orbits. *Astrophysical Journal Letters*, **309**, L83–L85. (Cited on page 121.)
- HAMANN, W.R. (1985). Line formation in expanding atmospheres - Accurate solution using approximate lambda operators. *Astronomy & Astrophysics*, **148**, 364–368. (Cited on pages 46 and 47.)
- HARPER, G.M. (1992). The outer atmospheres of the 'hybrid' bright giants - The chromospheres of Alpha TrA (K4 II), IOTA AUR (K3 II), Gamma AQL (K3 II) and Theta HER (K1 II). *MNRAS*, **256**, 37–64. (Cited on pages 83, 85 and 154.)
- HARPER, G.M. (2010). On Highly Clumped Magnetic Wind Models for Cool Evolved Stars. *Astrophysical Journal*, **720**, 1767–1771. (Cited on page 200.)
- HARPER, G.M., BROWN, A. & LIM, J. (2001). A Spatially Resolved, Semiempirical Model for the Extended Atmosphere of α Orionis (M2 Iab). *Astrophysical Journal*, **551**, 1073–1098. (Cited on pages 183 and 201.)
- HARPER, G.M., BROWN, A., BENNETT, P.D., BAADE, R., WALDER, R. & HUMMEL, C.A. (2005). VLA Observations of ζ Aurigae: Confirmation of the Slow Acceleration Wind Density Structure. *Astronomical Journal*, **129**, 1018–1034. (Cited on pages xvi, 135, 144, 146, 161, 162 and 180.)
- HARPER, G.M., O'RIAIN, N. & AYRES, T.R. (2013). Chromospheric thermal continuum millimetre emission from non-dusty K and M red giants. *Monthly Notices of the Royal Astronomical Society*, **428**, 2064–2073. (Cited on pages 82, 84, 91 and 189.)

REFERENCES

- HARPER, G.M., O'RIAIN, R.E.M., N. AND GRIFFIN & BENNETT, P.D. (2015). Periodic Photoexcited Si I Emission in Composite-Spectrum Binaries. *In Prep.* (Cited on pages xiv, 110 and 112.)
- HARPER, W.E. (1924). The Orbit of the spectroscopic binary Zeta Aurigae. *Publications of the Dominion Astrophysical Observatory Victoria*, **3**, 151–. (Cited on pages 16 and 111.)
- HARTMANN, L. & MACGREGOR, K.B. (1980). Momentum and energy deposition in late-type stellar atmospheres and winds. *Astrophysical Journal*, **242**, 260–282. (Cited on page 10.)
- HEITLER, W. (1954). *Quantum theory of radiation*. (Cited on page 34.)
- HEMPE, K. (1982). A study of ultraviolet spectra of Zeta Aur/VV CEP systems. I - Resonance line formation. *Astronomy & Astrophysics*, **115**, 133–137. (Cited on pages 18 and 141.)
- HOFFLEIT, D. (1943). Stellar Spectra. (Scientific Books: An Atlas of Stellar Spectra with an Outline of Spectral Classification). *Science*, **97**, 536–537. (Cited on page 3.)
- HÖGBOM, J.A. (1974). Aperture Synthesis with a Non-Regular Distribution of Interferometer Baselines. *Astronomy & Astrophysics Supplemental*, **15**, 417. (Cited on page 79.)
- HOLDEN, E. (2008). *Hand-Book of the Lick Observatory of the University of California*. BiblioBazaar. (Cited on page 66.)
- HUBENÝ, I. (1981). Non-LTE Line Transfer with Partial Redistribution. I. General Emission Profile. *Bulletin of the Astronomical Institutes of Czechoslovakia*, **32**, 271. (Cited on page 34.)
- HUBENÝ, I. (1985). *Progress in Stellar Spectral Line Formation Theory*, vol. 152 of *NATO ASI Series*. (Cited on page 34.)
- HUBENÝ, I. (2001). From Escape Probabilities to Exact Radiative Transfer. In G. Ferland & D.W. Savin, eds., *Spectroscopic Challenges of Photoionized Plasmas*, vol. 247 of *Astronomical Society of the Pacific Conference Series*, 197. (Cited on page 50.)
- HUBENÝ, I. & LANZ, T. (1995). Non-LTE line-blanketed model atmospheres of hot stars. 1: Hybrid complete linearization/accelerated lambda iteration method. *Astrophysical Journal*, **439**, 875–904. (Cited on page 120.)
- HUBENÝ, I. & LANZ, T. (2003). Model Photospheres with Accelerated Lambda Iteration. In I. Hubeny, D. Mihalas & K. Werner, eds., *Stellar Atmosphere Modeling*, vol. 288 of *Astronomical Society of the Pacific Conference Series*, 51. (Cited on page 48.)
- HUBENÝ, I. & MIHALAS, D. (2014). *Theory of Stellar Atmospheres*. (Cited on pages 22, 28, 29, 38, 153, 154 and 156.)
- HUMMER, D.G. (1962). Non-coherent scattering: I. The redistribution function with Doppler broadening. *Monthly Notices of the Royal Astronomical Society*, **125**, 21–37. (Cited on page 33.)
- HUMMER, D.G. (1981). Expressions for the computer-evaluation of the four kernel functions for line formation with Doppler and Lorentz profiles. *Journal of Quantitative Spectroscopy and Radiative Transfer*, **26**, 187–195. (Cited on page 51.)

REFERENCES

- HUMMER, D.G. (1988). A fast and accurate method for evaluating the nonrelativistic free-free Gaunt factor for hydrogenic ions. *ApJ*, **327**, 477–484. (Cited on page 88.)
- HUT, P. (1981). Tidal evolution in close binary systems. *Astronomy & Astrophysics*, **99**, 126–140. (Cited on pages 121 and 122.)
- IBEN, I., JR. (1967). Stellar Evolution Within and off the Main Sequence. *Annual Review of Astronomy & Astrophysics*, **5**, 571. (Cited on page 6.)
- IRONS, F.E. (1978). On the equality of the mean escape probability and mean net radiative bracket for line photons. *Monthly Notices of the Royal Astronomical Society*, **182**, 705–709. (Cited on page 52.)
- IRWIN, A.W. (1981). Polynomial partition function approximations of 344 atomic and molecular species. *Astrophysical Journal Supplemental Series*, **45**, 621–633. (Cited on page 148.)
- JACKSON, N. (2008). Principles of Interferometry. In F. Bacciotti, L. Testi & E. Whelan, eds., *Jets from Young Stars II*, vol. 742 of *Lecture Notes in Physics*, Berlin Springer Verlag, 193. (Cited on pages xiii and 74.)
- JEFFERIES, J.T. & THOMAS, R.N. (1959). Source Function in a Non-Equilibrium Atmosphere. III. The Influence of a Chromosphere. *Astrophysical Journal*, **129**, 401. (Cited on page 13.)
- JOHNSON, L.C. (1972). Approximations for Collisional and Radiative Transition Rates in Atomic Hydrogen. *Astrophysical Journal*, **174**, 227. (Cited on pages 152 and 153.)
- JORDAN, S.D. (1969). Why the Temperature Rise does not Occur in Radiative Equilibrium in Stellar Chromospheres of Dominant H⁻ Opacity. *Astrophysical Journal*, **157**, 465. (Cited on page 8.)
- JORDAN, S.D. & AVRETT, E.H., eds. (1973). *Stellar Chromospheres*, vol. 317 of *NASA Special Publication*. (Cited on page 180.)
- JUDGE, P.G. (1986). Constraints on the Outer Atmospheric Structure of Late Type Giant Stars with IUE Application to Alpha-Tauri K5III and Beta-Gruis M5III. *Monthly Notices of the Royal Astronomical Society*, **223**, 239. (Cited on pages 104 and 187.)
- JUDGE, P.G. (1990). On the interpretation of chromospheric emission lines. *Astrophysical Journal*, **348**, 279–296. (Cited on page 158.)
- JUDGE, P.G. (1994). The 'monochromatic density diagnostic' technique: First detection of multiple density components in the chromosphere of alpha Tauri. *Astrophysical Journal*, **430**, 351–359. (Cited on page 171.)
- JUDGE, P.G. & CARPENTER, K.G. (1998a). On Chromospheric Heating Mechanisms of "Basal Flux" Stars. *Astrophysical Journal*, **494**, 828–839. (Cited on pages xvi, 159 and 161.)
- JUDGE, P.G. & CARPENTER, K.G. (1998b). On Chromospheric Heating Mechanisms of "Basal Flux" Stars. *ApJ*, **494**, 828–+. (Cited on pages 83 and 171.)
- JUDGE, P.G., JORDAN, C. & FELDMAN, U. (1992). Fe II emission lines. II - Excitation mechanisms in cool stars. *Astrophysical Journal*, **384**, 613–623. (Cited on page 180.)

REFERENCES

- KALKOFEN, W., ULM SCHNEIDER, P. & AVRETT, E.H. (1999). Does the Sun Have a Full-Time Chromosphere? *ApJ*, **521**, L141–L144. (Cited on page 83.)
- KALLRATH, J. & MILONE, E.F. (2009). *Eclipsing Binary Stars: Modeling and Analysis*. (Cited on pages 56 and 57.)
- KARZAS, W.J. & LATTER, R. (1961). Electron Radiative Transitions in a Coulomb Field. *Astrophysical Journal Supplemental Series*, **6**, 167. (Cited on pages 22, 37 and 154.)
- KELCH, W.L., CHANG, S.H., FURENLID, I., LINSKY, J.L., BASRI, G.S., CHIU, H.Y. & MARAN, S.P. (1978). Stellar model chromospheres. VII - Capella /G5 III +/, Pollux /K0 III/, and Aldebaran /K5 III/. *ApJ*, **220**, 962–979. (Cited on page 83.)
- KIPPENHABN, R. (1977). Rotational darkening - Rotational brightening. *Astronomy & Astrophysics*, **58**, 267–271. (Cited on page 124.)
- KOPAL, Z. (1959). *Close binary systems*. (Cited on page 57.)
- KRAMIDA, A., YU. RALCHENKO, READER, J. & AND NIST ASD TEAM (2015). NIST Atomic Spectra Database (ver. 5.2), [Online]. Available: <http://physics.nist.gov/asd>. National Institute of Standards and Technology, Gaithersburg, MD. (Cited on pages 27, 148, 154 and 197.)
- KUNDU, M.R. (1965). *Solar radio astronomy*. (Cited on page 106.)
- KURUCZ, R. & BELL, B. (1995). Kurucz R., Bell B., Atomic Line Data, Kurucz CD-ROM No. 23. Cambridge, Mass.: Smithsonian Astrophysical Observatory. (Cited on pages 154, 158 and 197.)
- KURUCZ, R.L. (1970). Atlas: a Computer Program for Calculating Model Stellar Atmospheres. *SAO Special Report*, **309**. (Cited on pages 62 and 124.)
- LAFRASSE, S., MELLA, G., BONNEAU, D., DUVERT, G., DELFOSSE, X., CHESNEAU, O. & CHELLI, A. (2010). Building the 'JMMC Stellar Diameters Catalog' using SearchCal. In *Society of Photo-Optical Instrumentation Engineers (SPIE) Conference Series*, vol. 7734 of *Society of Photo-Optical Instrumentation Engineers (SPIE) Conference Series*, 4. (Cited on pages 103 and 164.)
- LAPKIN, I., NYSTRÖM, O., DESMARIS, V., DOCHEV, D., VASSILEV, V., MONJE, R., MELEDIN, D., HENKE, D., STRANDBERG, M., SUNDIN, E., FREDRIXON, M., FERM, S.E. & BELITSKY, V. (2008). Optics Design and Verification for the APEX Swedish Heterodyne Facility Instrument (SHeFI). In W. Wild, ed., *Nineteenth International Symposium on Space Terahertz Technology*, 351. (Cited on page 105.)
- LECAR, M., WHEELER, J.C. & MCKEE, C.F. (1976). Tidal circularization of the binary X-ray sources Hercules X-1 and Centaurus X-3. *Astrophysical Journal*, **205**, 556–562. (Cited on page 123.)
- LEE, H.W., SOHN, Y.J., KANG, Y.W. & KIM, H.I. (2003). Raman-scattered he ii 6545 line in the symbiotic star v1016cygni. *The Astrophysical Journal*, **598**, 553. (Cited on page 37.)

REFERENCES

- LENNON, D.J., DUFTON, P.L., HIBBERT, A. & KINGSTON, A.E. (1985). C II emission lines formed in optically thin plasmas. *Astrophysical Journal*, **294**, 200–206. (Cited on page 159.)
- LIM, J., CARILLI, C.L., WHITE, S.M., BEASLEY, A.J. & MARSON, R.G. (1998). Large convection cells as the source of Betelgeuse's extended atmosphere. *Nature*, **392**, 575–577. (Cited on pages 183 and 201.)
- LINSKY, J.L. (1980). Stellar chromospheres. In D.F. Gray & J.L. Linsky, eds., *IAU Colloq. 51: Stellar Turbulence*, vol. 114 of *Lecture Notes in Physics*, Berlin Springer Verlag, 248–277. (Cited on page 8.)
- LINSKY, J.L. & AYRES, T.R. (1978). Stellar model chromospheres. VI - Empirical estimates of the chromospheric radiative losses of late-type stars. *ApJ*, **220**, 619–628. (Cited on page 85.)
- LINSKY, J.L. & HAISCH, B.M. (1979). Outer atmospheres of cool stars. I - The sharp division into solar-type and non-solar-type stars. *Astrophysical Journal Letters*, **229**, L27–L32. (Cited on page 10.)
- LOUKITCHeva, M., SOLANKI, S.K., CARLSSON, M. & STEIN, R.F. (2004). Millimeter observations and chromospheric dynamics. *A&A*, **419**, 747–756. (Cited on pages xiii, 98 and 99.)
- LUCK, R.E. (1977). The chemical composition of late-type supergiants. II - Lithium abundances for 19 G and K Ib stars. *Astrophysical Journal*, **218**, 752–766. (Cited on page 143.)
- LUCY, L.B. (1967). Gravity-Darkening for Stars with Convective Envelopes. *Zeitschrift fr Astrophysik*, **65**, 89. (Cited on pages 63 and 124.)
- LUTTERMOSER, D.G., JOHNSON, H.R. & EATON, J. (1994a). The chromospheric structure of the cool giant star G Herculis. *ApJ*, **422**, 351–365. (Cited on pages 83, 87, 105 and 199.)
- LUTTERMOSER, D.G., JOHNSON, H.R. & EATON, J. (1994b). The chromospheric structure of the cool giant star G Herculis. *Astrophysical Journal*, **422**, 351–365. (Cited on page 104.)
- MARISKA, J.T. (1992). *The solar transition region*. (Cited on page 40.)
- MARSHALL, K.P. (1996). Non-LTE model chromospheres of zeta Aurigae stars. *Monthly Notices of the Royal Astronomical Society*, **280**, 977–999. (Cited on page 141.)
- MAURY, A.C. & PICKERING, E.C. (1897). Spectra of bright stars photographed with the 11-inch Draper Telescope as part of the Henry Draper Memorial. *Annals of Harvard College Observatory*, **28**, 1–128. (Cited on pages 16 and 111.)
- MAZZALI, P.A., RÖPKE, F.K., BENETTI, S. & HILLEBRANDT, W. (2007). A Common Explosion Mechanism for Type Ia Supernovae. *Science*, **315**, 825–. (Cited on page 6.)
- MCALESTER, H.A., TEN BRUMMELAAR, T.A., GIES, D.R., HUANG, W., BAGNUOLO, W.G., JR., SHURE, M.A., STURMANN, J., STURMANN, L., TURNER, N.H., TAYLOR, S.F., BERGER, D.H., BAINES, E.K., GRUNDSTROM, E., OGDEN, C., RIDGWAY, S.T. & VAN BELLE, G. (2005). First Results from the CHARA Array. I. An Interferometric and Spectroscopic Study of the Fast Rotator α Leonis (Regulus). *Astrophysical Journal*, **628**, 439–452. (Cited on page 77.)

REFERENCES

- MCKELLAR, A. & PETRIE, R.M. (1952). Intensity and radial-velocity measurements on the spectrum of Zeta Aurigae at recent eclipses. *Monthly Notices of the Royal Astronomical Society*, **112**, 641. (Cited on pages 18, 141 and 200.)
- MCLAUGHLIN, D.B. (1950a). 32 Cygni as an eclipsing binary. *Astrophysical Journal*, **111**, 449. (Cited on page 17.)
- MCLAUGHLIN, D.B. (1950b). Atmospheric Eclipse Effects in the Spectrum of 31 Cygni. *Publications of the Astronomical Society of the Pacific*, **62**, 13. (Cited on page 17.)
- MCMULLIN, J.P., WATERS, B., SCHIEBEL, D., YOUNG, W. & GOLAP, K. (2007). CASA Architecture and Applications. In R.A. Shaw, F. Hill & D.J. Bell, eds., *Astronomical Data Analysis Software and Systems XVI*, vol. 376 of *Astronomical Society of the Pacific Conference Series*, 127. (Cited on page 79.)
- MCMURRY, A.D. (1999). The outer atmosphere of Tau - I. A new chromospheric model. *MNRAS*, **302**, 37–47. (Cited on pages 83, 87, 89, 184 and 187.)
- MCWILLIAM, A. (1990). High-resolution spectroscopic survey of 671 GK giants. I - Stellar atmosphere parameters and abundances. *Astrophysical Journal Supplemental Series*, **74**, 1075–1128. (Cited on pages 90, 120 and 143.)
- MENZEL, D.H. (1936). The Structure of the Atmosphere of ζ Aurigae. *Harvard College Observatory Circular*, **417**, 1–9. (Cited on pages 17 and 95.)
- MENZEL, D.H. (1937). Physical Processes in Gaseous Nebulae. I. *Astrophysical Journal*, **85**, 330. (Cited on page 147.)
- MENZEL, D.H. & PEKERIS, C.L. (1935). Absorption coefficients and hydrogen line intensities. *Monthly Notices of the Royal Astronomical Society*, **96**, 77. (Cited on pages 37 and 153.)
- MIHALAS, D. (1978). *Stellar atmospheres /2nd edition/*. (Cited on pages 8 and 52.)
- MILKEY, R.W., SHINE, R.A. & MIHALAS, D. (1975). Resonance line transfer with partial redistribution. IV - A generalized formulation for lines with common upper states. V - The solar CA II lines. *Astrophysical Journal*, **199**, 718–733. (Cited on page 36.)
- MILNE, E.A. (1921). Radiative equilibrium in the outer layers of a star. *Monthly Notices of the Royal Astronomical Society*, **81**, 361–375. (Cited on page 124.)
- MORTON, D.C. (1991). Atomic data for resonance absorption lines. I - Wavelengths longward of the Lyman limit. *Astrophysical Journal Supplemental Series*, **77**, 119–202. (Cited on page 162.)
- MOURLARD, D., CLAUSS, J.M., MARCOTTO, A., PERRAUT, K., TALLON-BOSC, I., BÉRIO, P., BLAZIT, A., BONNEAU, D., BOSIO, S., BRESSON, Y., CHESNEAU, O., DELAA, O., HÉNAULT, F., HUGHES, Y., LAGARDE, S., MERLIN, G., ROUSSEL, A., SPANG, A., STEE, P., TALLON, M., ANTONELLI, P., FOY, R., KERVELLA, P., PETROV, R., THIEBAUT, E., VAKILI, F., McALISTER, H., TEN BRUMMELAAR, T., STURMANN, J., STURMANN, L., TURNER, N., FARRINGTON, C. & GOLDFINGER, P.J. (2009). VEGA: Visible spEctroGraph and polArimeter for the CHARA array: principle and performance. *Astronomy & Astrophysics*, **508**, 1073–1083. (Cited on page 78.)

REFERENCES

- MOZURKEWICH, D., ARMSTRONG, J.T., HINDSLEY, R.B., QUIRRENBACH, A., HUMMEL, C.A., HUTTER, D.J., JOHNSTON, K.J., HAJIAN, A.R., ELIAS, N.M., II, BUSCHER, D.F. & SIMON, R.S. (2003). Angular Diameters of Stars from the Mark III Optical Interferometer. *AJ*, **126**, 2502–2520. (Cited on pages xx, 90 and 103.)
- NEWELL, R.T. & HJELLMING, R.M. (1982). Radio emission from the extended chromosphere of Alpha Orionis. *Astrophysical Journal Letters*, **263**, L85–L87. (Cited on page 106.)
- O'GORMAN, E. (2014). (Cited on pages 78, 82 and 104.)
- O'GORMAN, E., HARPER, G.M., BROWN, A., DRAKE, S. & RICHARDS, A.M.S. (2013). Multi-wavelength Radio Continuum Emission Studies of Dust-free Red Giants. *Astronomical Journal*, **146**, 98. (Cited on pages 12, 106 and 107.)
- OHNAKA, K. (2013). Spatially resolved, high-spectral resolution observation of the K giant Aldebaran in the CO first overtone lines with VLTI/AMBER. *Astronomy & Astrophysics*, **553**, A3. (Cited on page 184.)
- OLSON, G.L. & KUNASZ, P.B. (1987a). Short characteristic solution of the non-LTE transfer problem by operator perturbation. I. The one-dimensional planar slab. *Journal of Quantitative Spectroscopy and Radiative Transfer*, **38**, 325–336. (Cited on page 46.)
- OLSON, G.L. & KUNASZ, P.B. (1987b). Short characteristic solution of the non-LTE transfer problem by operator perturbation. I. The one-dimensional planar slab. *JQSRT*, **38**, 325–336. (Cited on page 89.)
- OLSON, G.L., AUER, L.H. & BUCHLER, J.R. (1986). A rapidly convergent iterative solution of the non-LTE line radiation transfer problem. *Journal of Quantitative Spectroscopy and Radiative Transfer*, **35**, 431–442. (Cited on page 45.)
- OMONT, A., SMITH, E.W. & COOPER, J. (1972). Redistribution of Resonance Radiation. I. The Effect of Collisions. *Astrophysical Journal*, **175**, 185. (Cited on page 34.)
- ÖPIK, E. (1938). Stellar Structure, Source of Energy, and Evolution. *Publications of the Tartu Astrofizika Observatory*, **30**, C1–C115. (Cited on page 5.)
- ORANJE, B.J., ZWAAN, C. & MIDDELKOOP, F. (1982). Magnetic structure in cool stars. V - Chromospheric and transition-region emission from giants. *Astronomy & Astrophysics*, **110**, 30–36. (Cited on page 86.)
- O'RIAIN, N. & HARPER, G.M. (2015). Semi-Empirical Model of the Chromosphere of ζ Aurigae A, in prep. (Cited on page 140.)
- O'RIAIN, N., HARPER, G.M., GRIFFIN, R.E.M. & BENNETT, P.D. (2015). ζ Aurigae: Periodic Photoexcited Si I Emission. In G.T. van Belle & H.C. Harris, eds., *18th Cambridge Workshop on Cool Stars, Stellar Systems, and the Sun*, vol. 18 of *Cambridge Workshop on Cool Stars, Stellar Systems, and the Sun*. (Cited on page 110.)
- OSTERBROCK, D.E. (1962). The Escape of Resonance-Line Radiation from an Optically Thick Nebula. *Astrophysical Journal*, **135**, 195. (Cited on page 158.)
- PERAIAH, A. (2001). *An Introduction to Radiative Transfer*. (Cited on page 47.)

REFERENCES

- PÉREZ MARTÍNEZ, M.I., SCHRÖDER, K.P. & CUNTZ, M. (2011). The basal chromospheric Mg II h+k flux of evolved stars: probing the energy dissipation of giant chromospheres. *Monthly Notices of the Royal Astronomical Society*, **414**, 418–427. (Cited on pages xx, 85, 86, 90, 103 and 104.)
- PLASKETT, J.S. (1927). The Dominion Astrophysical Observatory. *Publications of the Astronomical Society of the Pacific*, **39**, 88. (Cited on page 66.)
- PRADHAN, A.K. & NAHAR, S.N. (2011). *Atomic Astrophysics and Spectroscopy*. (Cited on page 25.)
- PRESS, W.H., TEUKOLSKY, S.A., VETTERLING, W.T. & FLANNERY, B.P. (1992). *Numerical Recipes in C (2Nd Ed.): The Art of Scientific Computing*. Cambridge University Press, New York, NY, USA. (Cited on page 56.)
- PRŠA, A. & ZWITTER, T. (2005). A Computational Guide to Physics of Eclipsing Binaries. I. Demonstrations and Perspectives. *Astrophysical Journal*, **628**, 426–438. (Cited on pages 56 and 118.)
- RAFERT, J.B. & TWIGG, L.W. (1980). Observational determination of the gravity darkening exponent and bolometric albedo for close binary star systems. *Monthly Notices of the Royal Astronomical Society*, **193**, 79–86. (Cited on page 124.)
- ROBINSON, P.A. (1993). Stochastic-growth theory of Langmuir growth-rate fluctuations in type III solar radio sources. *Solar Physics*, **146**, 357–363. (Cited on page 22.)
- ROBINSON, R.D., CARPENTER, K.G. & BROWN, A. (1998). Goddard High-Resolution Spectrograph Observations of Cool Low-Gravity Stars. IV. A Comparison of the K5 III Stars alpha Tauri and gamma Draconis. *ApJ*, **503**, 396–+. (Cited on page 90.)
- ROWE, A.K. (1992). Photoionisation of CA II by Hydrogen Lyman Alpha. In M.S. Giampapa & J.A. Bookbinder, eds., *Cool Stars, Stellar Systems, and the Sun*, vol. 26 of *Astronomical Society of the Pacific Conference Series*, 561. (Cited on page 184.)
- RYBICKI, G.B. (1971). A modified Feautrier method. *Journal of Quantitative Spectroscopy and Radiative Transfer*, **11**, 589–595. (Cited on page 52.)
- RYBICKI, G.B. (1972). A Novel Approach to the Solution of Multilevel Transfer Problems. In *Line Formation in the Presence of Magnetic Fields*, 145. (Cited on page 48.)
- RYBICKI, G.B. (1984). *Escape probability methods*, 21–64. (Cited on page 50.)
- RYBICKI, G.B. & HUMMER, D.G. (1991). An accelerated lambda iteration method for multi-level radiative transfer. I - Non-overlapping lines with background continuum. *Astronomy & Astrophysics*, **245**, 171–181. (Cited on pages 48, 49, 52 and 55.)
- RYBICKI, G.B. & LIGHTMAN, A.P. (1979). *Radiative processes in astrophysics*. (Cited on pages 22 and 88.)
- SALARIS, M. & CASSISI, S. (2005). *Evolution of Stars and Stellar Populations*. (Cited on pages 4 and 7.)

REFERENCES

- SCHARMER, G.B. (1981). Solutions to radiative transfer problems using approximate lambda operators. *Astrophysical Journal*, **249**, 720–730. (Cited on page 49.)
- SCHARMER, G.B. & CARLSSON, M. (1985). A new approach to multi-level non-LTE radiative transfer problems. *Journal of Computational Physics*, **59**, 56–80. (Cited on page 48.)
- SCHLEGEL, D.J., FINKBEINER, D.P. & DAVIS, M. (1998). Maps of Dust Infrared Emission for Use in Estimation of Reddening and Cosmic Microwave Background Radiation Foregrounds. *Astrophysical Journal*, **500**, 525–553. (Cited on page 174.)
- SCHREIER, F. (2009). Comments on “A Common Misunderstanding about the Voigt Line Profile”. *Journal of Atmospheric Sciences*, **66**, 1860. (Cited on page 32.)
- SCHRIJVER, C.J. & ZWAAN, C. (2000). *Solar and Stellar Magnetic Activity*. (Cited on pages 7, 83 and 98.)
- SCHRÖDER, K.P. (1988). *What can we Learn from ζ AUR Binary Systems?*, 339. (Cited on page 141.)
- SCHRODER, K.P., POLS, O.R. & EGGLETON, P.P. (1997). A critical test of stellar evolution and convective core ‘overshooting’ by means of zeta Aurigae systems. *Monthly Notices of the Royal Astronomical Society*, **285**, 696–710. (Cited on pages 17 and 18.)
- SCHROEDER, K.P. (1983). Detection of a stellar prominence of the K supergiant 32 CYG. *Astronomy & Astrophysics*, **124**, L16–L18. (Cited on page 200.)
- SCHROEDER, K.P. (1986). A study of UV spectra of Zeta Aur/VV CEP systems. VIII - Chromospheric ionization and opacity. *Astronomy & Astrophysics*, **170**, 70–76. (Cited on pages xxi, 148 and 150.)
- SCHROEDER, K.P., GRIFFIN, R.E.M. & GRIFFIN, R.F. (1990). Optical spectra of Zeta Aurigae binary systems. II - The lower chromosphere of Zeta Aurigae. *Astronomy & Astrophysics*, **234**, 299–307. (Cited on pages xxi, 115, 144, 148 and 150.)
- SCHUSTER, A. (1905). Radiation Through a Foggy Atmosphere. *Astrophysical Journal*, **21**, 1. (Cited on pages 12, 14 and 53.)
- SEAQUIST, E.R. & TAYLOR, A.R. (1987). A detailed analysis of the radio emission from the symbiotic star RX Puppis. *Astrophysical Journal*, **312**, 813–821. (Cited on page 107.)
- SEATON, M.J. (1959). Radiative recombination of hydrogenic ions. *Monthly Notices of the Royal Astronomical Society*, **119**, 81. (Cited on pages 38 and 197.)
- SENNHAUSER, C. & BERDYUGINA, S.V. (2011). Magnetic Field Detection on Late-type Giants from Zeeman Component Decomposition. In C. Johns-Krull, M.K. Browning & A.A. West, eds., *16th Cambridge Workshop on Cool Stars, Stellar Systems, and the Sun*, vol. 448 of *Astronomical Society of the Pacific Conference Series*, 1255. (Cited on page 21.)
- SHEN, L.Z., BEAVERS, W.I., EITTER, J.J. & SALZER, J.J. (1985). A double-line spectroscopic orbit for Capella. *Astronomical Journal*, **90**, 1503–1510. (Cited on page 121.)

REFERENCES

- SHINE, R.A., MILKEY, R.W. & MIHALAS, D. (1975). Resonance line transfer with partial redistribution. VI - The Ca II K-line in solar-type stars. *Astrophysical Journal*, **201**, 222–224. (Cited on page 34.)
- SIRINGO, G., KREYSA, E., KOVÁCS, A., SCHULLER, F., WEISS, A., ESCH, W., GEMÜND, H.P., JETHAVA, N., LUNDERSHAUSEN, G., COLIN, A., GÜSTEN, R., MENTEN, K.M., BEELEN, A., BERTOLDI, F., BEEMAN, J.W. & HALLER, E.E. (2009). The Large APEX BOlometer CAmera LABOCA. *Astronomy & Astrophysics*, **497**, 945–962. (Cited on page 80.)
- SIVIERO, A., MUNARI, U., SORDO, R., DALLAPORTA, S., MARRESE, P.M., ZWITTER, T. & MILONE, E.F. (2004). Asiago eclipsing binaries program. I. V432 Aurigae. *Astronomy & Astrophysics*, **417**, 1083–1092. (Cited on page 62.)
- SOBOLEV, V.V. (1975). *Light scattering in planetary atmospheres*. (Cited on page 128.)
- SOCAS-NAVARRO, H. & TRUJILLO BUENO, J. (1997). Linearization versus Preconditioning: Which Approach Is Best for Solving Multilevel Transfer Problems? *Astrophysical Journal*, **490**, 383–392. (Cited on page 48.)
- SODERBLOM, D.R. & ET AL. (1995). *Goddard High Resolution Spectrograph Instrument Handbook v. 6.0*. (Cited on pages 70 and 72.)
- SOUBIRAN, C., LE CAMPION, J.F., CAYREL DE STROBEL, G. & CAILLO, A. (2010). The PASTEL catalogue of stellar parameters. *Astronomy & Astrophysics*, **515**, A111. (Cited on pages xx, 103 and 104.)
- STECHER, T.P. & DONN, B. (1965). On Graphite and Interstellar Extinction. *Astrophysical Journal*, **142**, 1681. (Cited on pages xviii and 174.)
- STENCEL, R.E., LINSKY, J.L., BROWN, A., JORDAN, C., CARPENTER, K.G., WING, R.F. & CZYZAK, S. (1981). Density sensitive C II lines in cool stars of low gravity. *Monthly Notices of the Royal Astronomical Society*, **196**, 47P–53P. (Cited on pages 42 and 156.)
- SUTMANN, G. & CUNTZ, M. (1995). Generation of mass loss in K giants: The failure of global oscillation modes and possible implications. *Astrophysical Journal Letters*, **442**, L61–L64. (Cited on page 106.)
- TAYAL, S.S. (2008). Collision Strengths for Electron Scattering from Si II. *Astrophysical Journal Supplemental Series*, **179**, 534–541. (Cited on pages xvii, xxi, 158, 159, 161 and 169.)
- THOMAS, R.N. (1957). The Source Function in a Non-Equilibrium Atmosphere. I. The Resonance Lines. *Astrophysical Journal*, **125**, 260. (Cited on page 180.)
- UITENBROEK, H. (1990). *Partial redistribution modeling of the CaII K line*. (Cited on page 178.)
- UITENBROEK, H. (2001). Multilevel Radiative Transfer with Partial Frequency Redistribution. *Astrophysical Journal*, **557**, 389–398. (Cited on pages 48 and 50.)
- UITENBROEK, H. (2014). (Cited on page 178.)

REFERENCES

- ULMSCHNEIDER, P. (1991). Acoustic Heating (With 9 Figures). In P. Ulmschneider, E. R. Priest, & R. Rosner, ed., *Mechanisms of Chromospheric and Coronal Heating*, 328–+. (Cited on page 83.)
- VAN BELLE, G.T., CIARDI, D.R., TEN BRUMMELAAR, T., McALISTER, H.A., RIDGWAY, S.T., BERGER, D.H., GOLDFINGER, P.J., STURMANN, J., STURMANN, L., TURNER, N., BODEN, A.F., THOMPSON, R.R. & COYNE, J. (2006). First Results from the CHARA Array. III. Oblateness, Rotational Velocity, and Gravity Darkening of Alderamin. *Astrophysical Journal*, **637**, 494–505. (Cited on page 124.)
- VAN CITTERT, P.H. (1934). Die Wahrscheinliche Schwingungsverteilung in Einer von Einer Lichtquelle Direkt Oder Mittels Einer Linse Beleuchteten Ebene. *Physica*, **1**, 201–210. (Cited on page 76.)
- VAN HOOF, P.A.M., MARTIN, P.G. & FERLAND, G.J. (2000). Current Development of Cloudy. In J. Franco, L. Terlevich, O. López-Cruz & I. Arétxaga, eds., *Cosmic Evolution and Galaxy Formation: Structure, Interactions, and Feedback*, vol. 215 of *Astronomical Society of the Pacific Conference Series*, 220. (Cited on page 52.)
- VAN LEEUWEN, F. (2007). Validation of the new Hipparcos reduction. *Astronomy & Astrophysics*, **474**, 653–664. (Cited on pages xx, 103 and 104.)
- VAN REGEMORTER, H. (1962). Rate of Collisional Excitation in Stellar Atmospheres. *Astrophysical Journal*, **136**, 906. (Cited on pages 30 and 156.)
- VECCHIO, A., CAUZZI, G. & REARDON, K.P. (2009). The solar chromosphere at high resolution with IBIS. II. Acoustic shocks in the quiet internetwork and the role of magnetic fields. *A&A*, **494**, 269–286. (Cited on page 83.)
- VERNAZZA, J.E., AVRETT, E.H. & LOESER, R. (1973). Structure of the Solar Chromosphere. Basic Computations and Summary of the Results. *Astrophysical Journal*, **184**, 605–632. (Cited on pages 146, 148 and 152.)
- VERNAZZA, J.E., AVRETT, E.H. & LOESER, R. (1976). Structure of the solar chromosphere. II - The underlying photosphere and temperature-minimum region. *ApJS*, **30**, 1–60. (Cited on pages xii, 7, 9, 83 and 154.)
- VERNAZZA, J.E., AVRETT, E.H. & LOESER, R. (1981). Structure of the solar chromosphere. III - Models of the EUV brightness components of the quiet-sun. *ApJS*, **45**, 635–725. (Cited on page 83.)
- VERNER, D.A., FERLAND, G.J., KORISTA, K.T. & YAKOVLEV, D.G. (1996). Atomic Data for Astrophysics. II. New Analytic FITS for Photoionization Cross Sections of Atoms and Ions. *Astrophysical Journal*, **465**, 487. (Cited on page 197.)
- VILLADSEN, J., HALLINAN, G., BOURKE, S., GÜDEL, M. & RUPEN, M. (2014). First Detection of Thermal Radio Emission from Solar-type Stars with the Karl G. Jansky Very Large Array. *Astrophysical Journal*, **788**, 112. (Cited on pages 12, 99 and 109.)
- VON ZEIPEL, H. (1924). The radiative equilibrium of a rotating system of gaseous masses. *Monthly Notices of the Royal Astronomical Society*, **84**, 665–683. (Cited on pages 63 and 124.)

REFERENCES

- WEDEMEYER-BÖHM, S., LUDWIG, H.G., STEFFEN, M., LEENAARTS, J. & FREYTAG, B. (2007). Inter-network regions of the Sun at millimetre wavelengths. *A&A*, **471**, 977–991. (Cited on page 83.)
- WEDEMEYER-BÖHM, S., LAGG, A. & NORDLUND, Å. (2009). Coupling from the Photosphere to the Chromosphere and the Corona. *Space Science Reviews*, **144**, 317–350. (Cited on pages xii and 8.)
- WEISSKOPF, V.F.I. (1933). The intensity and structure of spectral lines. *The Observatory*, **56**, 291–308. (Cited on page 34.)
- WENDKER, H.J. (1998). VizieR Online Data Catalog: Radio continuum emission from stars (Wendker, 1995). *VizieR Online Data Catalog*, **2199**, 0. (Cited on pages 100 and 108.)
- WHITE, S.M. (2000). The Contributions of the VLA to the Study of Radio Stars. In D.G. Finley & W.M. Goss, eds., *Radio interferometry : the saga and the science*, 86. (Cited on page 12.)
- WIEDEMANN, G., AYRES, T.R., JENNINGS, D.E. & SAAR, S.H. (1994). Carbon Monoxide Fundamental Bands in Late-Type Stars. III. Chromosphere or CO-mosphere? *ApJ*, **423**, 806–+. (Cited on page 89.)
- WILSON, O.C. (1957). The Analysis of the Chromosphere of Zeta Aurigae. *Journal of the Royal Astronomical Society of Canada*, **51**, 70. (Cited on page 69.)
- WILSON, O.C. & ABT, H.A. (1954). Chromospheric Structure of the K-Type Component of Zeta Aurigae. *Astrophysical Journal Supplemental Series*, **1**, 1. (Cited on pages 18, 115, 141, 143, 144, 181 and 200.)
- WILSON, O.C. & VAINU BAPPU, M.K. (1957). H and K Emission in Late-Type Stars: Dependence of Line Width on Luminosity and Related Topics. *Astrophysical Journal*, **125**, 661. (Cited on page 180.)
- WILSON, R.E. (1953). General catalogue of stellar radial velocities. *Carnegie Institute Washington D.C. Publication*, 0. (Cited on page 164.)
- WILSON, R.E. (1979). Eccentric orbit generalization and simultaneous solution of binary star light and velocity curves. *Astrophysical Journal*, **234**, 1054–1066. (Cited on page 57.)
- WILSON, R.E. (1990). Accuracy and efficiency in the binary star reflection effect. *Astrophysical Journal*, **356**, 613–622. (Cited on page 63.)
- WILSON, R.E. & DEVINNEY, E.J. (1971). Realization of Accurate Close-Binary Light Curves: Application to MR Cygni. *Astrophysical Journal*, **166**, 605. (Cited on pages 56 and 118.)
- WOOD, F.B. (1951). Photometry of Zeta Aurigae in the 1947-1948 Eclipse. *Astrophysical Journal*, **114**, 505. (Cited on page 111.)
- WOOTTEN, A. & THOMPSON, A.R. (2009). The Atacama Large Millimeter/Submillimeter Array. *IEEE Proceedings*, **97**, 1463–1471. (Cited on page 79.)

REFERENCES

- WRIGHT, K.O. (1959). The inner chromosphere of the K-type component of 31 Cygni as observed at the 1951 eclipse. *Publications of the Dominion Astrophysical Observatory Victoria*, **11**, 77–141. (Cited on pages 18, 141 and 200.)
- WRIGHT, K.O. (1970). The Zeta Aurigae stars. *Vistas in Astronomy*, **12**, 147–182. (Cited on page 111.)
- ZANSTRA, H. (1941). On the weakening of the polarisation effect by collision damping. *Monthly Notices of the Royal Astronomical Society*, **101**, 273. (Cited on page 34.)
- ZARRO, D.M. & RODGERS, A.W. (1983). Stellar chromospheres - H-alpha and CA II K profiles. *Astrophysical Journal Supplemental Series*, **53**, 815–868. (Cited on pages xviii, 177 and 178.)
- ZEILIK, M., GREGORY, S.A. & SMITH, E.V.P. (1992). *Introductory astronomy and astrophysics*. (Cited on page 3.)
- ZERNIKE, F. (1938). The concept of degree of coherence and its application to optical problems. *Physica*, **5**, 785–795. (Cited on page 76.)